BARNARD W O

STRUCTURAL AND ELECTRICAL INVESTIGATION OF OHMIC CONTACTS TO GALLIUM ARSENIDE AND INDIUM PHOSPHIDE

PhD UP 1991

Digitised by the Department of Library Services in support of open access to information, University of Pretoria, 2021

Structural and electrical investigation of ohmic contacts to gallium arsenide and indium phosphide

by

Wolsey Otto Barnard

Submitted in partial fulfillment of the requirements
for the degree:

Philosophiae Doctor

in the Faculty of Science at the
University of Pretoria, Pretoria

Promoter: Professor J B Malherbe
Co-promoter: Professor F D Auret

FEBRUARY 1991

Digitised by the Department of Library Services in support of open access to information, University of Pretoria, 2021

Opgedra aan Maureen, Conrad, Pa Hennie en Ma Kitty

------oOo------

Prediker 12: 12-13 *"Die belangrikste van alles is: My seun, wees versigtig! Daar kom nie 'n einde aan die skryf van baie boeke nie, te veel studie ooreis die liggaam. Die slotsom van alles wat jy gehoor het, is dit: Dien God en gehoorsaam sy gebooie. Dit is wat van die mens gevra word"*

Digitised by the Department of Library Services in support of open access to information, University of Pretoria, 2021

DANKBETUIGINGS

My opregte dank aan:

- Professor J B Malherbe vir sy studieleiding en volgehoue betrokkenheid in die voltooiing van die studie.

- Professor F D Auret vir sy ondersteuning en opbouende besprekinge.

- Mnr G Myburg vir sy hulp in verband met die vervaardiging van die kontakte, asook baie ure se stimulerende gesprekke en ondersteuning.

- Dr Le Roux Strydom en Mnr W Louw van MATTEK, WNNR wat goedgunstiglik, by verskeie geleenthede, die SAM aan my beskikbaar gestel het. Sonder hul openhartigheid sou die studie nie voltooi kon word nie.

- Mnr A M F M Van der Kallen, mnr R C Dumas en mnr R Van Weele vir tegniese bystand en die bou van apparaat.

- Al die lede van die Fisika Departement (U.P.) vir hul ondersteuning en bystand - hoe klein of groot dit ook al mag gewees het.

- Mev M van Wyk vir die groot opoffering met die tik van die proefskrif.

- Maureen en Conrad vir hul liefdevolle onderskraging en geduld tydens die voltooiing van die studie.

- Dr G Gouws en mev E Relling vir hulp in verband met die taalversorging van die proefskrif.

- WNNR en SNO vir geldelike bystand aan die Departement en wat gevolglik dit moontlik gemaak het om die studie te voltooi.

Digitised by the Department of Library Services in support of open access to information, University of Pretoria, 2021

OPSOMMING

Strukturele en elektriese ondersoek van ohmiese kontakte op galliumarsenied en indiumfosfied

deur

Wolsey Otto Barnard

Promotor: Prof J B Malharbe
Mede-promotor: Prof F D Auret

Proefskrif ingedien vir die graad Ph.D.

In die tesis word die vervaardiging en karakterisering van ohmiese kontakte op n-tipe GaAs en InP bespreek. Die hoof oogmerk met die studie was om aan te toon dat daar 'n duidelike korrelasie te vind is tussen die interdiffusie en metallurgiese verbindings wat plaasvind tussen die metaalkontakte en die halfgeleier substrate gedurende uitgloeiing, en die ooreenstemmende verandering in die elektriese eienskappe. Nadat 'n oorsig gegee is van die vervaardigingstegnieke en ohmiese metaal kontak sisteme wat op n-tipe GaAs en InP gebruik word, is huidige metaal-halfgeleier koppelingsteorie bespreek. Hierdie gedeelte bevat ook 'n bespreking oor die verskillende tegnieke wat gebruik word om spesifieke kontakweerstand te meet. Verder is die eksperimentele prosedures en apparatuur wat gebruik is ook bespreek.

Auger elektron spektroskopie (AES) is gebruik om die GaAs en InP oppervlakke te bestudeer na verskillende chemiese skoonmaak en ets behandelings. Die resultate is gebruik as agtergrondskennis

Digitised by the Department of Library Services in support of open access to information, University of Pretoria, 2021

tydens die vervaardiging van ohmiese kontakte. In die bestudering van Ni en In as benattingsmetale tesame met Au-Ge op n-tipe GaAs, is die gevolgtrekking gemaak dat Ni chemies en fisies 'n beter kontak lewer as die geval met In. Die morfologie van Ni/Au-Ge kontakte op GaAs is verbeter deur gebruik te maak van ioon-inplantering. Uit struktuurstudies volg dat die nie-egalige oppervlakke wat Au-Ge tipe kontakte veroorsaak, in verband gebring kan word met 'n Au-Ge-As fase wat gevorm word by die metaal-GaAs intervlak.

Kontakte op n-tipe InP is ook bestudeer. Duidelik waarneembare sydelingse vergroting van uitgegloeide Au en Au-basis kontakte op InP is ondervind. As gevolg hiervan, is daar geëksperimenteer met alternatiewe vervaardigingstegnieke en ohmiese kontaksisteme. Twee sulke sisteme is die Ti/Pt en Ti/Ni metaalkombinasies. AES, morfologie en spesifieke kontakweerstandmetings is uitgevoer op hierdie kontakte, wat beide op Ar^{+} verstuifde en nie-verstuifde InP substrate vervaardig is. Hierdie resultate is vergelyk met die van die algemeen gebruikte Ni/Au-Ge kontaksisteem. Die laasgenoemde sisteem het die laagste spesifieke kontakweerstand gelewer, maar die beste morfologie is verkry met die Ti/Ni kontaksisteem.

Digitised by the Department of Library Services in support of open access to information, University of Pretoria, 2021

SUMMARY

Structural and electrical investigation of ohmic contacts to gallium arsenide and indium phosphide

by

Wolsey Otto Barnard

Promoter: Prof J B Malherbe
Co-promoter: Prof F D Auret

Thesis submitted for the Ph.D. degree

This dissertation is concerned with the fabrication and characterization of ohmic contacts to n-type GaAs and InP. The main aim was to correlate the interdiffusional and metallurgical reactions that occurred between the metal and the semiconductor substrates during the annealing step, with the corresponding electrical observations. Following a review of the fabrication techniques and ohmic metallization contact systems used on n-type GaAs and InP, present metal-semiconductor junction theories are discussed. This includes a discussion of the various techniques used for specific contact resistance measurements. Furthermore, the experimental procedures and equipment used are also presented.

Auger electron spectroscopy (AES) was utilized to investigate GaAs and InP surfaces after different chemical cleaning and etching treatments. These results are used as background for the fabrication of ohmic contacts. By comparing Ni and In as wetting agents, together with Au-Ge on n-type GaAs, the deduction was made that Ni acts chemically and physically to produce a better

Digitised by the Department of Library Services in support of open access to information, University of Pretoria, 2021

contact than In. The morphology of Ni/Au-Ge contacts on GaAs was improved by introducing an ion implantation step. From structural investigations it follows that the non-uniformity of the Au-Ge based contacts can be related to an Au-Ge-As phase that was formed at the metal-GaAs interface region.

In parallel with the work on GaAs, contacts to n-type InP have also been studied. Noticeable lateral spreading of annealed Au and Au-based contacts to InP was observed. As a result, alternative fabrication techniques and ohmic contact systems were investigated. Two such systems were the Ti/Pt and Ti/Ni metallization schemes. AES, morphology studies and specific contact resistance (r_c) measurements of these contacts to Ar^+ sputtered and non-sputtered InP substrates were carried out. These results were compared with the widely used Ni/Au-Ge contact system. The latter system yielded the lowest specific contact resistance values, while the best surface morphology was observed with the Ti/Ni contact system.

Digitised by the Department of Library Services in support of open access to information, University of Pretoria, 2021

'I observed that in several natural and artificial sulphides, both single crystals and rough samples, the resistance was different by up to 30% depending on the direction and intensity of the current... The difficulty in these experiments lay in obtaining reliable contacts.'

F. Braun; Pogggendorff's Annalen **153** (1874) 556.

Although the technology has changed dramatically, the problem is still the same.

Digitised by the Department of Library Services in support of open access to information, University of Pretoria, 2021

INDEX

PAGE

CHAPTER 1: **INTRODUCTION** 1

CHAPTER 2: **OVERVIEW OF OHMIC CONTACT SYTEMS TO n-TYPE GaAs AND InP** 5

2.1 Introduction 5

2.2 Fabrication techniques 6

2.2.1 Introduction 6
2.2.2 Substrate preparation 7
2.2.3 Metallization 8
2.2.4 Annealing of metal-semiconductor systems 9

2.2.4.1 Alloy regrowth 9
2.2.4.2 Sintering 10
2.2.4.3 Ion beam mixing 11

2.2.5 Non-alloyed ohmic contacts 11

2.2.5.1 Ion implantation 11
2.2.5.2 Epitaxy 12
2.2.5.3 Sputter-etched surfaces 12

2.3 Problems in the processing of ohmic contacts 13

2.3.1 Introduction 13
2.3.2 Ohmic contacts to n-type GaAs 13

Digitised by the Department of Library Services in support of open access to information, University of Pretoria, 2021

PAGE

2.3.2.1 Annealing of ohmic contacts 13

2.3.2.1.1 Conventional annealed contacts 13
2.3.2.1.2 Sintered contacts 24
2.3.2.1.3 Laser and electron beam annealing 26

2.3.2.2 Ion beam mixing 30
2.3.2.3 Non-alloyed ohmic contacts 32

2.3.2.3.1 Ion implantation 32
2.3.2.3.2 Epitaxial layers 34

2.3.3 Ohmic contacts to n-type InP 37

2.3.3.1 Metallization systems 37
2.3.3.2 Metal/alloy - InP interface 38

2.4 Conclusions 41

CHAPTER 3: PROPERTIES AND CHARACTERIZATION OF OHMIC CONTACTS 43

3.1 Introduction 43

3.2 Metal-semiconductor contacts 43

3.2.1 Classical metal-semiconductor contacts 43
3.2.2 Width of the depletion region 47
3.2.3 Contacts in the presence of surface states . 47
3.2.4 Other models for barrier formation on semiconductors 51

3.3 Metal contacts on GaAs and InP 53

Digitised by the Department of Library Services in support of open access to information, University of Pretoria, 2021

PAGE

3.4 Current transport characteristics 56

3.4.1 Introduction 56
3.4.2 Thermionic emission 58
3.4.3 Tunneling 58
3.4.4 Recombination in the depletion region and hole rejection 60

3.5 Ohmic contacts 61

3.5.1 Introduction 61
3.5.2 Models of ohmic contacts 63

3.6 Specific contact resistance measurements 66

3.6.1 Cox and Strack technique 69
3.6.2 Four-point method 70
3.6.3 Shockley extrapolation model 72
3.6.4 Transmission line model 74
3.6.5 Kelvin resistor method 77

CHAPTER 4: EXPERIMENTAL PROCEDURES 79

4.1 Introduction 79

4.2 Sample preparation 79

4.2.1 Cleaning process 79
4.2.2 Photolithography 81
4.2.3 Evaporation step 84
4.2.4 Annealing process 88

4.3 Description of techniques used 90

4.3.1 Auger electron spectroscopy (AES) 90
4.3.2 Secondary ion mass spectroscopy (SIMS)...... 103
4.3.3 X-ray diffraction 105

Digitised by the Department of Library Services in support of open access to information, University of Pretoria, 2021

PAGE

4.3.4 Microscopy 107
4.3.5 I-V measurements 108
4.3.6 Specific contact resistance (r_c) measurements 110

CHARACTER 5: RESULTS AND DISCUSSION 113

5.1 General 113

5.2. GaAs substrate material 113

5.2.1 GaAs surface studies 114
5.2.2 Comparison of Ni and In as wetting agents .. 120
5.2.3 Investigation of ohmic contacts after ion implantation and annealing 139

5.3 Results of contacts on n-type InP 151

5.3.1 AES investigation of InP surfaces 152
5.3.2 Au-Ge/Ni contacts to n-InP 160
5.3.3 Structural investigation of Au contacts to InP 165
5.3.4 Ag based contacts to n-InP 181
5.3.5 Alternative ohmic contacts systems to n-InP. 189

5.3.5.1 Au/Ni/Au-Ge/InP contact system . 190
5.3.5.2 Au/Pt/Ti/InP contact system 199
5.3.5.3 Au/Ni/Ti/InP contact system 206

CHAPTER 6: CONCLUSIONS 214

6.1 Introduction 214

6.2 GaAs surface and ohmic contact characterization 214

Digitised by the Department of Library Services in support of open access to information, University of Pretoria, 2021

PAGE

6.2.1 GaAs surface studies 214
6.2.2 Comparison between Ni and In as wetting agents 215
6.2.3 Effect of ion implantation on ohmic contacts 215

6.3 InP surface and contact characterization 216

6.3.1 AES investigation of InP surfaces 216
6.3.2 Au-Ge/Ni ohmic contacts to n-InP 216
6.3.3 Au contacts to InP 217
6.3.4 Ag based contacts to InP 218
6.3.5 Alternative ohmic contacts to InP 218

6.3.5.1 Au/Ni/Au-Ge/InP contact system ... 218
6.3.5.2 Au/Pt/Ti/InP contact system 219
6.3.5.3 Au/Ni/Ti/InP contact system 219

REFERENCES 220

LIST OF WORK PUBLISHED DURING THIS STUDY 247

Digitised by the Department of Library Services in support of open access to information, University of Pretoria, 2021

CHAPTER 1

INTRODUCTION

The study of metal-semiconductor contacts goes back to 1874, when Brawn [Br 74] reported the asymmetrical nature of conduction between metal points and a lead-sulphide crystal. Due to the present practical importance of metal-semiconductor contacts, (ohmic and Schottky), more scientific interest has been generated by these contracts than any other during the last two decades. However, only ohmic contacts will be discussed in this dissertation.

In principle, the term "ohmic" refers to a contact between a metal and a semiconductor which has a linear current-voltage (I-V) characteristic in both directions. In practice however, the contact is considered ohmic if the contact resistance is very small compared with the device resistance [Pi 83].

GaAs and InP based devices have become increasingly important in the last ten to fifteen years due to a rapidly growing demand for high performance devices in the areas of communication, radar and electronic warfare. Compared to Si these III-V semiconductors have high mobilities and high saturated drift velocities. As a result, such devices can operate at microwave frequencies, where Si devices are unable to function. Further, the ability of III-V semiconductors to produce semi-insulating substrates allows low parasitics and true monolithic circuit implementation.

Most of the devices manufactured on GaAs and InP are made on n-type substrates. Field effect transistors (FET's) have dominated the GaAs device fabrication the last couple of years. The metal-semiconductor FET (MESFET) is the most commonly used FET. A cross-section diagram of such a FET is shown in Fig. 1.1. A MESFET consist of two ohmic contacts called the source and drain

Digitised by the Department of Library Services in support of open access to information, University of Pretoria, 2021

that allow current to flow into or out of the GaAs. The metal strip between these two contacts is called the gate, which consists of a metal Schottky barrier.

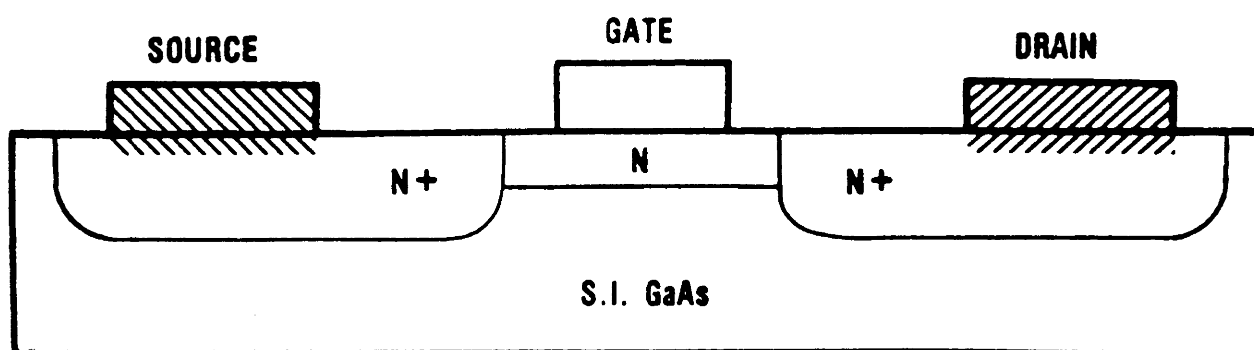

Figure 1.1: A cross-section of a MESFET. The highly doped n+ GaAs underneath the source and drain contacts serves to lower series resistance.

InP, on the other hand, plays an important role in modern optical communication systems. Interest in this field is centered on the wavelength range 1,3 to 1,5 μm, where optical fibers display very low attentuation and dispersion losses. Carefully designed semiconductor devices are thus required for this application. The semiconductor systems InGaAs and InGaAsP are the most promising for use in light sources and detectors, particularly since the alloys of these systems lattice match excellently with InP. Such a InGaAs/InP p-i-n photodiode is shown schematically in Fig. 1.2.

From the examples shown above, it is clear that for any semiconductor device to operate, at least one ohmic contact is required. These contacts provides the electrical link between the active region of the semiconductor and the external circuitry.

Digitised by the Department of Library Services in support of open access to information, University of Pretoria, 2021

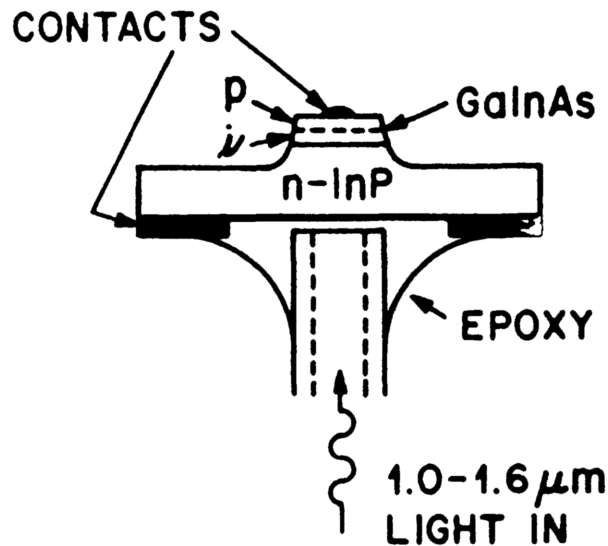

Figure 1.2: Schematic illustration of an InGaAs/InP p-i-n photodiode.

Originally, the demands on metallization for devices fabricated on III-V compounds were modest. This was due to the fact that it was mostly needed for devices such as lasers and solar cells. For these applications, a contact resistance in the range 10^{-1} - 10^{-5} Ωcm^2 was desirable. Very stringent requirements were however placed on ohmic contacts for devices such as metal-semiconductor field effect transistors (MESFET's), monolithic microwave integrated circuits (MMIC's), high electron mobility transistors (HEMT's), PIN/FET (a PIN diode integrated with a FET on the same substrate), etc. For ohmic contacts to these devices the following additional requirements are essential:

a) specific contact resistance of less than $5x10^{-6}$ Ωcm^2,
b) good surface morphology,
c) thermal stability, and
d) reproducibility.

Digitised by the Department of Library Services in support of open access to information, University of Pretoria, 2021

As a result, this dissertation sets out to investigate ohmic contact systems to n-type GaAs and InP that fulfill the above requirements.

In Chapter 2 an overview of the different techniques used to fabricate ohmic contacts is given. This chapter also includes a short literature survey for the period 1980-1990 of metal combinations that form ohmic contacts to n-type GaAs and InP. Further, a brief discussion on the shortcomings of the various metallization systems and annealing techniques is also given. Chapter 3 contains the theoretical background to the basic physics of metal-semiconductor junctions, with special reference to metal contacts to GaAs and InP. The theory of ohmic contacts and specific contact resistance measurement techniques is also discussed.

The general sample preparation procedures used for GaAs and InP are presented in Chapter 4. A description of apparatus used for structural and electrical investigations is also given in this chapter. The experimental results are presented and discussed in Chapter 5. This chapter is divided into two sections. These sections deal with results obtained from surface, structural and electrical studies on ohmic contacts to n-type GaAs and InP respectively.

Finally, some important conclusions drawn from this study are summarized in Chapter 6.

Digitised by the Department of Library Services in support of open access to information, University of Pretoria, 2021

CHAPTER 2

OVERVIEW OF OHMIC CONTACT SYSTEMS TO n-TYPE GaAs and InP

2.1 INTRODUCTION

During the past few years a number of review articles dealing with ohmic contacts to GaAs have appeared in the literature [Ri 75, Yo 80, Sh 81, Mo 81b, Pi 83 and Pa 85b]. Only one review paper has appeared concerning ohmic contacts to InP [Ku 81]. For GaAs, these review articles have been concerned with publications up to ~1982 and for InP up to ~1981. Therefore, this chapter fulfils an important purpose in extending these surveys concerning metallization systems and techniques utilized for ohmic contacts to these III-V compound semiconductors to include the most recent work.

Although both GaAs and InP belong to the III-V family, each has unique characteristics when metallized. The reason for this is that ohmic contacts can be seriously affected by a number of factors, such as interface layers, surface damage, minority carrier injection, energetically deep lying traps, etc. [Ri 75], that influence conduction through the metal-semiconductor contact. The study of these factors is not however the purpose of this chapter. Rather, the practical aspects of ohmic contacts to n-type GaAs and InP will be discussed, with particular reference to:

(a) fabrication techniques,

(b) metal systems (metal combinations used to form ohmic contacts) reported in literature for the period 1980-1990, and

(c) a brief discussion on the shortcomings of the various systems and annealing techniques.

Digitised by the Department of Library Services in support of open access to information, University of Pretoria, 2021

2.2 FABRICATION TECHNIQUES

2.2.1 Introduction

As a result of the problems influencing conduction through metal-semiconductor contacts mentioned in the previous section, the fabrication of ohmic contacts is sometimes considered to be more of an art than a science and every laboratory tends to have its own favourite "recipes" which involve particular metal or alloy systems, deposition methods and forms of heat treatment. Most of the recipes appear to depend on one of the following four principles [Rh 82].

(a) By creating a thin layer of very heavily doped semiconductor immediately adjacent to the metal, the depletion region is reduced. This, together with field emission results in the contact having a very low resistance at or close to zero bias.

(b) By growing a changing composition semiconductor layer on top of the substrate in such a way that the Fermi level of the newly formed semiconductor is pinned in the conduction band. An ohmic contact can be obtained by depositing a metal as the final layer.

(c) If the surface of the semiconductor is damaged, (e.g. by sand-blasting, ion etching, etc.) crystal defects may be formed near the surface. These act as efficient recombination centres. If the density of these is high enough, recombination in the depletion region will become the dominant conduction mechanism, and will cause a significant barrier height lowering and an accompanying decrease in the contact resistance.

(d) It should also be possible to create an ohmic contact to a n-type semiconductor by using a metal with a work function less than the work function of the semiconductor [Rh 78].

Digitised by the Department of Library Services in support of open access to information, University of Pretoria, 2021

The theory behind these principles is discussed in Chapter 3. The most widely used of these methods is that described in (a) above. The remainder of this section is devoted to the practical aspects of ohmic contact fabrication such as substrate preparation, metallization and annealing techniques.

2.2.2 Substrate preparation

The fabrication of ohmic contacts to n-type GaAs and InP usually involves similar processing steps. (However, more caution is needed in handling InP, because of its brittleness.) Therefore, the fabrication techniques will be discussed in general, but if a specific processing step is unique to one of the substrates, it will be discussed separately (also see Chapter 4).

Processing of a purchased wafer usually starts by degreasing the sample in organic solvents, followed by light etching, rinsing in DI water and drying. Metal masks or photolithography can be used to produce a selected pattern. Normally a light etching step is introduced following the photolithographic process. Prior to the deposition step, the surface may be heated or sputter cleaned in vacuum, to remove the oxide layer that formed during the loading of the samples. Sputtering of GaAs may introduce damage to the surface which might influence the long-term stability of the contacts [Wo 87], but for n-type GaAs the immediate result is a reduction in barrier height [Me 89a and Au 91b].

Williams [Wi 82] has observed that the InP surface was far more sensitive to Ar^+ bombardment than the GaAs surface under the same experimental conditions. It is a well documented result that with sputter etching of InP, an In rich surface is formed [Sk 80, Wi 82, Da 84, Gr 87, Ba 91, Ma 91] as well as results shown in Chapter 5. This In rich 'layer' can be regarded as a degenerate n-type 'layer' on which non-alloyed ohmic contacts can be formed [Sk 80 and Da 84]. This will be discussed in more detail in Chapter 5.

Digitised by the Department of Library Services in support of open access to information, University of Pretoria, 2021

2.2.3 Metallization

Metallic contact layers are usually deposited in a vacuum of better than 10^{-6} torr, except in the case where electrolytic deposition methods are used. Vacuum deposition methods include resistive heating, electron beam and sputter deposition. Other deposition techniques include metallic epitaxial growth by means of MBE or LPE.

The most widely used method for ohmic contact fabrication relies on the formation of a tunnelling metal/semiconductor junction by creating a thin n^+ semiconductor layer at the interface. This doped layer at the semiconductor interface is formed before the metal deposition (via methods such as diffusion, ion implantation or epitaxy) or during the metallization step. The metal layer deposited usually contains a dopant in order to form a n^+ layer at the semiconductor's surface after a suitable heat treatment.

In order to obtain smooth ohmic contacts, "wetting agents" such as Ni [Br 67], Pt [Ri 75. Le 80] and In [Ch 77, Ba 88] are deposited to improve the wetting of the metallic film and to increase the solubility of the semiconductor.

The properties of ohmic contacts depend critically on not only the order of the metal layers, but also on their thickness, metal deposition sequence, deposition conditions and heat treatment properties. In order to prevent the loss of volatile components such as As and P during heat treatment, the contacts are normally capped with SiO_2 [Na 82, La 86b], ZrB_2 [Sh 85], TiB_2 [Sh 86] or WSi_2 [Wu 87] films. These films are chemically inert during annealing but exert a stress which tends to keep the film on the surface, resulting in a smoother ohmic contact surface.

Annealing is normally performed in vacuum or in an inert atmosphere such as Ar or N_2-H_2-gas (forming gas). Annealing can also be done under an overpressure of As or P. This is achieved by annealing a GaAs or InP wafer at a higher temperature in the

Digitised by the Department of Library Services in support of open access to information, University of Pretoria, 2021

vicinity of the annealed samples. Alternatively, GaAs or InP wafers can be placed face down on the samples during the annealing step. In the next section the principles of each annealing technique will be discussed.

2.2.4 Annealing of metal-semiconductor systems

2.2.4.1 Alloy regrowth

The term 'alloy regrowth' means the growth of a highly doped semiconductor region at the metal-semiconductor interface by means of a dissolution-segregation process. Contacts are heated to a temperature higher than the eutectic temperature of the metallization layer(s). It is believed that during this heating, one or several contact components are molten and some of the semiconductor is dissolved in the melt. On cooling, the dopant segregates from the melt, together with the solidifying semiconductor. Hence, a metal/n^+ GaAs contact is formed.

The heating after metallization may be accomplished by several methods including furnace (oven), strip heater, flash lamp, sending a current through the semiconductor, laser and electron beam annealing. Ovens are at present the most popular choice for alloy regrowth of metal-semiconductor interfaces. The latter four methods are generally referred to as rapid thermal annealing techniques (RTA). The temperature rise time for strip heaters and flash lamps are however in the order of a few seconds, while the thermal annealing cycle of high power laser or electron beams are between 1 and 10^2 nanoseconds [Ba 84]. The use of flash lamps and graphite strip heaters seems especially promising for production annealing, while laser and electron annealing are still largely experimental.

With these latter methods, a laser or electron beam is used to anneal well defined, localized regions in the immediate vicinity of the surface of a semiconductor. These methods can be employed either to provide high electron concentrations through a process

Digitised by the Department of Library Services in support of open access to information, University of Pretoria, 2021

of liquid phase epitaxial growth of an ion-implanted semiconductor, or to mix metal overlayers with an underlying semiconductor through a process of rapid melting and resolidification so as to produce an ohmic contact.

As far as the energy absorption, necessary to alloy contacts, is concerned, pulsed electron beams are preferable to pulsed laser beams. This is because the high optical reflectivity of the metals does not affect the electron beam.

As described above, the local heating time during pulsed annealing is typically 1 to several hundreds of nanoseconds. Little solid phase diffusion or annealing can take place in this time, and the damage removal and alloying invariably result from melting of a semiconductor near-surface or from more localized interface (eutectic) melting phenomena. Annealing, alloying and solid phase reactions can also be induced in a time scale between that of the pulsed wave annealing and the long-time annealing of conventional furnace processing. A scanned continuous wave (CW) laser or electron beam can locally heat surface regions in about 1 to 10^2 ms, whereas rapid bulk heating methods can heat and cool the entire substrate in a matter of seconds. These methods allow annealing, diffusion and reaction processes to proceed in the solid phase, and can also be used to induce surface or interface melting and alloying in a more controllable manner than conventional furnace heating.

Lasers such as Nd:YAG, Ruby and CO_2 are commonly used for laser annealing, while electron beam processing is performed by PEBA (pulsed electron beam annealing), modified SEM's and spark annealing.

2.2.4.2 Sintering

In the sintering technique, ohmic contacts are formed by solid phase reactions resulting in a metal-semiconductor compound or compounds during longer heat treatment cycles that are normally used in the alloying regrowth technique. Since no melting is

Digitised by the Department of Library Services in support of open access to information, University of Pretoria, 2021

involved in this technique (due to the lower annealing temperature used in comparison to the alloy technique), good uniformity of the contacts is normally obtained. Furnace heating is normally used for the sintering of ohmic contacts.

2.2.4.3 Ion beam mixing

Ion beam mixing is the ability of a flux of energetic ions to produce physical mixing of atoms across an interface. In many respects, the process resembles thermal diffusion, although generally it can be achieved at relatively low substrate temperatures. These energetic ions can increase the sample temperature. Raising sample temperature has however a relatively small effect in the cascade mixing regime and can even help to speed up the reaction.

It is interesting to note that with ion beam mixing, one can choose either to implant electrically active ions (e.g. dopant ions such as Se, Te, Si, Ge or Sn) or to use the ions purely for interface mixing. If only mixing is wanted, implantation of As, Ga, Ar, Kr, etc. ions can be used. Generally, an acceleration voltage of between a few keV to 300 keV is used, depending on the metallization system and the layer thickness.

To date no ohmic contacts to InP have been obtained by means of this technique.

2.2.5 Non-alloyed ohmic contacts

2.2.5.1 Ion implantation

Shallow ion implantation with high doses are used to introduce dopants on the near surface region of a semiconductor. In order to activate these dopants, a post implant annealing step is required. This annealing step is also important to anneal out the defects introduced in the host substrate by the implanted ions. Various annealing methods are used and are the same as those utilized in ohmic contact processing, except that the annealing temperatures or energies are higher.

Digitised by the Department of Library Services in support of open access to information, University of Pretoria, 2021

A eutectic alloy or metal overlayer(s) are then deposited onto the heavily doped semiconductor surface. These contacts are then ohmic, without the need of an annealing step (non-alloyed ohmic contacts), because of the resultant tunneling metal-semiconductor junction.

2.2.5.2 Epitaxy

In this technique an ohmic contact is formed on a n^+ epitaxial grown semiconductor layer. An epitaxial layer can be grown by means of liquid phase epitaxy (LPE), vapour phase epitaxy (VPE), organic-metal vapour phase epitaxy (OMVPE) or molecular beam epitaxy (MBE). The metal(s) deposited on the highly doped epitaxially grown layer (homoepitaxial layer) is not alloyed or reacted with the semiconductor and the ohmic behaviour arises from current transport through the metal-semiconductor barrier by means of a tunnelling process.

It is also possible to form ohmic contacts by growing a GaAs expitaxial layer onto GaAs and onto this layer, an expitaxial graded ternary, such as a n-type InGaAs layer. By gradually changing the composition of this epitaxial layer, a smaller bandgap semiconductor is obtained. A metal is then deposited onto this hetero-expitaxial layer (heterojunction contacts) and a non-annealed ohmic contact is formed due to a lowering of the barrier height between the metal and the semiconductor.

2.2.5.3 Sputter-etched surfaces

In a previous section (2.2.2) the different behaviour of InP and GaAs surfaces under sputter etching was briefly discussed. The surface behaviour of InP has permitted the formation of non-alloyed ohmic contacts to n-type InP. The In rich surface is probably responsible for this contact behaviour, which is independent of the particular contacting material. Furthermore, with ion sputtering some defects, which can act as deep levels, may be introduced into the semiconductor [Au 91]. These deep levels will tend to narrow the depletion layer and hence

Digitised by the Department of Library Services in support of open access to information, University of Pretoria, 2021

tunneling through the layer will become the dominant conduction mechanism. This method permits the use of a barrier metal/noble metal combination for non-alloyed ohmic contacts to n-type InP.

2.3. PROBLEMS IN THE PROCESSING OF OHMIC CONTACTS

2.3.1 Introduction

From the above comments on contact fabrication techniques, one can choose a method which permits, in principle, the realization of contacts with lowest specific contact resistance (r_c). However, the precise comparison of the various techniques is hindered by the differences in experimental conditions. Furthermore, practical factors such as the availability and/or cost of equipment influence the choice of the ohmic contact processing method. Thus, instead of suggestions for 'the best method', it is more useful to discuss the problems of the ohmic contact technology and to show the possibilities offered by recently developed methods. Ohmic contacts to GaAs will be discussed first, followed by ohmic contacts to InP.

For ohmic contacts to GaAs, fabrication processes will be discussed according to the annealing methods, except for the last section which is devoted to non-annealed contacts. In the case of ohmic contacts to InP, the discussion is only divided into annealed (all the various annealing techniques grouped together) and non-annealed contacts.

2.3.2 Ohmic contacts to n-type GaAs

2.3.2.1 Annealing of ohmic contacts

2.3.2.1.1 Conventional annealed contacts

Furnace alloyed ohmic contacts have been extensively studied and are generally the favoured contact fabrication technique in present day device technology. Table 2.1 contains a summary of the metallization systems used, together with their references in

Digitised by the Department of Library Services in support of open access to information, University of Pretoria, 2021

the literature. (The convention used in this dissertation is as follows; Au/Ge/GaAs represents a layer of gold on top of a germanium layer on GaAs and Au+Ge/GaAs represents co-evaporation of Au and Ge on GaAs, while Au-Ge/GaAs represents an alloy of gold and germanium on GaAs.) Note that only furnace, graphite strip heater and lamp annealing (RTA) are covered in Table 2.1. From this table it is clear that the most commonly used ohmic contact systems are based upon the Au-Ge eutectic metallization scheme. In reality, the alloying techniques (furnace, lamp, etc. alloying) possess inherent problems. In particular, melting and resolidification often cause 'balling up' of overlay metals, which results in non-uniformity of the alloyed regions [Pa 85]. Although this problem is typically circumvented by adding Ni, In, Pt, etc. to the metallization system to wet the surface, the high reactivity of these metals with GaAs makes the alloying process very difficult to control [Ba 84]. Specific contact resistance values as low as 10^{-9} $\Omega.cm^2$ [Ni 88], but more typically ~10^{-6} $\Omega.cm^2$, are obtained. The resistance of ohmic contacts can also be expressed in terms of ohm.mm (Ω.mm), due to experimental evidence that the contact resistance does not critically depend on the source and drain size, but only on the width of the pad [Gu 86]. The reason is that with low resistivity contacts, almost all current flows through the front edge of the contact pad. Various capping layers have been used and these are also summarized in Table 2.1 (also see section 2.2.3).

Table 2.1: Conventionally annealed ohmic contacts to n-type GaAs

Metallization	Annealing		r_c	Remarks	Ref.
	°C	Time	(Ωcm^2)		
In	350	60 sec	$1x10^{-5}$	Bad morphology, InGaAs heterojunction	La 84
In	900	10 min	~$9x10^{-4}$	InGaAs interfacial layer	Ot 88

Digitised by the Department of Library Services in support of open access to information, University of Pretoria, 2021

Metallization	Annealing		r_c	Remarks	Ref.
	°C	Time	(Ωcm^2)		
Au	405	20 min	Ohmic	Ga-Au rich crystallites responsible for ohmic behaviour	Li 86
Ag/In	200	15 min	$5x10^{-2}$	AES; Ga-In-Al-As-growth on GaAs	Ku 82
In/Pt	500	15 sec	$2x10^{-6}$	InGaAs heterojunction improve r_c and morphology	Ma 85 Ma 86
In/Pd	500	20 sec	$1x10^{-7}$	RTA; uniform surface and stable during annealing cycles at 400°C	Al 87
Au/Ni/Sn-Ni	420	10 sec	$5x10^{-5}$	Low Sn concentrations in GaAs	Ay 81
Au/Sn/Pd	420	2 min	$2x10^{-5}$	Contacts were wet chemical deposited	La 85
Au/Pd	300	2 min	$1x10^{-4}$	Electroless deposition, graded junction	La 86
Ni/In/Ni/W	800-1000	1 sec	~0,3 Ωmm	No change in r_c during annealing for 100 h.	Mu 88
W/Ni/Ni+In/Ni	800-1000	1 sec	~0,3 Ωmm	Lamp annealing (RTA); surface morphology superior to the conventionally used AuNiGe contacts	Mu 87c Mu 88b Sh 89
W/Ni/Ni+In/Ni	800	~7 sec	~0,2 Ωmm	More stable for FET's than AuGeNi contacts	Mu 89

Digitised by the Department of Library Services in support of open access to information, University of Pretoria, 2021

Metallization	Annealing		r_c	Remarks	Ref.
	°C	Time	(Ωcm^2)		
Ni/Au-Te (6% Te)	510	1,5 min	$\sim 5x10^{-7}$	High vapor pressure of Te causes problems during evaporation	Gh 83
Au/Te/Au/Ni	510	15 min	$3x10^{-5}$	Surface morphology of laser annealed contacts superior to furnace annealed contacts	Wu 89
Au/Ag/Au-Ge	490		$\sim 1x10^{-6}$	SEM, EDS - Bad morphology	Mi 80
Pt/Au-Ge	480	3 min	$\sim 1x10^{-6}$	Overlayers result in increase of r_c	Le 80 Le 81
Ni/Au-Ge	480	3 min	$\sim 1x10^{-6}$	Stable with overlayers	Le 81
Ni/Au-Ge	450	2 min	$\sim 5x10^{-4}$	Review of characterization methods	Ro 80
Au/In-Ge	450		Ohmic	SED-EDS, Au-Ge-As and Au-Ge phases	Ra 81
Au/In-Ge	400-500	3 min	Ohmic	Intermetallic phases formed during annealing identified	Gr 83
Au/Au-Ge	450	2,5 min	$9x10^{-7}$	r_c depends on Au-Ge and Au-Ge-As formations	Il 83
Au/Ni/Au-Ge	410	2 min	$\sim 1x10^{-6}$	TEM study	Ku 83
Au-Ge Ni/Au-Ge Au/Ni/Au-Ge	490 490 490	30 sec 30 sec 30 sec	$6x10^{-6}$ $5x10^{-3}$ $6x10^{-5}$	AES and ageing investigations	Ma 83

Digitised by the Department of Library Services in support of open access to information, University of Pretoria, 2021

Metallization	Annealing °C	Annealing Time	r_c (Ωcm^2)	Remarks	Ref.
Au/Ti/Ni/Au/Ge	370		$3x10^{-7}$	Used as ohmic contacts to heterojunction bipolar transistors	It 84
Au/Au-Ge	540	3 sec	$\sim 2x10^{-6}$	IR lamp annealing	Ya 84
Au-Ge	470	45 sec	$1x10^{-5}$	r_C depends on Au-Ge thickness	Ka 84
Ni/Au-Ge Ni/Au/Ge	455 455	3 min 3 min	$\sim 1x10^{-5}$ $\sim 2x10^{-6}$	TEM and X-ray microanalysis	Fa 84
Au/Ni/Au-Ge	390	90 sec	$\sim 3x10^{-7}$	Hot plate annealing	He 84
Au-Ge-Ni	500	2 sec	$\sim 9x10^{-6}$	Lamp annealing	Mo 84
Au/Au/Ge	440	1 sec	$\sim 1x10^{-5}$	IR lamp annealing compared with graphite strip heater	Gu 84
Au/Ge	400	3 min	$8x10^{-6}$	Non-eutectic Au/Ge alloy	Wu 84
Au/Au-Ge-Ni Au/Au-Ge Au/Ni/Au-Ge Au/Au-Ge/Ni	550 420 420 528	2 sec 4 min 4 min 2 sec	$\sim 2x10^{-6}$ $\sim 8x10^{-6}$ $\sim 2x10^{-6}$ $\sim 9x10^{-7}$	Comparison between metal sequence and annealing cycles	La 85b
Au/Ni/Au-Ge	500	50 sec	$7x10^{-8}$	Different ohmic contact test structures for MODFET applications	Ke 85
Au-Ge	400	6 min	$\sim 6x10^{-6}$	X-ray diffraction, TEM, and SIMS characterization	Au 85

Digitised by the Department of Library Services in support of open access to information, University of Pretoria, 2021

Metallization	Annealing °C	Time	r_c (Ωcm^2)	Remarks	Ref.
Ni/Au-Ge	450	5 min	$3x10^{-6}$	Se doped GaAs	Kr 85
Ni/Au-Ge/Ni	365-450	5 min	Ohmic	AES and RBS vs annealing temperature	Bo 86
Ni/Au-Ge Au-Ge/Ni	450	3 min	<0,2 Ω.mm	Varying metal thicknesses to obtain optimal thickness vs r_c	Lo 86
Au/Ni/Au-Ge	~320	1 min	$\sim 1x10^{-5}$	Optimum Ni layer thickness for lower annealing temperatures	Pa 86
Ni/Au-Ge	420	5 min	$\sim 2x10^{-6}$	Contacts can be used for low temperature devices	Gu 86
Ni/Au/Ge	430	15 min	0,2 Ω.mm	GaAs sputter clean prior to metallization. Difference in morphology and increase in r_c if Au/Ge were deposited on non-sputtered surface	Ca 86
Au/Ni/Au-Ge Au/Ni/Au-Ge/Ni Au/Au-Ge/Ni	440 420 420	2 min 2 min 2 min	~0,1 Ω.mm ~0,1 Ω.mm ~0,2 Ω.mm	Metallization layer sequence important for lower r_c	Mu 86
Au-Ge	410	300 sec	$2x10^{-5}$	r_c min. when Ge to Ga ratio is 1	Ku 86
Au/Ge/Pd Au/Ge/Ni	450 450	3 sec 3 sec	$\sim 2x10^{-6}$ $\sim 3x10^{-6}$	Pd much smoother surface and well defined edges	Ch 86
Au/Ni/Ge	440	10 sec	$\sim 5x10^{-6}$	r_c vs heat treatment and	Br 87

Digitised by the Department of Library Services in support of open access to information, University of Pretoria, 2021

Metallization	Annealing °C	Time	r_c (Ωcm^2)	Remarks	Ref.
Au/Ni/Au-Ge Ni/Au-Ge	440 440	3 sec 90 sec	~$1x10^{-5}$ ~$9x10^{-6}$	microstructure	Br 87
Ni/Au-Ge Ni/Ag-Ge	450 600	4 min 4 min	~$7x10^{-5}$ ~$4x10^{-5}$	Furnace vs laser annealing. Good morphology for furnace annealing	Si 87
Au/Ag/Au-Ge	~450	~5 min	~10^{-6}	Morphology improved by thicker Ag layers	Kw 87
Au/Cr/Au/Ge	390	12 min	0,13 Ωmm	Current transport between Au grains and heavily doped semiconductor region	Wi 87
Ni/Au-Ge	430	3 min	~$9x10^{-6}$	Ni to Ge ratio vs r_c	Pr 87
Ni/Au-Ge/Ni	440	2 min	0,1 Ω mm	NiAs(Ge) grains at interface	Sh 87b
Au-Ge/Ni	300	13 min	Ohmic	EBIC, AES-analysis	Hi 88
Ni/Au-Ge	365-450	5 min	Ohmic	AES and RBS vs annealing temperature	Re 88
Ni/Au-Ge	450	~2 min	~$4x10^{-7}$	n^+-GaAs obtained by ion implantation prior to metal deposition	Sa 88
Au/Cr/Au/Ge	390	12 min	0,14 Ωmm	TEM-Smooth morphology and thermally stable	Wi 88
Au/Ni/Au/Ge Au/Ni/Au/Ge/Au/Ni	427-447 417-437	3-5 sec 3-5 sec	0,14 Ωmm 0,1 Ωmm	IR lamp-annealing for FET's	Gi 88

Digitised by the Department of Library Services in support of open access to information, University of Pretoria, 2021

Metallization	Annealing		r_c	Remarks	Ref.
	°C	Time	(Ωcm^2)		
Ni-Ge/Ni	~450°C	~10 sec	~2x10^{-7}	Lamp annealing; good surface morphology	Ne 89
Au-Ge/In	495	5 min	Ohmic	AES and electrical investigations suggest dual phase system	Ba 88
Au/Ni/Au/Ge/ Au/Ni/Au/Ge/ Au/Ni	3-5 sec 2 sec	430-450 420-440	0,14 Ωmm 0,1 Ωmm	Comparison between IR lamp annealing and graphite strip heater	Su 88
Au/Ti/Au/Ge/ Ni	475	1 min	~3x10^{-7}	Metallization layer on graded InGaAs layer	Me 89
Ag/Ge/In	620	3 min	Ohmic	SEM. Ge located on GaAs surface	Se 80
TiW/Ge	850	1-30min	~1x10^{-6}	Ge expitaxially grown layers on GaAs	An 80
Al/Ni/Ge	500	1-30min	1,4x10^{-6}	Can be used for dry etching applications to GaAs I.C fabrication	Zu 86
W/Mo/Ge	800	15 min	~1x10^{-6}	Annealing under As overpressure resulted in ohmic contact	Da 87
W/Mo/Ge	800		~1x10^{-6}	Annealed under As overpressure	Ag 87
W/Ge/Mo/Ge	780	10 min	0,3 Ωmm	r_c influenced by the Mo/Ge ratio and annealing temperature	Mu 87

Digitised by the Department of Library Services in support of open access to information, University of Pretoria, 2021

Metallization	Annealing °C	Annealing Time	r_c (Ωcm^2)	Remarks	Ref.
W/Mo/In/Ge	675	3 min	~0,9 Ωmm	InGaAs phase and fabrication process parameters affecting r_c.	Mu 87b
	940	2 sec	~0,45 Ωmm	Lamp annealing. Ternary InGaAs phase observed	
Au/W/Pd/Ge Au/W/Mo/Ge	800 850	5 sec 10 sec	$\sim 4x10^{-6}$ $\sim 2x10^{-6}$	These contacts systems can withstand RTA schedules used for ion implantation activation	Ch 87
Au/Ni/Au-Ge/Ni	440	2 min	~0,1 Ωmm	Furnace annealing. Unstable ß-AuGa phase.	Mu 89b
W/Ni/Ni-In/Ni	800	~7 sec	~0,3 Ωmm	RTA. Excellent thermal stability	
Pd/Ni/Au-Ge	497	~2sec	$\sim 5x10^{-6}$	RTA. Smooth surface due to reduction in loss of As and in regular Ni penetration	Sk 89
Al/Ni/Ge	425	3-4 min	ohmic	TEM and I-V investigations	Gr 88
W/Ge/In/Ge	900-980	1 sec	~0,5 Ωmm	r_c increase with 100h annealing at 400 °C	Mu 88
Co/Ge Ge/Co	500 500	30 min 30 min	$\sim 3x10^{-4}$ $\sim 3x10^{-4}$	Annealing higher than 400 °C changes the contracts from Schottky to ohmic behaviour	Ge 88
Ni/Au-Ge/Ni	450	2 min	0,1 Ωmm	Surface sputter cleaned prior to Ni deposition	Ca 90

16255 15
11 1771 2

Digitised by the Department of Library Services in support of open access to information, University of Pretoria, 2021

Metallization	Annealing °C	Time	r_c (Ωcm^2)	Remarks	Ref.
Ni/Au/Ge	340	20-60min	$3x10^{-6}$	Surface bombarded with 200 eV Ar^+ ion prior to metal deposition, which leads to a reduction of anneal time	Ne 88
Au/Ge/Ni	460	8-16 min	0,1 Ωmm	TEM, SEM and X-ray analysis	Go 89
Au/Ni/Au-Ge	400	30 sec	$\sim 1x10^{-6}$	RTA. Special end resistance measurements	He 89
Au/Ni/Au-Ge/Ni	425	20 sec	~0,1 Ωmm	Comparison between solid state and solid-state liquid reactions	Ba 89
SiO_2/Ge/Au/Ni	450	30 sec	$2x10^{-6}$	High cooling rate results in lower r_c	Na 82
SiO_2/Ge/Au/Ni	450 450	60 sec 30 sec	$5x10^{-7}$ $\sim 1x10^{-5}$	Ge-Ni (+Au) influence r_c. Lower r_c for SiO_2 cap contacts	He 82
SiO_2/Ni/Au/Ge	425		$5x10^{-7}$	Better reproducibility for IC fabrication	Al 85
SiO_2/Au-Ge	430	1 min	$3x10^{-6}$	SiO_2 passivation layer prevents the formation of a rough surface.	La 86b
SiO_2/In SiO_2/Sn	550 550	30 sec 30 sec	$\sim 2x10^{-4}$ $\sim 3x10^{-5}$	W strip heater SiO_2 serves as a passivation layer and results in contacts with smooth surfaces	Iv 89

Digitised by the Department of Library Services in support of open access to information, University of Pretoria, 2021

Metallization	Annealing		r_c	Remarks	Ref.
	C	Time	(Ωcm^2)		
Au/ZrB_2/Au/ Ge/Ni	580	20 sec	~$1x10^{-7}$	Diffusion barrier for Au	Sh 85
Au/TiB_2/Au/ Ge/Ni	580	20 sec	~$1x10^{-7}$	Contacts stable with long-term heating	Sh 86
Au/WSi_2/Ge	500	2 min	$5x10^{-5}$	Stable for long-term operation	Wu 87
Au/WSi_2/Ge/Pd Au/ZrB_2/Ge/ Au/Ni	330 440		0,04 Ωmm 0,06 Ωmm	Barrier layers have no influence on r_c	Al 88
Au/ZrB_2/Ge/Au/ Ni	440 444	1 sec 1 sec	0,14 Ωmm 0,06 Ωmm	Lamp annealing. MESFET's show minimal degration with temperature. Graphite strip annealing	He 88
SiO_2/Au/Ge/Ni	450	2 min	~$7x10^{-5}$	r_c reduced by spin on glass film	Pr 88
Au/Pt/Ti/Ge/Pd	325	30 min	0,12 Ωmm	Lower r_c than AuGeNi alloyed contacts	Pa 90
In+Pd	470	2 min	$6x10^{-6}$	Electroless deposition of contacts	St 90b
Au/WSi_2/Ge	500	2 min	$5x10^{-5}$	Thermally very stable contacts	Gu 90
Ni+Sb	500	30 min	$5x10^{-5}$	X-ray diffraction, AES and TEM used for this this investigation.	Du 90

Digitised by the Department of Library Services in support of open access to information, University of Pretoria, 2021

2.3.2.1.2 Sintered contacts

Since no melting is involved in this technique, good uniformity of the contacts is obtained. As can be seen from Table 2.2, sintered ohmic contacts have low specific contact resistances. However, they are normally used for GaAs with doping levels of 10^{18} cm^{-3} or higher [Pa 85b]. The reaction kinetics of the different metallic mixtures with GaAs and the mechanisms responsible for the ohmic behaviour are still not clearly understood. Therefore, considerably more work on sintered ohmic contacts on GaAs is needed for achieving an optimum ohmic contact.

Table 2.2: Sintered ohmic contacts

Metallization	Annealing		r_c	Remarks	Ref.
	°C	Time	(Ωcm^2)		
Pd/Ge	600	20 min	~$3x10^{-4}$	Relation between Ge diffusion into GaAs and ohmic contact formation	Gr 80
Pd/Ge	450	2 min	3,5 Ωmm	Contacts to HEMT structure	Ch 87b
Pd/Ge	325	30 min	~10^{-7}	Excess Ge grow epitaxial on GaAs	Yu 89
Pd/Si	375	30 min	~$2x10^{-6}$	Si on top of surface after sintering	Yu 89
Au-Ge	275	2 min	$2,5x10^{-5}$	Contacts relatively stable with annealing	We 81

Digitised by the Department of Library Services in support of open access to information, University of Pretoria, 2021

Metallization	Annealing		r_c	Remarks	Ref.
	°C	Time	(Ωcm^2)		
Au-Ge	~330	78 h	$3x10^{-6}$	SIMS analysis of contacts	Ka 81
Au-Ge	315 330	>3 h 1 h	$2x10^{-5}$ $3x10^{-6}$	Laterally non-uniform	Ai 82
TiW/Ge	700	25 min	$1x10^{-6}$		An 82
Pd/Ge	325	30 min	~0,16 Ωmm	RBS, SEM and TEM analysis	Pa 88
Au/Pd/Ge Au/Pd/Ni/Ge	450 450	135 min 150 min	$8x10^{-5}$ $5x10^{-5}$	Pd effective diffusion barrier for Au. Ni lowers r_c and improves the surface morphology.	Pr 89
Mo/Ge	750		$1x10^{-6}$	Good morphology and better temp. stability than alloyed AuGe system	Ti 83
$Au/W_6N_4/Ge/Ni$	500	10 min	$1x10^{-6}$	WN acts as diffusion barrier for Au	Ko 89

Digitised by the Department of Library Services in support of open access to information, University of Pretoria, 2021

3.2.1.3 Laser and electron beam annealing

In this section, laser and electron beam 'alloying' (transient annealing) of the metallic overlayers, will be considered. The main difference between laser and electron beam annealing arises from the difference in energy deposition. Metallic surfaces are good reflectors of light and therefore a significant part of the incident laser energy is reflected from the contact surface. The laser energy is a function of depth and therefore most of the energy is deposited at the contact surface. Thus, melting starts at the surface and propagates towards the GaAs substrate. The high absorption coefficient of the contact can result in a large degree of superheating of the liquid and contact evaporation [Ai 82b]. In the case of electron beams there are fewer problems of reflected energy and it is therefore easier to determine the deposited energy, which in this case depends upon the electron stopping power of the material. However, high energy electrons can cause radiation damage that is trapped at the surface of the semiconductor, which may seriously effect the electrical characteristics of the contacts.

In general, transient annealed contacts have comparable or lower contact resistances, and better surface morphology, although the stability of these contacts is still a cause of concern because of poorer adhesion than conventionally alloyed contacts [Pa 85b]. A further problem with pulse electron and laser annealing, is the non-uniform alloying that occurs over the contacts surface. Table 2.3 contains a summary of both laser and electron beam alloyed contacts.

Digitised by the Department of Library Services in support of open access to information, University of Pretoria, 2021

Table 2.3: Laser and electron beam annealed contacts

Metallization	Annealing Conditions (nm)	Time (ns)	Energy ($J.cm^{-2}$)	r_c ($\Omega.cm^2$)	Remarks	Ref.
Au/Ge	Nd:YAG	~30		$5x10^{-5}$	Microcracks form	Ba 80
Au-Ni/Au-Ge	0,51	4,3 mm/s	~640	$4,8x10^{-6}$	FET's have better performance than thermally annealed ones	Ec 80
Au-Ni/Au-Ge	PEBA ~10 keV	~100	~0,28	$\sim3,5x10^{-5}$		Ta 80
Au/Pt/Au-Ge	~0,51	4,3 m/s	~610	$1,5x10^{-5}$	r_c depends on the Pt, Ag and Ti layers for laser annealed contacts, but no change in r_c vs metal layers for PEBA	Ec 80
	PEBA ~10 keV	~100	~0,28	$\sim9x10^{-5}$		
Au/Ag/Au-Ge	~0,51	4,3 mm/s	~600	$2x10^{-4}$		
	PEBA ~10 keV	~100	~0,32	$2x10^{-5}$		
Au/Ti/Au-Ge	~0,51	2,3 mm/s	~135-	$1,8x10^{-5}$		
Pt/Au-Ge	PEBA ~20 keV	~100	~4,0	$4x10^{-5}$	Little intermixing	Le 80 Ta 80 Le 81b
TiW/Ge	Ruby laser	22	0,4-5	$\sim1x10^{-5}$	Epitaxially grown Ge on GaAs	An 80
Ta/Ge	Ruby laser	22	~0,7	$\sim1x10^{-6}$	Application to high temperature devices	An 81
Ni/Ge	Ruby laser	22	~0,1	$\sim2x10^{-6}$		
Au-Ge	0,69	25	0,3-0,7	poor ohmic	Poor surface morphology	Ma 81

Digitised by the Department of Library Services in support of open access to information, University of Pretoria, 2021

Metallization	Annealing Conditions				Remarks	Ref.
	(nm)	Time (ns)	Energy $(J.cm^{-2})$	r_c $(\Omega.cm^2)$		
Ni/Au-Ge	0,69	~25	~0,6	$\sim 1x10^{-5}$	Good morphology	
Au-Ge	106	~23	~1,5	$\sim 3x10^{-6}$	Deep penetration of Au and Ge.	Ai 81
	106	23	~2,65	$\sim 1x10^{-6}$	TEM, AES - little Ga	
	106	30	~1,6	$\sim 4x10^{-6}$	and As outdiffusion	Ai 81b
Au-Ge	106	20	0,3-0,5	$2x10^{-5}$	RBS - backside irradia-tion	Or 81
Au/Au-Sn/Sn	Spark alloying 50 kV			$4x10^{-6}$	Temperature rise during "annealing" is less than 50 °C	Da 81
Au-Ge/In	~0,51	4,3 mm/s	~565	$1x10^{-6}$	Uniform distribution of Ge after deposition	Le 81b Ec 80b
TiW/Ge	Ruby laser	22	0,1-5	$\sim 1x10^{-6}$		
Ta/Ge	Ruby laser	22	~0,7	$\sim 9x10^{-7}$	Compares laser and	An 82b
Mo/Ge	Ruby laser	22	~2	$\sim 6x10^{-6}$	thermal annealed con-	
Ni/Ge	Ruby laser	22	~0,1	$1x10^{-6}$	tacts	
Au-Ge	Nd:YAG laser	23	0,3-2,5		r_c vs depth of surface etched away	Ai 83
Au/Ge/Ni	CO_2 laser			$\sim 10^{-5}$	Back-surface irradia-tion. r_c for laser an-nealing is one order lower than furnace annealing	Ts 83
Au-Ge	Nd:YAG laser	30	1,1	$7x10^{-6}$	Frontside irradiation. RBS vs electri-cal measurements	Sa 84

Digitised by the Department of Library Services in support of open access to information, University of Pretoria, 2021

Metallization	Annealing Conditions				Remarks	Ref.
	(nm)	Time (ns)	Energy ($J.cm^{-2}$)	r_c ($\Omega.cm^2$)		
Al/Ge	~308	~40	0,5	ohmic		Si 84
Au/Ge/Ni	Xe-gas discharge flashlamp	~600 μsec	15-20	ohmic	Smooth surface	Ka 85
Au-Ge-Ni	é-beam	3 sec	600 mW	$\sim 3x10^{-5}$	Less redistribution of elements than with furnace annealing	Na 85
Au-Ge/Ni	é-beam 5 keV	25 sec	1,5 W/cm2	$1x10^{-6}$	SEB annealed contacts undergo less ageing degradiation than surface annealed contacts	Ka 87
Au-Ge/Ni	5 keV	24 cm/s		$2x10^{-6}$	SEB contacts more stable	Ka 87b
Ni/Au-Ge	308	40	0,5	$\sim 2x10^{-5}$	Laser annealed contacts have smoother surface than furnace annealed contacts	Si 80
Ni/Ag-Ge	308	40	0,35	$\sim 3x10^{-5}$		Si 87
Al-Ge	308	40	0,39	$\sim 5x10^{-5}$		
SiO_2/Au/Ge/Ni	é-beam 4 keV	1 scan/cm	1,6 W/cm^2	$\sim 1x10^{-5}$	Capped SEB contacts have better r_c values and surface morphology than capless alloyed contacts	Pr 88
SiO_2/Au-Ge/Ni	450	2 min		$\sim 1x10^{-6}$	Best r_c measurements obtained with samples capped with	Pr 89b

Digitised by the Department of Library Services in support of open access to information, University of Pretoria, 2021

Metallization	Annealing Conditions				Remarks	Ref.
	(nm)	Time (ns)	Energy ($J.cm^{-2}$)	r_c ($\Omega.cm^2$)		
					thin glass film. Compares furnace and beam annealing contacts	
Au/Au-Ge	193	20	0,72	$\sim 1x10^{-6}$		
	248	25	1,39	$\sim 6x10^{-7}$	AES, SEM good morphology	Im 87
Ni/Au-Ge	193	20	1,17	$\sim 2x10^{-6}$		
Au-Ge/Ni	193	20	2,88	$\sim 1,5x10^{-6}$		
Au/W/Si/.../Si/W/Au	é-beam	2,5-5 sec	Peak temp. 635 °C	$3,7x10^{-5}$	XPS and RBS. Lower r_c values for contacts with additional Ni layer	Wu 89
Au/W/Si.../Si/W/Ni/Au	20 keV	2,5-5 sec	Peak temp. 635 °C	$2,4x10^{-5}$		
Ni/Au/Te	458-514		3,6W	$\sim 7x10^{-6}$	RBS, AES - Smooth surface	Wu 89b
Au/Pd/Ge		100 sec	4 Wcm^{-2}	$2,1x10^{-5}$	Scanspeed of 1 scan in 25 sec. SEB annealed contacts have lower r_c than furnace annealed contacts	Pr 89
Au/Pd/Ni/Ge		75 sec	4 Wcm^{-2}	$7x10^{-6}$		

2.3.2.2 Ion beam mixing

One of the greatest problems with ohmic contacts to GaAs is the existence of an interfacial layer between the metal overlayer and the GaAs. This interfacial layer consists mostly of oxides and hydrocarbons [Pa 85]. If the interface is mixed using an ion beam

Digitised by the Department of Library Services in support of open access to information, University of Pretoria, 2021

prior to annealing, the interface layer can be dispersed and hence a more uniform reaction may occur.

One of the main problems with this technique is the damage that is induced by the ion beam in the GaAs surface. Therefore, the damage has to be annealed out. However, more research into the technique of ion beam mixing is necessary. The various ion beam mixing experiments are listed in Table 2.4.

Table 2.4: Ohmic contacts fabricated by means of ion beam mixing

Metallization	Ion Beam		Annealing		r_c	Remarks	Ref.
	Ion	Energy (keV)	°C	Time	($\Omega.cm^2$)		
Au-Ge-Ni	As^+	150	420	30 sec	$1,5x10^{-3}$ $1x10^{-4}$	Room temp. implanted contacts. N_2 liquid implanted contacts. Interface mixing improves uniformity of contacts surface	Pa 85
Ni	Ge^+	300	800	~20 sec	Ohmic	Lamp RTA. Te^+ can be used in place of Ge^+	Sm 85 Sm 86
Pt	Si^+	160	800	30 sec	$5x10^{-4}$	Selective formation of ohmic and Schottky contacts	Ts 84 Fu 86
Ge	As^+	60	450 + 800	~15 min ~6 min	Ohmic Ohmic	RTA required to form ohmic contacts. Two step annealing	Fu 86 Fu 87
Au-Ge-Ni	As^+	150	420 + 560	30 sec 15 min	Ohmic Ohmic	Improved morphology	Pa 85b
3x Au/Ge/Ni	Si^+	80	340	5 min	$3x10^{-4}$	Improvement in surface morphology compared to conventional alloyed contacts	Bh 85

Digitised by the Department of Library Services in support of open access to information, University of Pretoria, 2021

Metallization	Ion Beam		Annealing		r_c	Remarks	Ref.
	Ion	Energy (keV)	°C	Time	($\Omega.cm^2$)		
Au-Ge/Ni	Ar^+	170	450	5 min	Ohmic	Enhances interdiffusion between metallization and GaAs	Ba 88b
Au-Ge/Ni	Ar^+	260	450	2 min	~$1x10^{-5}$	AES, SIMS- Improved morphology	Ba 88c Ba 90
Ge/Ni Au was evaporated after ion implantation	Se^+	100	420	2 min	~$9x10^{-5}$	Ion beam mixing improved morphology. Lower r_c can be obtained by using donor ion such as Se^+	Ji 88
Ge Ni/Au was evaporated after ion implantation	Se^+ at 450°C	100	870 420	2 sec 2 min	~$4x10^{-6}$	Surface features	Ji 88

2.3.2.3 Non-Alloyed Ohmic Contacts

For non-alloyed ohmic contacts, a thin, heavily doped, n-type GaAs layer is formed either by means of ion implantation or by growing an epitaxial layer prior to the deposition of the metal(s). Metals so deposited do not alloy or react with the GaAs and the ohmic behaviour arises from current transport through the metal-GaAs barrier, because of a tunnelling process. Two of these methods are discussed below.

2.3.2.3.1 Ion implantation

The major problem with shallow ion implantation lies in the radiation damage introduced in the host material by implanted ions. Furthermore, in most cases the problem is not simply to

Digitised by the Department of Library Services in support of open access to information, University of Pretoria, 2021

obtain high concentration impurity atoms in the GaAs, but also to make them electrically active. Therefore, a post-implant treatment which anneals out the defects and activates the dopants is required. Since the temperatures needed for this step may be of the order of 900 - 1 000 °C, care must be taken to minimize the effects of thermal dissociation of the GaAs.

Conventional furnace annealing for activating an implant is generally limited to doping levels up to about $(2\text{-}5)\times10^{18}$ cm^{-3} [Mo 87c]. Laser annealing [Ku 79, Fa 79] and pulse-electron beam annealing (PEBA) [Gr 79, Li 79] have also been applied to implanted III-V compounds. With these techniques short heating times and fast freeze epitaxial regrowth are obtained, which results in reduced molecular dissociation and better annealing of the regions of ion-implanted damage respectively. Unfortunately, although pulsed annealing can give rise to high doping levels, the layers produced have poor mobilities. Extended line defects and planar defects are thought to be primarily responsible for this low mobility [An 82b]. Results of ohmic contacts produced in this way are shown in Table 2.5.

Table 2.5: Ohmic contacts fabricated by means of ion implantation

Dopant Layer	Metallization	r_c ($\Omega.cm^2$)	Remarks	Ref.
GaAs n^+ (Si^+)	Au/Ni/Au-Ge Au/Ni/Au-Ge	~3×10^{-6} ~3×10^{-7}	Little metal/GaAs interaction	Li 80
GaAs n^+	Al	6×10^{-6} 10^{-6}	PEBA for activation of Se ions	Pi 80b
GaAs >2×10^{19}(Se^+) or >2×10^{19}(Se^+)	Al Al	~6×10^{-6} ~5×10^{-6}	Substrate heated to 350 °C during implantation	Pi 80
GaAs 1×10^{19} or >2×10^{19}(Sn^+)	Au/Ni Au/Ni	~1×10^{-6} ~4×10^{-6}	±500Å GaAs removed prior to metallization	Wo 82

Digitised by the Department of Library Services in support of open access to information, University of Pretoria, 2021

2.3.2.3.2 Epitaxial layers

The use of epitaxial layers to obtain high concentration impurity layers shows promise for fabricating ohmic contacts, because of the low contact resistance obtained ($<1x10^{-7}$ $\Omega.cm^2$). However, the epitaxial process is not as reproducible and is more costly than the alloying process which is most widely used to form a highly doped layer beneath the metal contact. The non-reproducibility is believed to be due to contamination, usually oxides, at the semiconductor interface. To get rid of this contamination, high substrate temperatures are required, which are not compatible with conventional lithography for semiconductor devices. Furthermore, earlier work has indicated that non alloyed contacts may be unreliable under low temperature (~250 °C) long-term heating, because either deactivation of the interfacial dopant concentration or the reaction of the metals with GaAs during such cycles is possible. Therefore, it has been suggested that for non-alloyed contact, metals which do not react during heat treatment with GaAs should be used [Pi 81].

Contacts have been fabricated on epitaxial layers which possess excellent surface morphology. A summary of the contacts fabricated in this way are given in Table 2.6.

Table 2.6: Heteroepitaxial and homoepitaxial ohmic contacts

Dopant layer	Metallization	$\Omega.cm^2$	Remarks	Ref.
Ge $>1x10^{20}$ cm^{-3}	Au/Mo	$\sim 9x10^{-6}$	Ge epitaxial layer	De 80
	Au	$\sim 1x10^{-7}$		St 81
In_xGa_{x-1} As	Ag	$\sim 5x10^{-7}$	Graded epitaxial layer	Wo 81
Ge n^+	Ge/Pd	$\sim 1x10^{-6}$	r_c reproducible. TEM study	Sa 85b

Digitised by the Department of Library Services in support of open access to information, University of Pretoria, 2021

Dopant layer	Metallization	$\Omega.cm^2$	Remarks	Ref.
$In_{0,53}Ga_{0,47}As$ $5x10^{19}$ cm^{-3}	W_5Si_3	$5x10^{-6}$	Contacts stable even after 900 °C annealing	Is 86
$In_{0,65}Ga_{0,35}As$ $1,5x10^{19}$ cm^{-3}	Au/Pt/Ti	$5x10^{-8}$	r_c depend on InAs mole fraction	Ni 86
InAs ~$5x10^{19}$ cm^{-3}	WSi_x	$1x10^{-6}$	Best r_c obtained with RTA at 800-850 °C	Wr 86
$In_xGa_{1-x}As$ $2x10^{19}$ cm^{-3}	Au/Pt/Ti WSi	$5x10^{-9}$ $1x10^{-8}$	WSi proved a better thermally stable ohmic contact under annealing	Ni 88
5xGaAs/InAs Superlattice + 5xInGaAs/InAs superlattice + InAs $4x10^{18}$ cm^{-3}	Metal	$8x10^{-8}$	Low r_c caused by the lowering of the bulk barrier height by the structure	Pe 88
$In_xGa_{1-x}As$	Au/Ti/Au/Ge/Ni	$5x10^{-7}$	Best r_c obtained at 475 °C annealing (r_c=$2x10^{-7}$)	Ne 89
GaAs $2x10^{18}cm^{-3}$	Au/Pt/Ti	~$1x10^{-6}$	SnO_2/SiO_2 spin on and laser irradiation for activation	Ni 81
GaAs $2x10^{19}cm^{-3}$	Al	$7x10^{-7}$	Modification of the GaAs surface by H_2S adsorption	Ma 81b

Digitised by the Department of Library Services in support of open access to information, University of Pretoria, 2021

Dopant layer	Metallization	$\Omega.cm^2$	Remarks	Ref.
GaAs n^+ (Si)	Au	$5x10^{-7}$	Diffusion of Si into GaAs by pulsed laser annealing	Ni 82
GaAs $1x10^{19}$	Au/Ni	$4,6x10^{-6}$		Wo 82
GaAs n^+	Ge/Pd/Sb/Pd	$\sim 10^{-5}$ 10^{-6}	Solid phase expitaxy through Pd	Ma 84 Ma 85b Ma 87
GaAs	Ni/Au-Ge	$3x10^{-5}$	Se doped GaAs by laser induced diffusion	Kr 85
GaAs n^+(Si)	Ag	$1,3x10^{-6}$	Space-charge density at the GaAs/metal interface equal to the Si density	Ki 85
GaAs n^+ (Sn-Si)	Ni/Au-Ge	$\sim 8x10^{-5}$	n^+ layer obtained by Ruby laser irradiation of the tin-silica films	Ka 85b
GaAs n^+ (Sn)	Au	$8x10^{-5}$	Ohmic up to a few hundred mA	Sh 86
GaAs $2x10^{19}cm^{-3}$	Ni/Au/Ge	$\sim 2x10^{-7}$	Results explained in terms of a new thermionic field-emission model	Sh 87

Digitised by the Department of Library Services in support of open access to information, University of Pretoria, 2021

Dopant layer	Metallization	Ω.cm^2	Remarks	Ref.
GaAs $2x10^{19}cm^{-3}$ n^+	Ge/Pd	~$1x10^{-6}$	Both contacts are ohmic to 25K	Wa 88
	Si/Pd	~$5x10^{-6}$	Si/Pd contacts more thermally stable than Ge/Pd	
GaAs $10^{17}cm^{-3}$	Ge/Pd	~0,16Ωmm	Very stable during annealing for 200h at 300 °C	Pa 88
InGaAs $1x10^{19}cm^{-3}$	Au/Pt/Ti	$1x10^{-7}$	Excellent FET characteristics obtained	Es 89
InGaAs n^+	Au/Ni/Au-Ge	~$1x10^{-6}$	Ohmic down to contacts with diameter as small as 1500 Å	Ra 89

2.3.3 Ohmic contacts to n-type InP

2.3.3.1 Metallization systems

The fabrication of ohmic contacts to n-type InP can generally be divided into two methods. The first method consists of the evaporation of a metal/alloy, followed by annealing (Table 2.7), while the second method has a sputtering step prior to deposition of the metallization system and no annealing (Table 2.8). These tables contain a summary of the metallization systems used on n-type InP from 1980, together with their relevant references in the literature.

From these tables it is clear that most of the ohmic contact systems used are based on metallization schemes which have proved to be reliable for III-V semiconductors in general. However,

Digitised by the Department of Library Services in support of open access to information, University of Pretoria, 2021

specific contact resistance values in the lower 10^{-7} $\Omega.cm^2$ range, but more typically ~10^{-6} $\Omega.cm^2$, have been reported with these contacts.

2.3.3.2 Metal/alloy - InP interface

The metal/alloy - InP interface has not been studied as thoroughly as for instance the metal/alloy - GaAs interface, because InP might well be described at present as a semiconductor with more potential than applications. It is taken for granted that the metal - InP interface reacts in the same way as the other III-V semiconductors (for instance GaAs). However, Williams et al. [Wi 77] have shown that the surface chemistry of InP plays an important role in determining the electrical properties of the contract.

A failure to recognize the critical role played by the surface of InP in contact formation has been found to be largely responsible for the poor contact performance often experienced [Sk 80]. It is perhaps not surprising that the unique surface behaviour of InP has enabled a new type of ohmic contacts to be made. This contact is formed by Ar^+ etching prior to deposition of a single metal such as Al or Ag [Sk 80]. It was also shown by W C Dautremont Smit et al. [Da 84] that non-alloyed ohmic contacts to n-InP can be formed by sputter deposition of Pt and In onto a sputter-etched InP surface. Excellent contact resistance has been obtained in this way. However, the specific contact resistance increase, the smaller the contact area becomes.

An example of the different behaviour of InP in comparison with GaAs is that the lowest specific contact resistance is found below the Au-Ge eutectic temperature for Ni/Au-Ge contacts to InP [Er 79, Gr 83]. Therefore, the alloy regrowth mechanism responsible for ohmic contact formation in the Ni/Au-Ge/n-GaAs system does not imply to the Ni/Au-Ge/n-InP system, since low resistance contacts were only found above the Au-Ge eutectic temperature for this contact system to n-GaAs. A further difference is the spreading of Au-based metallization systems to InP along certain crystallographic planes [Ke 81]. This feature make the fabrication of small size Au-based contacts to InP very difficult.

Digitised by the Department of Library Services in support of open access to information, University of Pretoria, 2021

Table 2.7: Annealed ohmic contacts to n-type InP

Metallization	Annealing		r_c	Remarks	Ref.
	°C	Time (min)	(Ωcm^2)		
Au/Sn	400	30 sec	$1,8x10^{-6}$	Bad surface morphology	Ba 81
Au/Sn/Au	420	10	ohmic	Metal-semiconductor interaction related to amount of Au	Ca 82
Au/Ni/Au-Ge-Ni	400	7 sec	$2x10^{-5}$	InP was Si implanted and annealed prior to metallization	Ya 81
Au/Ni/Au-Ge	450	25 sec	$5x10^{-7}$	Used for InP microwave FET's	Mo 81
Au/Sn/	400	5	$1,2x10^{-4}$	Island formation	
Au/Sn/In	400	2	$3,10^{-4}$	Smooth surface	Ku 81
Ni/Au-Ge	350	2	$1,2x10^{-6}$	Smooth surface	
Ni/Au-Ge/Ni	400	1	$2,3x10^{-6}$	Smooth surface	
Au/Sn/Au	420	3	$2x10^{-5}$	Spreading of Au along certain crystallographic planes	Ke 81
Ni/Au/Ge	340	1	$\sim 1x10^{-6}$	AuGeP phase close to interface	Gr 83b
Ge/Au/Ni	Ruby laser $\sim 1 J.cm^{-2}$	25 nS	$<10^{-5}$	Au-In alloying	To 83
Au-Ge	450	15	$7x10^{-5}$	Various compound formations detected after annealing	Au 85

Digitised by the Department of Library Services in support of open access to information, University of Pretoria, 2021

Metallization	Annealing °C	Annealing Time (min)	r_c (Ωcm^2)	Remarks	Ref.
Ni/Au-Ge	430	~1,5	$2x10^{-6}$	AES study	Pr 86
Au/Ni/Au-Ge	450	5 sec	$2x10^{-7}$	RTA. Interactions take place very fast and are sensitive to temperature	Ba 87
Au/Ni/Au-Ge	375	3	$8x10^{-6}$	Used different annealing techniques	Pa 87
Ni/Au-Ge	400	30 sec	~0,1 Ωmm	Lamp annealing - Four different regimes were detected for the annealed contacts	De 88
Au/Ti/Ni/Au-Ge	400	30 sec	~0,02Ωmm		
Ni/Au/Ge	375	1	$3x10^{-6}$	Correlation between TEM, SIMS and electrical measurements	An 88
Ag/In	420	1	Ohmic	MBE deposition of contacts. Pre-treatment of InP surface can generate Schottky or ohmic contacts	Sa 85
Ni			$3x10^{-6}$	No high temperature treatment	Ap 86
Au/Ni_2P	300	30	$3x10^{-6}$	Ni_2P-sputter-deposited. Efficient diffusion barrier.	Ap 87
Pd	300-350	2	$3x10^{-7}$	Electroless deposition	St 90

Digitised by the Department of Library Services in support of open access to information, University of Pretoria, 2021

Table 2.8: Non-annealed ohmic contacts to n-type InP

Metallization	r_c (Ω.cm^2)	Remarks	Ref.
Al Ag	Ohmic	Prior to metallization the InP surface was Ar^+ sputtered. In island observed.	Sk 80
Ge metal with overlayers such as Au-Cr; Au-Ti; Au or Ni	$8x10^{-6}$	During Ge deposition, the InP surface were held at a temperature between 350-425 °C. The n^+-Ge layers obtained, were excellent ohmic contacts. The metals were deposited prior to r_c measurements.	Ts 81
Pt/Ti	$3,7x10^{-7}$	Ar^+ sputtering prior to metal deposition. Ohmic up to $5x10^4$A cm^{-2}	Da 84
Au-Ti	$<1x10^{-6}$	Ar^+ sputtering before metallization	Ka 88
Sb	Ohmic	Ohmic due to barrier height of less than 0,04 eV	Za 88
Pt/Ti	$8x10^{-7}$	Ti effective diffusion barrier	Ka 90

2.4. CONCLUSIONS

It is clear from the above data that ohmic contacts to n-type GaAs have been investigated thoroughly, while contacts to n-type InP has not been studied to the same extend. The reason can possible be found in the fact that

(a) it is easier to obtain ohmic contacts to GaAs than to InP due to a lower barrier height of the latter and a difference in depletion widths under the same experimental conditions (also see section 3.5.2).

Digitised by the Department of Library Services in support of open access to information, University of Pretoria, 2021

(b) Historically, the technological demand for excellent ohmic contacts to GaAs devices were much higher than that for devices manufactured on InP.

However, there are still areas that need further investigation, such as how to improve the morphology of ohmic contacts, annealing methods, alternative metallization system, optimized existing fabrication methods, etc. This study sets out to investigate some of these areas for GaAs and InP.

Digitised by the Department of Library Services in support of open access to information, University of Pretoria, 2021

CHAPTER 3

PROPERTIES AND CHARACTERIZATION OF OHMIC CONTACTS

3.1 INTRODUCTION

This chapter is devoted to the basic physical and electrical characteristics of ohmic and rectifying metal-semiconductor contacts. The chapter is divided into two main sections; (a) metal-semiconductor contact theory with reference to metal contacts on GaAs and InP and (b) the theory of ohmic contacts and specific contact resistance measurement techniques. A More complete description of the relevant physics may be found in references such as Rhoderick [Rh 88], Sze [Sz 81], Sharma [Sh 84] and Henisch [He 84a].

3.2 METAL-SEMICONDUCTOR CONTACTS

In this section the emphasis will be on metal-semiconductor contacts in general, ranging from the classical approach to a discussion on barrier formation theories.

3.2.1 Classical metal-semiconductor contacts

The junction between a metal and a semiconductor falls into one of two groups, namely ohmic or rectifying contacts (also termed Schottky or Schottky barrier contacts). In the classic metal-semiconductor junction approach, the relative work functions of the metal and the semiconductor determines the nature of the contact. To illustrate this a junction between a metal and n-type semiconductor is used as an example. Consider firstly, the situation when the work function of the metal, Φ_m, is less than the work function of the semiconductor, Φ_S. For such a junction an ohmic contact is said to be established. Figure 3.1(a) illustrates the energy-band diagrams before contact is made, with

Digitised by the Department of Library Services in support of open access to information, University of Pretoria, 2021

E_f the respective Fermi energy levels. After contact (see Fig. 3.1(b)), electrons flow from the metal into the semiconductor until the Fermi levels coincide. Note that the electrons on the metal side "sees" a small energy difference between the conduction bands and therefore electrons can flow with ease in both directions.

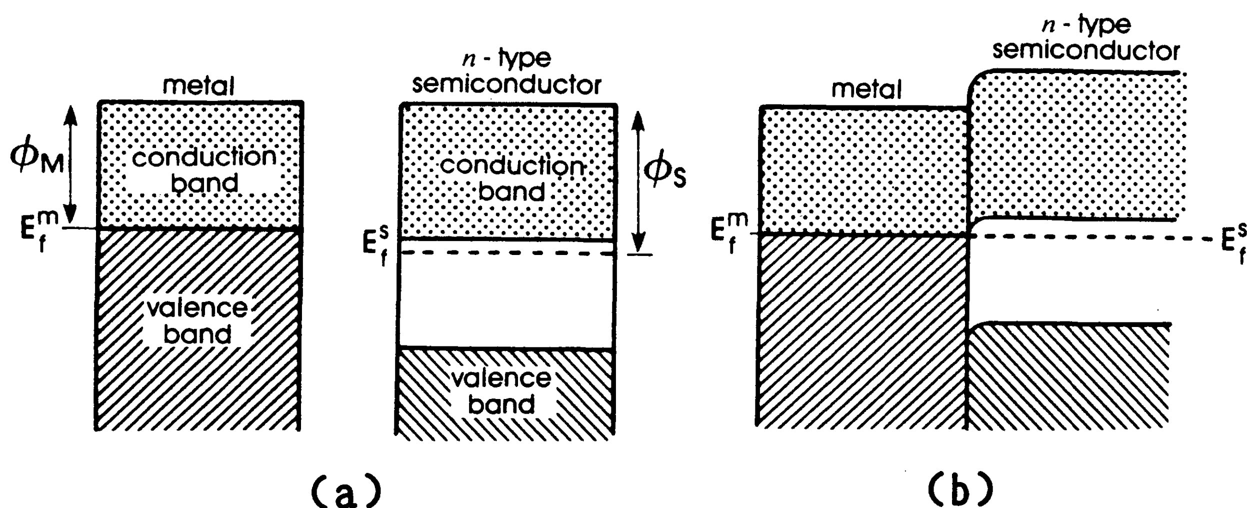

Figure 3.1: Energy-band diagrams for metal-to-semiconductor contact where $\Phi_m<\Phi_s$. (a) Before contact, and (b) after contact (ohmic contact) [Mo 76].

Secondly, for the opposite situation, where $\Phi_m>\Phi_s$, the current can flow unrestricted only in one direction. In this case a rectifying contact is obtained. Figure 3.2(a) schematically shows the energy-bands before contact. Upon contact, the electrons flow from the semiconductor to the metal, until the Fermi levels are aligned. Note that the band bending near the interface is to equalize the two Fermi levels. The equilibrium energy band structure after contact is shown in Figure 3.2(b). Under equilibrium conditions a potential barrier exists to electron flow from the semiconductor to the metal and is given by the quantity $\Phi_m-\Phi_s$. The potential barrier to electron flow from the metal is

Digitised by the Department of Library Services in support of open access to information, University of Pretoria, 2021

$$\Phi_b = \Phi_m - \chi_s , \qquad \text{....... (3.1)}$$

where Φ_b is the barrier height and χ_s the electron affinity of the semiconductor. Such a metal-semiconductor junction is rectifying and is also called Schottky barrier contact.

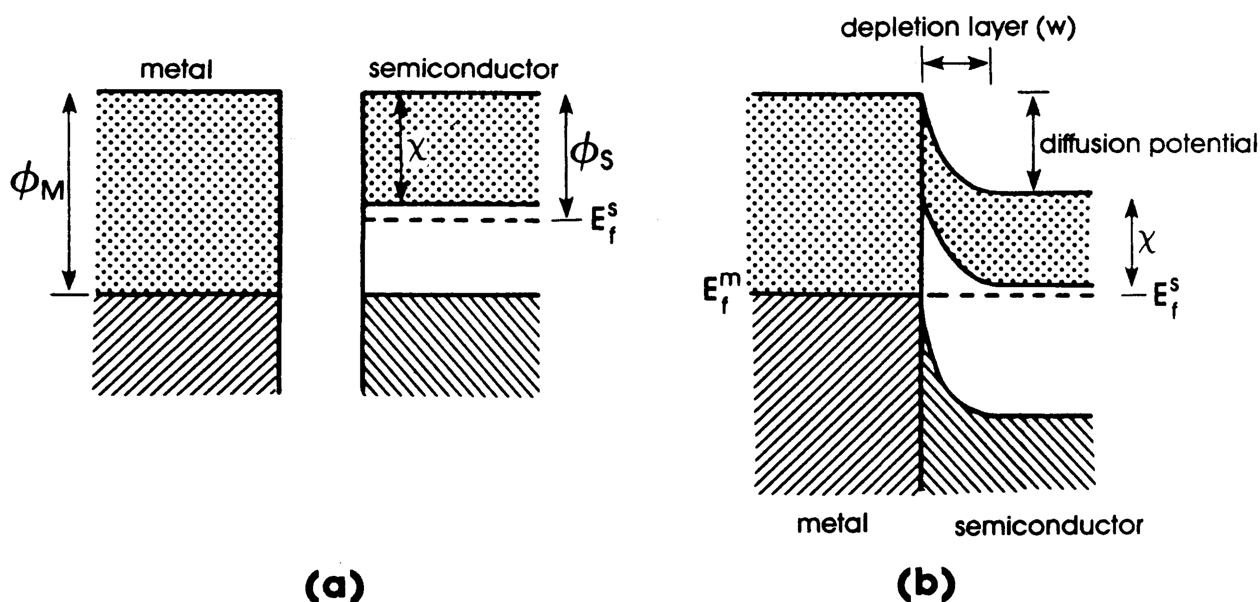

Figure 3.2: Energy-band diagrams for metal-to-semiconductor contact where $\Phi_m > \Phi_s$. (a) Before contact, and (b) after contact (Schottky contact) [Mo 76].

Equation (3.1) was originally independly proposed by Mott [Mo 38] and Schottky [Sc 38]. However, they differed in their interpretation of the resulting charge distribution. Schottky proposed a uniform space charge region, whilst Mott favoured the idea of a thin layer of donors adjacent to the metal. Afterwards it was realised that in the vast majority of cases the suggestion of Schottky prevails, which lead to the so-called Schottky barrier.

There is a region known as the depletion layer (normally denoted by w, see Fig. 3.2(b)) on the semiconductor side of the junction

Digitised by the Department of Library Services in support of open access to information, University of Pretoria, 2021

in which there is no free charge, since the electrons in that region have transferred to the metal. The resistivity of this region is therefore much higher than that of the semiconductor bulk. Thus, current flow can only take place from the semiconductor, if a voltage is applied to the junction. The relative barrier heights for the electrons from the semiconductor can be changed by applying a forward or reverse voltage to the junction (see Fig. 3.3). However, the barrier "seen" by the electrons coming from the metal remains constant. If a forward bias is applied (semiconductor negative) a net current is obtained from the semiconductor to the metal (see Fig. 3.3(a)) due to a lower barrier "seen" by the electrons coming from the semiconductor. If a reversed bias is applied to the junction only a small current is obtained from the semiconductor, because the barrier as "seen" from the semiconductor side is high (see Fig. 3.3(c)). Depending on the type of metal and semiconductor used, the difference between the forward and reverse currents can be as high as nine to eleven order. Thus, a rectifying junction is formed which permits current to flow easily in the forward direction, with practically no current flow in the reverse direction.

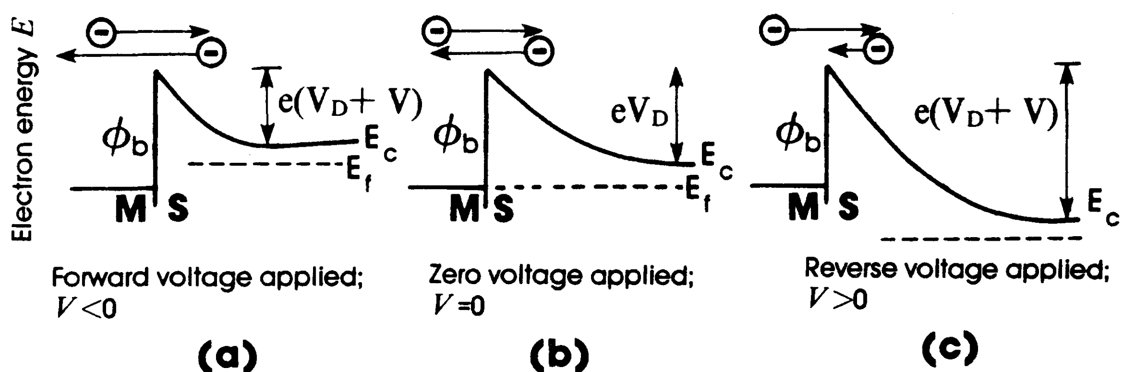

Figure 3.3: **Schematic illustration of the influence on a potential barrier when a forward voltage (a), zero voltage (b) and reverse voltage (c) is appied. V_D represent the built-in diffusion potential and V the appied voltage [He 84a].**

Digitised by the Department of Library Services in support of open access to information, University of Pretoria, 2021

3.2.2 Width of the depletion region

In calculating capacitance-voltage characteristics of a Schottky barrier junction, the electric field and potential distributions in the depletion region are frequently needed. These properties can be obtained by the solution of a one-dimensional Poisson equation. From these equations, the depletion region width, w, is obtained and is given by [Sz 81].

$$w = \sqrt{\frac{2\epsilon_s}{qN_d}(\Phi_b - V_n - V)} \quad .... (3.2)$$

where ϵ_s is the permittivity of the semiconductor, q the magnitude of the charge on an electron, N_d the doping concentration of the n-type semiconductor, Φ_b the barrier height of the metal-semiconductor contact, V_n the potential difference between the Fermi level and the conduction band and V the applied voltage (positive for forward bias and negative for reverse bias).

3.2.3 Contacts in the presence of surface states

The classical contact model proposed above does not predict the experimentally observed relationship between the barrier height and the metal work function. In reality there exists a very weak dependence, the reason being that in the metal-semiconductor contact approach the band structure describes the situation between a metal and an infinite semiconductor (bulk). However, the surface itself differs from the characteristic of the bulk. In that sense, the band structure is expected to be different (distorted) at the surface, due to additional states that appear between the valance and the conduction band (see Fig. 3.4).

This theory of surface states was first proposed by Bardeen [Ba 47]. He assumed that intrinsic surface states at the semiconductor energy gap are pinning the Fermi level. This leads to the concept of the so-called neutral level Φ_o, which is the energy to which the surface states must be filled if the

Digitised by the Department of Library Services in support of open access to information, University of Pretoria, 2021

semiconductor surface is to be electrically neutral (see Fig. 3.4). It is usual to measure Φ_o from the top of the valence band, in which case the barrier height is now defined as

$$\Phi_b = E_g - \Phi_o \qquad \text{...... (3.3)}$$

which is known as the Bardeen limit, with E_g the energy bandgap. Note that the experimentally observed barrier height will be somewhere between the two limits suggested by equations (3.1) and (3.3), depending on the surface states.

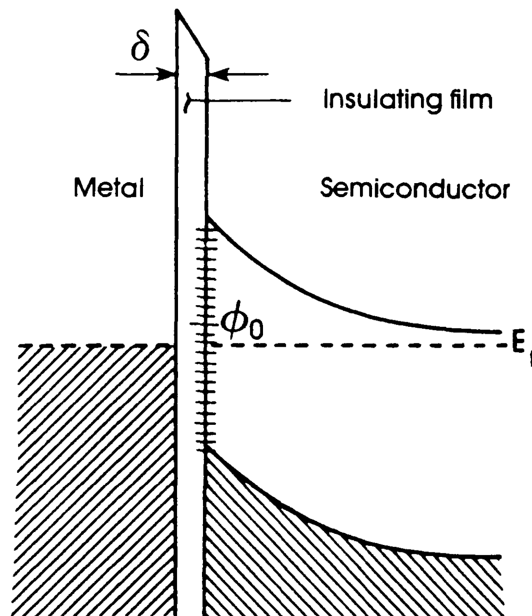

Figure 3.4: Schematical illustration of a metal-semiconductor contact with surface states [Rh 88]

It is a known fact that in most practical contacts a thin oxide layer separates the metal and semiconductor. This situation, shown in Fig. 3.4, includes an insulating layer of thickness δ and dielectric constant ϵ_i. This interfacial layer is normally very thin (<2 nm) and electrons can easily tunnel through the thin layer and hence the transport properties of the junction are not significantly affected [Pa 87a]. However, the model described above ignores the possibility that the charge in the

Digitised by the Department of Library Services in support of open access to information, University of Pretoria, 2021

surface states, together with its image charge on the surface of the metal, will constitute a dipole layer. Further, the model also assumes that the interface states can be represented by point charges, whereas in practice they are spread out over a distance of 5-10 nm [Rh 88]. This dipole layer will alter the potential difference between the semiconductor and the metal and will change the barrier height.

Under this condition the charge in the depletion region vanishes and the charge on the metal side is balanced by the charge in the interface states on the semiconductor side. Therefore, the barrier height equations (3.1) and (3.3) will change due to a flat band situation on the semiconductor side of the contact under these conditions. It was shown by Cowley and Sze [Co 65] that according to the Bardeen model, the flat band barrier height for a rectifying contact on a n-type semiconductor is given by

$$\Phi_b = \gamma(\Phi_m - \chi_s) + (1-\gamma)(E_g - \Phi_o) \quad \ldots\ldots\ (3.4)$$

where

$$\gamma = \frac{\varepsilon_i}{\varepsilon_i + q\delta D_s}$$

with δ the thickness of the interfacial layer, ϵ_i its total permittivity, D_s the density per electron-volt per unit area, and the rest of the symbols have the same meaning as before.

The flat band barrier height Φ_b in equation (3.4) is obtained when there is no electrical field in the semiconductor. In general, this is not true because band bending occurs in the semiconductor which gives rise to an electric field and this affects the barrier height, making it a function of the voltage across the depletion region. Because an electric field exists in the semiconductor at zero bias, the barrier height is different from the flat band barrier height at zero bias. There are a

Digitised by the Department of Library Services in support of open access to information, University of Pretoria, 2021

number of factors which cause the barrier height to depend upon the electric field in the depletion region. Only two of these effects will be mentioned here [see Rh 88 and Sh 84 for a more detailed discussion of these effects]. Firstly, the presence of the electric field in the semiconductor alters the potential drop in the interfacial layer and thus modifies the barrier height (field dependence of the barrier height). The second effect is caused by the so-called image force or Schottky effect. This effect induces a lowering of the potential energy (and therefore the barrier height) for charge carrier emission when an electric field is applied (schematically illustrated in Fig. 3.5). The lowering is due to the combined effects of the applied field and image force between an electron and the surface of the metal. The influence of the image force on the experimentally obtained barrier heights (Φ) is illustrated in Fig. 3.6 for different n-GaAs doping levels.

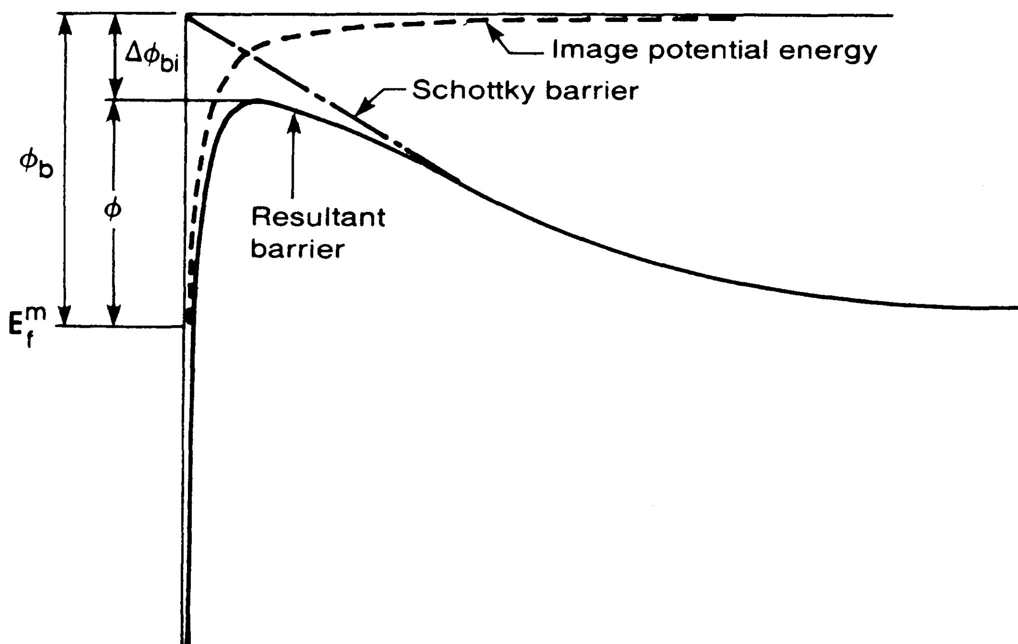

Figure 3.5: Image force lowering of the barrier. Note that Φ_b is the Schottky barrier height, Φ the experimentally measured barrier height and $\Delta\Phi_{bi}$ the lowering of the barrier due to the image force [Rh 88].

Digitised by the Department of Library Services in support of open access to information, University of Pretoria, 2021

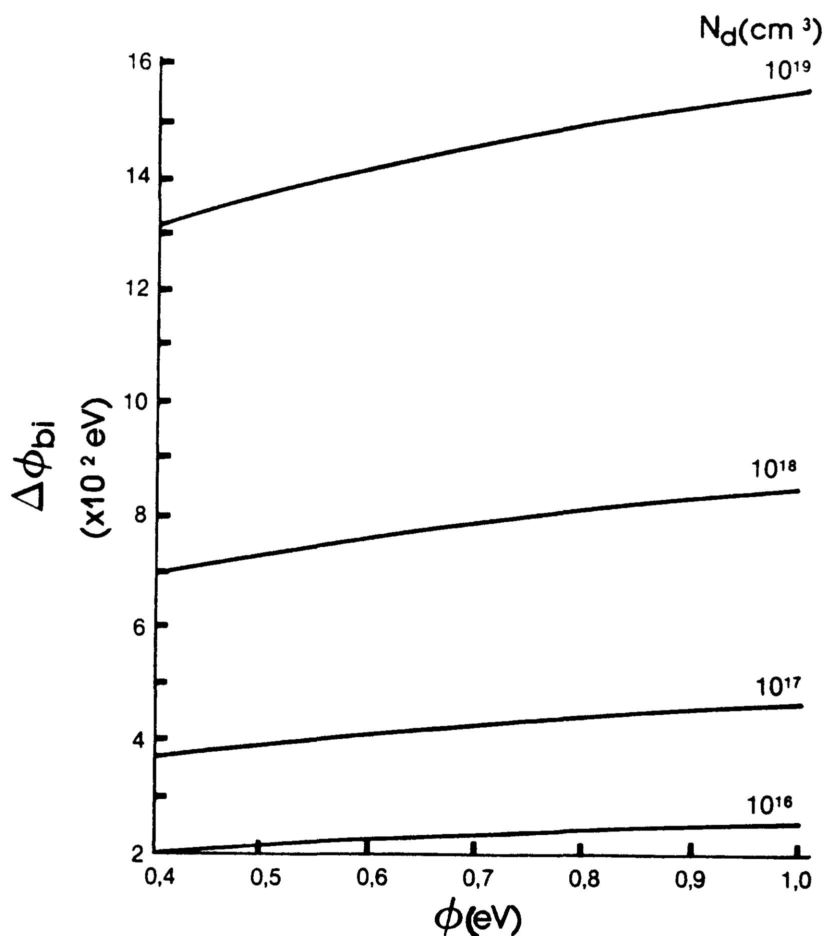

Figure 3.6: The influence of the image force lowering on the experimentally measured barrier heights (Φ) for n-type GaAs at different doping levels ($\Phi + \Phi_{bi} = \Phi_b$).

3.2.4 Other models for barrier formation on semiconductors

In section 3.2.1 the shortcomings of the Schottky model were pointed out. Although the Bardeen model was an improvement on the model of Schottky, this model fails to explain the origin of the high density of interface states [Pa 87a]. Various different models were developed during the last four decades, but in a sense they are generalisations of these two classical models. In this section four of these more recent models will be briefly discussed.

Digitised by the Department of Library Services in support of open access to information, University of Pretoria, 2021

Recently the theoretical and experimental results of semiconductor interfaces have emphasized the relevance of two specific models [Fl 87]. These are the induced density of interface states [Te 77] and the unified defect models [Sp 79]. In the former model an ideal and abrupt interface is assumed to exist between the metal and the semiconductor, while the position of the Fermi-level pinning is obtained by analysing the total density of interface states in the semiconductor's energy gap. It is also possible to introduce effects such as interlayers or chemical reactivity into the model.

The unified defect model relates the pinning of the Fermi level to the metal-induced formation of defects during the initial stages of metal deposition. The main assumption of this approach is that the deposition of the metal on the semiconductor surface can release the energy necessary to create these defects. Since the pinning is not influenced by the overlaying material, the Bardeen approach can be used by replacing the neutral level Φ_o by the pinning level Φ_p.

Two totally different models, if compared with the two discussed above, were proposed by Woodall and Freeouf [Wo 81a and Wo 82a] and Brillson [Br 78] respectively. Both are related to the phases that form at the interface. Woodall and Freeouf claim that the Schottky barrier can be explained by applying the Schottky model to the junction formed at the interface, due to a chemical reaction between the semiconductor and the metal. (The so-called effective work function model.) Brillson however suggests that the in-diffusion of the metal into the semiconductor will cause the semiconductor lattice to change. According to Brillson's model, this change will determine the kind of electrically active states that pin the Fermi level.

In conclusion, it should be stressed that these theories predict very idealised models and should not be expected to explain the detailed behaviour of practical barrier formation. The reason is that in the practical situation any slight departure from an ideal semiconductor surface will create sufficient surface states (it is more correct to think of interface states) to profoundly

Digitised by the Department of Library Services in support of open access to information, University of Pretoria, 2021

affect its characteristics [Gu 76 and Pa 82]. However, for many practical purposes these models provide a useful working picture, as will be discussed in the sections that follow.

3.3 METAL CONTACTS ON GaAs AND InP

The above section dealt with the different barrier theories, while this section will be concerned with experimental studies of different metals on GaAs and InP. The initial interactions of metal overlayers on these semiconductors have been widely investigated, with the (110) interface the most extensively studied surface [Rh 88]. These investigations have been applied to very thin metal layers as well as thicker contacts. The latter contacts are mostly used for Schottky barrier height measurements by using methods such as current-voltage (I-V), capacitance-voltage (C-V) and photoresponse. Surface science techniques have also been applied to study the chemical and metallurgical interactions at interfaces between metals and GaAs and InP [Wi 85 and Sp 86]. The purpose of this section is to briefly discuss the most relevant experimental results obtained for metal overlayers on n-type GaAs and InP.

Before proceeding with this discussion, it is important to compare selected properties of InP and GaAs (see Table 3.1). It is clear from this table that in general GaAs has an edge over InP, due to its electronic properties. However, for InP the theoretical predicted advantages over GaAs due to higher peak (at 77K) and saturation electron velocities, higher breakdown voltages, a higher thermal conductivity, larger intervalley energy gap, smaller ionisation coefficients and dielectric constant, etc. have not been materialized to date, because of low barrier heights of metal-InP contacts and less than expected commercial demands.

The barrier height is one of the most important parameters of rectifying metal-semiconductor contacts. One of the most powerful methods of measuring the barrier height is the photo-emission of electrons excited by monochromatic synchrotron radiation. In this way Spicer et al. [Sp 82] has analysed GaAs

Digitised by the Department of Library Services in support of open access to information, University of Pretoria, 2021

Table 3.1: Comparison of the properties of bulk GaAs and InP [Sh 84]

Properties	Unit	InP	GaAs
Melting point	°C	1058	1238
Energy gap	eV	1,35	1,43
Maximum mobility of electrons (77K)	cm^2/Vsec	23500	22000
Maximum mobility of electrons (300K)	cm^2/Vsec	4600	8000
Maximum mobility of holes (300K)	cm^2/Vsec	150	400
Effective electron mass		0,077	0,067
Effective hole mass		0,64	0,48
Intrinsic carrier concentration	cm^{-3}	$1,1x10^7$	$1,8x10^6$
Density	g/cm^3	4,787	5,316
Resistivity (25°C)	Ω cm	$\sim 10^8$	$>10^8$
Electron affinity	eV	4,4	4,07
Thermal expansion coefficient	10^{-6}/°C	4,5	6
Thermal conductivity	W/cm °C	0,68	0,54
Dielectric constant		12,4	13,1
Lattice constant	Å	5,869	5,654
Vapour pressure at melting point	Torr	$1,5x10^4$	740
Maximum useful temperature of operation	°C	250	400
Intrinsic electron concentration (25°C)	cm^{-3}	$2x10^7$	$2x10^6$
Crystal structure		Zinc blende	Zinc blende

Digitised by the Department of Library Services in support of open access to information, University of Pretoria, 2021

and InP surfaces, and it was found that cleaved surfaces of these III-V semiconductors have no detectable surface states within the band gap and that surface states are generated after very small quantities of metal are brought into contact with these surfaces (Fermi-level pinning). Further, the positions of the surface states were within an energy range that was found to be independent of the overlayer surface atoms.

Mead [Me 69] concluded that for many covalent semiconductors (InP and GaAs are also partly covalent with the same electro-negativity difference [Sz 81]), the barrier height (Φ) of n-type semiconductors equals ±2/3 the value of the energy band gap (E_g) and ±1/3 E_g for p-type semiconductors, due to Fermi-level pinning. In particular, Mead's rule has been confirmed for n-GaAs with Φ in the order of 0,7 - 0,9 eV and for p-GaAs with $0,45 \leq \Phi \leq 0,65$ eV [Sz 81 and Me 69]. This is consistent with the finding that GaAs contacts show a high density of surface states [Sp 80, Sp 80b and Rh 88]. However, InP is an exception to Mead's rule, since Φ is in the range of 0,2 - 0,6 eV for various metals on n-InP [Wh 78 and Rh 88], and about 0,75 eV for Au on p-InP [Ku 81].

Furthermore, the energy distribution of the density of surface states for GaAs is parabola-like, with an increase at the band edges and a minimum in the middle of the bandgap [We 79]. The energy distribution of the density of surface states in InP is also parabolic; however, its minimum is positioned near the conduction band edge [Fr 80] and it increases towards the valence band edge [Ku 81]. The result of this is that the surface of n-InP is only slightly depleted, which corresponds with the low Φ measured on n-InP and high Φ of p-InP. Therefore, it should be easier to obtain ohmic contacts to n-InP than to n-GaAs.

In general, for a specific metal, few differences in the barrier height were reported between contacts fabricated on cleaved GaAs, in comparison with contacts fabricated on chemically etched GaAs surfaces [Is 84, Ke 85a and Rh 88]. Although the oxygen at the interface appears to have little effect on the barrier height of the GaAs contacts, sulphur, caesium and selenium atoms at the interface do appear to have a significant effect by lowering the

Digitised by the Department of Library Services in support of open access to information, University of Pretoria, 2021

barrier height to as low as 0,4 eV [Ma 80 and Wa 84]. It could also be possible that the thin oxide does not completely separate the metal and the semiconductor, since diffusion of metal atoms through the oxide and chemical reactions between the metal and the oxide can occur. It could also be argued that the existence of this oxide layer separating the metal and semiconductor should considerably reduce the density of any metal induced states in the semiconductor [Rh 88].

In the case of InP, the reported barrier heights appear to be more dependent on the detailed chemistry of the interface than was the case for metals on GaAs. Schottky barrier heights measured for metals on both clean and oxidized InP show considerable scatter. The barrier appear to be influenced by phase segregated In at the interface and by the formation of compounds. The production of a mixed phase interface has also been reported [Mc 80 and Wi 86]. It is also possible that these mixed phases at the metal/InP interface may account for the lack of reproducibility of barrier height measurements, according to the effective work function model. The oxide layer on InP is also a complex one. Thermodynamically the most stable oxide is $InPO_4$, which is a wide bandgap insulator [Cl 80]. The presence of an oxide such as P_2O_5 have also been reported [Wa 81 and La 81]. A more detailed discussion on the oxidation of InP is given in Chapter 5. These variations in the composition of the interfacial oxide may also be the cause of the variation in the barrier heights for a given metal on chemically etched InP [Wi 77]. The complicated behaviour of metals on InP makes it difficult to form stable Schottky contacts on n-type material and reliable ohmic contacts to InP in general.

3.4 CURRENT TRANSPORT CHARACTERISTICS

3.4.1 Introduction

As mentioned above, metal/semiconductor contacts show either rectifying or ohmic behaviour. The current transport of both

Digitised by the Department of Library Services in support of open access to information, University of Pretoria, 2021

these contacts is determined by one or a combination of the following four transport processes [Ty 84 and Rh 88].

1) Thermionic emission (TE) of carriers over the top of the barrier (The dominant process for Schottky contacts).

2) Thermionic field emission (TFE) is the tunneling of electrons through the top of the barrier (when high doping levels cause a narrowing of the depletion layer).

3) Field emission (FE) is tunneling through the whole barrier (and is responsible for most ohmic contacts).

4) Recombination of carriers in the depletion region or in the neutral region of the semiconductor, i.e. minority carrier injection (hole injection for n-type material).

The four processes in which current can be transported through a metal-semiconductor contact under forward bias are shown schematically in Fig. 3.7. The inverse processes occur under reverse bias. These transport mechanisms will be discussed briefly in the following subsections, while a detailed discussion of these processes may be found elsewhere [Rh 88, Sz 81 and An 84].

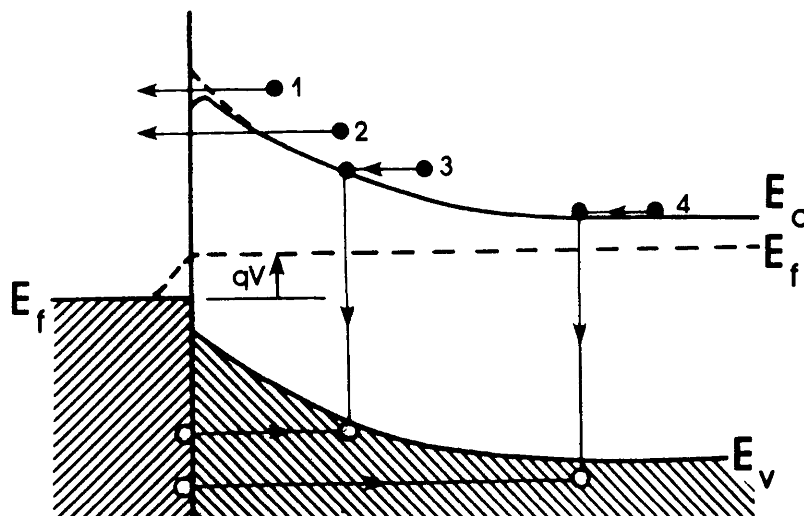

Figure 3.7: The transport processes under forward bias for a metal/n-semiconductor contact [Rh 88].

Digitised by the Department of Library Services in support of open access to information, University of Pretoria, 2021

3.4.2 Thermionic emission

Generally two steps are needed for this process to occur. Electrons must first move from "inside" the semiconductor through the high field depletion region to the interface. In crossing this region, the motion of the electrons is governed by the mechanisms of diffusion and drift that is normally experienced in an electric field. When they arrive at the interface, their emission into the metal is determined by the density of available states in the metal. Therefore, these two processes are effectively in series and the one which offers the higher resistance determines the current.

The consequence of this two step process is that two theories were developed separately to explain the specific current transport mechanism. A diffusion theory, which is normally applicable to low mobility semiconductors, was developed by Wagner [Wa 31] and Schottky and Spenke [Sc 39]. For high mobility semiconductors the carrier transport can be adequately described by the thermionic emission theory of Bethe [Be 42] and Crowell and Sze [Cr 66]. Both models result in a forward biased current-voltage (I-V) characteristic of the form [Rh 88]

$$J = J_s[\exp(qV/kT) - 1] \qquad \text{....... (3.5)}$$

where $$J_s = A^*T^2\exp(-q\Phi/kT) \qquad \text{....... (3.6)}$$

and A^* the effective Richardson constant, which takes into account the effective mass, phonon scattering and quantum mechanical reflection [Wi 87a]. Further, q is the magnitude of electronic charge, V the applied bias voltage, k Boltzmann's constant, T absolute temperature and Φ the barrier height.

3.4.3 Tunneling

Thermionic field emission (TFE) and field emission (FE) are two ways in which tunneling can occur through a metal-semiconductor junction under certain conditions. This process is schematically illustrated in Fig. 3.8. The Fermi level for this semiconductor

Digitised by the Department of Library Services in support of open access to information, University of Pretoria, 2021

lies above the bottom of the conduction band (semiconductor doped to degeneracy). Further, for heavily doped semiconductors, the depletion region is very thin and electrons with energies close to the Fermi level can tunnel through the barrier, even at low temperatures (FE). The two mechanisms can be distinguished by the observation that TFE occurs at higher temperatures with tunneling through the top of the barrier.

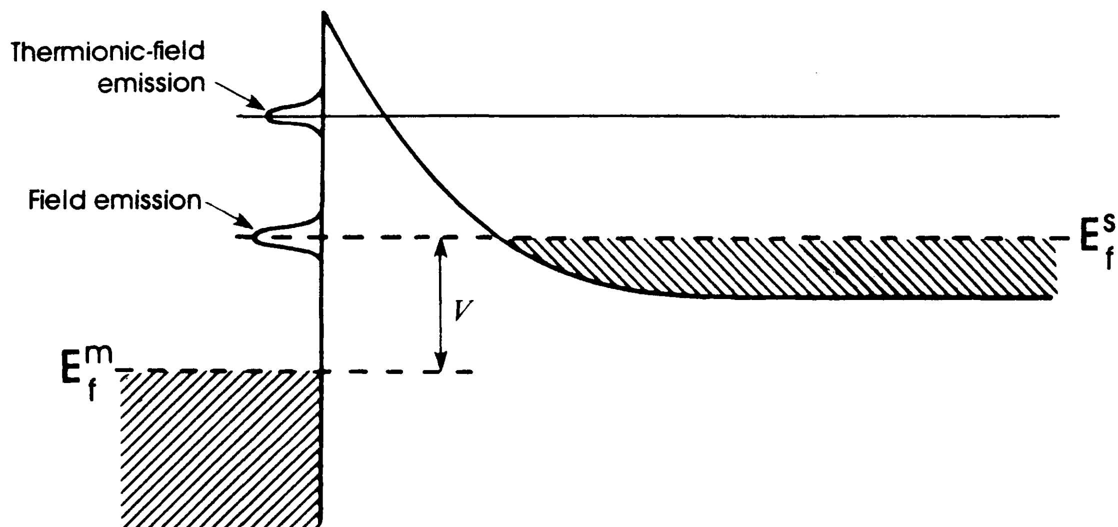

Figure 3.8: Field emission and thermionic field emission for a degenerated doped n-type semiconductor [Pa 66].

The tunneling theory was originally developed by Padovani and Stratton [Pa 66] and refined by Crowell and Rideout [Cr 69]. The I-V characteristics in the presence of tunneling can be described by [Rh 88]

$$J = J_s \exp(V/E_o) \qquad \text{....... (3.7)}$$

where

$$E_o = E_{oo} \coth(qE_{oo}/kT) \qquad \text{....... (3.8)}$$

and

$$E_{oo} = h/4\pi \, (N_d/m^*\epsilon_s)^{\frac{1}{2}} \qquad \text{....... (3.9)}$$

Digitised by the Department of Library Services in support of open access to information, University of Pretoria, 2021

where N_d is the doping level of the semiconductor, m* the electron effective mass, h Planck's constant and ϵ_s the semiconductor's permittivity ($\epsilon_s=\epsilon_r\epsilon_o$).

Note that the difference between FE and TFE can be detected via the energy E_{oo} parameter, due to the temperature independence of the FE mechanism. Further, the kT/E_{oo} term is a measure of the relative importance of the TE and tunneling process. At low temperatures, i.e. $kT/qE_{oo}<<1$ and $E_o \approx E_{oo}$, while the slope of the ln J vs V plot is independent of T. This is the case for FE. At high temperatures, where $kT/qE_{oo}>>1$, or $E_o \approx kT$, the slope of ln J vs V is q/kT, which corresponds to TE. For temperatures in the range where $kT \approx qE_{oo}$, TFE will dominate.

3.4.4 Recombination in the depletion region and hole injection

Due to the fact that recombination currents (caused by the recombination between a hole and an electron) are a common cause of departure from ideal behaviour in Schottky diodes, they will therefore only be briefly discussed here.

The importance of recombination in the depletion region has originally been considered in a paper by Yu and Snow [Yu 68]. The recombination normally takes place via localized states and according to the theory the most effective centres are those with energies lying near the middle of the bandgap and is given by [Rh 88]

$$J = J_r \exp (qV/2kT) \qquad \ldots\ldots (3.10)$$

where

$$J_r = qn_i w/\tau$$

with n_i the intrinsic concentration, which is proportional to exp $(-qE_g/2kT)$, w the depletion width and τ the lifetime within the depletion region. The recombination component is more important in semiconductors with high barrier values and low lifetimes at both low temperatures and low bias voltages. (It is therefore much more important in GaAs than in Si Schottky contacts.)

Digitised by the Department of Library Services in support of open access to information, University of Pretoria, 2021

Besides the majority carrier (electron) current in a metal/n-semiconductor contact, minority carrier (hole) current also exists due to hole injection from the metal to the semiconductor, although under normal conditions the majority carrier current is orders of magnitude higher than minority carrier current. A theoretical treatment of minority carrier injection in metal/n-semiconductors has been considered by Scharfetter [Sc 65] and is also discussed by Ya and Snow in their paper on recombination [Ya 68].

If the Schottky barrier height of a contact to an n-type semiconductor is greater than half the bandgap of the semiconductor, the region of the semiconductor adjacent to the metal has a high concentration of holes and thus has a p-type nature. Under a forward bias the electrons from the semiconductor flow into the metal and same of the holes diffuse into the depletion region, causing injection of holes from the metal into the semiconductor. Therefore, the minority carriers current originate when these holes recombines with electrons as they diffuse into the neutral semiconductor.

For junctions to n-type semiconductors which have a high electron mobility (such as GaAs and InP), the current is usually limited by thermionic or thermionic-field emission which leads to ideal diode characteristics. In such a situation the hole injection and recombination in the depletion region is neglected. However, if the abovementioned effects are important, departure from the ideal behaviour is obtained. For such a behaviour the current flow characteristics cannot easily be dealt with analytically, but numerical modelling techniques are used. A discussion of numerical computation is beyond the scope of this chapter and the reader is referred to the following references in literature [Ma 81c, El 85 and He 85a].

3.5 OHMIC CONTACTS

3.5.1 Introduction

Ohmic contacts may be considered as a special type of Schottky barriers in which the depletion region is so thin that the

Digitised by the Department of Library Services in support of open access to information, University of Pretoria, 2021

transport of carriers from the semiconductor to the metal occurs predominantly by tunneling [Ri 70]. Generally speaking, the term ohmic contact, as defined in the beginning of Chapter 1, refers to a metal-semiconductor contact which has linear I-V characteristics in both directions. However, it does not always have to imply a linear I-V curve, but in practice a contact is considered an ohmic contact if it can conduct a required current density with a resultant voltage drop over it, that is sufficiently smaller than the drop across the active region of the device [Ri 75].

The transition from Schottky contact to an ohmic contact can in general be directly related to the doping level in the semiconductor. As the doping increases, the metal-semiconductor junction should pass gradually from TE to TFE and finally FE, due to the lowering of the barrier and the decreasing depletion width. This change in the transport mechanism due to different doping levels is clearly illustrated in the I-V plot shown in Fig. 3.9 for Au contacts on GaAs [Me 69].

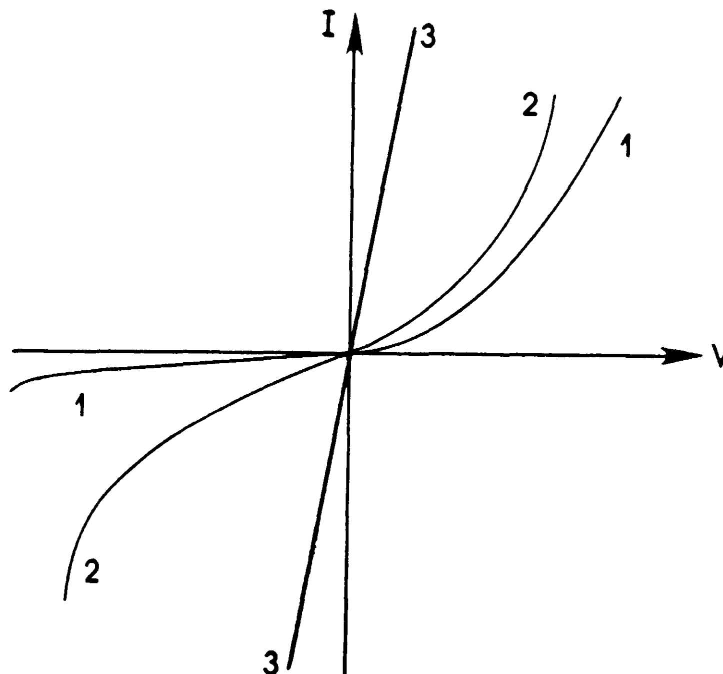

Figure 3.9: Different I-V characteristics for Au contacts on GaAs due to different doping levels [Me 69]. These I-V graphs refer to the respective transport mechanisms; 1: Thermionic emission, 2: Thermionic-field emission and 3: Field emission.

Digitised by the Department of Library Services in support of open access to information, University of Pretoria, 2021

In Chapter 2 the different methods for the fabrication of ohmic contract were discussed. However, different theoretical explanations are given in literature for the various ohmic contact formations. These theories will be briefly discussed below while the importance of low specific contact resistance (r_c) will also be considered, as well as the different r_c measuring techniques.

3.5.2 Models of ohmic contacts

In Fig. 3.10(a) an ideal n-type GaAs or InP energy band diagram is shown. As already discussed above, it is not possible to obtain a GaAs or InP surface that is without distortion or contamination as shown in Fig. 3.10(a). It has been shown that even after 0,01 monolayer coverage of the GaAs surface by a metal or oxygen, the Fermi level becomes "pinned" and its energy position (energy) is roughly independent of the metal or oxide [Sp 80]. The pinning position is roughly 0,8 and 0,5 eV below the conduction band minimum for n-type GaAs and InP respectively. Since 0,8 and 0,5 eV are also the approximated Schottky barrier heights most metals form on n-type GaAs and InP, it was suggested that the Fermi-level pinning and the Schottky barrier formation might be determined by the same mechanisms [Me 64 and Wo 87].

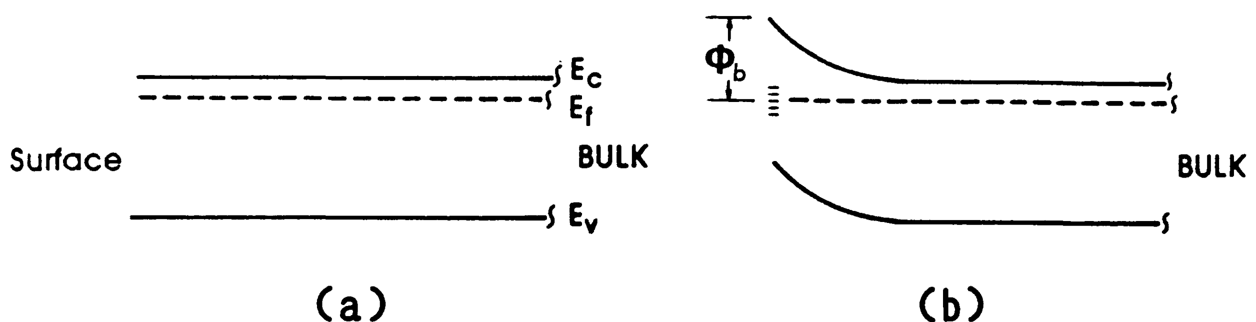

Figure 3.10: Schematic energy band diagram of an (a) ideal and (b) pinned n-type GaAs or InP surface [Br 86].

Digitised by the Department of Library Services in support of open access to information, University of Pretoria, 2021

For the fabrication of ohmic contacts, the barrier heights normally obtained for Schottky barriers are too high. As was pointed out in section 2.2.1, most of the ohmic contact fabrication methods depend on four principles, with the first two being the most relevant models. Firstly, by increasing the donor concentration near the interface, the barrier width and height can be decreased. A theoretical prediction of the change in the barrier with doping for InP and GaAs is shown in Fig. 3.11. Therefore, the carrier transport mechanism can be changed from TE to FE as is illustrated in Fig. 3.12(a) and (b).

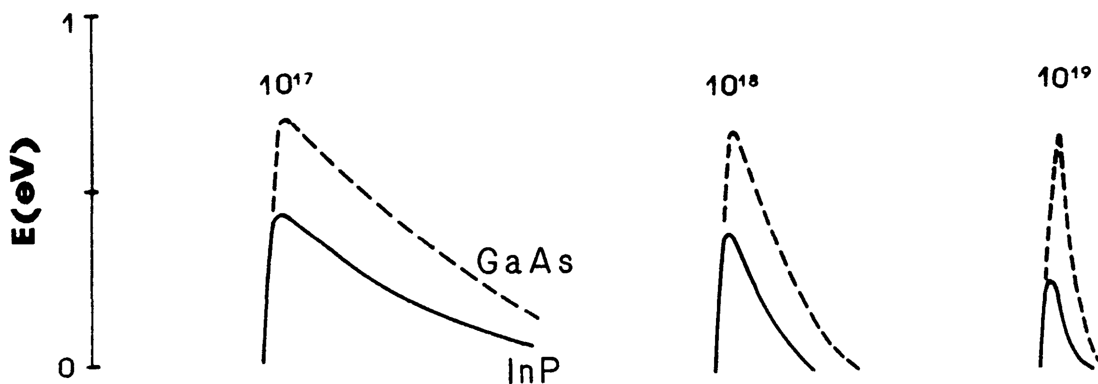

Figure 3.11: Theoretical prediction of the effect of doping on the barrier heights of InP and GaAs surfaces.

Fermi levels are not always pinned in the midgap as is the case with GaAs. It is a well documented fact that n-InAs exhibit pinning in the conduction band [Me 63 and Wa 71]. This gives rise to the second method in which the composition of the semiconductor adjacent to the metal-semiconductor interface is changed in such a way that the Fermi-level of the newly grown semiconductor (normally epitaxially grown), is pinned in the conduction band (see Fig. 3.12(c)). Such a structure was

Digitised by the Department of Library Services in support of open access to information, University of Pretoria, 2021

fabricated by Woodall [Wo 81a] by means of MBE and consisted of a n-GaAs layer deposited onto a GaAs substrate. This was followed by a graded n-$In_{1-x}Ga_xAs$ layer, starting at $Ga_{0,999}In_{0,001}As$ and ending with InAs.

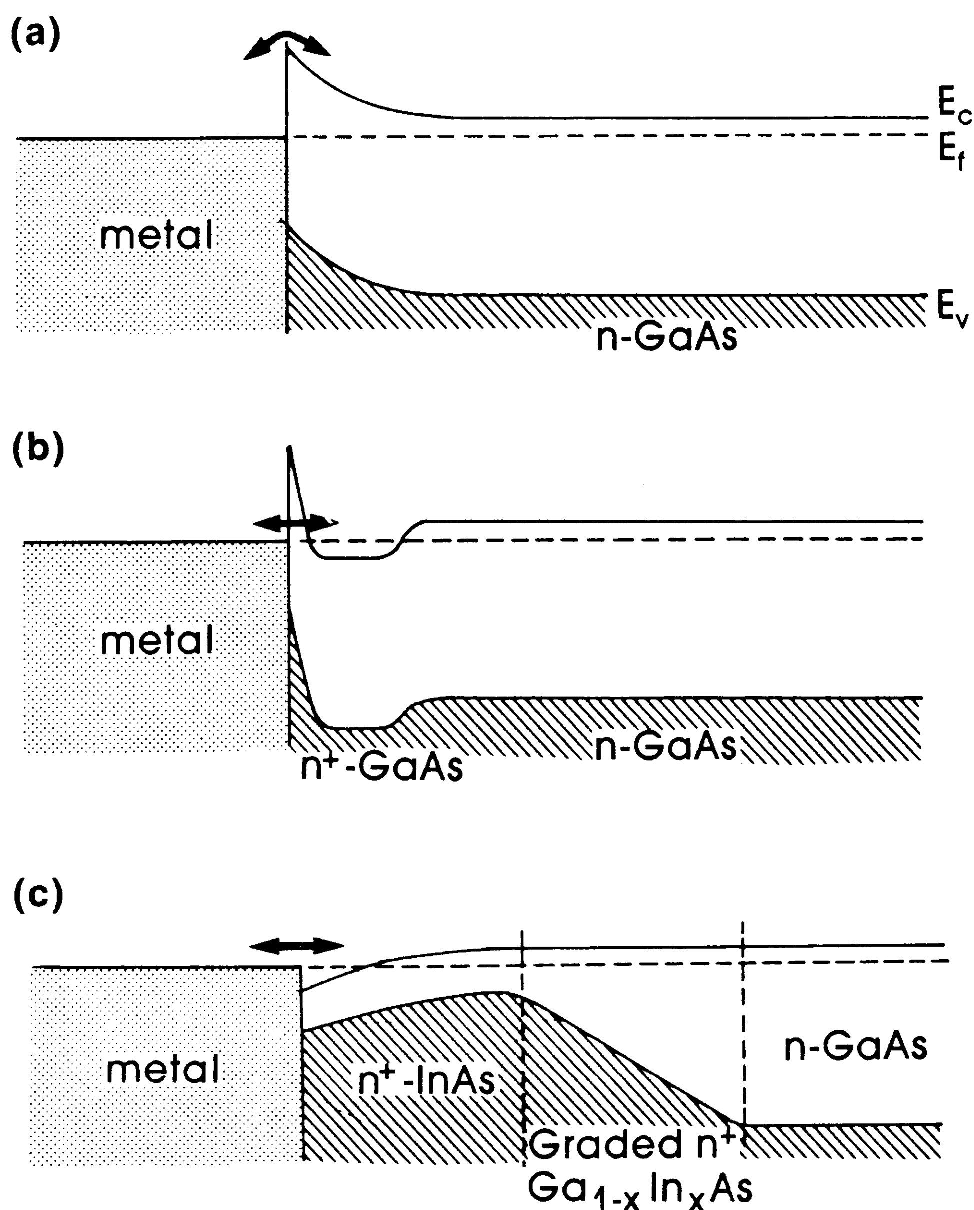

Figure 3.12: Energy band diagram of contacts to n-GaAs: (a) After metal deposition. (b) Metal/GaAs ohmic contact with heavily doped interface. (c) Ohmic contact on a graded layer from GaAs at the substract to InAs at the interface. [Wo 81a].

Digitised by the Department of Library Services in support of open access to information, University of Pretoria, 2021

Note that ohmic contacts fabricated by means of the first method, have to be subjected to an annealing step, (also known as alloying) in order to heavily dope the interfacial region of the semiconductor. With the second method, non-alloyed ohmic contacts with specific contact resistances as low as $5x10^{-9}$ Ωcm^2 [Ni 88] have already been obtained. Unfortunately, although excellent ohmic contacts are obtained by using epitaxially grown methods, such metallization techniques are impractical. This is not only due to the expense and complexity of MBE systems, but also because of the high substrate temperatures that are required during epitaxial growth. These temperatures are incompatible with conventional lithography used for device processing [Pa 85a and Sa 89]. It is therefore not surprising that the most frequently used ohmic contact fabrication technique still consist of an annealing step in order to obtain a heavily doped interface.

3.6 SPECIFIC CONTACT RESISTANCE MEASUREMENTS

Apart from possessing excellent mechanical properties, ohmic contacts must also, firstly, be electrically stable. The electrical quality of an ohmic contact is characterized by its specific contact resistance (r_c), which ideally is the resistance per unit area of the metal-semiconductor interfacial layer and is defined as [Rh 88]

$$r_c = (\partial J/\partial V)^{-1}_{V=0} \qquad \text{...... (3.11)}$$

where J is the current density flowing across the contact and V the potential drop across the interface around zero bias.

Yu [Yu 70] has calculated the specific contact resistance (r_c) by using equation (3.11) for the three regions discussed in section 3.3.4 and observed that r_c is determined predominantly by the following factors:

$$\exp [\Phi/kT] \quad \text{for TE;} \qquad \text{...... (3.12)}$$

$$\exp [\Phi/(E_{oo} \coth (E_{oo}/kT))] \quad \text{for TFE} \qquad \text{...... (3.13)}$$

Digitised by the Department of Library Services in support of open access to information, University of Pretoria, 2021

and

$$\exp\,[\Phi/E_{oo}] \text{ for FE} \qquad \ldots\ldots \ (3.14)$$

where E_{oo} is the tunneling parameter and the rest of the symbols have their usual meaning as defined previously. The predicted behaviour of r_c from the calculations of Yu [Yu 70] is shown in Fig. 3.13. In the FE region ln r_c depends linearly on $N_d^{-\frac{1}{2}}$. However, for practical contacts the relationship has been found to be closer to N_d^{-1} [Go 70, Br 81 and Di 86]. In the TE region r_c is independent of N_d, while TFE is the transition between the two regions.

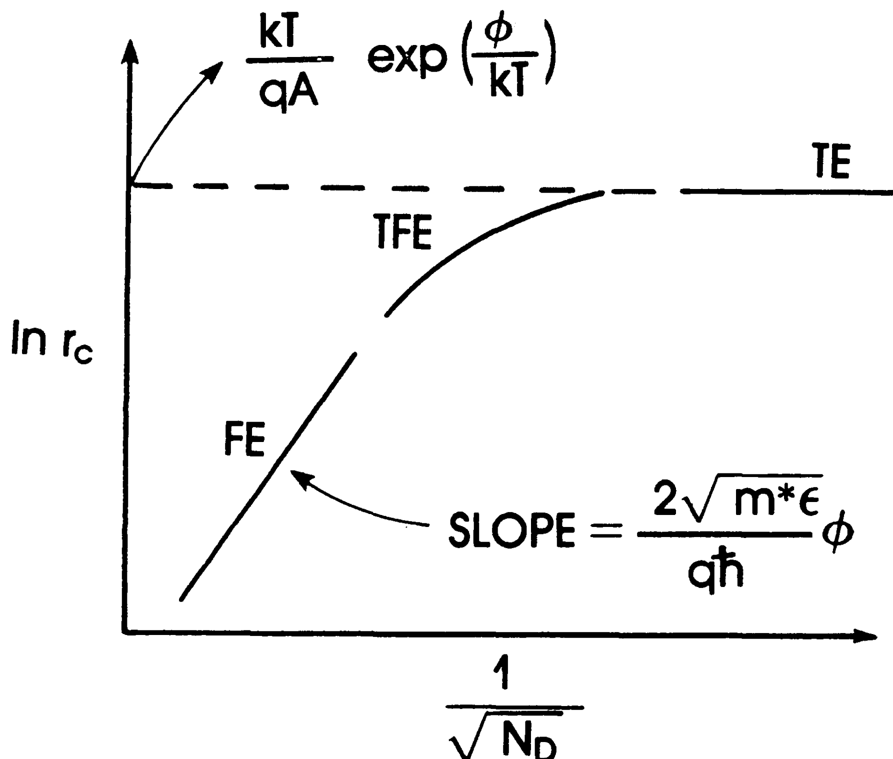

Figure 3.13: **Theoretical dependence of r_c on the doping concentration N_d [Yu 70].**

Digitised by the Department of Library Services in support of open access to information, University of Pretoria, 2021

A knowledge of the factors that determine the specific contact resistance is of critical importance, not only for fabrication purposes, but also for assessment of device performance. The influence of the specific contact resistance on the noise figure of a FET device is schematically illustrated in Fig. 3.14. It is thus important to be able to measure the specific contact resistance as accurately as possible.

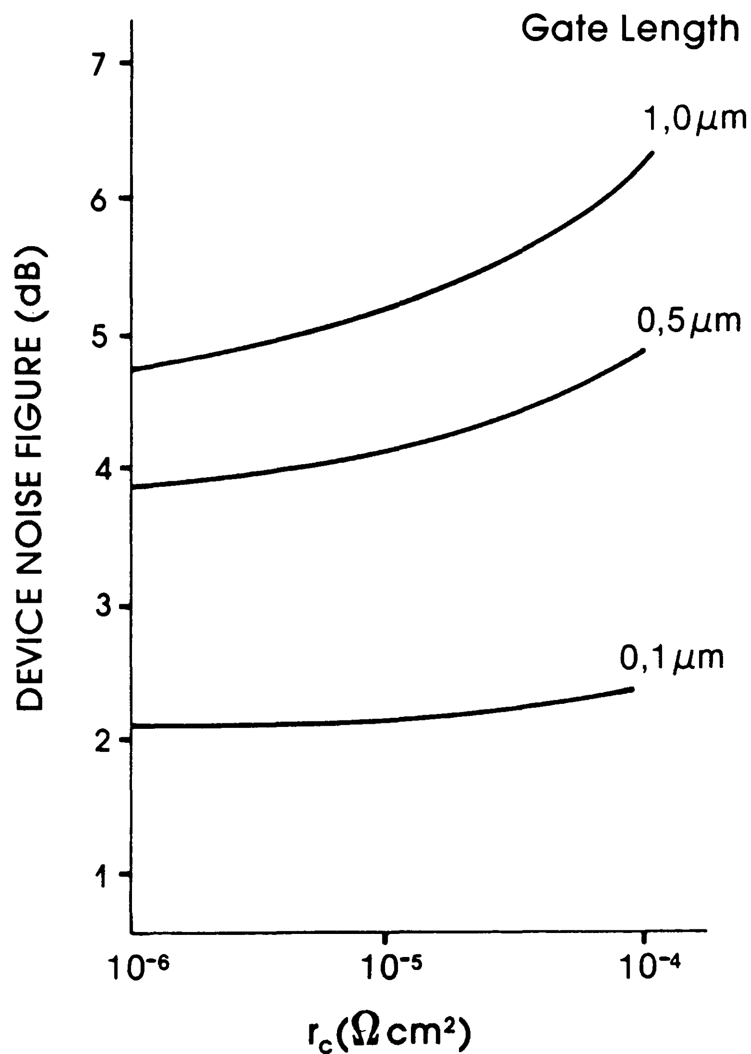

Figure 3.14: **The effect on a FET noise figure with changes in the specific contact resistance (Frequency: 34 GHz; Gate width: 50 μm).**

Digitised by the Department of Library Services in support of open access to information, University of Pretoria, 2021

Before discussing the different methods that can be used to measure r_c, it is important to note that none of the presently available methods is capable of directly giving r_c. The measured resistance (R_t) of a contact on a semiconductor will be composed of [Ro 85]:

a) The resistance of the measuring circuit and contact material (R_o),
b) the resistance of the contact (R_c),
c) the spreading resistance under the contact (R_s) and
d) the resistance of the semiconductor between the contacts (R_m).

Hence

$$R_t = R_o+R_s+R_c+R_m \qquad \text{...... (3.15)}$$

with

$$R_c = r_c/A$$

and A the contact area.

Accurate determination of r_c is most often carried out by using the following methods:

(1) the technique of Cox and Strack [Co 67],
(2) the four point method [Te 69],
(3) the Shockley extrapolation technique [Sh 64],
(4) the transmission-line model [TLM] [Mu 69], or
(5) the Kelvin resistor method [Sh 74].

These models will only be discussed briefly here, but various reviews on r_c measurement techniques and models can be found in literature [Co 83, Ro 85 and Sc 88].

3.6.1 Cox and Strack technique

In this technique metallization is required for both the back and the front surfaces of the semiconductor wafer and it can be used for epitaxial layers or bulk samples. The spreading resistance

Digitised by the Department of Library Services in support of open access to information, University of Pretoria, 2021

for a layer of resistivity ρ and thickness t with a circular contact of radius a is given by [Ro 85]

$$R_s = (\rho/a)\ F \qquad ......\ (3.16)$$

where F was found by Cox and Strack to have the approximate form

$$F(a/t) \approx \frac{1}{\pi} \arctan\ (2t/a) \qquad ......\ (3.17)$$

However, Brooks and Mathes [Br 71] have numerically developed an integral expression for F(a/t) in the form of a universal curve. The specific resistance can be calculated from the following equation

$$R_t = r_c/\pi a^2 + (\rho/a)F + R_o + R_m \qquad ......\ (3.18)$$

which is obtained from equations (3.15) and (3.16). Normally, contacts with different areas are used, in order to obtain more accurate r_c values when using eq. (3.18). For n-type GaAs epitaxial layers, it is possible to obtain r_c values down to $\sim 1\times10^{-6}$ Ωcm^2, with an error of about ±25% [Ro 85].

3.6.2 Four-point method

The four-point probe method [Te 69] requires metallisation of only one surface of a bulk or an epitaxially grown semiconductor (see Fig. 3.15). The voltages V_1 and V_2 are measured between contacts 1 and 2 and 2 and 3 respectively, while the current I is applied between contacts 1 and 4. These equidistance contacts with the same diameter are arranged on a straight line. Kuphal [Ku 81] developed a modified four-point method which differ from the original model of Terry and Wilson [Te 69] in two ways. Firstly, spreading resistance (R_s) is included in the model of Kuphal. In his model, R_s is calculated for radial current flow from a circular contact of radius d, by using the TLM calculations given by Fang et al. [Fa 79a] in the form of an infinite series

Digitised by the Department of Library Services in support of open access to information, University of Pretoria, 2021

$$R_S = \frac{4r_c}{\pi d^2} \left[\frac{\sum_{m=0}^{\infty} y^m/(2^{2m}(m!)^2)}{\sum_{m=0}^{\infty} y^m/(2^{2m}(m!)^2(m+1))} \right] \qquad \text{...... (3.19)}$$

where

$$y = \frac{\rho d^2}{4r_c t}$$

infinite series with ρ the resistivity, d the contact diameter and t the semiconductor thickness. For $y \leq 1$, $R_S \leq 0.12R_C$, which is negligible in most cases (R_C contact resistance).

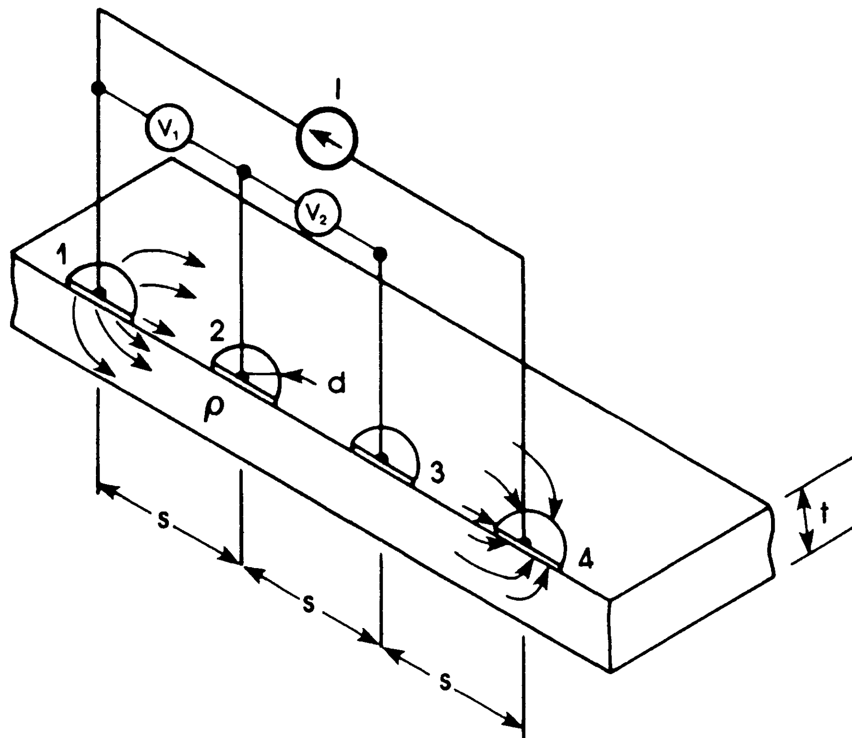

Figure 3.15: Measurement of r_c with the four-point method [Ro 85].

In the original four-point model, it was assumed that the resistance of the semiconductor between the contacts is the same everywhere for known V_1, V_2 and I values. Hence for circular contacts

Digitised by the Department of Library Services in support of open access to information, University of Pretoria, 2021

$$V_1 - V_2 = I\ (R_C + R_S)$$

or $$r_c = \pi d^2 (V_1/I - V_2/I - R_s)$$

It must be noted that R_o is negligible in ohmic contacts where high potentials are measured on highly doped substrates. Secondly, Kuphal pointed out that the potential distribution under the circular contacts, in the plane of the semiconductor layer, is logarithmic rather than linear as was assumed above. Consequently, the correct expression for the specific contact resistance is [Ku 81]

$$r_c = \pi d^2 \left(V_1/I - \frac{V_2 \ln(3s/2d - 0{,}5)}{I(2\ln 2)} - R_s\right) \qquad \text{...... (3.20)}$$

if d<<s and t<<s. If $y \leq 1$ is satisfied, then R_s can be neglected in eq. (3.20). Kuphal [Ku 81] used this technique to measure values of r_c as small as $1{,}2 \times 10^{-6}\ \Omega cm^2$ with ±10% accuracy for ohmic contacts to n-InP.

3.6.3 Shockley extrapolation model

This technique is also called the transfer length method (not TLM) and was first proposed by Shockley [Sh 64]. This method of obtaining r_c can only be used for semiconductor layers on semi-insulating substrates. The technique consists of measuring the voltage variation along the semiconductor layer, directly under the contact.

Up to the edge of the metal contact, current flow is assumed to be laminar and by using the definition of resistivity, the voltage drop can be calculated from [Wi 87a]

$$dV = \frac{-I\rho}{zt}\, dx \qquad \text{...... (3.21)}$$

where I is the current flow through the semiconductor of width z, thickness t and resistivity ρ (see Fig. 3.16). The relation of ρ/t is normally defined as the sheet resistance of the

Digitised by the Department of Library Services in support of open access to information, University of Pretoria, 2021

semiconductor layer and is given by

$$R_{sh} = \rho/t \qquad \text{...... (3.22)}$$

Thus

$$dV = -\frac{I\ R_{sh}}{z}\,dx \qquad \text{...... (3.23)}$$

From eq. (3.23) it is clear that the voltage drop up to the edge of the collecting contact is linear. From the slope of the straight line resulting from the V vs distance (x) graph, the sheet resistance and ρ of the semiconductor layer can be obtained

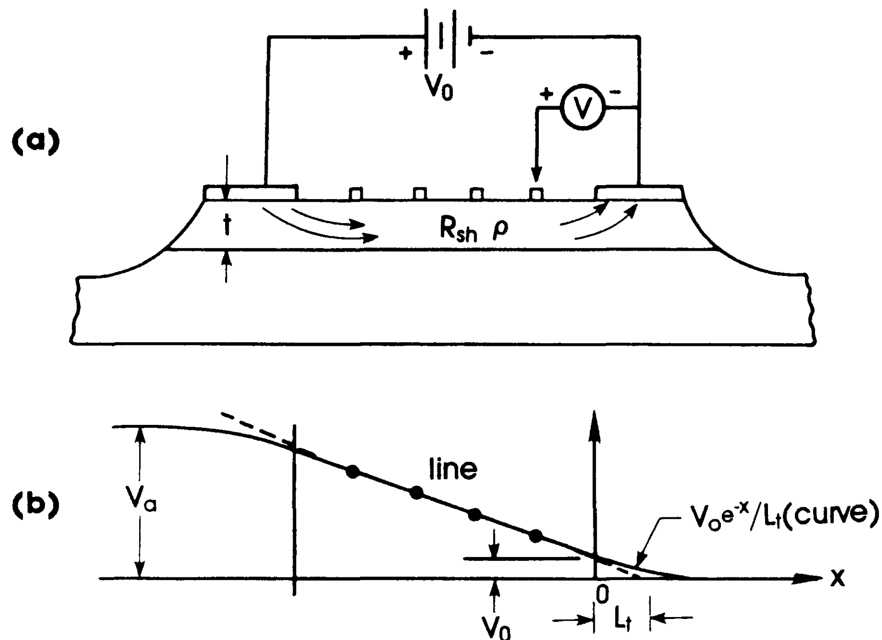

Figure 3.16: Shockley technique of measuring r_c. The various symbols are explained in the text [Ro 85]

by using equations (3.22) and (3.23). However, because R_{sh} and r_c are non-zero, the current is non-uniformly distributed and current crowding occurs under the contacts. Hower et al. [Ho 71] have shown that the potential distribution under the contact is more accurately given by

$$V(x) = V_o \exp(-x/L_t) \qquad \text{...... (3.24)}$$

Digitised by the Department of Library Services in support of open access to information, University of Pretoria, 2021

where $L_t = (r_c/R_{Sh})^{\frac{1}{2}}$ ...... (3.25)

Since the electric field is continuous at x=0 (see Fig. 3.14(b)), the slopes of the line and the curve must match at this point ($V=V_o$) and therefore [Wi 87a]

$$\left.\frac{dV}{dx}\right|_{x=0}^{line} = \left.\frac{dV}{dx}\right|_{x=0}^{curve} \qquad \text{...... (3.26)}$$

and $$\frac{IR_{Sh}}{z} = \frac{V_o}{L_t} \qquad \text{......... (3.27)}$$

thus $$L_t = \frac{V_o z}{IR_{Sh}} \qquad \text{......... (3.28)}$$

From the straight line plot mentioned above, V_o and therefore L_t can be determined. The specific contact resistance value can then be obtained from eq. (3.25). For L_t measurements within ±1 μm accuracy, it should be possible to measure r_c down to $\pm 5\times10^{-7}$ Ωcm^2 with ±25% accuracy for ohmic contacts to n-GaAs.

3.6.4 Transmission line model

The use of the transmission line model (TLM) avoids the necessity of measuring the V(x) distribution of the Shockley method and hence is somewhat simpler to implement. In the TLM the contact is treated as a resistive transmission line with uniform sheet resistance. Different variations exist for the TLM, which was introduced by Shockley [Sc 64] and refined by Berger [Be 72 and Be 72a] and by Murrmann and Widmann [Mu 69 and Mu 69a]. This method can only be used for semiconductor layers on insulating semiconductor substrates.

This technique involves forcing a constant current, I, through adjacent pairs of contacts of different spacings (see Fig. 3.17). The voltage drop ΔV is measured as a function of contact spacing. From equations (3.24) and (3.28), the voltage drop under a contact, for the situation where the length of the contact is much greater than L_t, is given by [Wi 87a]

$$V=V_o = \frac{IR_{Sh}L_t}{Z} \qquad \text{...... (3.29)}$$

Digitised by the Department of Library Services in support of open access to information, University of Pretoria, 2021

By using equations (3.27) and (3.29) the total voltage drop across two pads with spacing d is given by

$$\Delta V = IR_{Sh} \left(\frac{d}{Z} + \frac{2L_t}{Z}\right) \quad \ldots\ldots (3.30)$$

The graph of ΔV vs d yields a straight line of gradient IR_{Sh}/Z and intercept $2IR_{Sh}L_t/Z$. From this, R_{Sh} and L_t can be determined and therefore also r_c because

$$r_c = L_t^2 R_{Sh}$$

For the TLM a linear array of rectangular, square or circular contact geometry is commonly used (see Fig. 3.17). For

(a)

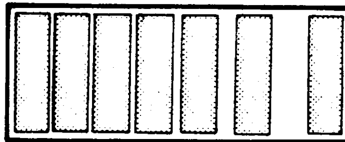

(b)

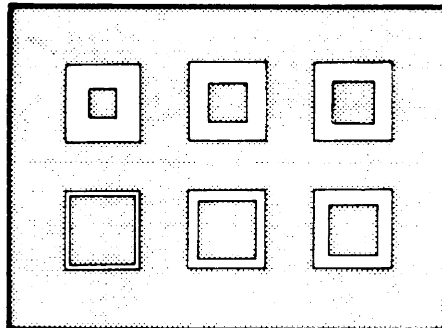

(c)

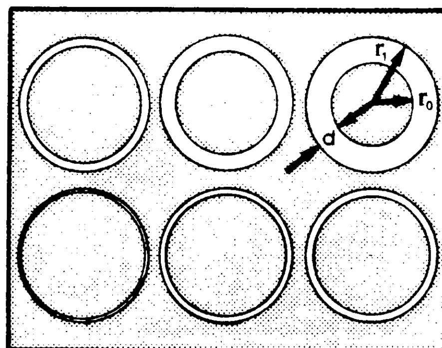

Figure 3.17: Different patterns used for r_c measurements in the TLM. (a) Rectangular (b) square and (c) circular contact geometry [Wi 84].

Digitised by the Department of Library Services in support of open access to information, University of Pretoria, 2021

rectangular and square contacts, mesa structures are needed in order to eliminate unwanted current flow patterns due to edge effects, which are not accounted for in the TLM theory. However, this complication can be totally avoided by using a circular test pattern, but the resultant equations can sometimes be considerably more complex than those obtained for the other two contact systems.

By passing a constant current through the circles with different d spacings, the voltage drop ΔV across the circles can be plotted against d and is given by [Ni 71]

$$\Delta V = \frac{IR_{sh}}{2\pi}\left[\ln\left(\frac{r_1}{r_0}\right) + \frac{L_t I_1(r_0/L_t)}{r_0 I_2(r_0/L_t)} + \frac{L_t K_0(R_1/L_t)}{r_1 K_1(r_1/L_t)}\right] \qquad \ldots\ldots (3.31)$$

where I_1, I_2, K_o and K_1 are the modified Bessel functions, r_o and r_1 the radii that define the separation d (see Fig. 3.15(c)), R_{sh} the semiconductor sheet resistance and L_t the transfer length. When r_o and r_1 are greater than L_t by a factor of at least 4, then both I_1/I_2 and K_o/K_1 approximate unity [Ma 82]. Thus, equation (3.31) becomes

$$\Delta V \simeq \frac{IR_{sh}}{2\pi}\left[\ln\left(\frac{r_1}{r_1-d}\right) + L_t\left(\frac{1}{r_1} + \frac{1}{r_1-d}\right)\right] \qquad \ldots\ldots (3.32)$$

Numerical calculations based on equation (3.32) are used to obtain actual curve fits to experimental data. The intersection with the d-axis yields $2L_t$. From the slope of the curve and with the value for L_t, one obtains R_{sh} Therefore r_c can be determined from equation (3.25). Values of r_c as low as 5×10^{-9} Ωcm^2 to GaAs have been reported, by using the TLM [Ni 88], but the accuracy of this value is doubtful.

Digitised by the Department of Library Services in support of open access to information, University of Pretoria, 2021

3.6.5 Kelvin resistor method

Shih and Blum [Sh 72] were the first to use this structure to measure contact resistance. Until recently, only a few papers had been reported using this technique. Interest has been renewed after publications by Cohen [Co 83] and Procter et al. [Pr 83].

In the Kelvin resistor method a four (or six) terminal structure is used to measure R_C directly [Co 83 and Sc 88]. The measurements consist of forcing a known current from pad 1 to pad 3 (see Fig. 3.18), while the voltage drop is measured between pads 2 and 4. In order to determine R_C, a two dimensional resistor network model was developed by Proctor et al. [Pr 83]. From this model R_C is obtained by using the equation

$$R_C = \frac{V_2 - V_4}{I} \qquad \text{...... (3.33)}$$

The specific contact resistance, r_C, can be calculated from the measured R_C and the contact window area.

It is interesting to note that most of the reported cases where the Kelvin structure was used, referred to contacts on ion implanted Si substrates [Pr 83 and Ch 84]. However, Bahir et al. [Ba 87] recently used this technique for Au-Ge/Ni ohmic contacts on InP and measured r_C values as low as 2×10^{-7} Ωcm^2.

In conclusion, the measurement of specific contact resistance values and other associated parameters can be performed relatively easily by using a suitable test pattern. However, it is more difficult to obtain accurate specific contact resistance values. Extract accurate r_C values from experimental measurements requires the assumption of a model establishing the relationships among the various parameters.

Digitised by the Department of Library Services in support of open access to information, University of Pretoria, 2021

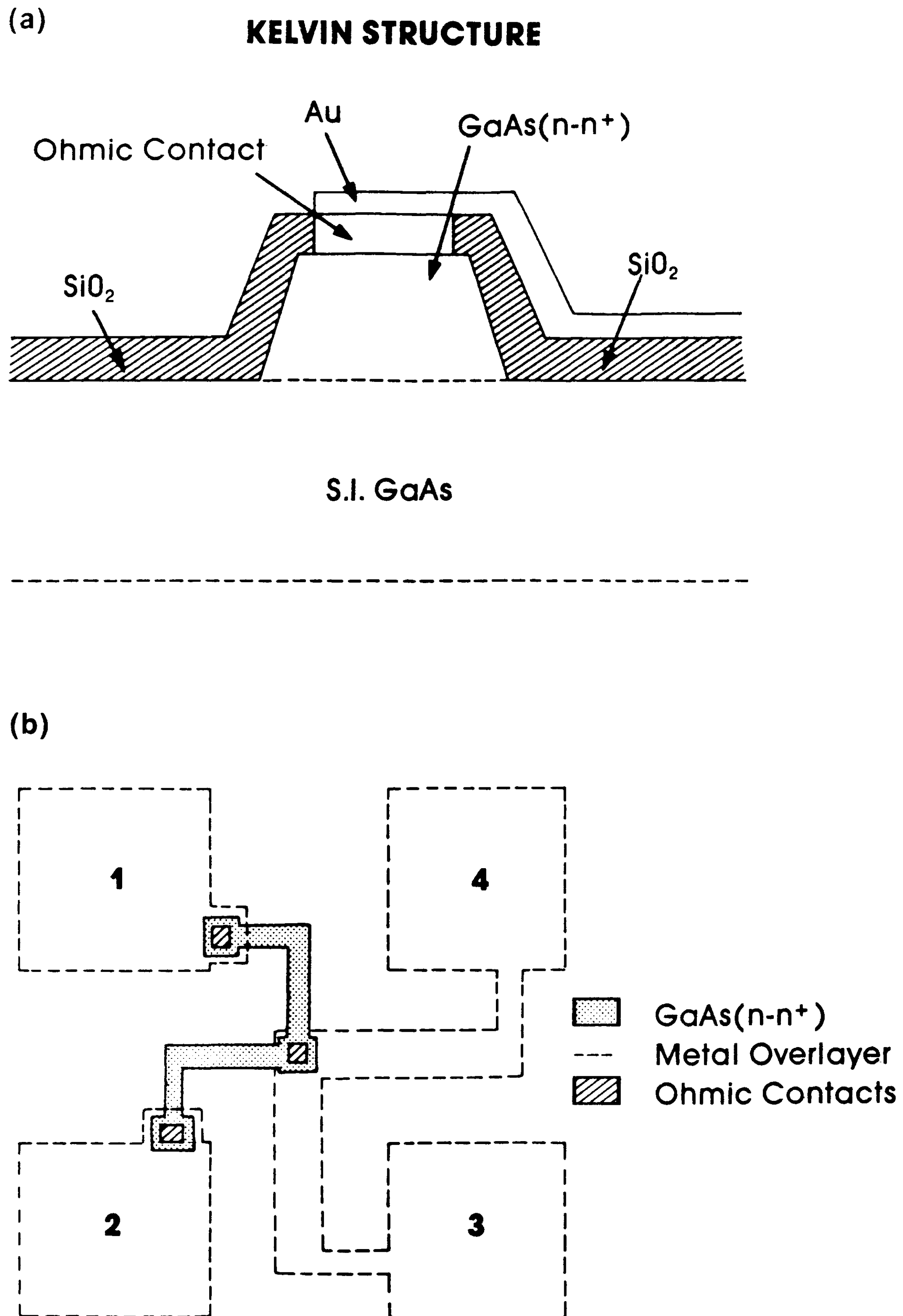

Figure 3.18: A cross-sectional (a) and planar (b) view of a four-terminal Kelvin resistor structure [Ba 87].

Digitised by the Department of Library Services in support of open access to information, University of Pretoria, 2021

CHAPTER 4

EXPERIMENTAL PROCEDURES

4.1 INTRODUCTION

The background and theory of ohmic contacts to n-type GaAs and InP have been dealt with in the previous two chapters. The purpose of this chapter is to explain the experimental methods and apparatus used in this study. This chapter is divided into the following two sections:

(i) Sample preparation procedures, and

(ii) Description of apparatus used for structural and electrical investigations.

4.2 SAMPLE PREPARATION

An atomically clean and ordered semiconductor surface, free of oxides, which form a dielectric medium between the substrate and the metallization layer, is essential for a good and stable ohmic contact. As a result, the semiconductor wafers used in this study had to undergo a chemical cleaning process, prior to the deposition of the metal layers. In order to obtain an ohmic contact, the contact system was subjected to an annealing step. (The various fabrication and annealing techniques are discussed in Chapter 2.) Once this preparation was complete, structural and electrical analysis was carried out on the contacts.

4.2.1 Cleaning process

Bulk grown GaAs (100) and InP (100) wafers were obtained from Sumitomo and Nippon Mining Company respectively. The GaAs substrates, grown by the horizontal Bridgeman process, were Si doped ($8x10^{17}$ - $2x10^{18}cm^{-3}$). The InP substrates were LEC grown and S doped ($1-3x10^{18}cm^{-3}$). All the wafers were factory polished on one side only. All the wafers had a thickness of between 0,3-

Digitised by the Department of Library Services in support of open access to information, University of Pretoria, 2021

0,4 mm. One set of contacts was investigated on an epitaxially grown GaAs layer. These epitaxial layers were organic-metal vapour phase epitaxy (OMVPE) grown on S.I. GaAs at the CSIR. The layers were Te doped $8x10^{17}cm^{-3}$, with a thickness of ±5 μm.

The following cleaning procedure was used for the GaAs wafers prior to the photolithographic step.

(a) Degreasing:

(i) Trichlorethylene (at ±50 °C for 2 minutes, repeated 3 times)

(ii) Isoproponol (at ±40 °C for 2 minutes, repeated 3 times)

(iii) Rinse in de-ionized water (for 1 minute, repeated 3 times)

(iv) Blow dry with pure N_2 gas.

(b) Etch:

(i) $H_2SO_4:H_2O_2:H_2O$ (5:1:1) (for 2 minutes). Note that this etch was chosen above the following two etchants: $NH_3:H_2O_2:H_2O$ (3:1:150) (for 2 minutes) and $H_3PO_4:H_2O_2:H_2O$ (1:1:150) (for 2 minutes). See Chapter 5, sub-section 2.1).

(ii) Rinse in de-ionized water (repeated 4 times). (This step served a dual purpose, firstly to stop the etching process and secondly, to re-oxidize the surface.)

(iii) Blow dry with pure N_2 gas.

Digitised by the Department of Library Services in support of open access to information, University of Pretoria, 2021

(c) Oxide leach:

(i) $HCl:H_2O$ (1:1) (for 3 minutes).

(ii) Rinse in de-ionized water (repeated 3 times).

(iii) Blow dry with pure N_2 gas.

The degreasing procedure for the InP wafers was the same as for the GaAs. The rest of the process for InP is as follows.

(a) Etch:

(i) HF (10%) (for 1 minute).

(The HF etch resulted in lower surface contamination than the surfaces etched in $H_2SO_4:H_2O_2:H_2O$ (5:1:1) and Br/CH_3OH respectively. See Chapter 5, sub-section 3.1).

(ii) Rinse in de-ionized water (repeated 3 times).

(iii) Blow dry with pure N_2 gas.

4.2.2 Photolithography

In order to obtain small dimension contacts, patterning techniques instead of mechanical masks had be used. In this technique an energy sensitive chemical substance, called photoresist, is applied as a thin film on the substrate surface. By selectively exposing the resist film to light, electrons, ions, etc. through a pattern (mask), exposed areas are created. The resist film is then subjected to a development process that selectively removes either the exposed or the unexposed resist. Metal is deposited onto the resist and open areas. By using a solvent which dissolves the resist, the metal on top of the resist is then "lifted-off".

The same lithography process was used for the processing of the InP substrates. The following pattering procedure was followed:

Digitised by the Department of Library Services in support of open access to information, University of Pretoria, 2021

(i) Following the degreasing and etching steps discussed above, the wafer was subjected to a pre-bake step at ~90 °C for 10 minutes, to remove any moisture on the surface.

(ii) A 1-1,5 μm thick film of positive photoresist was spun on. (Headway Research Inc. spinner). The spinning speed and time depended on the type of photoresist.

(iii) Post-bake at ±100 °C for 10-20 minutes. (This was a function of the type of photoresist.)

(iv) The photoresist layer was exposed with an ultraviolet light source through a mask. (The exposure time depended on the type of photoresist used and the light source intensity.)

(v) The exposed photoresist was developed.

(vi) The sample was rinsed in de-ionized water (repeated 3 times.)

(vii) The sample was blown dry with pure N_2 gas.

(viii) The sample was dipped in a HN_3:H_2O (1:15) solution.

(ix) The sample was rinsed in de-ionized water.

(x) The sample was blown dry with pure N_2 gas.

It is important to note that due to the lack of sufficient funds an ultraviolet source was built in-house (see Fig. 4.1). It consists primarily of a mercury source, a 1,2 m column and a shutter. The simplicity of the design restricts it to be used only for single layer structures. Line widths of 5 μm could be developed with this ultraviolet source. As an example of the efficiency of the source, Fig. 4.2 shows a SEM micrograph of a 10 μm wide ring opening after lift-off of a Ni/Au-Ge (20 nm/150 nm)

Digitised by the Department of Library Services in support of open access to information, University of Pretoria, 2021

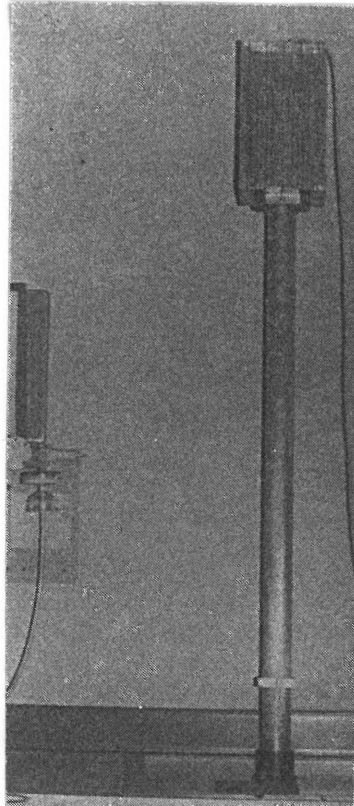

Figure 4.1: Ultraviolet light source used for exposure of the photoresist.

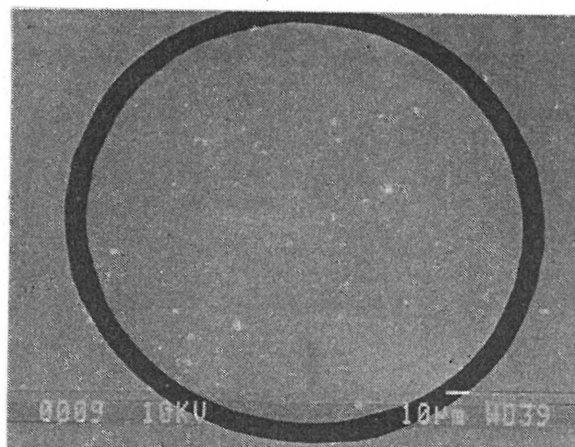

Figure 4.2: SEM micrograph of a 10 μm wide ring after lift-off of a Ni/Au-Ge (20/150 nm) metallization layer. The exposure was done with the ultraviolet source shown in Fig. 4.1.

Digitised by the Department of Library Services in support of open access to information, University of Pretoria, 2021

metallization system. The gray areas are the metallization layer which is on top of the GaAs substrate, shown in black.

4.2.3 Evaporation step

The evaporation system used in this study was a 15 keV Leybold-Heraeus system, which consists of an all metal seal vacuum chamber (see Fig. 4.3). Two unique features of this system are the attachment of a fast introduction system and an ion sputter gun (PHI 20-115). The following items are also present on the system.

(i) Thickness monitor (Inficon XTC).
(ii) Allumina resistive heating boats and power source.
(iii) 15 keV electron beam evaporation system (Leybold-Heraeus)
(iv) Turbo pump (Leybold-Heraeus CSV 350 l/s) which maintains a base pressure of ~$5x10^{-8}$ mbar in the main chamber.
(v) Vacuum monitor meter (Leybold-Heraeus Thermovac TM230).

After the photolithography step, the samples were loaded as quickly as possible onto the sample holder shown in Fig. 4.4. The introduction sample holder consists of a holder that can take a wafer of up to 2", a pushrod and a perspex flange. A viton "O" ring was situated in the flange to maintain vacuum while the pushrod was moved forward and backwards. The front part of the pushrod screwed into the sample holder.

The introduction sample holder fitted onto the introduction chamber, on the left hand side of the evaporation system shown in Fig. 4.3(a). The vacuum in the introduction system was obtained with a turbo pump (Leybold-Heraues CSV 350 l/s). It took ±5 minutes to obtain a vacuum of $1x10^{-4}$ m bar in the intro-duction chamber, whereafter the introduction sample holder was pushed into the main chamber via a 4" gate valve. The introduction sample holder slid into a spring clamped holder, situated in the top section of the main chamber. After the sample holder was

Digitised by the Department of Library Services in support of open access to information, University of Pretoria, 2021

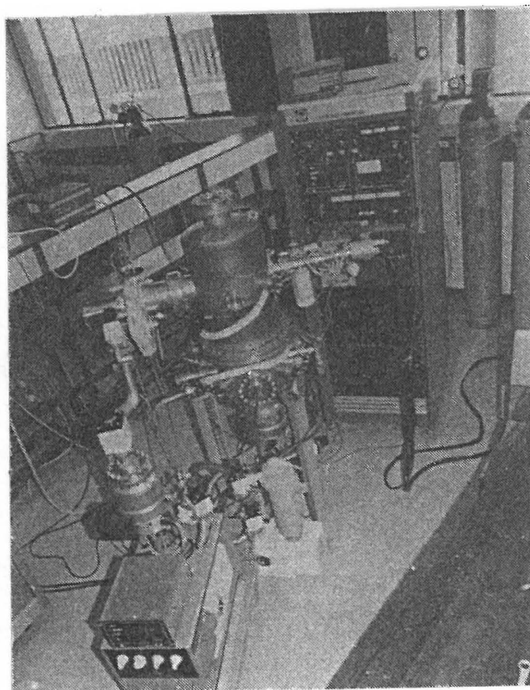

(a)

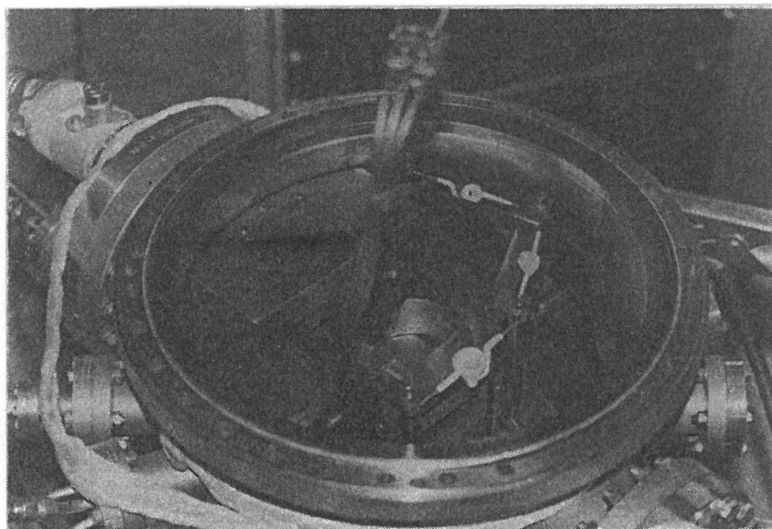

(b)

Figure 4.3: Photographs of (a) the complete evaporator system and (b) the bottom half of the main chamber.

Digitised by the Department of Library Services in support of open access to information, University of Pretoria, 2021

positioned, the rod was screwed out and pulled back into the introduction system. A vacuum of $\sim 1\times10^{-7}$ mbar was reached in the main chamber within ±15 minutes.

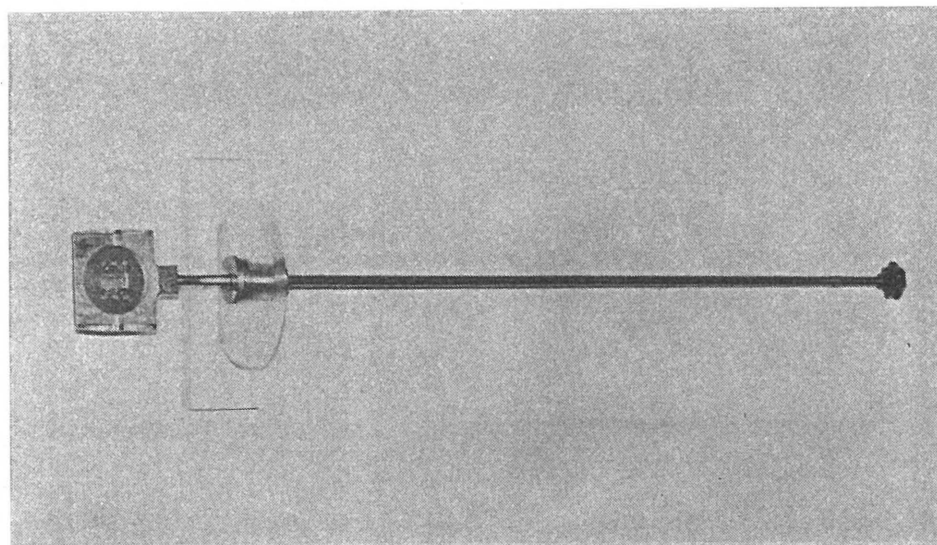

Figure 4.4: Introduction sample holder.

The metals used for evaporation were degreased and etched, prior to loading into the crucibles. Pt, Au and Au-Ge (88-12 at. wt%) were all etched in warm aqua rega, while Ti and Ni were etched in $H_2O:HNO_3:HF$ (10:3:3) and hot $H_2O:HNO_3$ (1:1) respectively. The metals used were of the highest purity obtainable, ranging from 99,95 % to 99,9995 %. Only Ni, Pt and Ti were evaporated by means of the electron gun. All the other metals or alloys used were evaporated by means of resistive heating. Each metal was degassed prior to evaporation, with the back of the sample holder turned towards the evaporation source.

Digitised by the Department of Library Services in support of open access to information, University of Pretoria, 2021

The thickness of the layers deposited as well as the deposition rates were monitored using a crystal thickness monitor (Inficon XTC). This monitor operates on the principle of the change in frequency of a vibrating quartz crystal as a function of accumulated thickness. A microprocessor was used to determine the rate of evaporation and the thickness of the layers. These values were obtained by determining the relative densities of the metal and quartz and by determining a constant depending on the shear modulus of the metal and quartz. A so-called "tooling factor" was used to correct the displacement of the crystal monitor in relation to the actual position of the sample with respect to the evaporation source. By analyzing as-deposited standards from time-to-time, Rutherford backscattering spectroscopy (RBS) results showed that the measurements obtained from the thickness monitor were correct.

The pressure during the evaporation process was between 6×10^{-7} and 1×10^{-6} mbar, depending on the metal deposited. The deposition rate, which also depended on the specific metal, was between 0,2 and 0,5 nm/sec. Sequential evaporation was obtained by turning the back side of the sample holder towards the evaporation source prior to deposition of the next metal. Note that the convention used for the metallization layer sequence in this study is the same as that in Chapter 2. Au/Ni/GaAs represents a layer of Ni on GaAs with a Au layer on the Ni, while Au-Ge/GaAs represents an alloy of gold and germanium on GaAs. However, when only the metallization layer notation such as Ni/Au is used, it refers to a contact system with the Ni layer deposited onto the substrate and the Au on top of the Ni layer. (It therefore refers to a Au/Ni/GaAs metallization scheme.)

Some of the InP substrates were also sputtered prior to metal deposition. High purity Ar gas was leaked into the main chamber until a pressure of 1×10^{-5} mbar was reached. A 2 keV Ar^+ ion beam, which produced a sample current of 15 μA, was used to sputter the sample surface for ±20 minutes. These sputter conditions were kept constant for each sputter experiment.

Digitised by the Department of Library Services in support of open access to information, University of Pretoria, 2021

4.2.4 Annealing process

The annealing process was carried out in a closed, tubed furnace. The furnace used was a Lindberg heavy-duty annealing system and is shown in Fig. 4.5. The right hand side of the quartz tube was attached to the cold end of the high purity Ar gasline. The gas outlet was on the left hand side of the tube. Both ends of the tube were connected to the inlet and outlet tubes via a double "O" ring attachment. A chromel-alumel thermocouple was attached to a quartz sliding boat and served a dual purpose. It was used for accurate temperature measurement at the sample itself, while acting as a pushrod for the sliding boat. The furnace was mounted onto the temperature controller. The furnace had a temperature range from 150-1200 °C and was controlled by a built-in thermocouple.

Once a pre-set temperature was reached, the sample or samples were loaded into the boat on the cold end of the tube and sealed. High purity Ar gas was then introduced to provide an inert ambient prior to the annealing step. After ±15 minutes of Ar gas flow through the closed tube, the boat was pulled to the middle of the furnace. When the required annealing time at the specific temperature expired, the boat was pushed back to the cold end of the tube and allowed to cool down to room temperature. The Ar gas flow through the tube was maintained during the annealing and cooling process. A characteristic temperature vs time graph, for the annealing temperature measured at the samples in the sliding boat is shown in Fig. 4.6. This graph is drawn for a sample which reached 200, 300 and 400 °C respectively, kept at the specific temperature for 2 minutes and then allowed to cool down to room temperature. The method used to obtain this data was as discussed above.

Digitised by the Department of Library Services in support of open access to information, University of Pretoria, 2021

Figure 4.5: Annealing furnace on top of the temperature controller box. The gas inlet on right hand side and gas outlet on left hand side is also visible.

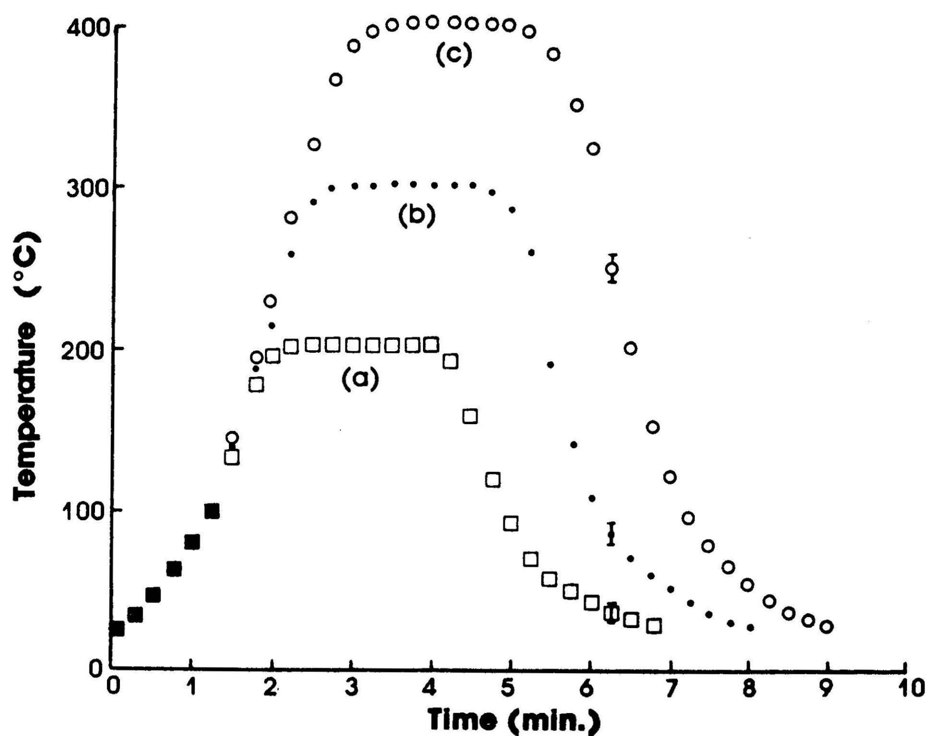

Figure 4.6: Characteristic temperature vs time graph for a sample allowed to reach (a) 200 °C, (b) 300 °C and (c) 400 °C respectively and then allowed to cool to room temperature. These measurements were obtained with the thermocouple attached to the sliding boat.

Digitised by the Department of Library Services in support of open access to information, University of Pretoria, 2021

4.3. DESCRIPTION OF TECHNIQUES USED

The description of the techniques are divided into compositional/ structural and electrical techniques. The following techniques will be discussed as structural techniques:

(a) Auger electron spectroscopy (AES),
(b) Secondary ion mass spectroscopy (SIMS),
(c) X-ray diffraction (XRD),
(d) Secondary electron microscopy (SEM) and optical microscopy.

The discussion on electrical techniques will be restricted to current voltage (I-V) and specific contact resistance (r_c) measurements.

4.3.1 Auger electron spectroscopy (AES)

Numerous review articles and some books on AES have been published, a few of which are given in reference [Pa 72, Br 83 and Ma 89]. In this sub-section the theoretical aspects of AES are only briefly considered, while the two AES systems used will also be discussed.

AES has developed rapidly over the last two decades into a powerful method for chemical analysis of solid surfaces. AES is accomplished by irradiating the surface of a solid with a primary electron beam, while an energy analysis is performed on the secondary electrons. A specific case of the Auger process is illustrated in Fig. 4.7. In AES the primary excitation is caused by electron bombardment. The vacancy is immediately filled by another electron, depicted by an L_1 to K transition in Fig. 4.7. The excess energy is transferred to another electron, e.g. in the L_2 level, which is ejected as an Auger electron.

The Auger electron energy can be measured or determined from X-ray tables of electron energies with a typical accuracy of a few eV. However, in practice, the identification of Auger peaks is performed using charts of the principal Auger electron energies [St 71], together with experimentally determined spectra of most elements and some important compounds [Da 78 and Mc 79].

Digitised by the Department of Library Services in support of open access to information, University of Pretoria, 2021

ATOMIC VIEW

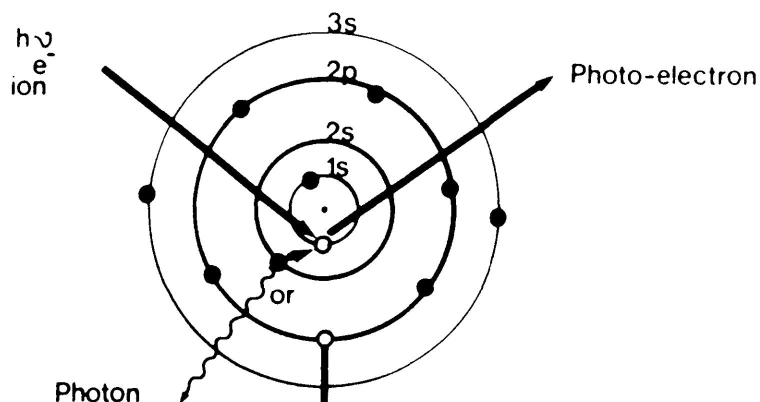

ELECTRON ENERGY DIAGRAM

$KL_1L_{2,3}$ Auger Electron

$E = E_K - E_{L_1} - E_{L_{2,3}}$ - CORRECTION TERM

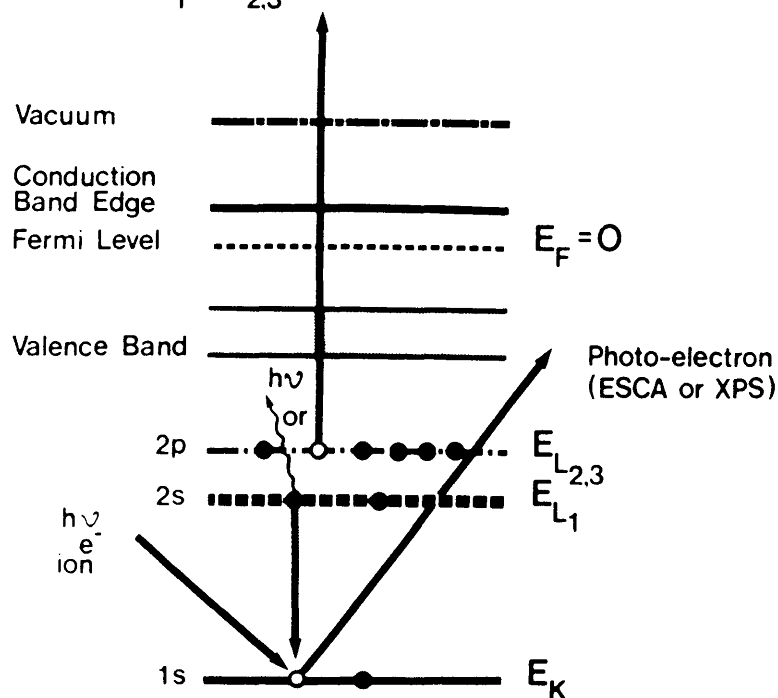

Figure 4.7: Schematic diagrams showing the mechanism for Auger electron emission.

Digitised by the Department of Library Services in support of open access to information, University of Pretoria, 2021

From the above discussion it is obvious that two energy states and three electrons take part in the Auger process. Therefore, no Auger transitions exist for H, He and isolated Li. In metallic Li or in lithium compounds the conduction electrons or valence electrons are shared and Auger transitions are thus possible.

In the case of solids, the Auger electrons are superimposed on a slowly varying background of inelastically scattered electrons. With certain types of analysers the electron energy distribution is given as either E.N(E) or N(E). To reduce the slowly varying background, thus enhancing the Auger features, these energy distributions are differentiated, either numerically or electronically. In the differentiated spectra, the Auger transitions are designated at the most negative excursion of the Auger peak, resulting in different values for a specific transition, if compared to the true peak in the N(E) distribution. In Fig. 4.8 a comparison between the two kinds of displays can be seen.

Performing quantitative analysis from first principles is difficult because various factors such as ionisation cross-section, the Auger yield, backscattering factors, etc., must be known to the desired degree of accuracy [Pa 73]. However, in practice two methods are used for quantification. The first involves the measurement of standard samples of known concentration and comparing it with that from the test sample. The choice of these standards should be such that the matrix of the standard samples and the test sample are as close as possible. This method can thus present a practical problem in that the standards are not the best suited to the sample being analysed.

The second method makes use of one standard element, while the relative sensitivity of all other elements are normalised to this standard. Although this method is less accurate, it is widely used and is also the method used in this study. The relative sensitivity, S_x, between any element X, and pure silver can be obtained from standard published Auger spectra [Da 78]. However, these sensitivity factors do not refer to the specific instruments used. To determine S_x with this technique, the

Digitised by the Department of Library Services in support of open access to information, University of Pretoria, 2021

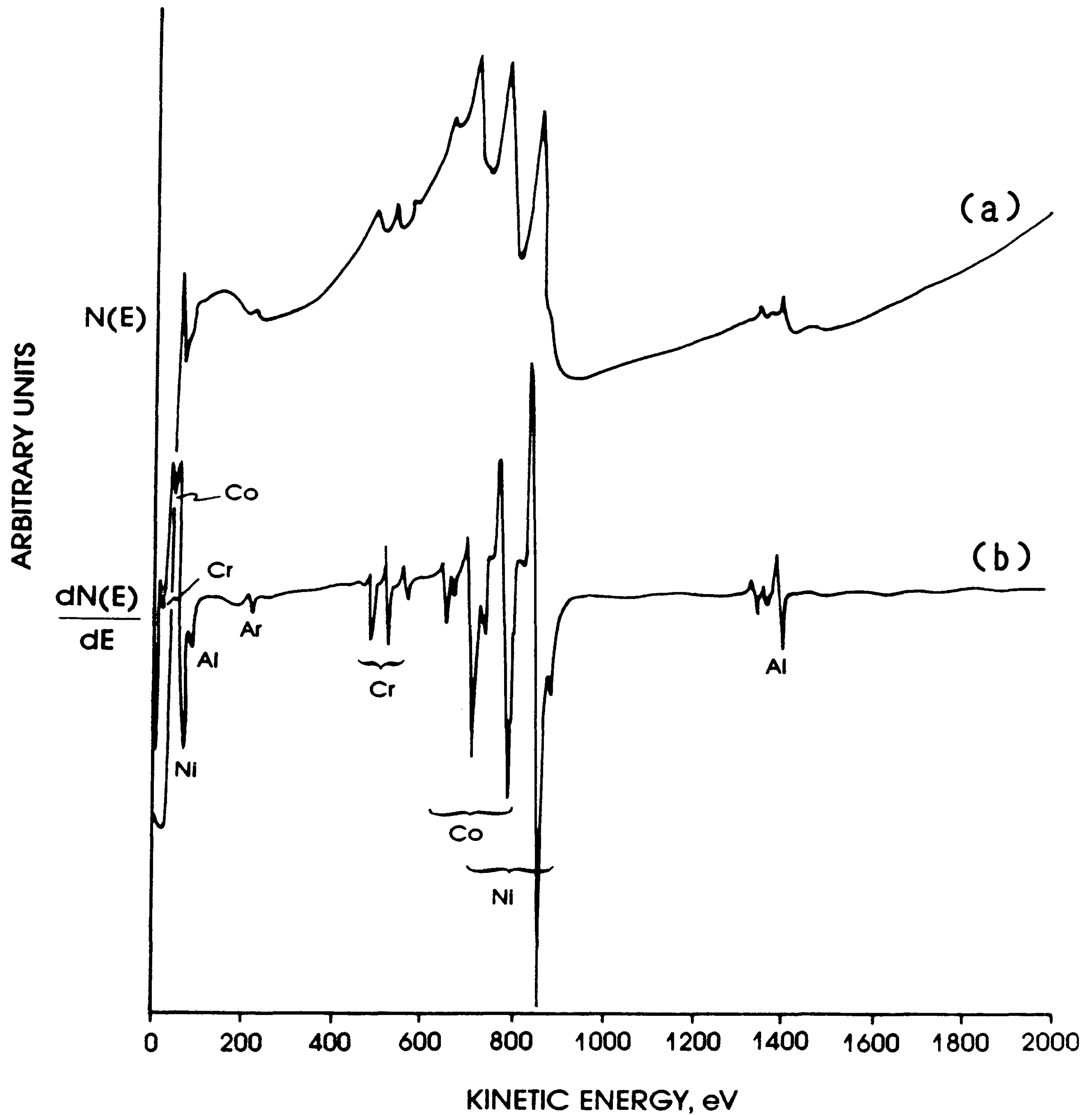

Figure 4.8: An example of both the original (a) N(E) and the differentiated (b) N'(E) Auger spectra showing different elements.

following equation can be used [Da 78], but only if the atomic concentration of the element in the sample under investigation is known.

Digitised by the Department of Library Services in support of open access to information, University of Pretoria, 2021

$$S_X = \frac{I_X}{C_X I_{Ag} D_X} \qquad \text{....... (4.1)}$$

,where I_X is the peak-to-peak amplitude of element X from the known sample, I_{Ag} the amplitude from the Ag standard, C_X the atomic concentration of element X and D_X is a relative scale factor between the spectra from the known sample and the silver, if obtained at different experimental conditions with the same instrument. Assuming that meaningful sensitivity factors can be assigned to all elements, the atomic concentration of element X in any other unknown sample, can be expressed as,

$$C_X = \frac{I_X / S_X}{\sum_i I_i / S_i} \qquad \text{....... (4.2)}$$

,where the summation is over all elements present on the surface. Of course, these calculations assume that the surface composition of the sampled area is homogeneous.

The relative sensitivity factors for Ga, As, In and P were determined for each instrument used. The rest of the elemental sensitivity factors used in this study are indicated in Table 4.1 and were obtained from either the "Handbook of AES" [Da 78] or the software library supplied with the PHI 595 system. Except for the PHI 595 Scanning Auger Microprobe (SAM), a PHI 545 spectrometer was also used. The basic layout of the two systems are given in Fig. 4.9, while photographs of the two respective spectrometers are shown in Fig. 4.10. Although different in construction, both systems make use of basically the same fast introduction system. In the case of the PHI 545, the introduction system and carousel was built and installed in-house, while for the PHI 595, it was factory built. In both cases the samples were left in the introduction chamber until a vacuum of ~5×10^{-4} mbar was reached. The samples were then transferred to the working chamber. For both spectrometers, Auger spectra and depth profiles were recorded, by using a sample holder with a 30° angle between the primary electron beam and the normal of the sample.

Digitised by the Department of Library Services in support of open access to information, University of Pretoria, 2021

(a)

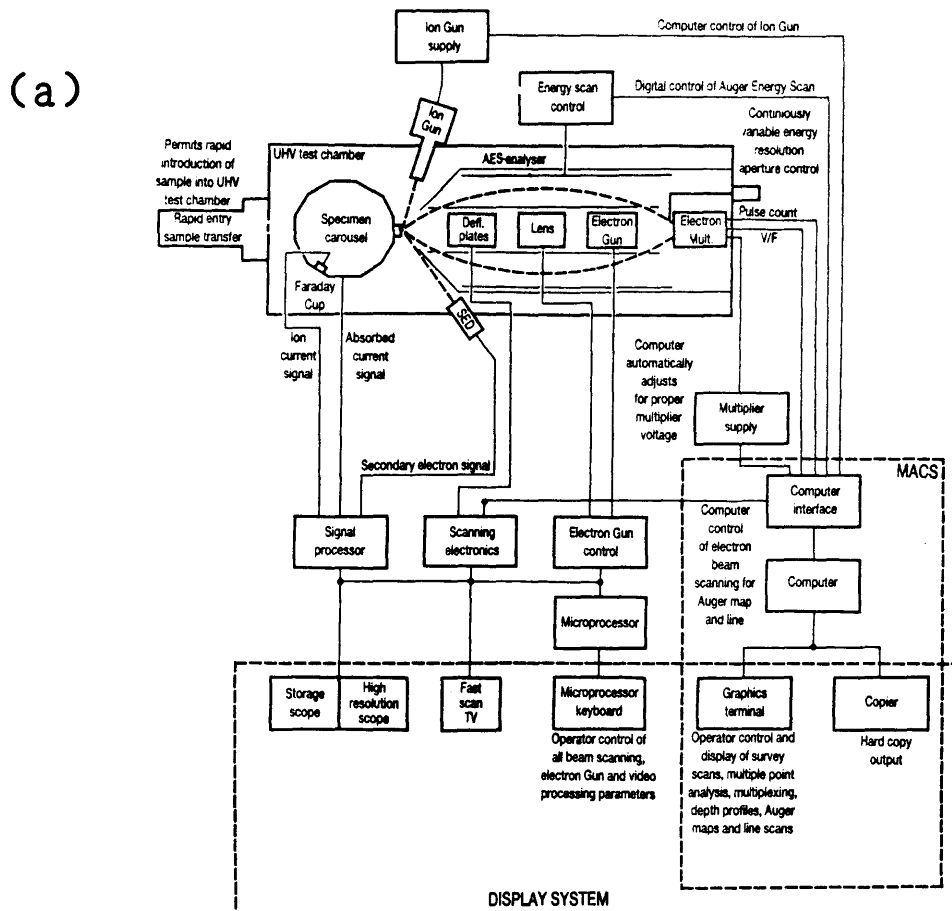

(b)

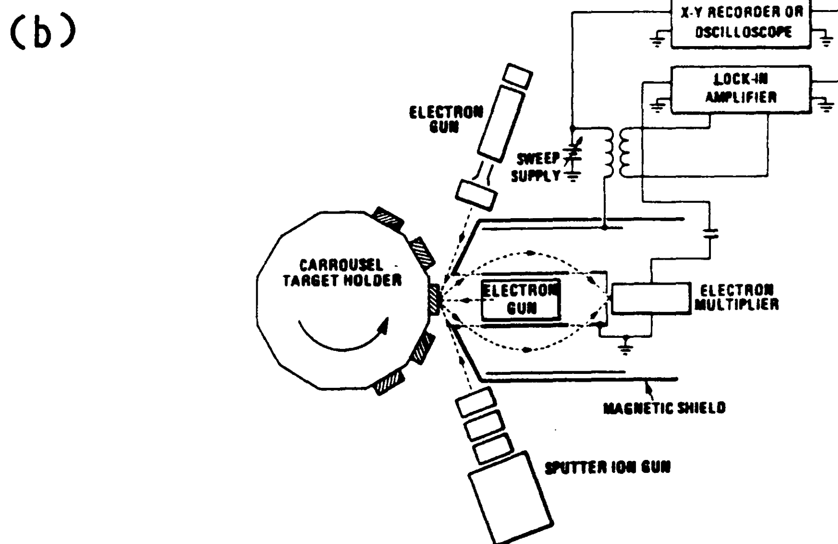

Figure 4.9: Schematic representation of the layout for the (a) PHI 595 and (b) PHI 545 systems respectively.

Digitised by the Department of Library Services in support of open access to information, University of Pretoria, 2021

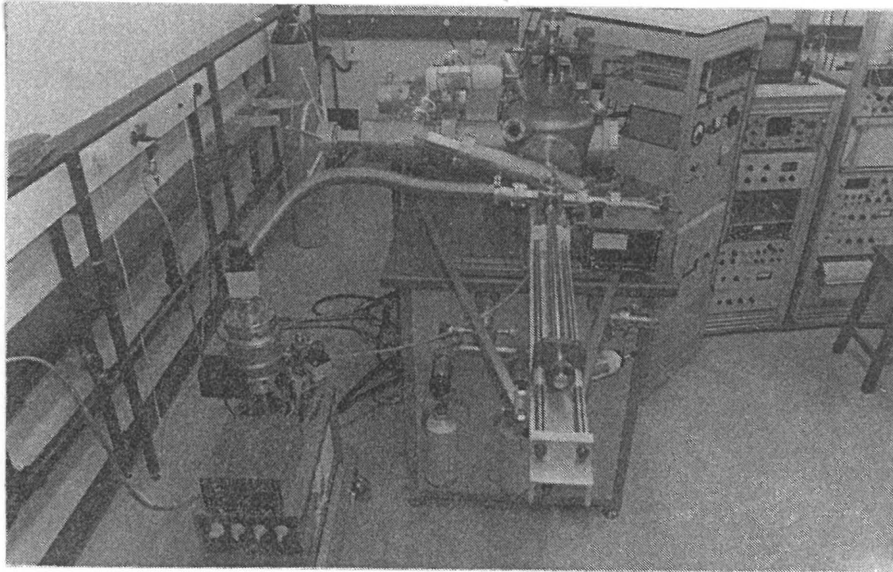

(a)

(b)

Figure 4.10: Photographs of (a) the PHI 545 and (b) the PHI 595 SAM spectrometers respectively.

Digitised by the Department of Library Services in support of open access to information, University of Pretoria, 2021

Table 4.1: Relative sensitivity factors of the elements used in this Auger study. (Note that these values refer to different primary electron beam energies utilized for the respective spectrometers.)

Element	Auger Transition (Peak energy in eV)*	PHI 595 (3 keV)	PHI 545 (5 keV)
C	KLL (273)	0,18[1]	0,15[2]
O	KLL (510)	0,50[1]	0,45[2]
P	LMM (120)	0,62±0,03[3]	0,55±0,04[3]
S	LMM (152)	0,80[1]	0,80[2]
Cl	LMM (181)	1,10[1]	1,00[2]
Ar	LMM (215)	1,00[2]	1,00[2]
Ti	LMM (387)	0,32[1]	-
Ni	LMM (848)	0,27[1]	-
Ga	LMM (1070)	0,13±0,01[3]	-
Ge	LMM (1147)	0,10[1]	-
As	LMM (1228)	0,11±0,02[3]	-
Ag	MNN (351)	0,95[1]	1,00[2]
In	MNN (404)	0,86±0,02[3]	0,78±0,03[3]
Sn	MNN (430)	0,80[1]	-
Pt	MNN (64)	0,33[1]	-
Au	MNN (69)	0,44[1]	-

1: PHI 595 software library

2: From "Handbook of AES" [Da 78)

3: Calculated for respective spectrometers.

* These energies refer to peaks in the N'(E) mode.

In the case of the PHI 545 a 5 keV primary beam of 2 to 2.5 μA, giving a current density of approximately 0.2 A.cm^{-2}, was used. A lock-in-amplifier with a 2 eV modulation amplitude was used to obtain the Auger peaks in the differentiated mode. Smaller modulation voltages did not resolve the Auger peaks any further. The different Auger peaks were recorded at very slow recording

Digitised by the Department of Library Services in support of open access to information, University of Pretoria, 2021

speeds, with typical spectrum scanning rates of 1 eV/s, in general, and 0.1 eV/s for the main peaks. The various Auger peaks were monitored by means of a single pass cylindrical mirror analyzer (CMA), with an energy resolution of 0.6% at an operating pressure of $8x10^{-10}$ torr. Ar^+ sputtering was performed with a 5 keV PHI 20-115 sputtergun at various energies (0,5-5 keV). During the various sputtering cycles, the operating pressure was increased to $2,5x10^{-5}$ torr by leaking high purity Ar gas into the working chamber.

For the PHI 595, the Auger spectra were obtained with a 3 keV primary beam, with a pressure of $\sim 10^{-11}$ torr in the main chamber. A CMA with an integral coaxially mounted electron gun, containing a lanthanum hexaboride (LaB_6) cathode which can produce an electron beam with a spatial resolution between 0,01-0,02 μm, was used. The electron gun can operate at energies between 2,5 and 30 keV. The Auger system was interfaced with a PDP 11/04 computer, using the MACS software for data storage and manipulation of functions. The operating conditions for the PHI 595 system used in this investigation are summarized in Table 4.2.

Table 4.2: Operating conditions for the PHI 595

Action	Conditions
Primary electron beam:	
Acceleration voltage	3 keV
Current (measured on sample)	0,1 μA
Ion beam:	
Acceleration voltage	1 keV
Current density	30-40 $\mu A/cm^2$
Base pressure (working chamber)	$8x10^{-8}$ Torr

Digitised by the Department of Library Services in support of open access to information, University of Pretoria, 2021

In obtaining depth profiles, it is important to choose the energy region for each element such that no other elemental transition is possible in the specific energy region. (Please note that the data for each element in the depth profiles was obtained in the N(E) mode.) However, in some cases it is difficult to prevent the overlapping of two transitions within one energy region. One such example of overlapping can be found from the metallization of layers used in this study. The Pt(NOO) and Au (NOO) transitions overlap in the energy region 62-70 eV, while the Au(NOO) and Ni (MNN) transitions overlap in the energy region 62-72 eV. Furthermore, the Ti(LMM) and In(MNN) transitions overlap in the energy region 400-415 eV.

In order to illustrate this effect, Fig. 4.11 shows Auger spectra obtained from a clean (a) Pt and (b) Au sample respectively. It is clear that all the major Auger transitions occur within ±5 eV from each other. (Although higher energy Pt and Au transitions also occur, their relative intensities are very low and difficult to distinguish above the background noise.) The depth profile in Fig. 4.12 illustrates the effect of overlapping very clearly for a Au layer deposited on Pt. After experimenting with different energy regions, it was concluded that for depth profiles which contain Pt and Au as neighbouring layers, the lowest Pt wrongly detected in 100 % Au is 17%. Further, ±28 % Au is also wrongly observed in 100 % Pt. These values were obtained for a Pt energy region beginning at 59 eV, with a range of 4 eV, while the Au energy region was chosen from 72 eV to 77 eV. As a result, the depth profiles shown in Chapter 5 were drawn by subtracting the respective wrong atomic concentrations indicated in Fig. 4.12. (The same energy regions were used throughout this study whenever both Pt and Au were present.)

A further example of how overlapping can influence the depth profiles is shown in Fig. 4.13. These depth profiles were obtained from an as-deposited Au/Ni/Ti/InP metallization system.

Digitised by the Department of Library Services in support of open access to information, University of Pretoria, 2021

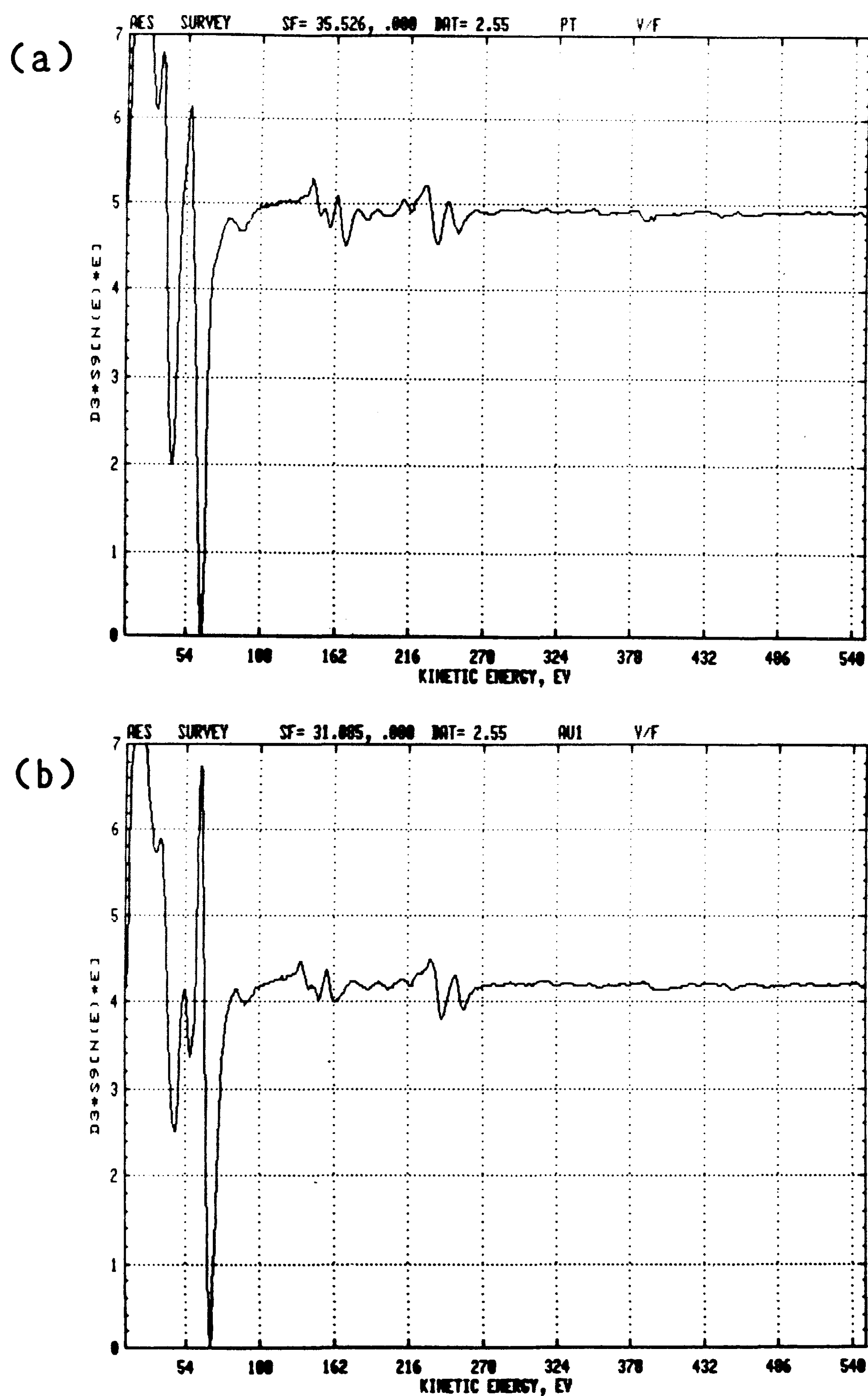

Figure 4.11: **Auger spectra obtained from a clean Pt (a) and Au (b) surfaces respectively.**

Digitised by the Department of Library Services in support of open access to information, University of Pretoria, 2021

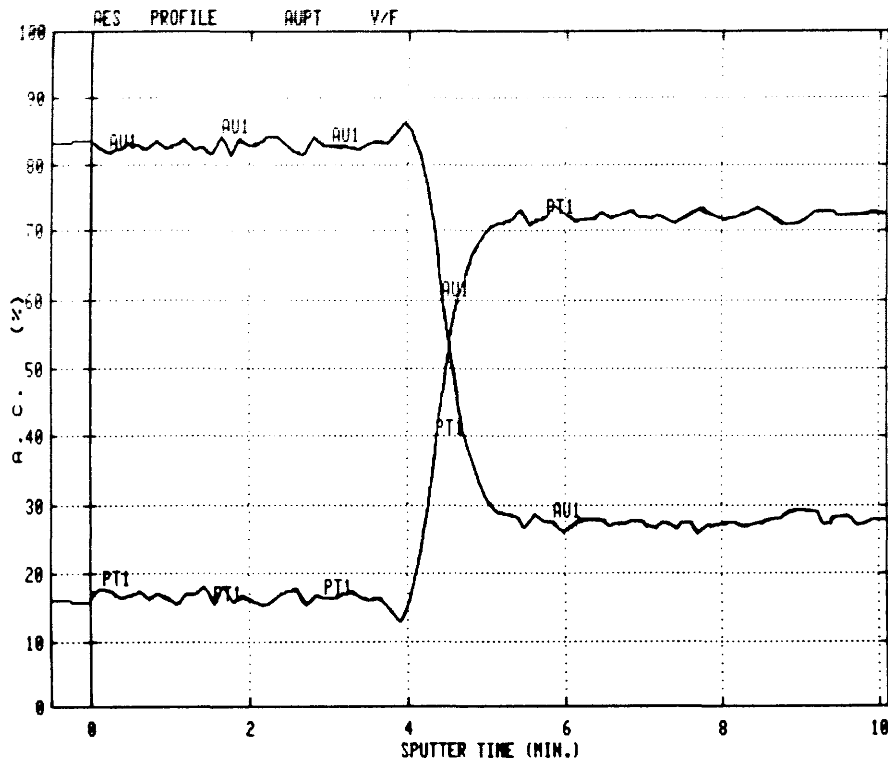

Figure 4.12: Auger depth profile of a as-deposited Au layer on a Pt sample.

The depth profile in Fig. 4.13(a) was obtained with a 15 eV energy range for each element indicated in the depth profile. A Au tail is observed in the Ni due to the overlapping of the Au (NOO) and Ni (MNN) transitions. Furthermore, In is wrongly detected in Ti and also Ti in the InP substrate. However, if the energy region for Au was chosen to be between 72 eV and 77 eV, for Ti between 382 and 386 eV and In between 397 eV and 405 eV, the depth profile in Fig. 4.13(b) is obtained. It is clear that with these energy regions the influence of overlapping on the depth profile data was minimized.

Digitised by the Department of Library Services in support of open access to information, University of Pretoria, 2021

(a)

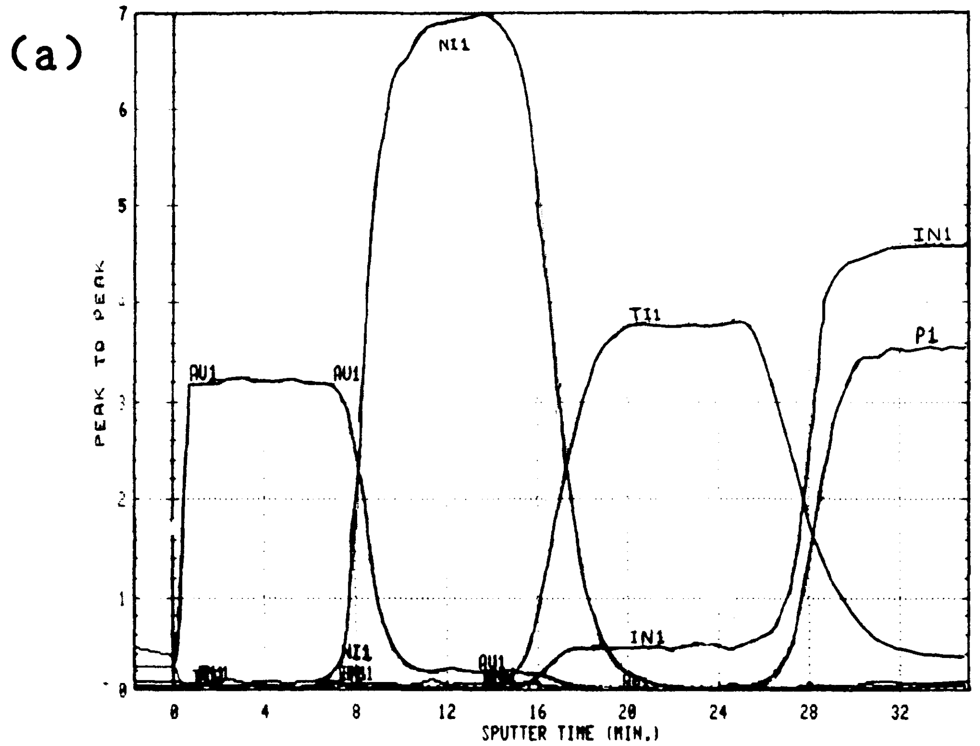

(b)

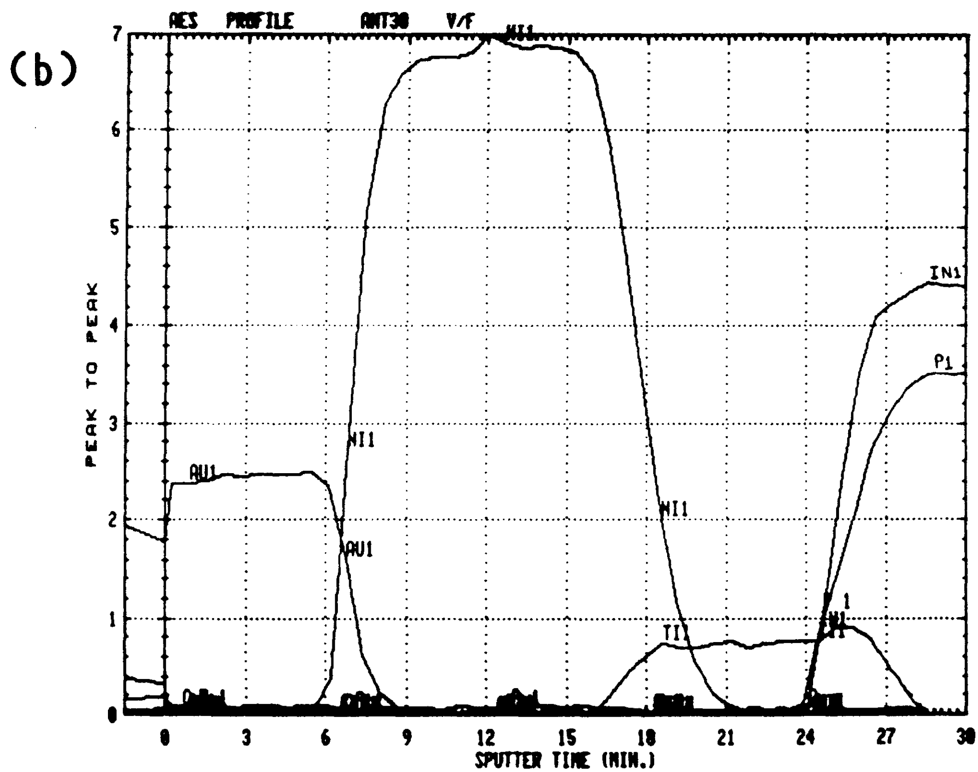

Figure 4.13: Depth profiles of an as-deposited Au/Ni/Ti/InP metallization scheme. (a) Profile obtained with a 15 eV energy range used for each element. (b) No overlapping of Auger transitions observed when energy regions are chosen as set out in the text.

Digitised by the Department of Library Services in support of open access to information, University of Pretoria, 2021

In general, the energy regions for each element was monitored for possible energy shifts, due to the different chemical state a specific element can have. It must also be noted that the depth profiles shown in chapter 5 are averaged profiles, obtained from various depth profiles on different samples. All these samples were identically processed and treated. The samples used to produce the Auger data were processed simultaneously with the samples which were used to produce the test patterns for specific contact resistance measurements. As a result, the conclusions drawn from the Auger studies could be directly related to the specific contact resistance measurements.

Furthermore, the C and O contaminants are only indicated on the depth profiles if they have a direct influence on the results. Otherwise they were left out for clarity when interpreting the depth profiles. It must be noted that in general the Auger data shown in chapter 5 is representative of several similarly treated samples.

4.3.2 Secondary Ion Mass Spectroscopy (SIMS)

This very sensitive technique uses an ion beam to sputter material from the surface of a sample. The resulting secondary ions (from the sample) are then analyzed using a mass spectrometer. The sputtered ions have a wide range of energies and must be electrostatically accelerated prior to entering the mass spectrometer. This process is referred to as secondary ion mass spectrometry. Figure 4.14 shows a schematic layout of the sputtering process. The bombarding species can be either positive or negative ions while the sputtered ions can be either positive, negative or neutral particles. By applying the correct accelerating voltages, either the positive or negative species can be accelerated towards the detector.

The primary ions commonly used are argon and oxygen. Caesium and gallium (liquid metal) ion sources have recently been introduced

Digitised by the Department of Library Services in support of open access to information, University of Pretoria, 2021

and are used in more specialised situations. The ions are finely focused into a well defined beam, usually with rastering capabilities. The current density of the sputtering beam determines the rate at which material is removed from the surface. As a result three modes are distinguishable for SIMS:

(i) Static SIMS, which employs very low current densities in the nA/cm^2 range.

(ii) Dynamic SIMS in which the ion optics allow submicron images of the sample to be produced for different elements. The high primary ion flux densities cause the surface to be eroded as the measurements occur and as a result depth profiles can be obtained.

(iii) Imaging SIMS uses microfocussed liquid metal ion sources. In these sources metal ions are field ionized from a sharp tungsten tip, allowing excellent beam focusing (<200 nm beam diameter). By raster scanning the beam across an area and collecting the secondary ions at each point, a chemical image can be generated. This allows comparison between the secondary electron image and the ion images.

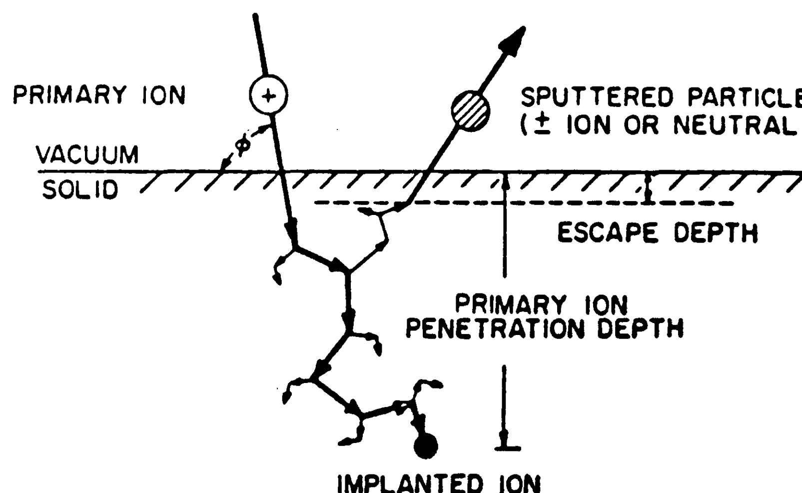

Figure 4.14: The ion-solid interaction and the resultant sputtering process [Cz 75].

Digitised by the Department of Library Services in support of open access to information, University of Pretoria, 2021

The SIMS results in this study were obtained from a VG ESCALAB MK II fitted with a 50 B duoplasmatron ion source and a 0-800 amu quadrupole mass spectrometer. A 10 keV oxygen primary beam was rastered over an area of 2x2 mm^2, with an ion beam current of ±400 nA. A typical beam diameter of ≤0,01 μm was used. Data was recorded using 5 % beam blanking in order to disregard ions originating from the sloping sides of the sputtered crater.

4.3.3 X-ray diffraction

This section presents a very brief survey of the fundamental principles regarding X-ray diffraction when an incoming X-ray beam strikes a powder crystal or fine grained polycrystalline solid. For a more detailed description of this technique, the reader is referred to the following references [Kl 74 and Ba 80c].

Diffraction from a crystal is analogous to reflection from a series of semitransparent mirrors. If an X-ray beam is directed at a few layers of equally spaced atoms, each atom will be a source of scattered waves, which reinforce in certain directions to produce zero-, first-, second-, and higher order diffracted beams. The condition for reinforcement of the reflected rays is given by Bragg's law.

$$\lambda n = 2d\sin\Theta \qquad \text{....... (4.3)}$$

where n=0,1,2,3..., etc. λ is the wavelength and d the spacing of the atom planes.

It is important to note that the directions of the reflected beams are governed entirely by the geometry of the crystal lattice (i.e. by the orientation and spacing of the planes of atoms, from the point of view of Bragg's law). In other words, the size and shape of the unit cell determines where the diffracted beams will go. Furthermore, the distribution of atoms within the unit cell governs the intensities of the diffracted beams. Ewald [Kl 74 and Ba 80c] introduced the reciprocal space, which is called the reflection sphere or Ewald's sphere. If a

Digitised by the Department of Library Services in support of open access to information, University of Pretoria, 2021

beam of X-rays enters the crystal in an arbitrary direction (not fulfilling Bragg's law), there may be no intersection of the reflection sphere with any reciprocal lattice point, in which case there can be no diffracted beams. But if the crystal is rotated with respect to the incoming beam, then the reciprocal lattice points touch the sphere one after another.

The recording of diffracted beams is carried out by a diffractometer. Diffractometers in general consist of a X-ray source, counter tubes or detector, counting circuit and recording system. As indicated by Fig. 4.15, X-rays diverging from the slit at the X-ray tube falls on a flat plate of a specimen and is received by a slit at the counter. The two slits and the specimen are located on the circumference of a circle in order that the conditions of parafocusing is met. The parafocusing is retained by having the plane of the powder rotate at half the angular speed of the counter, i.e., retaining a $\theta/2\theta$ relationship with each other. In this a way a 2θ vs intensity recording can be obtained. The respective diffraction peaks are then related to a specific 2θ value.

Qualitative analysis is carried out by using the fact that any crystalline substance can be identified by the d spacings and relative intensities of the reflections in its diffraction pattern. Identification of several substances in a mixture is often possible, since the diffraction pattern for the mixture is a superposition of the patterns for the individual constituents of the mixture.

The powder pattern of a substance effectively serves as a fingerprint by which it can be identified. As a result of a cooperative effort of many investigators around the world, files have been assembled, analogous to a fingerprint file, containing the diffraction patterns of most substances. An unknown substance may be identified by comparing its diffraction pattern with those in a specific file to find one that matches. A mixture of two, three, or sometimes even more substances can be analyzed similarly, as the superposition of patterns in the file.

Digitised by the Department of Library Services in support of open access to information, University of Pretoria, 2021

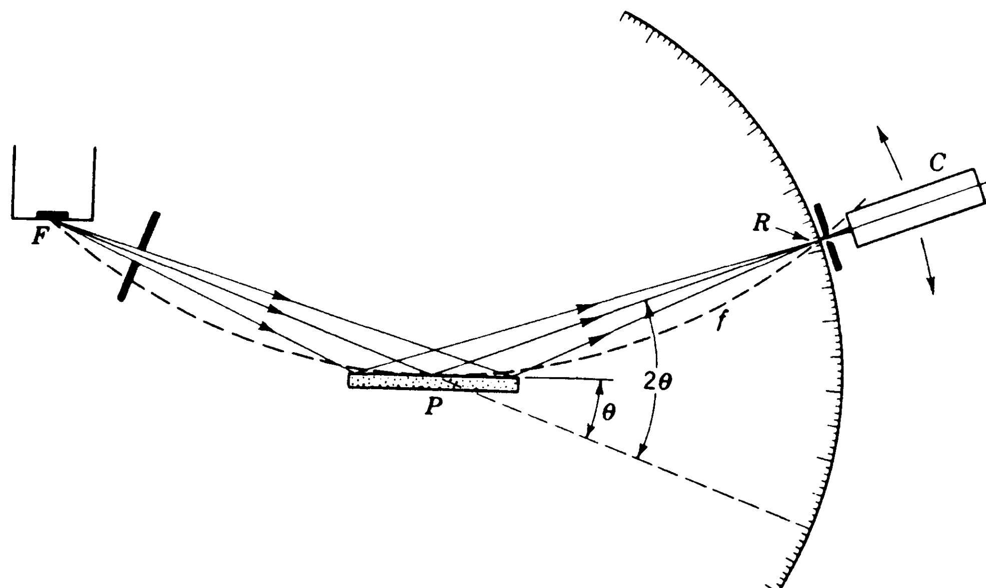

Figure 4.15: Focusing geometry of a diffractometer. F = focal spot; P = powder specimen, F = focusing circle, R = receiving slit and C = counter. [After Ba 80c].

In this study a Seifert X-ray diffractometer which contain a MZ II goniometer and a sintilation counter was used. The X-rays were generated from a Cu target with a Ni filter which operated at 30 keV and 30 mA. The identification of the compounds were carried out with diffraction data from the JCPDS powder diffraction file system [JCPDS].

4.3.4 Microscopy

The surface morphology of the contact surfaces was investigated by means of a secondary electron microscope (SEM) and an optical microscope. A PSEM 500 Philips SEM was used with an acceleration voltage between 5-10 keV. The optical investigations were carried out with a Nikon optiphot metallurgical microscope, using a halogen lamp. Micrographs on the SEM were obtained with

Digitised by the Department of Library Services in support of open access to information, University of Pretoria, 2021

a 60 mm camera and in the case of the optical microscope, a polaroid camera was used.

4.3.5 I-V measurements

The I-V measurement apparatus is shown in Fig. 4.16 and consists basically of a HP 4140B pico-ammeter/DC voltage source (A), a Signatone probe station (B) and a HP Vectra PC 308 personal computer (C). The HP 4140B voltage source operates on the principle that a DC voltage is supplied, while the current through the leads and contacts is measured. Further, by increasing the applied voltage stepwise, starting from a negative value, the current is measured. In such a way the I-V relation or I-V curve is obtained.

Electrical contact between the measuring equipment and the small contacts is accomplished by a probe station. The probe station is fitted with a stereo microscope (D), a X-Y moveable sample stage (E), probe stage (F) and micropositioners (G) mounted on the probe stage. The moveable sample stage was also fitted with a vacuum chuck which was gold plated. The vacuum ensures that the sample is in position on the sample stage and that good electrical contact to the back of the contact and the chuck is obtained, if needed. (However, all the contacts used in this study were deposited only on one side of the substrate.) The micro-positioners were fitted with Osmium probe tips. The whole probe station is mounted in a black painted metal box with a sliding door. In such a way total darkness can be obtained when very low current measurements ($<10^{13}$A) are performed on Schottky diodes.

Shielded leads are used between the measuring equipment and the switch box (H), in order to eliminate unwanted noise. The control of the HP 4140B voltage source and data acquisition was carried out by the HP Vectra personal computer. The software for the I-V measurements was developed in-house by M Myburg [My 91]. The I-V data shown in Chapter 5 are representative of the I-V

Digitised by the Department of Library Services in support of open access to information, University of Pretoria, 2021

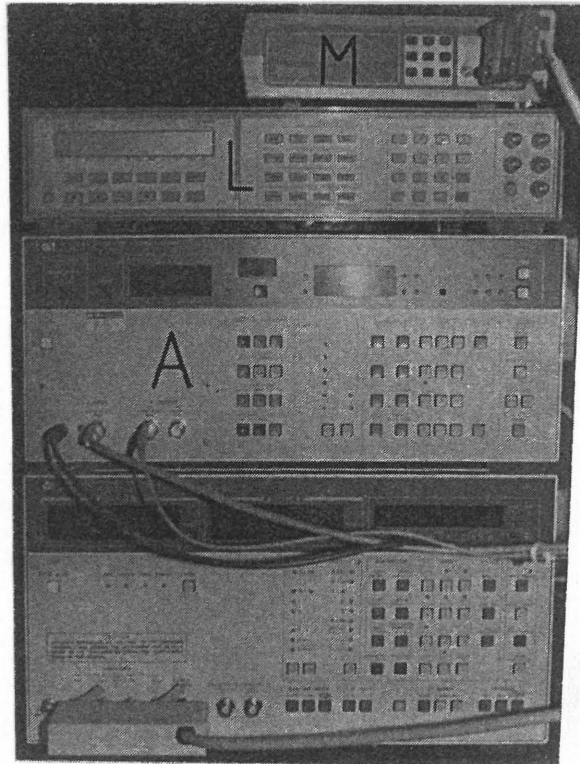

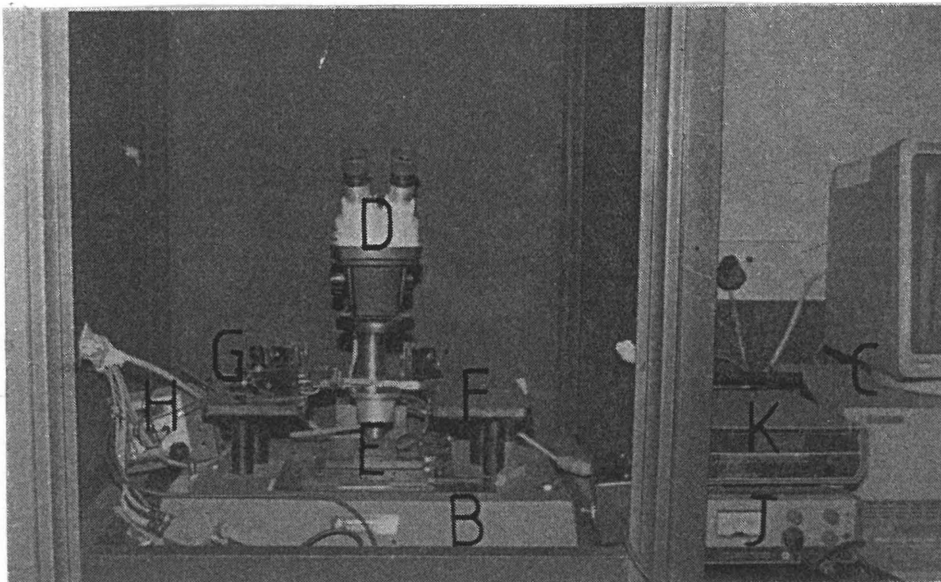

Figure 4.16: Photographs of apparatus used to obtain I-V and r_c measurements. The symbols are explained in the text.

Digitised by the Department of Library Services in support of open access to information, University of Pretoria, 2021

measurements obtained on various contacts fabricated and treated in the same manner.

4.3.6 Specific contact resistance (r_c) measurements

The transmission line model (TLM) and the four point method were used to measure r_c of the ohmic contacts to n-GaAs and n-InP respectively. These two techniques are discussed in sections 3.6.2 and 3.6.4 respectively.

The instruments and probe station used for the I-V measurements were also utilized to measure the specific contact resistance. For both measuring techniques, the same specific contact resistance mask was used. The mask consists of 36 identical rectangular test patterns, such as shown in Fig. 4.17. (Note that the light areas represent the metallization layer and the dark area the substrate.) Each test pattern consists of 10 circular contacts, each with a different r_o radius. Furthermore, each contact is situated inside a circular opening in the metallization layer with a fixed radius of r_1=200 μm. As a result, for each test pattern different d spacings are obtained between each contact and the outer metallization layer. The respective spacing, d, for each test pattern was 5, 10, 15, 20, 25, 35, 45, 55, 65 and 75 μm.

In using the TLM method a graph of the voltage drop (ΔV) between each contact and the metallization layer, vs d is obtained for a constant applied current. By using the Borland software package called "Eureka" [Bo 87], an actual curve fit is obtained for the experimental data points. From such a graph and eqs. (3.25) and (3.32), the r_c of a specific test pattern was determined. An average r_c value and a standard deviation was calculated from the r_c values measured on the different test patterns that were annealed at the same temperature. From these data, graphs of r_c vs annealing temperature were obtained.

The constant current for r_c measurements was supplied by a HP 6177C DC current source (J) (see Fig. 4.16). The multimeter (K) was used to monitor the constant current of 5 mA supplied by the

Digitised by the Department of Library Services in support of open access to information, University of Pretoria, 2021

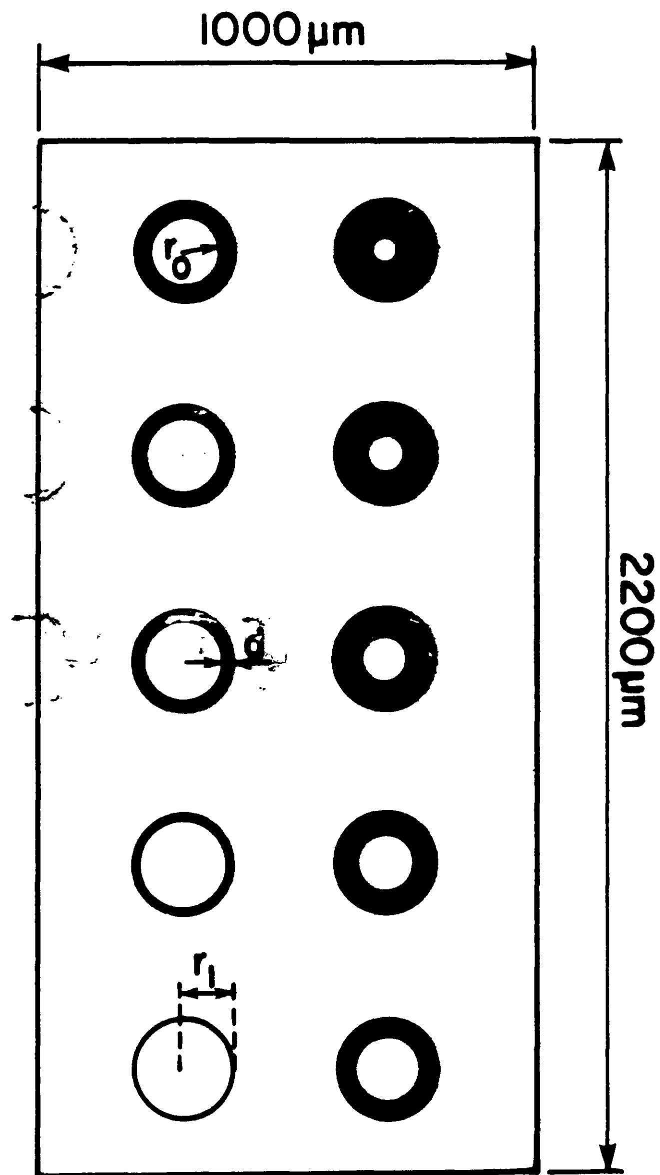

Figure 4.17: The circular test pattern used for specific contact resistance measurements. (The light areas represent the metallization layer and the dark areas the substrate.)

Digitised by the Department of Library Services in support of open access to information, University of Pretoria, 2021

current source. The voltage drop over the spacing d was measured by the HP 3457A multimeter (L).

The advantage of the mask discussed above is the fact that it is also suitable for the four point method. Four contacts with the same diameter in a row or in a group were utilized to obtain r_c measurements with this technique. With s values of 3,200 mm and 4,110 mm for contacts in a row and a group respectively, the dimensions and spacings of the two smallest contacts (i.e. diameters of 50 and 70 μm) satisfy the requirements set to use eq. (3.20). As a result the spreading resistance term was neglected in the calculations.

By applying a constant current of 5 mA through the two outer contacts, the voltages V_1 and V_2 (see section 3.6.2) were measured with multimeters (L) and (M) respectively. The r_c values were then calculated by substituting the above measurements into eq. (3.20). By repeating these measurements on the two smallest contacts, two r_c values were obtained from a set consisting of 4 test patterns. These measurements were repeated on at least three different sets, which were similary processed. An average r_c value and standard deviation was determined from such a set of r_c measurements.

It must be noted that no comparative studies between these two r_c measuring techniques were carried out for ohmic contacts to the same substrate material. The TLM technique was only used for contacts to GaAs epilayers, while the four point probe method was utilized on contacts on InP bulk material. Furthermore, the error bars indicated on the r_c vs annealing temperature graphs in Chapter 5 correspond to a statistically calculated standard deviation and do not include any estimation of systematical or any other errors.

Digitised by the Department of Library Services in support of open access to information, University of Pretoria, 2021

CHAPTER 5

RESULTS AND DISCUSSION

5.1 GENERAL

This chapter is divided into two main sections. Both sections deal with results obtained from surface, structural and electrical studies on ohmic contacts to n-type GaAs and n-type InP substrates.

In general, each section follows a logical pattern. However, some of the results are not part of this pattern and must be seen as an additional research project on the specific semiconductor material. The main emphasis of this study was to obtain structural and electrical information on ohmic contact systems to these III-V compound semiconductors. Therefore, most of the results given below were obtained by using techniques such as Auger electron spectroscopy (AES), scanning electron microscopy (SEM), optical microscopy, current-voltage (I-V) measurements and specific contact resistance measurements (r_c). Apart from these investigations, secondary ion mass spectrometry (SIMS) and X-ray diffraction analyses were also performed on a few selected samples.

5.2 GaAs SUBSTRATE MATERIAL

This section is devoted to research conducted on n-type GaAs and covers the following subjects:

(i) AES surface studies of chemically etched and Ar^+ sputtered surfaces;

(ii) Comparison of Ni and In as wetting agents for Au-Ge based ohmic contacts;

(iii) The improvement of ohmic contact surface morphology by ion beam mixing.

Digitised by the Department of Library Services in support of open access to information, University of Pretoria, 2021

5.2.1 GaAs surface studies

Substrate surface preparation is extremely important for the electrical characteristics and morphology of ohmic and Schottky contacts. This is due to the fact that unwanted and uncontrolled residues left on the surface can diffuse into the metal overlayer and into the substrate during the evaporation or annealing steps. AES is a surface sensitive analytical probe and provides information on residues left on the substrate surface after cleaning. In this sub-section results of an AES investigation of the surface composition of GaAs after three independent etching steps, vacuum cleaving and Ar^+ sputtering treatments are discussed. Note that all the Auger results presented in this sub-section were obtained from a PHI 595 scanning Auger microprobe (SAM).

Figure 5.1(a) shows the typical low- (MNN) and high-energy (LMM) Auger transitions for Ga and As, obtained from a vacuum cleaved (110) GaAs surface. The spectra shown in Fig. 5.1(b) and (c) were obtained from Ar^+ sputtered GaAs samples at energies of 1 and 3 keV respectively. (Note that both spectra were obtained after a steady state surface composition had been attained). Apart from the normal variation experienced from one analysis to another, no dramatic differences were observed between the (100) and (110) GaAs Ar^+ sputtered surfaces. The peak-to-peak Ga/As ratios for the high and low energy Auger transitions obtained from various spectra are summarized in Table 5.1. All the results presented here were obtained for a 30° angle between the normal of the sample and the incident primary electron beam.

Table 5.1: Summary of Ga/As peak-to-peak ratios for the high and low energy Auger transitions

Treatment	Ga/As ratio	
	MNN (low)	LMM (high)
Vacuum cleaved	0,33 ± 0,02	1,19 ± 0,10
1 keV Ar^+	0,68 ± 0,03	1,78 ± 0,15
3 keV Ar^+	0,87 ± 0,03	1,92 ± 0,22

Digitised by the Department of Library Services in support of open access to information, University of Pretoria, 2021

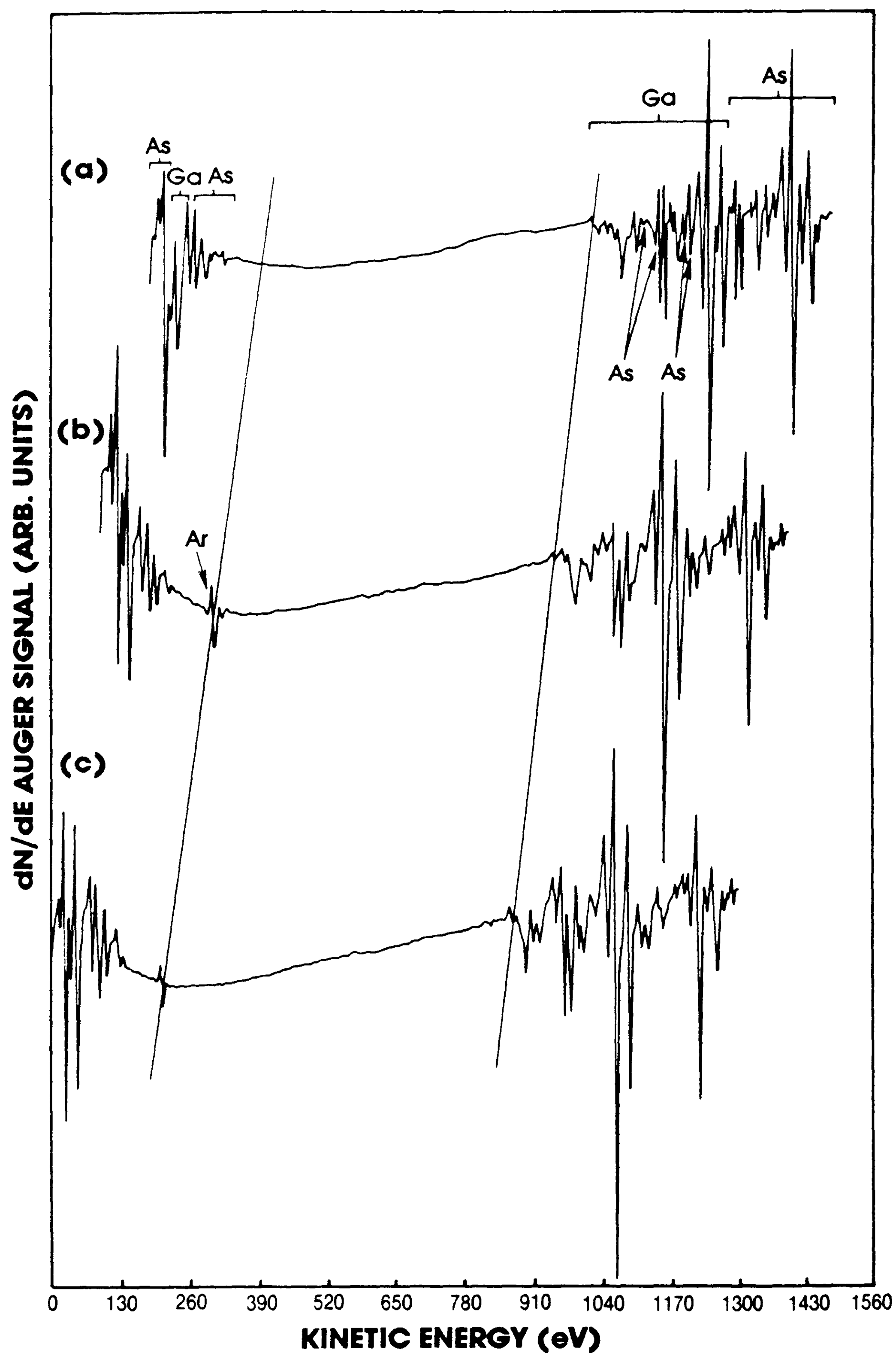

Figure 5.1: Typical Auger spectra for (a) vacuum cleaved (110) GaAs, (b) 1 keV and (c) 3 keV Ar^+ sputtered surfaces.

Digitised by the Department of Library Services in support of open access to information, University of Pretoria, 2021

From Table 5.1 it is clear that preferential sputtering occurred for the GaAs. Basically the same Ga/As ratios were observed for the sputtered (100) and (110) GaAs surfaces. In order to calculate the surface composition of the sputtered surfaces, the relative sensitivity factors must be known. The vacuum cleaved surface was used to calculate the relative sensitivity factors as explained in Chapter 4. Only the sensitivity factors for the high energy Auger transitions (LMM) were calculated, because only the results for these transitions will be discussed here. By using a 3 keV primary beam the sensitivity factors were determined to be 0,13 ± 0,01 and 0,11 ± 0,02 respectively for Ga and As. (In using eq. 4.1 to determine these values, it was assumed that the vacuum cleaved (110) has the same stoichiometry as an atomically clean (100) surface.) Although these sensitivity factors differ by about 50 % from that given by Chang et al. [Ch 77b] for GaAs, it must be noted that their sensitivity factors were normalized to the Si 92 eV peak and apply to spectra recorded at 45° incidence.

For the 1 keV Ar^+ sputtered surfaces, the composition of the surface layer was calculated to be 60 ± 2% Ga, while the 3 keV sputtered surfaces yielded 63 ± 2% Ga. Although this increase of the surface concentration, with increased Ar^+ energy is small, this effect was also reported by Singer et al. [Si 81] and McGuire [Mc 78]. It seems likely therefore, that the sputter yield of Ga is a function of the sputter energy. This effect, and the reason for the selective sputtering of As is not clearly understood. However, these points lie beyond the scope of this study and the reader is referred to the literature for more information. [So 63, Mc 78, Ro 81, Sz 82, Ta 82 and Wa 84b].

The phenomenon of preferential sputtering of As has recently been used in a positive manner in device design. It was demonstrated by Auret et al. [Au 91b] that the barrier height of Au Schottky barrier diodes manufactured on n-type GaAs decreased monotonically with increasing sputter etch dose, from 0,93 eV for contacts to unsputtered surfaces to 0,48 eV for contacts to sputter etched surfaces, at a dose of $2x10^{15}$ ions/cm^2.

Digitised by the Department of Library Services in support of open access to information, University of Pretoria, 2021

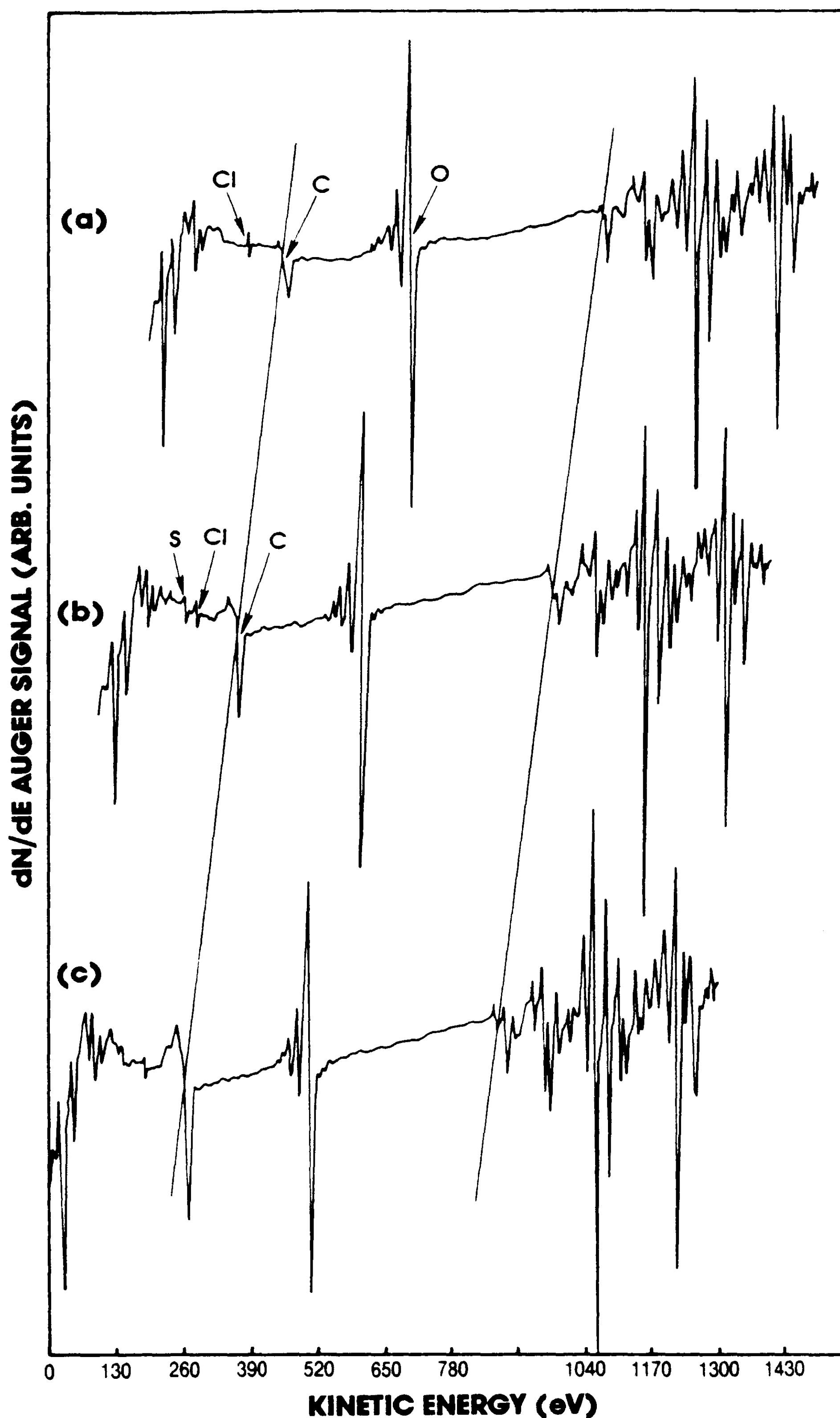

Figure 5.2: Auger spectra obtained from (100) GaAs surface after the three different etching steps (detailed on page 118) were used: (a) (i); (b) (ii) and (c) (iii).

Digitised by the Department of Library Services in support of open access to information, University of Pretoria, 2021

The following three etching steps seemed to be most frequently used on (100) GaAs surfaces [Wi 84, Mu 85 and Lu 89]:

(i) $NH_3:H_2O_2:H_2O$ (3:1:150) followed by $HCl:H_2O$ (1:1)
(ii) $H_2SO_4:H_2O_2:H_2O$ (5:1:1) followed by $HCl:H_2O$ (1:1)
(iii) $H_3PO_4:H_2O_2:H_2O$: (1:1:150) followed by HCl: H_2O (1:1).

Prior to the etching steps given above, the samples were degreased as described in Chapter 4. The etching treatment was followed by a thorough rinse in DI water and a blow dry in N_2. The samples were then loaded into the fast introduction chamber of the AES system. The time delay between the N_2 drying step and the loading of the samples into the introduction chamber was ±5 minutes, which is similar to the time taken for the samples to be loaded into the introduction chamber of the evaporation system before device manufacture.

Auger spectra obtained from GaAs (100) samples etched in the etchants given above, are shown in Fig. 5.2. The spectra in Fig. 5.2 illustrate the general trend observed for each etched sample after various spot analyses were performed on these samples. Although no dramatic differences are observed in these Auger spectra, the relative concentrations of C and O differ on average from one type of etched sample to another. These differences are best illustrated by comparing the relative atomic concentrations of each element (see Table 5.2).

Table 5.2: Etching step vs atomic concentrations

Etching Step	Atomic Concentration (%)					
	C	O	Ga (LMM)	As (LMM)	S	Cl
(i)	5 ± 1	12 ± 2	43 ± 3	41 ± 2	-	1 ± 0,5
(ii)	8 ± 1	10 ± 3	41 ± 2	40 ± 2	1 ± 0,5	1 ± 0,5
(iii)	11 ± 2	8 ± 2	42 ± 2	38 ± 3	-	1 ± 0,5

Digitised by the Department of Library Services in support of open access to information, University of Pretoria, 2021

The various atomic concentrations were calculated by using eq. 4.1. The sensitivity factors used were obtained from Table 4.1. Although, strictly speaking, this method of determining the atomic concentrations is not exact (it is more accurate to determine the sensitivity factors of each element from a set of standards for a specific instrument), the purpose is not to determine the elemental concentrations exactly, but rather to obtain a comparison of the surface contaminants left behind after etching with the different etchants.

According to Table 5.2 etch (1) gives the lowest C concentration for the 3 etchants, while etch (iii) gives the lowest O concentration. Although etch (ii) gave a balance between these two etchants, if the O- and C-concentration levels are considered, a low concentration of S is then also found on the GaAs surface as can be seen in Fig. 5.2(b). Due to the final HCl etching step, very low concentrations of Cl are detected on all the etched surfaces. The primary source of O and C on the samples is probably the hydrocarbons, H_2O, O_2 and CO_2 present in the laboratory air. The H_2SO_4:H_2O_2:H_2O etch was decided on as an etchant for the contacts processed on GaAs for the following reasons: (1) historic reasons (in order to compare some of my results with contacts manufactured previously in the same laboratory using this etchant) and (2) very little difference was observed between the three etchants.

During the lithographic process the whole surface is covered with photoresist. However, after the pattern is developed, the C concentration on the uncovered photoresist areas of the GaAs surface tends to increase. AES results have shown that a NH_3:H_2O (1:15) dip followed by a DI water rinse step, lowers the C levels to essentially the same levels indicated in Table 5.2.

The results obtained from this sub-section were used to provide answers concerning (a) the choice of an etchant to be used during the processing step to manufacture ohmic contacts and (b) relative sensitivity factors for Ga and As respectively. The latter result is important because (a) sensitivity factors differ from one instrument to another and (b) the factors obtained from

Digitised by the Department of Library Services in support of open access to information, University of Pretoria, 2021

the standard Auger electron spectroscopy handbooks refer not to the compound GaAs, but rather to the respective elemental forms or they are obtained from other compounds containing gallium and arsenic [Da 78 and Mc 79].

5.2.2 Comparison of Ni and In as wetting agents

Metallization systems based on Au-Ge have been used extensively to form ohmic contacts to n-type GaAs (see Chapter 2). The normal alloying of these contact systems is achieved by heating the structure to temperatures of 360 °C or higher. In practice there are inherent problems in the alloying step. Upon alloying of the Au-Ge system, a Au-Ga compound forms [Og 80]. This leaves dissociated GaAs and unreacted As. The presence of As at the Au-Ge/GaAs interface then lowers the reactivity of the Au and Ga. This in turn causes excess Au at the interface, which "balls up" and results in a non-uniform contact surface [Pa 85b]. This problem is typically circumvented by adding wetting agents such as Pt [Ri 75], In [Ch 77] or Ni [Br 67] because it is believed that these metals increase the solubility of the GaAs by reacting with the As.

Various papers have reported on Ni as a wetting agent (see Chapter 2). However, only a small number of papers [Ch 77, Ch 79 and Gr 83b] have reported on the wetting influence of In. It should also be noted that the barrier height Ni formed with etched GaAs is ~0,80 eV, while the barrier height for In is somewhat lower at ~0,64 [Sm 69, Ra 73 and Kw 79]. Therefore, this section is devoted to the comparison between the Ni/Au-Ge and In/Au-Ge ohmic contact systems. In this comparison, some metallurgical and I-V properties will be considered.

The In/Au-Ge and Ni/Au-Ge results will be given and discussed separately. The AES results will be discussed first, followed by the current-voltage (I-V) measurements. SIMS and X-ray diffraction results will also be presented for the 450 °C annealed Ni/Au-Ge contacts.

Digitised by the Department of Library Services in support of open access to information, University of Pretoria, 2021

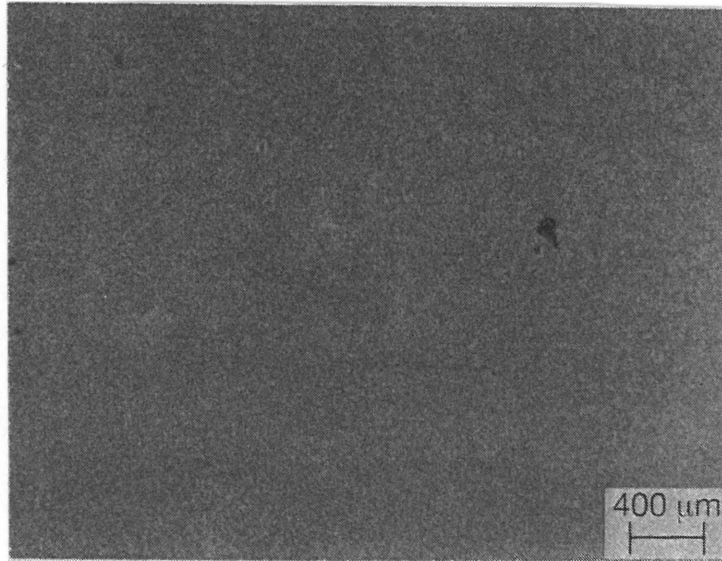

(a)

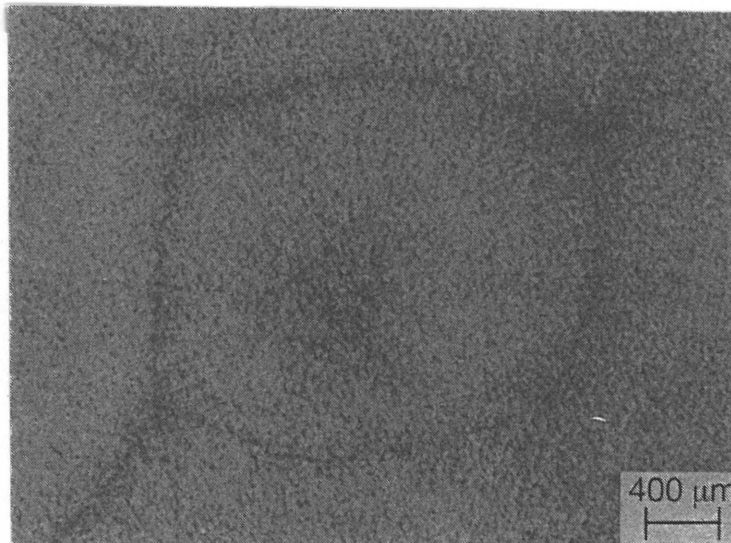

(b)

Figure 5.3: Optical micrographs of the In/Au-Ge contact system after annealing at (a) 300 °C and (b) 495 °C for 5 minutes respectively.

Digitised by the Department of Library Services in support of open access to information, University of Pretoria, 2021

Figure 5.3 shows optical micrographs of the In/Au-Ge contact system after annealing at 300 °C (a) and 495 °C (b) for 5 minutes, while optical micrographs of the Ni/Au-Ge contacts annealed at 300 °C and 450 °C respectively for the same time are shown in Fig. 5.4. It is interesting to note that even after the metallization step, prior to any intentional annealing, a difference in the outer surface of these two systems was evident. The as-deposited In/Au-Ge films had a copper-like colour in contrast to the more gold-like colour of the Ni/Au-Ge metallization system. However, upon annealing, the difference was even more pronounced. At an annealing temperature of 300 °C the surface of the In based metallization system was uneven and consisted of small grains which had a metallic colour (see Fig. 5.3(a)). With increasing annealing temperature these grains increased in size up to a temperature of 450 °C after which the size of the grains stayed constant. The grains had a hexagonal shape, resulting in a very poor surface morphology (see Fig. 5.3(b)).

In comparison, (see Fig. 5.4) the Ni based contact system yielded a very smooth surface after annealing at 300 °C. (The black spots on photo (a) in Fig. 5.4 are a combination of dust particles and dirt on the microscope lens system.) Upon annealing at higher temperatures (up to 450 °C) small grains appeared on the surface (5-50 μm in size), which had a copper-like colour. (This effect is discussed in more detail in the following section.) However, in general, the morphology of the Ni/Au-Ge contacts was much better than that of the In/Au-Ge metallization system.

The Auger depth profiles of the In/Au-Ge metallization system were carried out for as-deposited samples and for samples annealed at 300 °C, 350 °C, 400 °C, 450 °C, 495 °C and 525 °C respectively. However, only the as-deposited, 350 °C, 400 °C and 495 °C annealed contacts will be discussed, because noticeable changes only occurred at these temperatures. Furthermore, these changes coincided with changes in the I-V characteristics. Figure 5.5 represents the Auger depth profile data of the In/Au-Ge system.

Digitised by the Department of Library Services in support of open access to information, University of Pretoria, 2021

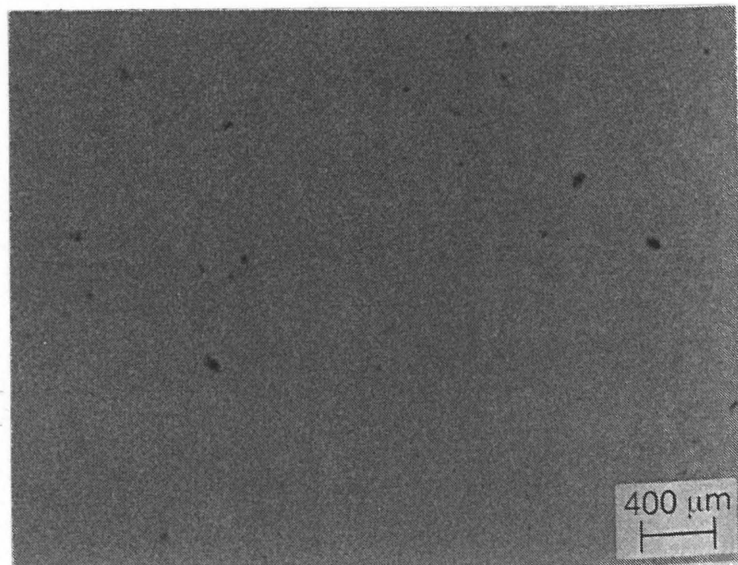

(a)

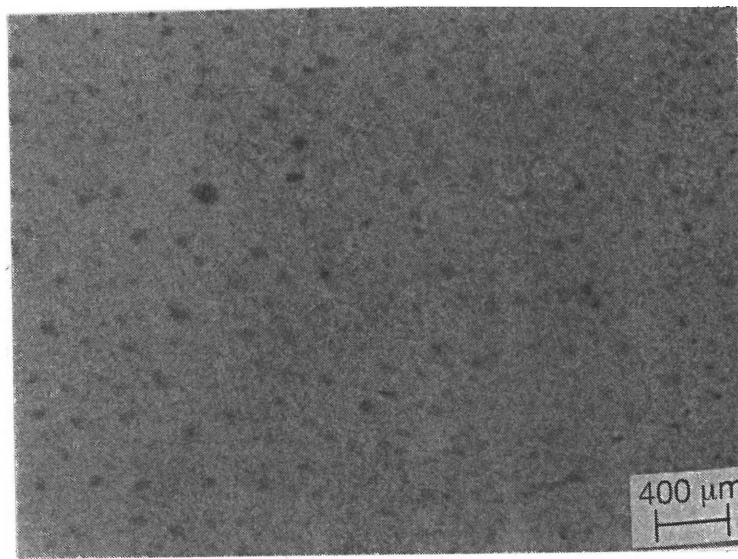

(b)

Figure 5.4: Optical micrographs of the Ni/Au-Ge contacts annealed at (a) 300 °C and (b) 450 °C for 5 minutes respectively.

Digitised by the Department of Library Services in support of open access to information, University of Pretoria, 2021

From the Auger depth profile shown in Fig. 5.5(a) it is clear that for the as-deposited case, the interface between the layers is not sharp, as compared with the depth profile for the as-deposited Ni/Au-Ge system (see Fig. 5.7(a)). According to this depth profile, diffusion within the films is observed, even at room temperature. (The In layer was deposited on the GaAs, followed by the Au-Ge.) Although it is not possible to detect various phases accurately using only AES, the elemental distributions obtained from the depth profiles and AES spot analysis, together with structural analysis reported in literature on the same metallization systems, has been used to identify some of the phases.

For the as-deposited samples, the substrate was not intentionally heated. However, during the evaporation process the substrate temperature could be as high as ±75 °C. Simic and Marinkovic [Si 77] found that at room temperature, In diffuses into Au forming various intermetallic-compounds, depending on the In content in the Au. An Au-In phase was also reported by Finstad et al. [Fi 75] to form on unannealed samples for an Au/In contact to GaAs. For the layer thicknesses used in this study the as-deposited In/Au-Ge films had a copper-like colour in comparison with the more gold-like colour of a Ni/Au-Ge metallization layer, which is an indication that diffusion/reaction also occurred in this layer system. Although no positive identification of an Au-In phase was made in these samples with AES, the depth profile in Fig. 5.5(a) indicate clearly the interdiffusion of Au and In. Therefore, on the basis of above-mentioned studies [Si 77 and Fi 75], it is highly probable that an Au-In phase is present in these samples.

In Fig. 5.5(b) a depth profile of a contact annealed at 350 °C is presented. The Ge surface concentration is higher than that of the bulk alloy, while some out-diffusion of Ga and As into the contact layer is also observed. The accumulation of Ge on the surface of the contact is characteristic of the Au-Ge contact

Digitised by the Department of Library Services in support of open access to information, University of Pretoria, 2021

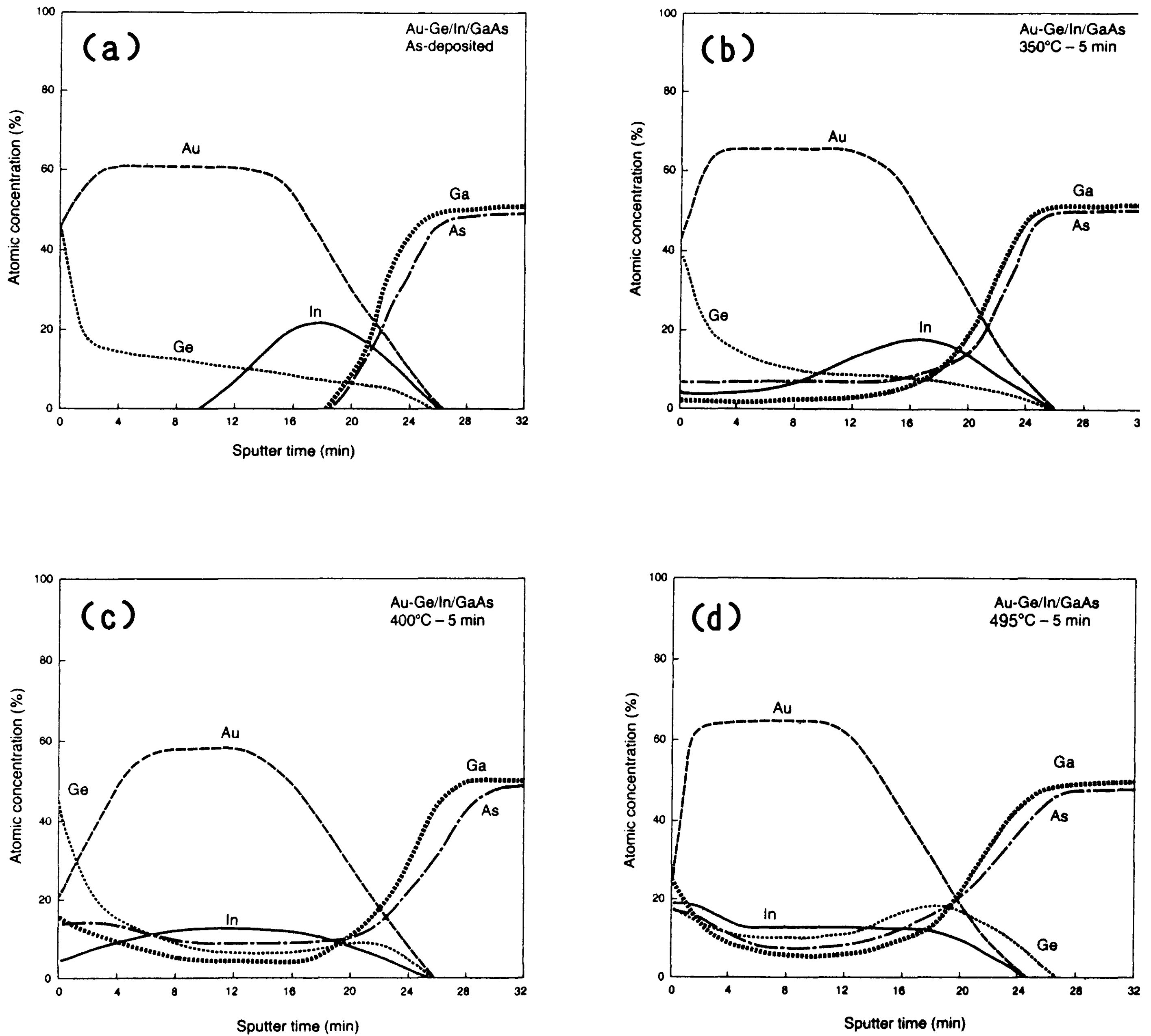

Figure 5.5: Auger depth profiles of the In/Au-Ge contact (40 nm/270 nm): (a) as deposited, (b) after annealing for 5 minutes at 350 °C, (c) 400 °C and (d) 495 °C.

Digitised by the Department of Library Services in support of open access to information, University of Pretoria, 2021

system. The Au and In interdiffusion still exists and therefore also the possibility of an Au-In compound, but is spread out more than in the previous case. Auger spot analysis revealed some In on the contact surface, which is an indication that some In diffused out towards the outer surface. This is also evident from the depth profiles.

The depth profile in Fig. 5.5(c) was obtained from one of the grains of a contact, after annealing at 400 °C. In contrast to the above cases, the Ge accumulated at the metal/semiconductor interface. A number of compounds can form at the interface region at 400 °C annealing temperature. This is due to the fact that at this annealing temperature, which is above the eutectic temperature of the Au-Ge, the GaAs is in contact with the metallization melt and can dissolve into the melt. Since the Au-rich metallization melt has a higher solubility for gallium than for arsenic, cooling results in the solidification of gallium-deficient GaAs. Therefore, Ge can substitute preferentially for Ga in the precipitated GaAs, increasing the Ge concentration at the interface. It has previously been shown that in the presence of Au, some of the out-diffused Ga associated with the Au to form a AuGa phase [Og 80 and Ra 81].

According to the SEM images the observed surface close to the interface after sputter etching shows some light areas. AES spot analysis on these areas revealed higher concentrations of Ge, As and Au than on the surrounding areas. Loveluck [Lo 77], Grovenor [Gr 83b] and Rackham and Steeds [Ra 81] showed that for similar specimens various metastable Au-Ge-As phases, covering a wide composition range, are formed at this annealing temperature. This, together with the AES results, suggest that one or another Au-Ge-As compound has formed. The In is now distributed throughout the contact layer and is not localized close to the interface as in the previous case, but is more evenly distributed between the interface and surface region.

Analyses obtained on the boundary of the grain areas after 30 seconds of sputtering (low O and C contamination), revealed

Digitised by the Department of Library Services in support of open access to information, University of Pretoria, 2021

an increase of approximately 5% arsenic atomic concentration compared to the analyses obtained on the grains. The increase in As at the boundaries can be explained by out-diffusion of As. The excess As, therefore, diffuses along the grain boundaries to the outer contact surface.

The outstanding feature of the Auger depth profile for the contact annealed at 495 °C is the increase in the Ge accumulation at the interface (see Fig. 5.5(d)). (This profile was also obtained on a grain area.) The increase of the Ge accumulation may be the result of more Ge being trapped in the postulated Au-Ge-As compound at the interface. This metastable phase could also act as a reservoir for Ge. According to Yoder [Yo 80] the Ge sits on the substitutional Ga sites created by the Ga out-diffusion, thereby forming a n^+ layer on the outer surface of the substrate. Furthermore, In is now evenly distributed throughout the contact with more Ga, As and In present on the surface of the contact than in the previous annealed cases. In general, more As was detected at the boundaries of the grains. This is in agreement with the findings on the 400 °C annealed contacts. The rest of the elemental distribution was basically the same as before.

The I-V and forward bias log I-V data for the above contacts are indicated in Figure 5.6. It must be noted that these I-V measurements were obtained by probing on large and small area contacts respectively. Furthermore, both contacts were on the same side of the substrate and as a result these contacts were exposed to the same heat treatment. Therefore, two back-to-back diodes are measured and as a result the forward current measured for a specific contact is influenced by the reverse current component from the other contact and vice versa. Instead of showing the ordinary I-V curve for the as-deposited contact, the log I vs V curve is shown in Fig. 5.6(a). The result is a "S" shaped curve. It can be argued that the divergence from a linear log I vs V characteristics is due to the influence of series resistance (top section of curve) and recombination currents (bottom section of curve). However, after annealing at 400 °C a linear log I vs V curve is obtained (see Fig. 5.6(c)), while the

Digitised by the Department of Library Services in support of open access to information, University of Pretoria, 2021

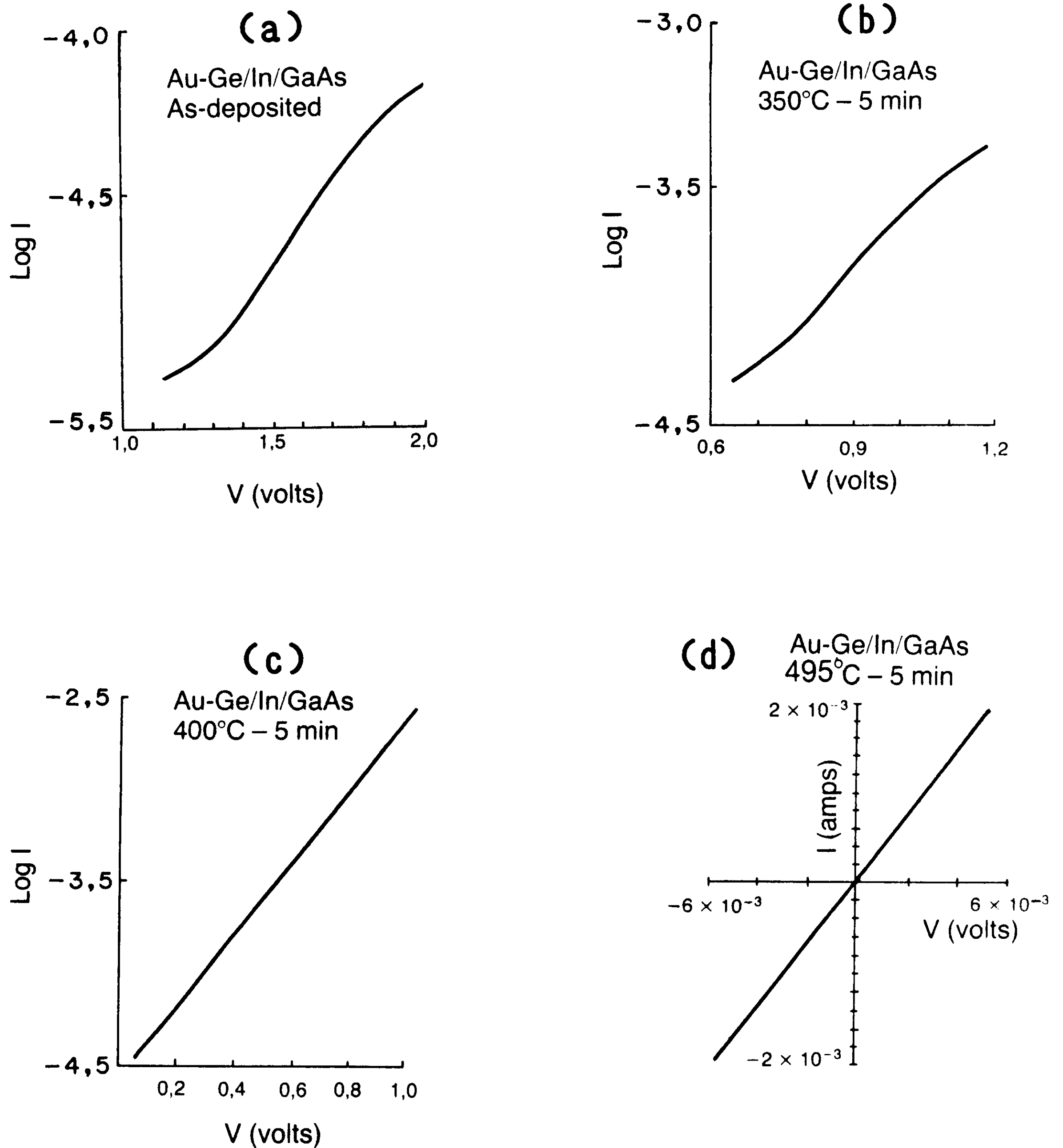

Figure 5.6: Typical I-V and log I-V data for the Au-Ge/In/GaAs system.

Digitised by the Department of Library Services in support of open access to information, University of Pretoria, 2021

contact is still non-ohmic in character. This is an indication of the absence of the current limiting factors mentioned above. Therefore, an alternative interpretation is proposed. Such a log I-V curve has been related to the idea of multiple phase contacts [Ch 86b]. One can explain the curve by the fact that the Schottky barrier height values are not reproducible due to different slopes in the curve in Fig. 5.6(a). This curve consists of low slope sections on the ends linked by a high slope part in the middle. The important ingredient is that two barrier heights coexist under the contact. This effect can be related to the effective work function model of Freeouf and Woodall [Fr 81], which relates each phase to its own work function and therefore barrier height (see section 3.2.4). It seems therefore from the above I-V results that more than one phase is present at the interface region. This result can be explained by the Au and In interdiffusion observed from the AES depth profile, which may be related to an Au-In phase coexisting with the as-deposited metallization layers at the interface region.

This log I-V character is retained after annealing of the contact at temperatures up to 350 °C (see Fig. 5.6(b)). At higher annealing temperatures the "S" characteristic disappears and one returns to a linear plot (see for example Fig. 5.6(c)). According to the Auger depth profile (Fig. 5.5(c)) the Au and In interdiffusion is much more evenly distributed throughout the contact layer at this annealing temperature. It seems as though the "S" shaped characteristics are only present when the possible Au-In phase is located close to the interface, but disappears when the phase is spread out through the contact layer. Recently it was shown by Murakami et al. [Mu 87b] that the transition of Schottky to ohmic behaviour for a Mo/Ge/In/W metallization system is strongly related to the formation of InGaAs phases at the metal/GaAs. It seems as if this might also be the case here, but with Au-Ge-As phases formed on certain areas of the interface. These low barrier and high conducting regions dominate the current conduction through the contact after annealing at 400 °C. However, no positive evidence of an InGaAs compound could be found from the AES results in this study. Furthermore, the ohmic

Digitised by the Department of Library Services in support of open access to information, University of Pretoria, 2021

behaviour after annealing at 495 °C, (see Fig. 5.6(d)) is related to tunneling through the barrier due to the n^+ doping of the substrate surface by the substitution of Ge.

The Auger depth profiles of the Ni/Au-Ge system is presented in Fig. 5.7 for the as-deposited contact, and contacts annealed at 300 °C, 370 °C and 450 °C respectively. However, investigations were also carried out on samples annealed at 350 °C, 415 °C and 435 °C, but will not be discussed here, since no significant changes to the results were noticed.

Figure 5.7(a) shows the depth profile for the as-deposited sample. Sharp interfaces between the contact layers are obtained and therefore it is concluded that very little diffusion has taken place. It can also be seen that the Ge accumulated on the contact's outer surface, while the Ni remained at the metal/GaAs interface.

At 300 °C annealing (see Fig. 5.7(b)) the Ge starts to accumulate between the Au-Ge alloy and the Ni layer and the Au starts to diffuse towards the GaAs. The out-diffusion of Ga and As into the Ni and towards the contact surface is also evident. The rapid diffusion of Ge is in agreement with other results [Ro 80, Ma 83, Bo 86 and Re 88], indicating that Ni is a sink for Ge in the form of a Ni-Ge compound. Furthermore, the decomposition of the interfacial GaAs is mainly due to the reaction between Au and GaAs and the availability of Ni. Ogawa [Og 80] proposed the following reaction:

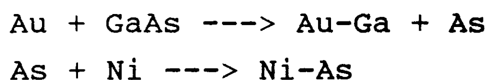

Au + GaAs ---> Au-Ga + As

As + Ni ---> Ni-As

Thus, the elemental diffusion observed in Fig. 5.7(b) might be due to the coexistence of Au-Ga, Ni-As and Ni-Ge compounds, together with Au-Ge. The phases reported in literature for this metallization system at 300 °C annealing temperature are Ni_2Ge [Ki 87], Ni-As [Og 80] and ß Au-Ga [Sa 87b] phases respectively.

Digitised by the Department of Library Services in support of open access to information, University of Pretoria, 2021

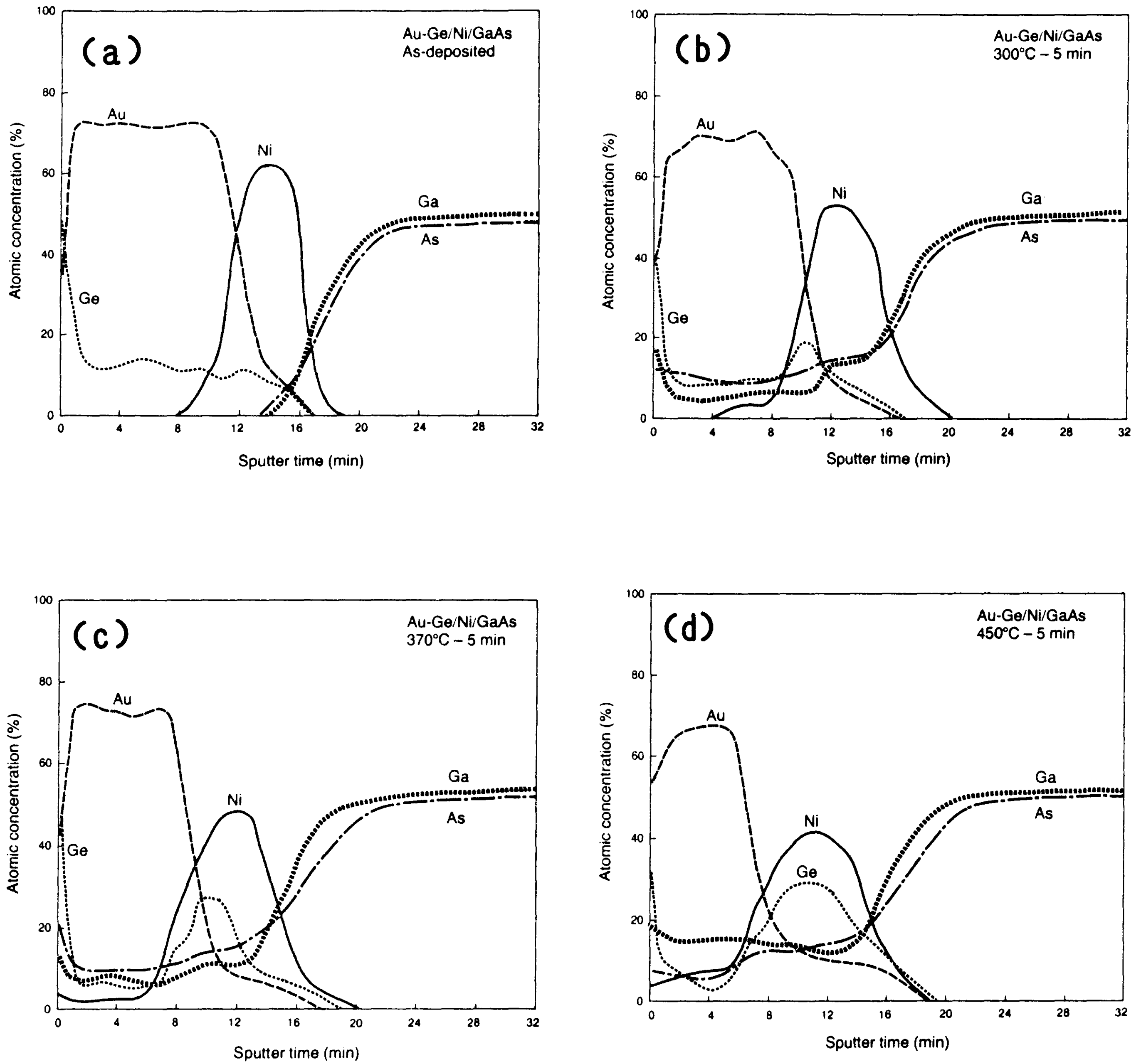

Figure 5.7: Auger depth profiles of the Ni/Au-Ge (40 nm/270 nm) contact system, (a) as-deposited, (b) after annealing for 5 minutes at 300 °C, (c) 370 °C and (d) 450 °C.

Digitised by the Department of Library Services in support of open access to information, University of Pretoria, 2021

At 370 °C annealing far more diffusion is observed for the different elements (see Fig. 5.7(c)). The Au-Ge (88-12% at wt) alloy melts at an eutectic temperature of about 360 °C [Ch 79]. Therefore, more Ge is available and can be trapped by the Ni. The increased Ni-Ge region extends towards the interface region which consists mainly of Ni-As due to the increased level of arsenic that segregated in the Ni-rich region. An increase in the Ga is also observed at the substrate interface probably due to the formation of a postulated Au-Ga compound, as explained in the previous paragraph. It seems reasonable to suppose that at this stage some Ge can enter the surface of the GaAs via the Ni-As region due to the increased availability of Ge from the Ni-Ge region.

The metallurgical properties of the contacts annealed at 450 °C were investigated by means of AES, SIMS and X-ray diffraction. Figure 5.7(d) presents the AES depth profile of such an annealed contact. The AES depth profile shows that the Ge diffused almost completely into the Ni layer, where according to X-ray diffraction measurements (see Fig. 5.9(b)), a Ni-Ge compound is formed. Furthermore, the Ni_2GeAs phase is also a well documented phase identified in the Au-Ge ohmic contact system [Ku 83], but the possibility of a Ni-As compound cannot be ruled out in this region. There also exists the possibility that some of the Ge is captured by such a Ni-As compound, in order to form an alloy of Ni-As containing Ge (Ni-As(Ge)). It has also been reported in the literature that the Ge-rich compounds occurred in localized areas at the substrate interface [Br 81 and Ku 83].

Using a higher magnification than that used in Fig. 5.4, the morphology of the contact surface annealed at 450 °C, revealed 'balling up' regions. Auger spot analysis indicated more Ge and As on these regions than on the surrounding areas, while Au was present covering the outer surface. The occurrence of such balling up regions has also been reported in the literature [La 84b and Au 85]. These publications attribute such regions to a ternary Au-Ge-As compound. Therefore, according to the AES spot analysis it is concluded that this compound is also located

Digitised by the Department of Library Services in support of open access to information, University of Pretoria, 2021

at the 'ball-up' regions. One possible explanation for the formation of this ternary compound can be found in the increased amount of the Ni-Ge compound observed in Fig. 5.7(d) which was obtained from a homogeneous region. Thus, less Ni is available to capture the As out-diffusing from the substrate. As a result, some of this As is then captured by the Au and Ge at the contact surface during the cooling process. The reason why this compound caused the surface to "ball up" is not clear. It is suggested that the out-diffusion of As occurred non-uniformly. This can be related to the uneven penetration depths (also called spikes) observed for the Au-Ga compound [Yo 84 and Ra 87]. Therefore, more As is available in some areas than in other areas to be captured by Au and Ge.

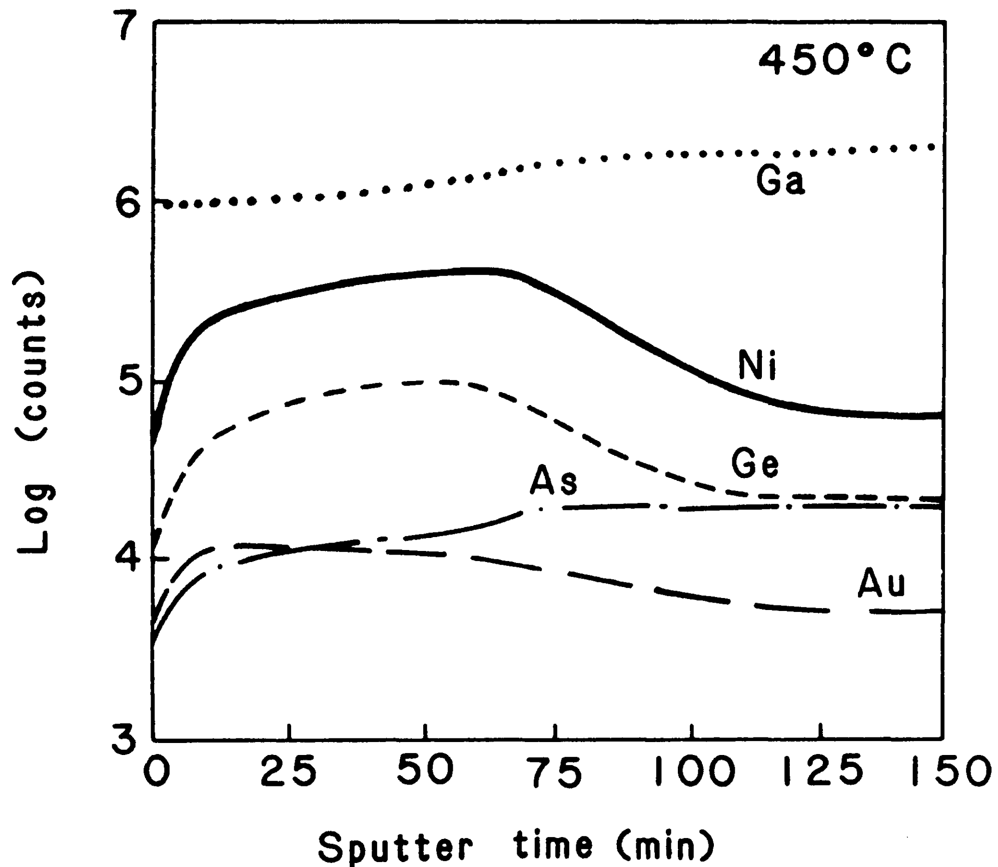

Figure 5.8: SIMS depth profile for the Ni/Au-Ge contact after annealing at 450 °C.

Digitised by the Department of Library Services in support of open access to information, University of Pretoria, 2021

The SIMS results obtained from these contacts are shown in Fig. 5.8. These results reveal basically the same observations as those obtained from the AES depth profiles. It is clear from this profile that the Ni, Ge and As and the Au and Ga respective elemental distribution display the same behaviour. This is also in line with the AES results. From the SIMS results it was not clear if the interface region consists of a Ni-As(Ge) or a Ni-As-Ge alloy.

In Fig. 5.9 the X-ray diffraction spectra obtained for the (a) as-deposited contacts and (b) the contacts annealed at 450 °C for 10 minutes, are shown. For the as-deposited contacts only the diffraction peaks that corresponded to Au; Ni; Au-Ge and GaAs (indicated by (i); (ii); (iii) and (iv) respectively) were observed. However, after annealing at the above temperature, some of these peaks disappeared and new peaks, relating to the appearance of different types of compounds, were found.

The peaks indicted by (v) originated from a ß Au-Ga phase and according to Cooke et al. [Co 66] it consists of a hexagonal closed packed (hcp) structure with a=0,773 nm and c=0,874 nm. Furthermore, the peaks indicated by (vi) were also obtained from a hcp structure with a=0,380 nm and c=0,496 nm. Two phases have been reported in the literature which have this structure, namely Ni-As [He 48] and Ni_2GeAs [Ku 83]. However, as with the AES and SIMS results, it is not possible to distinguish between these two compounds. It is therefore concluded that either a Ni_2GeAs phase or a Ni-As alloy formed which contains some Ge and is represented in the form Ni-As(Ge). The peaks indicated by (vii) originated from a Ni-Ge compound, which corresponds to an orthorhombic structure with a=0,581 nm; b=0,538 nm and c=0,343 nm [Pf 50].

The last phase identified was indicated by (viii) and is related to the ternary Au-Ge-As phase which has a monoclinic structure with lattice constants a=0,711 nm; b=0,643 nm; c=0,684 nm and

Digitised by the Department of Library Services in support of open access to information, University of Pretoria, 2021

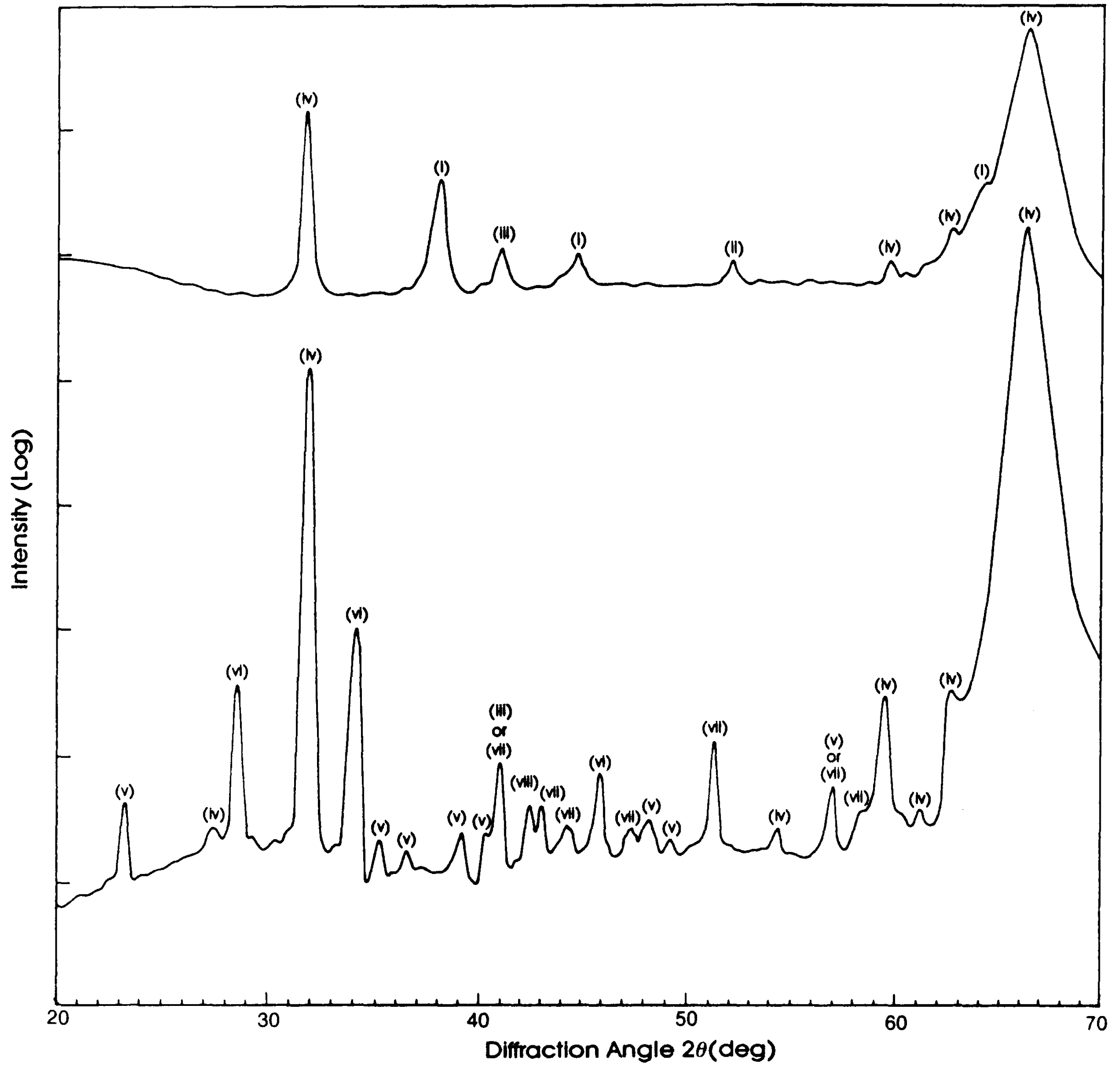

Figure: 5.9: X-ray diffraction profile obtained from an (a) as-deposited Au-Ge/Ni/GaAs contact and (b) after annealing at 450 °C for 10 minutes. The respective peak indexes are explained in the text.

Digitised by the Department of Library Services in support of open access to information, University of Pretoria, 2021

ß=126° [St 81b]. According to Rackham and Steeds [Ra 77] the Au-Ge-As phase is a metastable ternary phase, which can exist over a broad composition range. Apart from the fact that this phase is related to the non-uniformity of the contact surface, using the AES results presented above, it was also reported that the Au-Ge-As compound might increase the contact resistance since some of the Ge is present in this phase on the contact outer surface, while less Ge is then available to dope the substrate [La 84b and Go 83].

The results above show that good agreement is obtained between the AES, SIMS and X-ray diffraction observations in identifying a wide range of intermetallic compounds formed at or close to the metal/GaAs interface at 450 °C annealing.

Figure 5.10 shows a series of forward bias log I-V and I-V characteristics for the Ni/Au-Ge/GaAs samples annealed at various temperatures for 5 minutes. (Note that 2 back-to-back contacts on the same side of the substrate were measured). In contrast to the In/Au-Ge results, the I-V results from Fig. 5.10 seem to be compatible with the field emission theory due to the linear log I vs V characteristics (see Fig. 5.10(a)), which is expected for these doping conditions [Pa 71].

Below 370 °C the contacts are not ohmic in character (Fig. 5.10(b)), probably due to the lack of Ge at the interface to dope the GaAs surface (see Fig. 5.7(b)). Around 370 °C the contacts are observed to be ohmic (see Fig. 5.10(c)). The Au-Ge alloy melts at an eutectic temperature of about 360 °C [Ch 79]. Thus, more Ge is now trapped in the Ni-Ge region. However, some of the Ge also diffused out of this region into the postulated Ni-As compound to form a Ni-As(Ge) or Ni_2GeAs region, which formed next to the interface. The ohmic behaviour in this metallization system is believed to be due to the n^+ GaAs surface caused by the excess Ge atoms on the substitutional Ga sites, created by the Ga out-diffusion.

Digitised by the Department of Library Services in support of open access to information, University of Pretoria, 2021

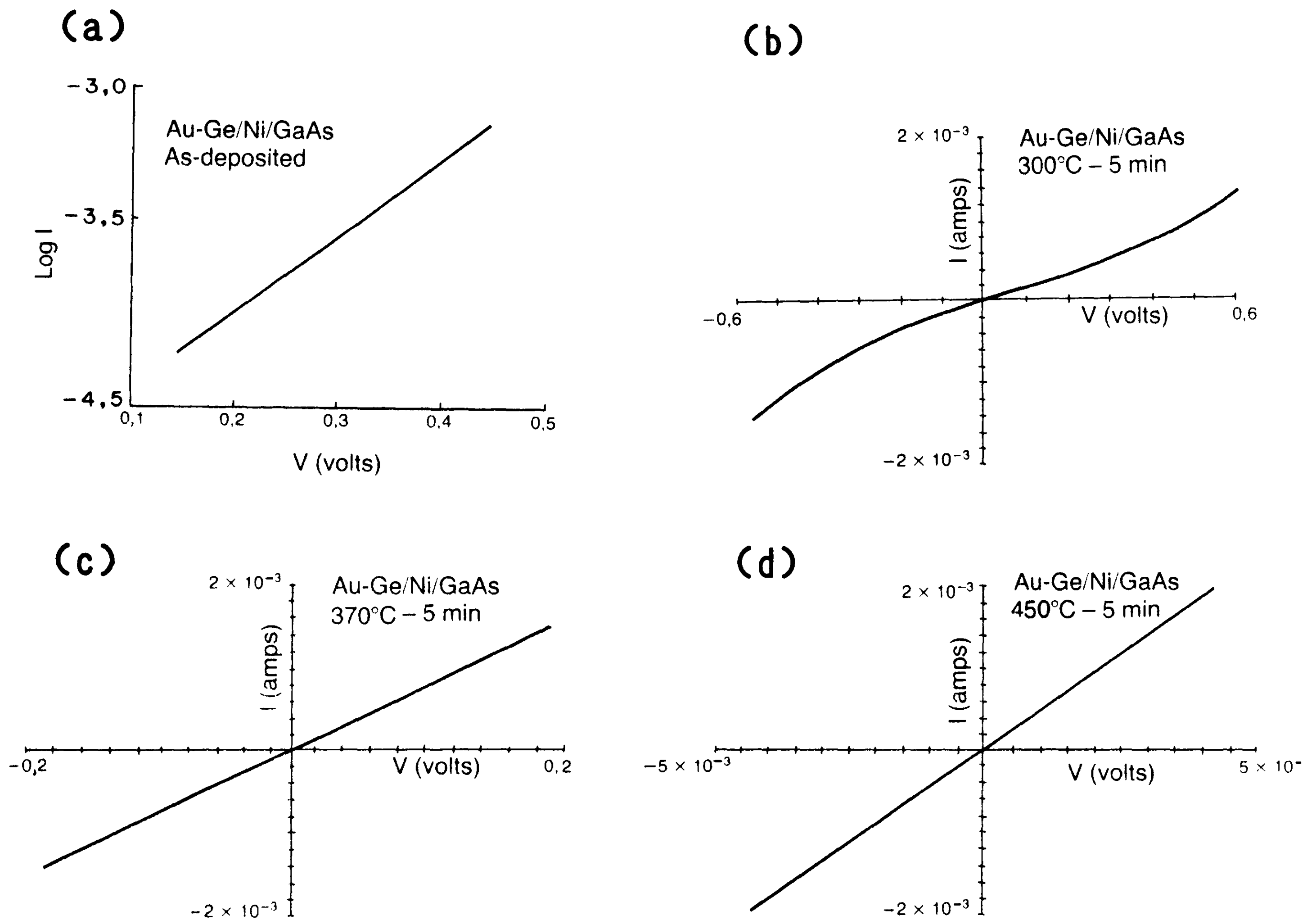

Figure 5.10: I-V and log I-V data for the Au-Ge/Ni/GaAs contact system.

Digitised by the Department of Library Services in support of open access to information, University of Pretoria, 2021

As the annealing temperature was increased further to 450 °C the Ge content in the Ni-As(Ge) phase increased (Fig. 5.7(d)), with a resultant increase in Ge at the interface. Thus, more germanium substitutes preferentially for gallium in the precipitated GaAs, resulting in highly doped n-type GaAs in contact with the metal overlayer and a tunneling ohmic contact is obtained. Normally at this annealing temperature, the lowest specific contact resistance values are experienced (see Table 2.1 in Chapter 2). This will also be discussed in the following sub-section.

It is interesting to note that the Au-Ge-As phase occurred in both the In/Au-Ge and Ni/Au-Ge annealed contacts. In the former contacts, this phase was observed at the interface, while in the latter case it was mostly present on the contact outer-surface. Furthermore, in both cases the Au-Ge-As phase can be related to the non-uniformity of the contact surface, even though the morphology of the In/Au-Ge contacts was much poorer than that of the Ni/Au-Ge contacts. The different behaviour of the Au-Ge-As phase can be ascribed to the different roles of the Ni and In metallization layers. In this study, as with other structural investigations where Ni was originally used as a so-called wetting agent [Bo 86 and Sh 87b], the Ni is the primary driving force for the Ge accumulation at the interface, first via the Ni-As compound formation, followed by the Ni-As(Ge) or Ni_2GeAs compound formation. However, in contrast, the In formed an In-Au phase, even for the as-deposited case, with the result that the In moves away from the interface area, while the Au diffuses towards the interface. In comparison with the Ni in the Ni/Au-Ge contact system, much less In is present at the interface in order to capture the rapid out-diffused As. Instead, the As is absorbed by the metastable Au-Ge-As compound and the In-Ga-As compound at the interface. Thus, it seems that not only the presence of the Au-Ge-As compound, but also its position influences the degree of surface roughness for the Au-Ge based metallization systems. This result may explain the observation that different metallization combinations of Ni and Au-Ge caused dramatic differences in the respective surface morphologies [Mu 86 and Br 87].

Digitised by the Department of Library Services in support of open access to information, University of Pretoria, 2021

The Au-Ge-As phase can cover a large percentage of the contact area and is thus expected to have some influence on the electrical nature of the ohmic contact. It has been suggested that the Au-Ge-As phase has a current-limiting effect [Ra 77] but this is very difficult to establish experimentally, because of the difficulty in producing this phase in isolation to investigate its electrical characteristics.

From the above study it is evident that the Ni produced a better surface morphology contact, but due to the increasing demand for smaller devices, the surface morphology must be much better than that obtained above. The purpose of the next sub-section is to investigate a technique for improving the surface morphology of the Ni/Au-Ge contact system.

5.2.3 Investigation of ohmic contacts after ion implantation and annealing

Ion beam mixing has been used very effectively in the formation of ohmic contacts to Si [Ts 80 and Ba 80b]. After Bower [Bo 71] first made ohmic contacts to GaAs using ion beam mixing, this technique in thin film-GaAs systems has received very little attention in comparison with the subject of ohmic contacts to GaAs.

From the discussion above, it is clear that one of the biggest problems from which the alloyed Au-Ge/Ni ohmic contacts suffer, is the non-uniformity of the contact layer. A model which explains this poor surface morphology, is given by Palmstrøm et al. [Pa 85] and is schematically illustrated in Fig. 5.11. According to this model, it is believed that the presence of a thin interfacial layer on the surface of the GaAs, due to the absorption of oxides and hydrocarbons from the atmosphere prior to metallization, may be responsible for non-uniform alloying through weak spots in this layer. Support for this argument is found in the AES spectra shown in Fig. 5.2, which clearly illustrate the presence of O and C on the chemically cleaned GaAs surface. (Note that these AES results were obtained in order

Digitised by the Department of Library Services in support of open access to information, University of Pretoria, 2021

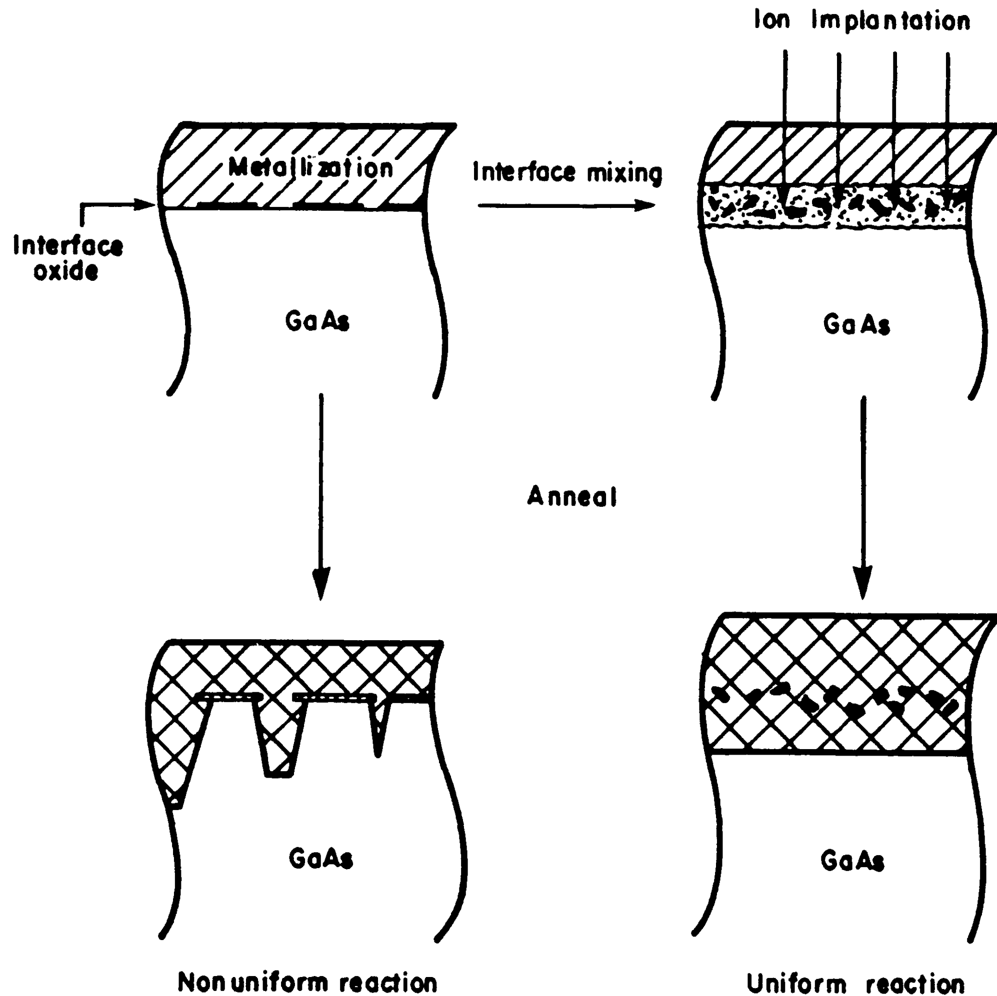

Figure 5.11: Schematic illustration of the cracking of the interfacial layer by ion implantation and the resultant improved surface morphology [Pa 85].

to simulate the situation prior to the metallization step). In order to overcome this effect, Palmstrøm et al. [Pa 85] proposed that ion beam mixing be used to disperse the interfacial layer.

Digitised by the Department of Library Services in support of open access to information, University of Pretoria, 2021

Recently, the application of the technique of ion beam mixing followed by some thermal anneal treatment has been extended to contact formation on GaAs, using various metal-semiconductor combinations. In most cases the mixing has been carried out using inert gas ions such as Ar^+ or Kr^+ ions to mix Au/GaAs [Ja 87 and Ba 87b] and Au-Ge/Ni/GaAs [Ba 88b] metal/semiconductor interfaces. Other studies have used dopant ions such as Si^+ on Ni/Ge/Au/GaAs [Bh 85] and Ge/Au/GaAs [In 85], Ge^+ on Ni/GaAs [Sm 85] and Se^+ on Ge/Ni/GaAs [Ji 88]. The results indicate an improved surface morphology compared to contacts that were subjected to only thermal treatments.

From the above discussion it seems reasonable that ion implantation through the metallization layer has a role to play in ohmic contact formation to GaAs by increasing the carrier concentration at the surface and to improve surface morphology. The emphasis in this study was placed on the metallurgical and electrical properties of ohmic contacts manufactured conventionally, compared with contacts Ar^+ ion-implanted before annealing. AES, SIMS and X-ray diffraction analysis were used to obtain metallurgical information, while the electrical characterization of these contacts was limited to current-voltage (I-V) and specific contact resistance measurements.

Two sets of samples were prepared in order to obtain a comparison between the unimplanted and the Ar^+ ion implanted contacts. Electrical properties were obtained for both sets on as-deposited samples, and samples annealed at 350 °C, 375 °C, 400 °C, 425 °C, 450 °C and 475 °C, respectively. However, AES and SIMS depth profiles will only be discussed for the as-deposited contacts, and the contacts annealed at 450 °C, while X-ray diffraction results were only obtained for the contacts annealed at 450 °C.

Figure 5.12 shows typical optical micrographs for both the unimplanted and ion implanted Au-Ge/Ni/GaAs contact systems, after annealing at 450 °C for 2 minutes. The implanted contact surface (see Fig. 5.12(a)) is far more uniform compared

Digitised by the Department of Library Services in support of open access to information, University of Pretoria, 2021

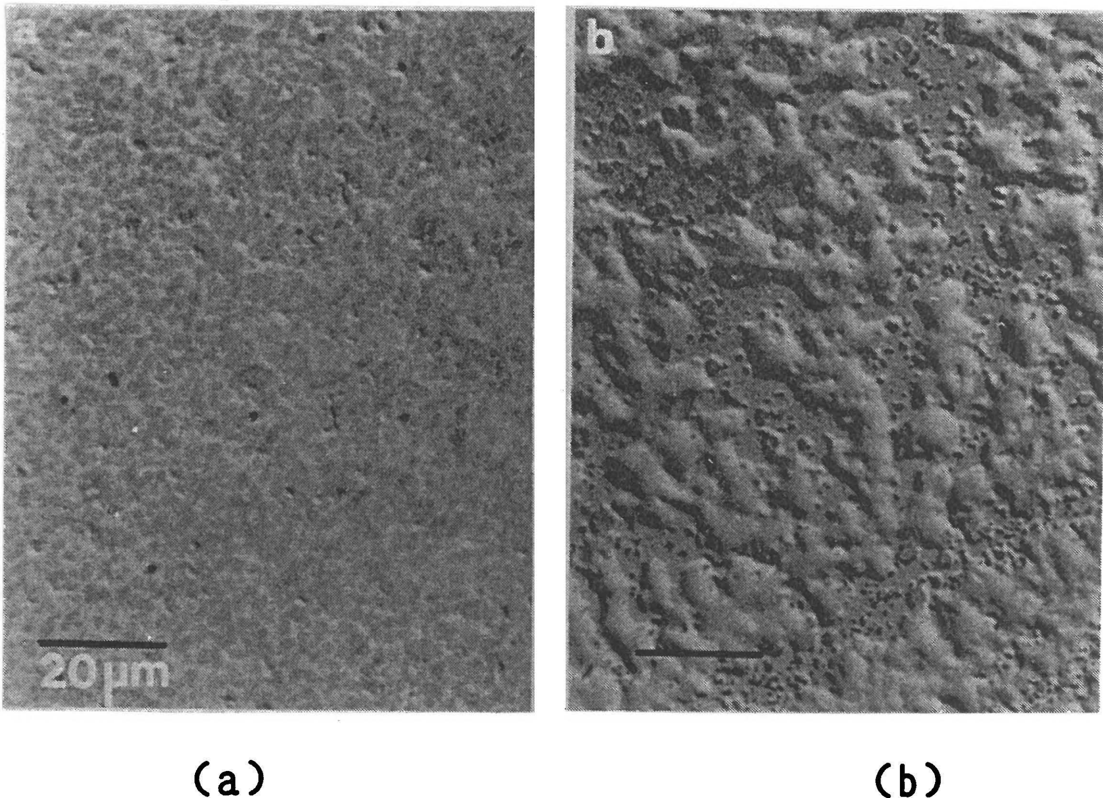

Figure 5.12: Optical micrographs of (a) implanted and (b) unimplanted contacts after annealing at 450 °C for 2 minutes. (The markers represent 20 µm).

with the unimplanted contacts (see Fig. 5.12(b)). Although the layer thicknesses and annealing times used here, differed from those used in the previous section, the relative surface morphologies were the same.

Most of the reported metallization systems (see Chapter 2) consisted of the traditional Au-Ge/Ni system, with the Ni layer deposited on top of the Au-Ge. In the present study Ni was deposited between the Au-Ge alloy and the substrate (Ni/Au-Ge), since it was reported recently that this system reduces contact resistance and increases the stability of the contact upon aging [Br 87].

Digitised by the Department of Library Services in support of open access to information, University of Pretoria, 2021

The diffusion of Au, Ge and Ni into the GaAs during the alloying process is sufficiently complicated that it is very difficult to obtain accurate in-depth information with a single depth profiling technique. The metallurgical investigation was therefore performed with both AES and SIMS. The sensitivity of SIMS is at least an order of magnitude better than that for AES analyses. The sputtering rate is however different when one changes from one matrix to another, with the result that a rough surface is produced and therefore the depth scale is not the same for all elements. On the other hand, with AES, quantitative depth profiles can be obtained without some of the complications experienced with SIMS. Due to these problems the correlation between the AES (see Fig. 5.13) and SIMS (see Fig. 5.14) depth profiles was poor in some cases. The general trends could, however, be determined from a comparison of the two sets of depth profiles. In the case of the as-deposited samples, (see Figs 5.13(a) and 5.14(a) respectively) the depth profiles correspond to the expected structure. The AES depth profile clearly shows individual metal layers on the GaAs substrate. The diffusion of Ni into the GaAs, as observed in the SIMS depth profile, is certainly an artifact induced by the sputtering process. Kats et al. [Ka 81] has shown how the matrix can influence an in-depth analysis, when profiling layered structures.

The depth profiles for the as-deposited ion implanted contacts are shown in Fig. 5.13(b) and Fig. 5.14(b) respectively. From these figures it is clear that some mixing of the elements in the metallization layer has occurred upon implantation. The AES depth profile shows that the Ge is now far more evenly distributed throughout the Au. Some movement of Au and Ge into the Ni layer is also observed. It seems therefore that intermixing between the Ni and Ge has occurred but that this mixing is insufficient to produce a completely uniform Ni-Ge alloy. The broader distribution of Ni also indicates movement towards the substrate and contact surface. This movement could be explained in terms of radiation-enhanced diffusion and heat generation during the implantation steps. According to the X-ray diffraction results, no real difference between the as-deposited and ion implanted as-

Digitised by the Department of Library Services in support of open access to information, University of Pretoria, 2021

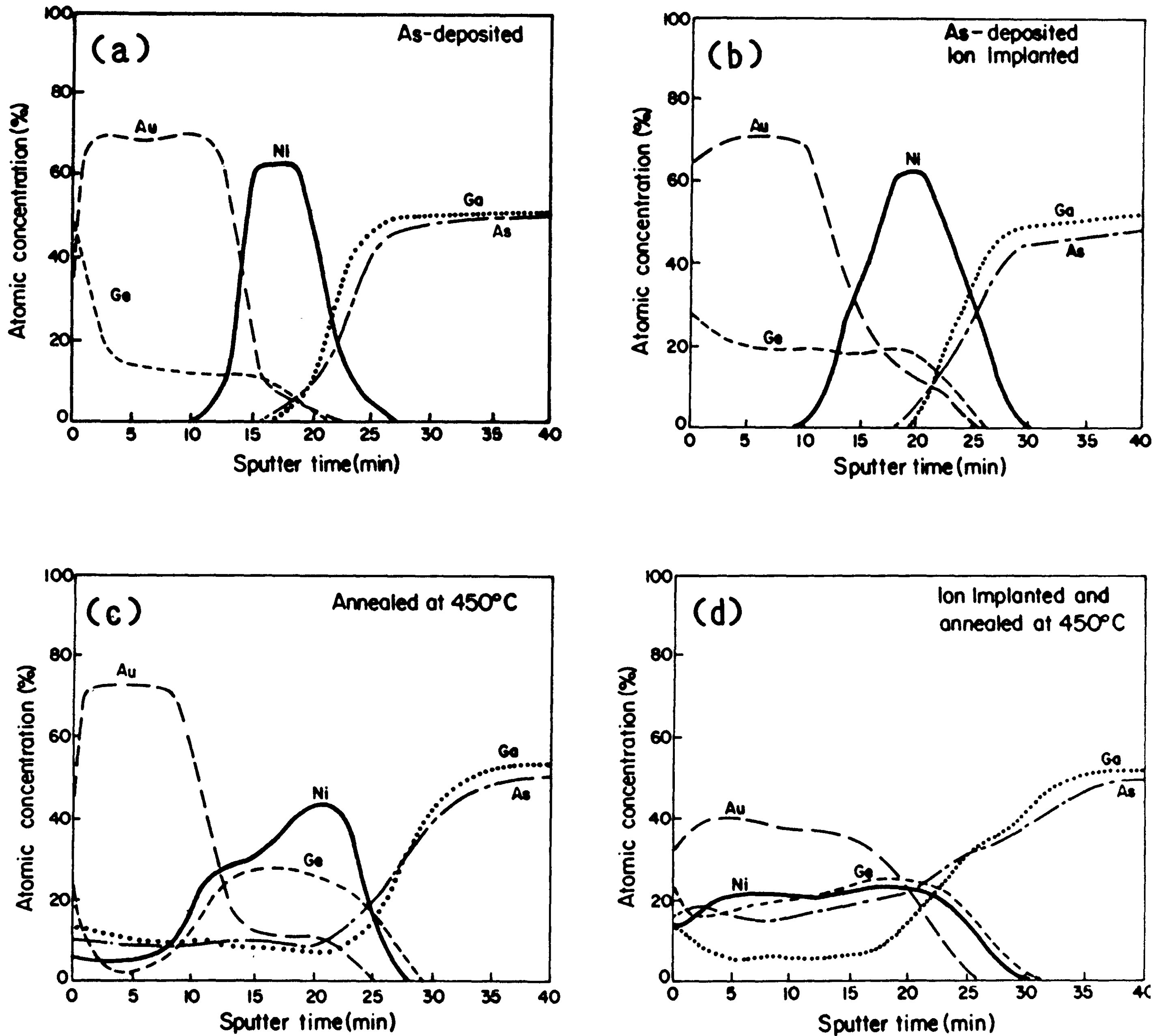

Figure 5.13: Auger depth profiles of Ni/Au-Ge (75 nm/200 nm) contacts (a) as-deposited, (b) as-deposited and ion implanted, (c) annealed at 450 °C and (d) ion implanted and annealed at 450 °C.

Digitised by the Department of Library Services in support of open access to information, University of Pretoria, 2021

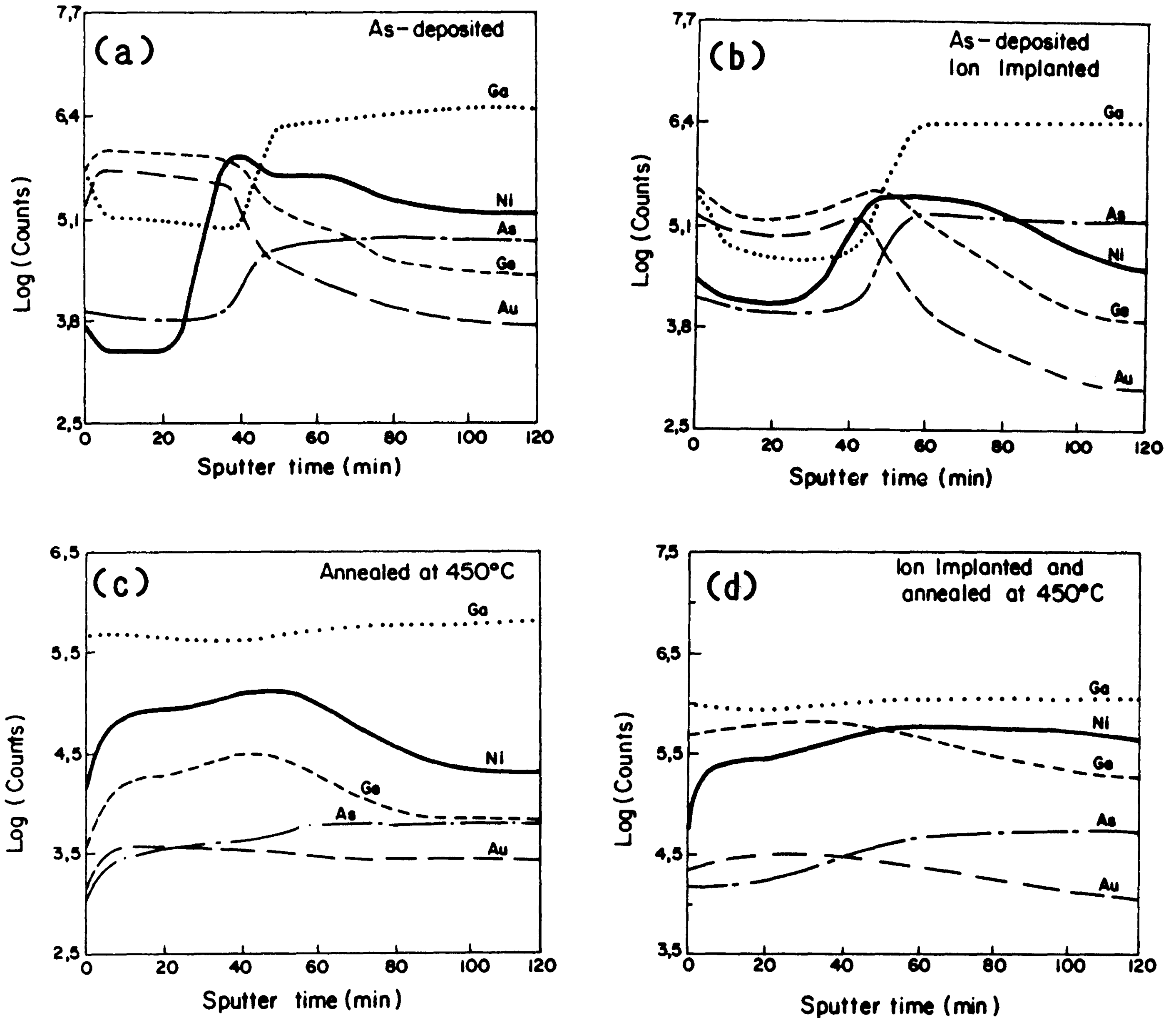

Figure 5.14: SIMS depth profiles of Ni/Au-Ge (75 nm/200 nm) contacts (a) as-deposited, (b) as-deposited and ion implanted, (c) annealed at 450 °C and (d) ion-implanted and annealed at 450 °C.

Digitised by the Department of Library Services in support of open access to information, University of Pretoria, 2021

deposited samples could be observed. In addition to the compounds identified in the X-ray diffraction profile for the as-deposited samples in Fig. 5.9, there is a possibility that small amounts of phases which could not be identified by the presently used X-ray diffraction technique could be present in the ion implanted samples.

Both unannealed contacts were non-ohmic as can be seen from the I-V curves shown in Fig. 5.15(a). These I-V measurements were also carried out on large and small area back-to-back diodes, deposited on the same side of the substrate. The reason why the ion implanted contacts were not ohmic, could be related to the absence of sufficient mixing at the metallization substrate surface as discussed above. By using a higher implantation energy or dose, the probability of more mixing would be higher. However, this could introduce detrimental radiation damage in the GaAs substrate [Bh 85]. Furthermore, it was also shown recently that the series resistance of Al and Au diodes to GaAs increase after Ar ion bombardment at a fluence above 10^{14} cm^{-2} [Co 88 and Au 91b]. This experiment was carried out at a fluence of $6x10^{14}$ cm^{-2}, and as a result it already falls in the region where the series resistance starts to increase. This therefore also explains the non-ohmic character, if it is assumed that the same defects are introduced by sputtered Ar ions [Co 88 and Au 91b] as by the implanted Ar ions. Furthermore, from Fig. 5.15(b) it is clear that the unimplanted contacts had lower resistances than the implanted contacts. This result is also reflected in the specific contact resistance measurements discussed below.

The TLM method, consisting of a circular test pattern, was employed to find the specific contact resistance (r_c) of the ohmic contacts at different annealing temperatures. Figure 5.16 gives r_c as a function of annealing temperature for the implanted (see Fig. 5.16(a)) and unimplanted contacts (see Fig. 5.16(b)). These data were obtained from various measurements on different sets of contacts which have been annealed at the respective temperatures. The presentation and measurements of the r_c values are discussed in section 4.3.6.

Digitised by the Department of Library Services in support of open access to information, University of Pretoria, 2021

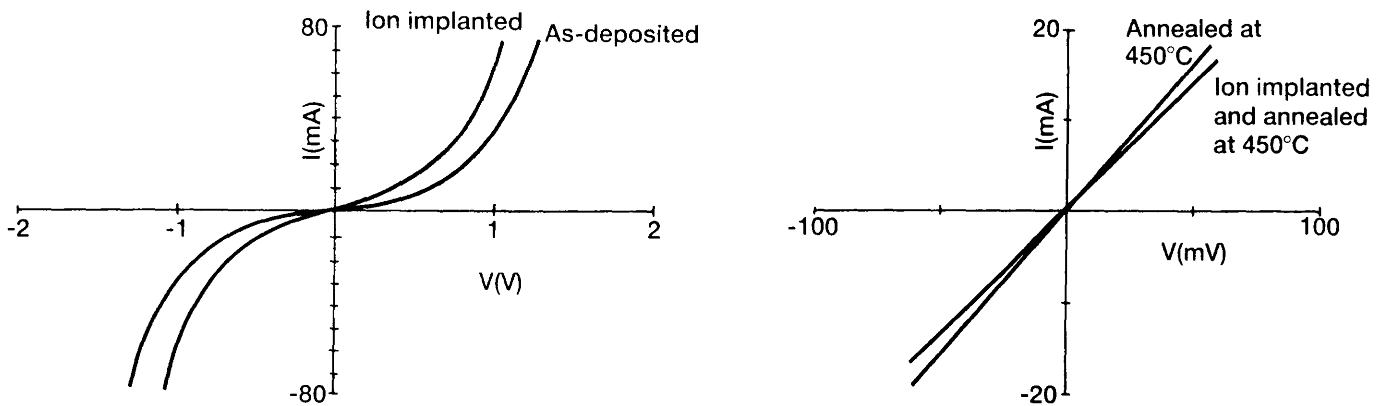

Figure 5.15: I-V characteristics of (a) as-deposited contacts and (b) contacts annealed at 450 °C for 2 minutes; with and without the Ar-implantation step.

In general, the specific contact resistance decreases with increasing annealing temperature, up to about 450 °C, whereafter r_c increases. The best specific contact resistance obtained after annealing at 450 °C was 5×10^{-6} Ωcm^2 for the unimplanted and 1×10^{-5} Ωcm^2 for the ion implanted contacts. These results are in agreement with the I-V measurements shown in Fig. 5.15(b). The higher contact resistance measured for the implanted contacts may be related to the damage produced at the GaAs surface. Although the calculated range for 260 keV Ar^+ ions, according to the Monte Carlo simulation program, TRIM [Bi 80], indicates very little penetration of the incident ions across the metallization/GaAs interface (the projected range is 94 nm), dislocation loops may be present in the substrate, as observed by Bhattacharya et al. [Bh 85]. The Ar depth distribution of 260 keV Ar^+ ions through these metallization layers is shown schematically in Fig. 5.17.

It is interesting to note that the lower annealed contacts revealed a much higher scatter in the r_c values than that of the contacts annealed at higher temperatures. This effect can possibly be explained by the observation in section 5.2.2 that as the annealing temperature increased to 450 °C, the Ge content in the Ni-As(Ge) phase also increased. As a result the possibility to obtain high conduction regions increased with increased annealing temperature.

Digitised by the Department of Library Services in support of open access to information, University of Pretoria, 2021

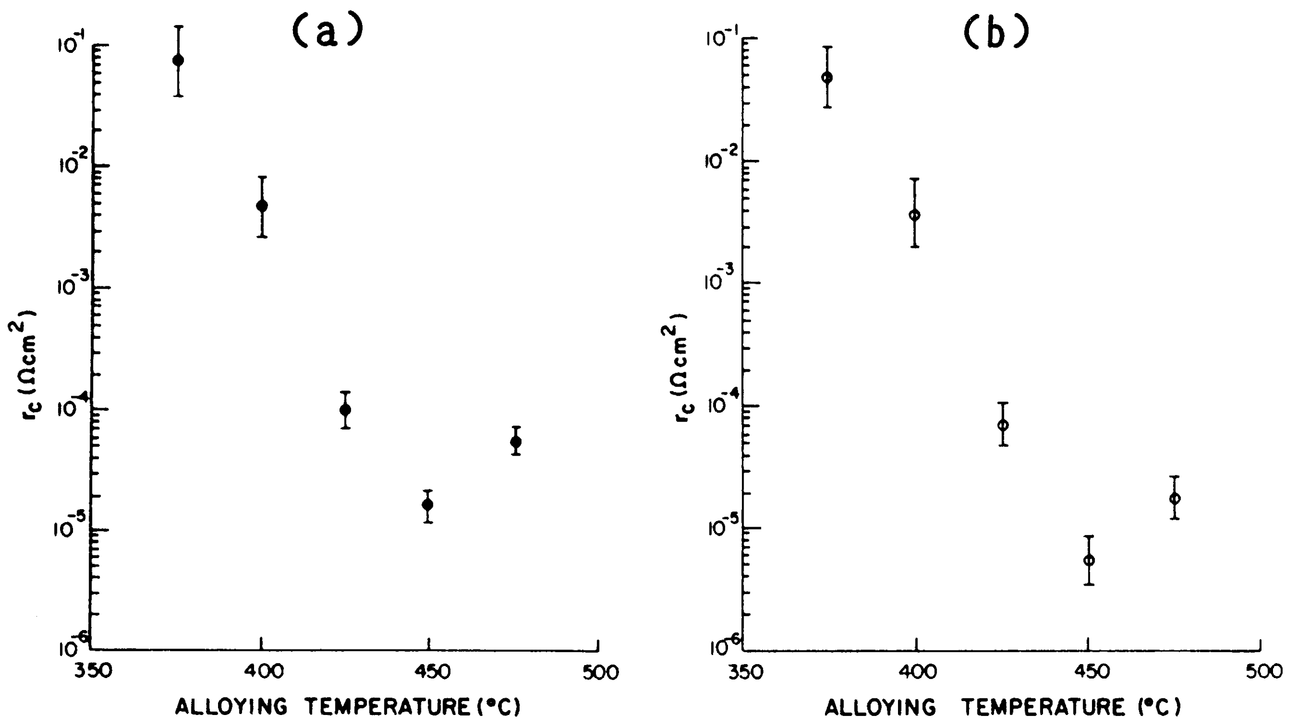

Figure 5.16: Variation of specific contact resistance with alloying temperature for (a) ion implanted and (b) unimplanted ohmic contacts. The annealing was carried out for 2 minutes at each temperature.

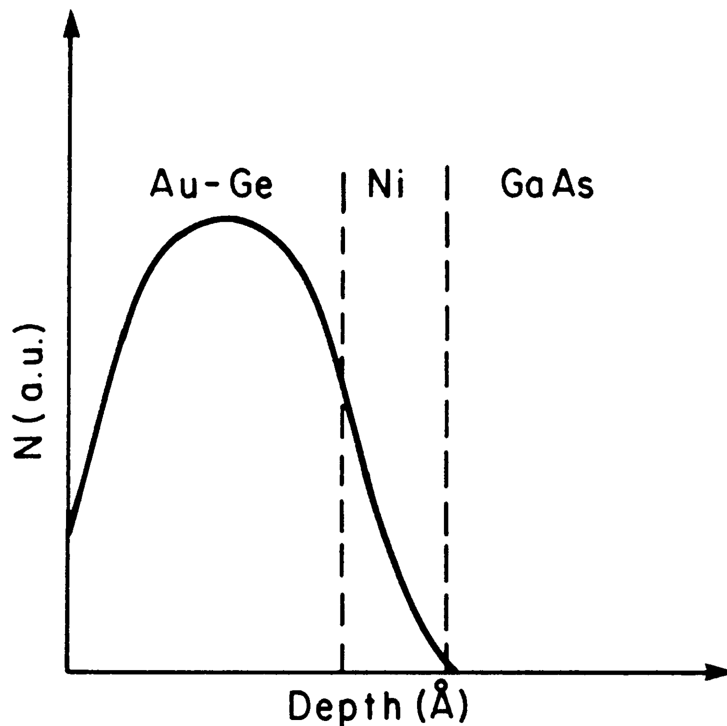

Figure 5.17: The depth distribution of 260 keV Ar ions obtained from the TRIM computer code [Bi 80].

Digitised by the Department of Library Services in support of open access to information, University of Pretoria, 2021

Due to the fact that the lowest r_c values in both cases were obtained after annealing at about 450 °C, the structural investigations for the respective contacts will be discussed only for the contacts annealed at this temperature. (This also applies to the surface morphology.)

Although different metallization thicknesses and shorter annealing times were used, compared to the Ni/Au-Ge contact system discussed in the previous section, the AES, SIMS and X-ray diffraction techniques revealed basically the same trends. (Compare Fig. 5.7(d) with 5.13(c) and Fig. 5.8 with Fig. 5.14(c).) Thus, the metallurgical characteristics of these contacts after annealing at 450 °C are the same as those discussed in the previous section and are therefore not repeated in this section. The depth profiles of ion implanted contacts, annealed at 450 °C are shown in Fig. 5.13(d) and Fig. 5.14(d) respectively. The outstanding feature is the even distribution of the elements, compared to the annealed contacts. The interface between the Au-Ge and Ni can no longer be seen as the Ni is now distributed evenly from the interfacial region through to the contact surface (compare with Fig. 5.7(d) and Fig. 5.8) , while more Au has moved to the GaAs surface. More Ga and As have also diffused out to the contact surface, compared to the annealed contact. The distribution of the elements supports the findings by Kameneckas et al. [Ka 86], namely that ion implantation of the Au-Ge/Ni system leads to a higher diffusion rate of the elements during the annealing process. From these depth profiles it is evident that the metallization layer consists of an almost uniformly mixed layer of Au, Ni, Ge, Ga and As. From the above discussions it follows that it is highly probable that some of the elements have formed several intermetallic compounds.

The X-ray diffraction results for the ion implanted and annealed contacts are shown in Fig. 5.18. As explained in the previous section, the peaks indicated by (vi) are caused by either Ni-As(Ge) or Ni_2GeAs. The rest of the X-ray diffraction profile consists of ß-Au-Ga (v), GaAs (iv) and Ni-Ge (vii) peaks. It is

Digitised by the Department of Library Services in support of open access to information, University of Pretoria, 2021

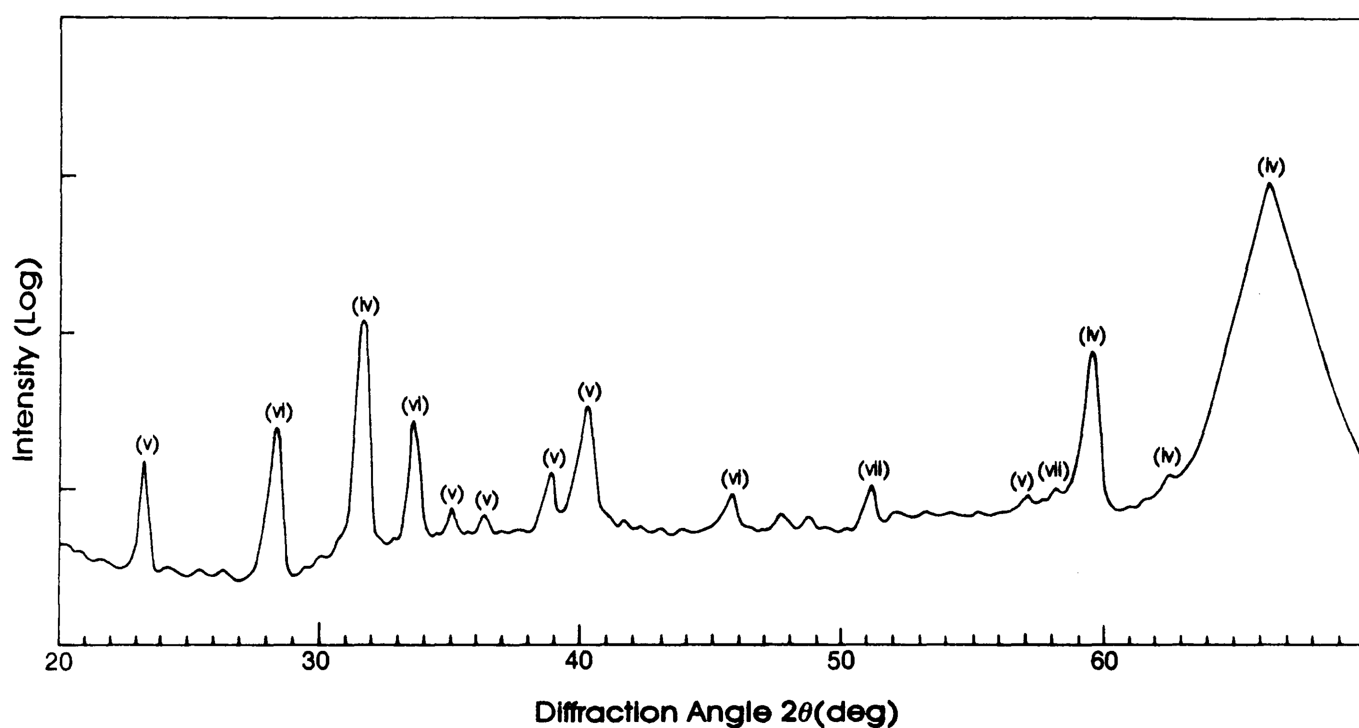

Figure 5.18: X-ray diffraction spectra obtained from the ion implanted and 450 °C annealed contacts (10 minutes). The respective peak indexes are explained in the text.

Digitised by the Department of Library Services in support of open access to information, University of Pretoria, 2021

interesting to note that the Ni-Ge compound was not observed in the AES and SIMS investigations. Thus, from the above results it is evident that the AES, SIMS and X-ray diffraction technique form a very powerful combination for investigating metallization/ GaAs interactions.

Furthermore, it is interesting to note that the Au-Ge-As compound was not observed for the implanted and annealed contacts. It seems that this compound can be related to the poor surface morphology of the Au-Ge based contacts, given the results in the previous, and in this section. Thus, it is possible that the absence of the Au-Ge-As compound, and the uniformly mixed layer obtained for the ion-implanted contacts and/or the mixing of the interfacial layer, could contribute towards the better surface morphology. However, a compromise must be reached between the ion implantation range (influenced by the metallization layer thickness) and the specific contact resistance before this technique can be used productively for device purposes.

5.3. RESULTS OF CONTACTS ON n-TYPE InP

InP has become an important III-V semiconductor in the opto-electronic field and because of its use in TED's [Tr 78], Schottky barrier FET's [Gl 78 and Ba 75], MISFET's [Ka 80], solar cells [Tu 80] and IR lasers [Hu 78]. These devices require low contact resistance and well-defined ohmic contact regions. However, alloyed contacts to InP have the disadvantage of poor surface morphology and edge definition due to complicated reactions occuring at the metal-InP interface, even during the deposition process [Rh 88].

Furthermore, there is a serious problem in cleaning InP substrates prior to epitaxial growth or device manufacture. The reason for this is that thermal cleaning, which is very efficient for other semiconductors, is difficult to perform in this case because of the low thermal stability of InP. This treatment is impractical because the complete desorption of the oxidized InP surface is achieved at a temperature above the congruent

Digitised by the Department of Library Services in support of open access to information, University of Pretoria, 2021

evaporation temperature of InP [Fa 74]. Therefore, InP is subjected instead to various chemical cleaning procedures prior to the processing step.

In the remainder of this chapter the nature of the InP surfaces, as well as different metallization systems to n-InP will be discussed.

5.3.1 AES investigation of InP surfaces

In device processing it is important to understand the nature of the InP surface, since Schottky and ohmic contacts depend on the semiconductor surface. Various surface science techniques such as AES [Wi 75, Wa 83, Pe 83 and So 88], LEED [Wi 75 and Ts 80b], XPS [Be 81, Gu 84 and So 88], EELS [Tu 82 and Xi 87], RBS [Wi 82] and SIMS [Br 86b] have been used to study these properties. In this section, the results obtained for UHV cleaved, Ar^+ sputtered and chemically treated InP surfaces, investigated by means of AES and SEM, will be discussed.

Typical AES spectra for as-received, vacuum cleaved and Ar^+ sputtered InP surfaces are shown in Fig. 5.19. (Note that the AES results in this sub-section were obtained on a PHI 545 system). The Auger spectra for the vacuum cleaved InP were obtained from a (110) cleaved surface, while the rest of the Auger data was obtained from a (100) surface.

The spectra for the as-received sample (see Fig. 5.19(a)) shows C and large O Auger peaks due to hydrocarbon contamination and oxide formation on the InP. With AES it is not possible to determine the chemical composition of this native oxide, and even using XPS, contradicting compositions of this oxide(s) have been reported [Wa 83 and Gu 84]. For example, Guivarc'h et al. [Gu 84] observed not a single compound, but a mixture of different compounds.

The first derivative Auger signal very clearly signal shows changes in the P peak and to some extent changes in the In peaks, compared to those of the vacuum cleaved surface. The reason that

Digitised by the Department of Library Services in support of open access to information, University of Pretoria, 2021

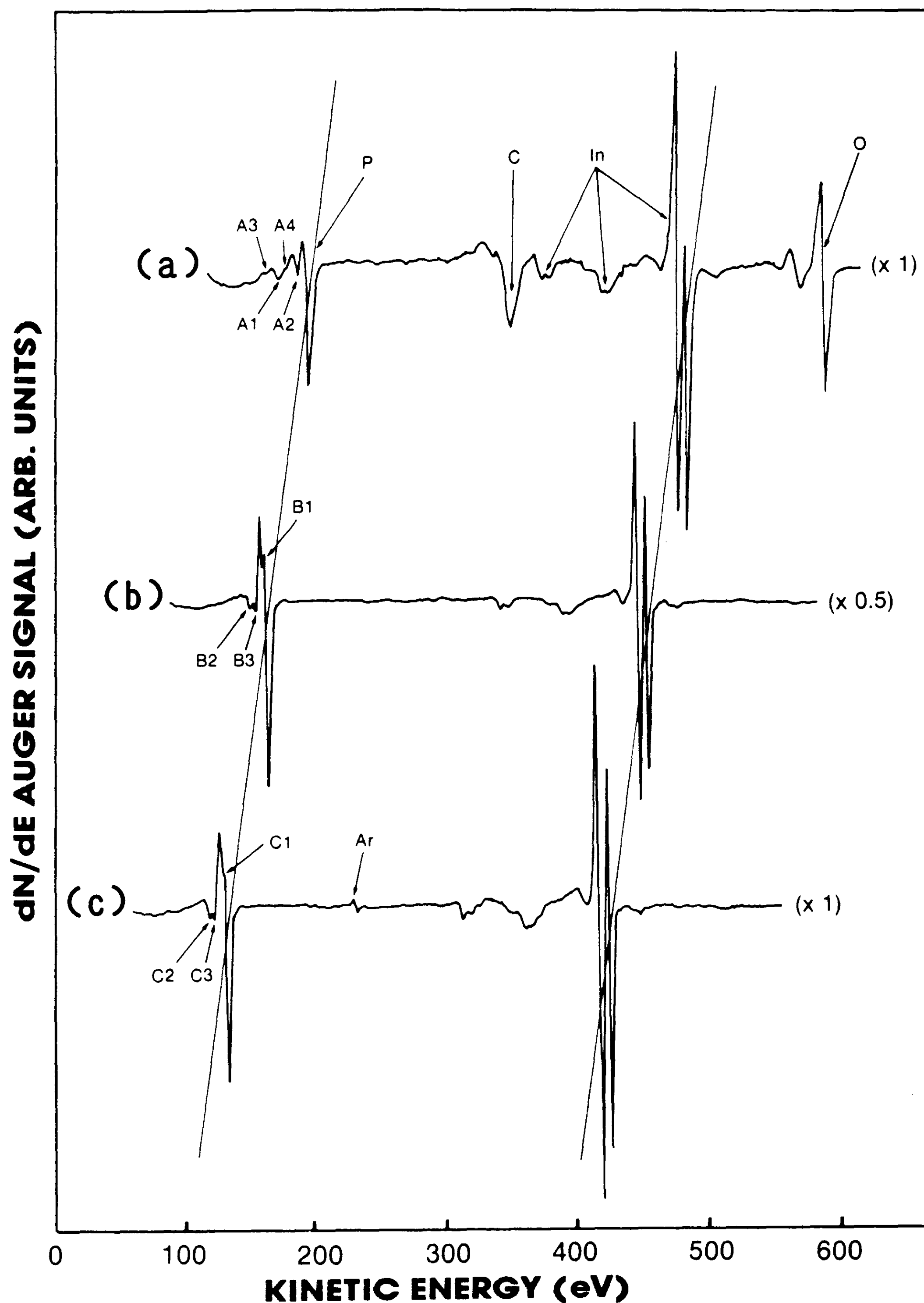

Figure 5.19: AES spectra of (a) as-received InP (100) surface, (b) vacuum cleaved (110) surface and (c) a (100) surface cleaned by Ar^+ sputtering. Note the changes in the In/P peak-to-peak ratio between the spectrum in (b) and (c). These spectra were obtained with a PHI 545 system.

Digitised by the Department of Library Services in support of open access to information, University of Pretoria, 2021

the P (120 eV) peak shows far more dramatic changes than those for the In peaks is that the LVV transition is more sensitive to the chemical environment than the MNN In transition [Ts 80b]. Furthermore, the resolution of the In doublet at 404 and 410 eV in (a) is poorer than that for the In peaks originating from the other surfaces (see Fig. 5.19(b) and (c)). In these cases the In peak at 410 eV has a higher negative excursion than that for the In peak at 404 eV, compared to Fig. 5.19(a). On all the highly oxidized InP surfaces, the In peak shown in Fig. 5.19(a) was observed. Furthermore, two additional smaller peaks with minima at 97 and 110 eV (A1 and A2) and two extra shoulders at 86 and 103 eV (A3 and A4) appear on the left hand side of the phosphorus 120 eV peak, compared to the vacuum cleaved (110) and Ar^+ sputtered surfaces. Freshly Ar^+ sputtered and vacuum cleaved surfaces were exposed to high purity oxygen gas and to air which were leaked into the vacuum system. With increasing exposures the Auger spectra of these surfaces tend to display the above-mentioned features in Fig. 5.19(a).

In order to compare the vacuum cleaved (110) surface with the (100) surface, two assumptions were made. Firstly, the vacuum cleaved (110) and (100) surfaces are assumed to yield the same respective Auger peaks as well as the same In/P peak ratios, if the surfaces are exposed to the same chemical treatment; an assumption which has been substantiated by work of Sodhi et al. [So 88]. The additional peaks at A1 and A2 correspond to the peak positions obtained by these authors on an oxidised (110) vacuum cleaved surface. It was suggested by Williams and McGoven [Wi 75] that these peaks represent multiple cross transitions of phosphorus and oxygen atoms. Secondly, the further assumption was made that the vacuum cleaved surface has a stoichiometric surface composition, because no changes from the initial In/P peak height ratio were observed with time, or from one analysis to another. According to Tsang et al. [Ts 80b] this latter assumption is substantiated by Fermi level and XPS measurements. Furthermore, one of the cleaved samples did not have a clean break along the (110) surface. Auger spectra taken from different points on the vicinal planes gave the same results as for the (100) and (110) surfaces.

Digitised by the Department of Library Services in support of open access to information, University of Pretoria, 2021

Using these assumptions, sensitivity factors for the P (120 eV) and In (404 eV) peaks were determined from the vacuum cleaved surface for a given set of analysis conditions. These conditions were maintained during the recording of all the Auger data obtained in this study. From the peak-to-peak heights in the differentiated mode, sensitivity factors calculated for P and In were 0,55 ± 0,04 and 0,78 ± 0,03 respectively for the PHI 545 system. However, for the PHI 595 system, the respective sensitivity factors for P and In were calculated to be 0,62±0,03 and 0,86±0,02. These factors were obtained by comparing the 351 eV Ag peak under the same experimental conditions.

A close inspection of the phosphorus peak (see Fig. 5.19(b)) of vacuum cleaved InP revealed two distinct features which are not reported in the P spectrum of the commonly used "Handbook of Auger Electron Spectroscopy" (HAES) [Da 78]. Firstly, a double minimum at 107 and 110 eV (B2 and B3 respectively) is visible to the left of the 120 eV peak. Secondly, a well resolved peak is observed at 115 eV (B1). Although it is not as well resolved in the other Auger spectra, this peak is still present for the chemically etched surfaces, while a shoulder is visible for the Ar^+ bombarded spectrum. The In/P peak ratio for the vacuum cleaved surfaces was 1,4±0,1. The P peak for the "as-received" samples was observed at 117 eV, but for the remaining spectra obtained in Fig. 5.19, this peak occurred at 120 eV. Except for the as-received Auger spectrum, no changes in the In peaks were observed, when compared to the HAES.

The Auger spectrum of 0,5 keV Ar^+ sputtered InP is shown in Fig. 5.19(c). After an equilibrium value for the In/P peak height ratio of 2,0±0,1 was reached, no change in the ratio with further sputtering was observed. The smaller peaks at 107 and 110 eV (C2 and C3) and the peak at 115 eV (C1) are not as well resolved. The same observations were made for both the (100) and (110) sputtered surfaces independently of the ion energy.

According to the above sensitivity factors, the sputtered surface region has a (40±2) at% P and (60±2) at% In composition. Thus, an indium enriched surface is obtained with Ar^+ bombardment,

Digitised by the Department of Library Services in support of open access to information, University of Pretoria, 2021

because of the different sputtering rates for In and P [Ts 80b and Pe 83]. It is important to note that the In surface concentration was calculated assuming a uniform distribution over the depth from which the Auger electrons originated. However, this is not the case since the concentration of the very top layer differs from that of the bulk. Thus, the actual surface concentration is actually much higher than 60 %, because the In signal detected originates from several layers and is averaged over the high surface value and the relative low bulk values. As a result, it is not possible to determine the outer surface composition of a sputtered InP surface accurately with AES. (This is true in general for any non-stoichiometric surface investigated with AES). In order to obtain more accurate measurements of the top surface layer, a surface sensitive technique such as ion scattering spectroscopy (ISS), which analyses only the first or second monolayers, has to be used. However, apart from the differences in the respective elemental concentrations calculated above, no differences were observed between the equilibrium composition of the (100), (110) and the vicinal InP surfaces after prolonged Ar^+ bombardment. This suggests that the Ar^+ bombardment amorphized the InP, thus preventing ion channeling effects from influencing the surface composition. This result is confirmed by the fact that InP is easily amorphized by Ar^+ bombardment [Wi 82]. Furthermore, it is also interesting to note that in our case no noticeable difference (apart from the standard variation from analysis to analysis) was obtained for the In/P peak ratio from surfaces sputtered with ion energies ranging from 0,5 to 5 keV.

According to Sodhi et al. [So 88], who used angle resolved XPS, the In/P peak ratio obtained was the same for 1 and 3 keV Ar^+ sputtered surfaces. Unfortunately, no indication of the Ar^+ sputter angle was given. However, according to Peacock [Pe 83], less depletion of surface phosphorus was observed as the energy of the normal incident Ar^+ was increased from 0,5 to 3 keV. The main difference between his experimental set-up and ours is that in our case the angle of the Ar^+ gun was 40° with respect to the normal of the sample. Peacock explained his preferential sputtering results in terms of ion channeling effects.

Digitised by the Department of Library Services in support of open access to information, University of Pretoria, 2021

Figure 5.20 is a scanning electron micrograph of a bombarded InP surface. The sample was subjected to 0,5 keV Ar^+ ions for 15 min (according to the In/P Auger peak ratio, an equilibrium value was reached after 12 min of sputtering). The surface is covered with small particles which are all of roughly equal cross section of between 30-90 nm. Auger analysis recorded immediately after the 15 min sputtering (see Fig. 5.19(c)), showed an indium-rich surface. The mechanisms for these structural effects, caused by low energy ion beams are not fully understood. According to Malherbe and Barnard [Ma 91] the mass difference between the In and P atoms is the major factor contributing to preferential sputtering of InP, while the effect of surface binding energies of the two atomic species is of a secondary importance. However, a detailed analysis of the models used to explain these effects is beyond the scope of the present work and can be found in existing publications [Ro 81, Gr 87 and Ma 91].

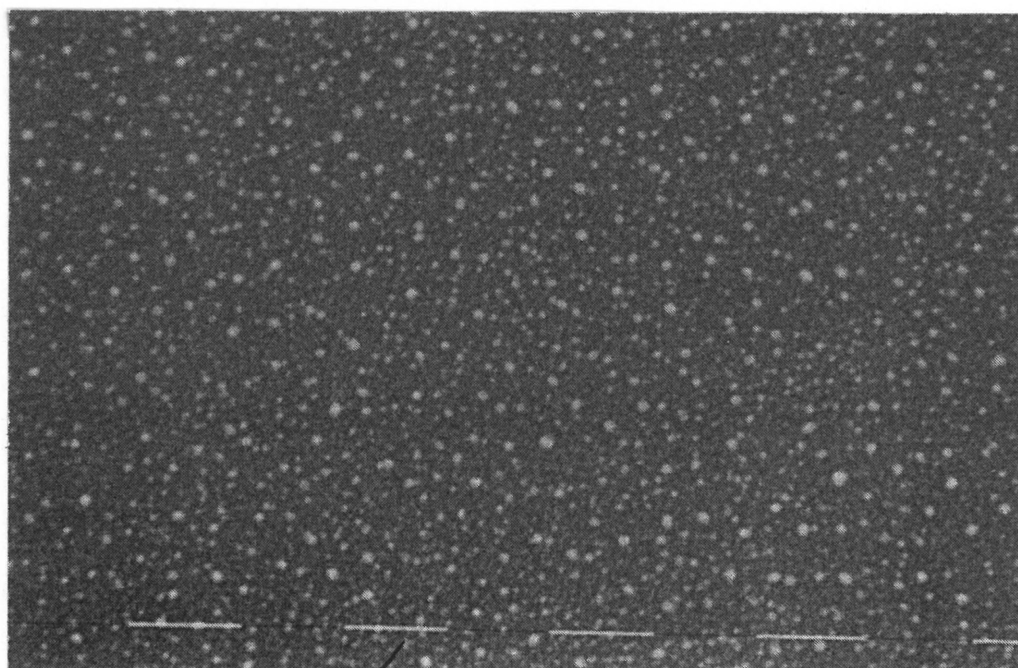

Figure 5.20: SEM photograph of InP (100) surface topography after sputtering with 0,5 keV Ar^+. (The marker represent 0,5 μm.)

Digitised by the Department of Library Services in support of open access to information, University of Pretoria, 2021

Figure 5.21 displays the Auger spectra of InP (100) surfaces etched in (a) $H_2SO_4:H_2O_2:H_2O_2$ (5:1:1) (b), Br/CH_3OH (1%) and (c) HF (10 %) solutions respectively. Apart from the P, C, In and O Auger peaks, spectrum (a) also shows a S peak. However, no surface Br or F was detected in the Auger spectra of (b) and (c). There is a noticeable decrease in the oxygen peak from (a) to (c), while the C peak increased from (a) to (c).

From the above spectra, it is clear that exposure of the InP surface to the $H_2SO_4:H_2O_2:H_2O$ (5:1:1) solution causes more oxidation than that experienced by InP etched in HF. This is clearly evident in the peaks to the left of the phosphorus peak which are somewhat similar to those in Fig. 5.19(a). However, no changes in the In peaks were observed (see for example Fig. 5.19(a)). The fewer oxides detected on the surface, the more closely the P peak resembles that of the vacuum cleaved surface. In Fig. 5.21(c) the phosphorus peak shows none of the small peaks observed in Fig. 5.21(a), apart from the two peaks at 107 and 110 eV. The In/P peak ratios of the etched surfaces are an indication that the etched surfaces are depleted of phosphorus, similarly to the sputtered surfaces (Fig. 5.19(c)). The HF etch produces a relatively oxide free surface (no evidence of the small peaks to the left of the P peak) although the level of carbon is higher than those of the other etchants. The same observation was made by Clark et al. [Cl 80]. As a result the HF etch was used prior to ohmic contact manufacture.

Several XPS studies have been published on etched InP surfaces and the formation of oxide films. The different phosphate species identified were $InPO_4$ [Cl 80], H_3PO_4 [Wa 81 and Br 86b] and P_2O_5 [La 81 and Wi 78]. With AES it is very difficult to distinguish between these oxidation species. There is, however a remarkable difference between the as-received (native oxidised species) InP surface and that of the chemically etched surface.

Digitised by the Department of Library Services in support of open access to information, University of Pretoria, 2021

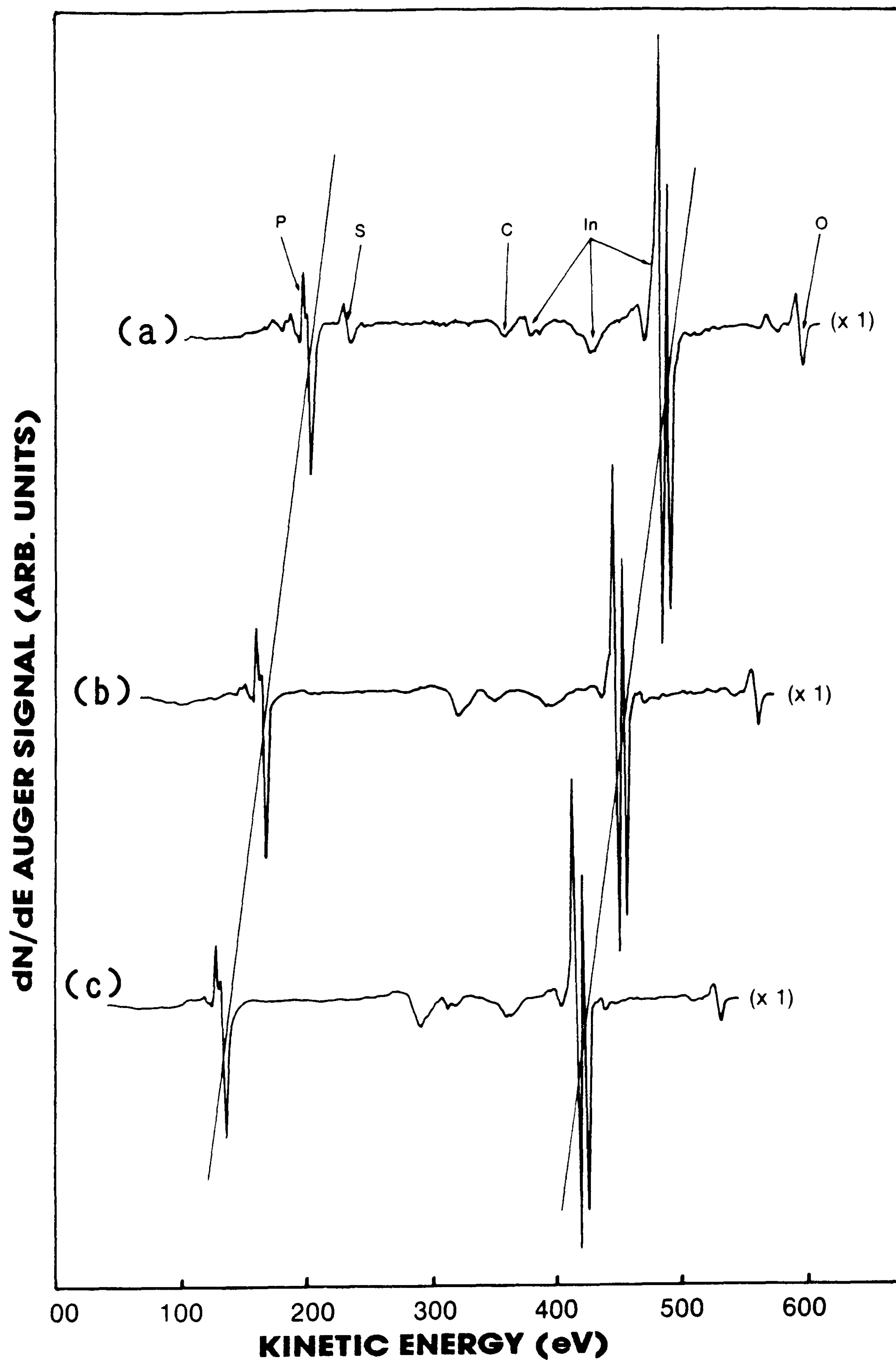

Figure 5.21: AES spectra of InP (100) after various chemical treatments: (a) $H_2SO_4;H_2O:H_2O$ (5:1:1), (b) Br/methanol (1%) and (c) HF (10%). This AES investigation was carried out in a PHI 545 system.

Digitised by the Department of Library Services in support of open access to information, University of Pretoria, 2021

5.3.2 Au-Ge/Ni contacts to n-InP

From the overview of ohmic contact systems to n-type GaAs and InP in Chapter 2, it is clear that the metal-InP interface has not been studied as intensively as the metal-GaAs interface, because InP may well be described as a semiconductor with more potential than applications at present. As a result, it is often taken for granted that the metal-InP interface reacts in the same way as other III-V semiconductors, such as GaAs. It is therefore not surprising that the majority of ohmic contacts to InP are based on the Au-Ge metallization system. However, Williams et al. [Wi 77] has shown that the surface chemistry of InP plays an important role in determining the electrical properties of a contact.

An example of the difference in behaviour of InP when compared to that of GaAs, is the fact that the lowest specific contact resistances are obtained below the Au-Ge eutectic temperature for contacts to InP but above the eutectic temperature for GaAs [Er 79, Gr 83 and section 5.3.5]. Therefore, the alloy regrowth mechanism responsible for ohmic behaviour in the Ni/Au-Ge/GaAs system does not apply to the Ni/Au-Ge/InP system.

Although ohmic contacts to InP is the subject of this section, the difference in the electrical behaviour of n-InP, when compared to that of n-GaAs for the same metallization system will also be discussed. The Au-Ge/Ni ohmic contact system to n-InP was examined by similar techniques as were used for n-GaAs in section 5.2.2. of this chapter. In this sub-section only preliminary results of the electrical and metallurgical properties of the Au-Ge/Ni film system will be reported, and will be discussed in more detail in section 5.3.5.

Figure 5.22 shows room temperature I-V curves for as-deposited and annealed Au-Ge/Ni contacts to n-InP. From the linear I-V measurements it is clear that the contacts are ohmic, even for the as-deposited contacts. (Contacts not intentionally heated).

Digitised by the Department of Library Services in support of open access to information, University of Pretoria, 2021

A similar result was also reported for Au-Sn-Au [Ke 81], Sb [Za 88] and Al [Is 87] contacts to n-InP. In the present study the as-deposited ohmic contacts retained their linear characteristics up to a current density of $\approx 4x10^2$ A/cm^2, beyond this value the resistance over the contacts increased to infinity, due to the destruction of the ohmic contacts. For annealed contacts the breakthrough current density increased to between 2-5x10^4 A/cm^2.

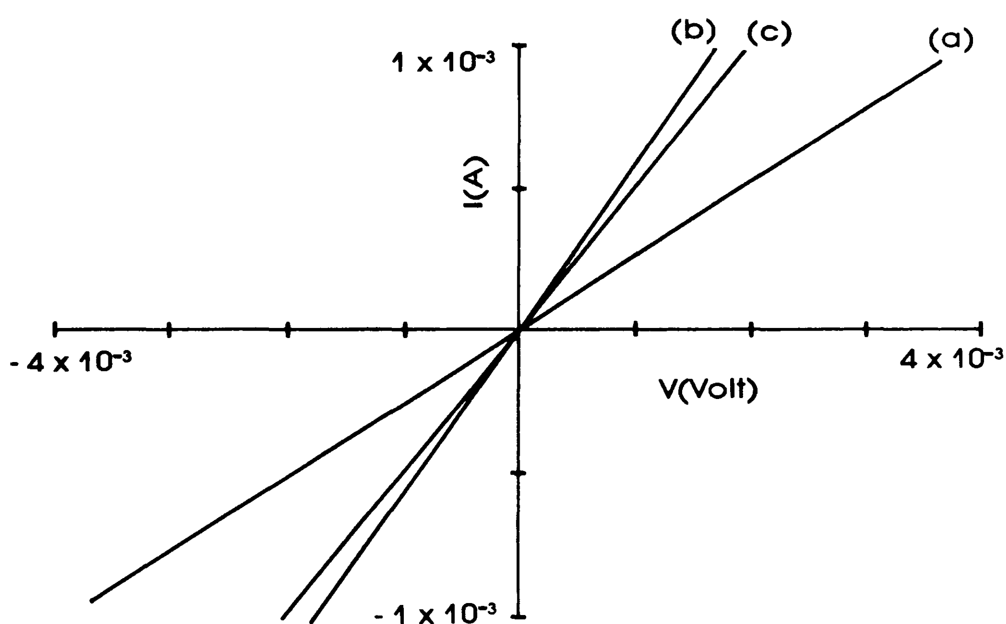

Figure 5.22: Room temperature I-V curves for (a) as-deposited, (b) 350 °C and (c) 450 °C annealed Au-Ge/Ni contacts to n-InP for 2 minutes.

It is interesting to note that the Au-Ge/Ni contacts to ~2x10^{18}cm^{-3} doped InP are ohmic prior to any annealing, while the same contact system to similarly doped GaAs only became ohmic after annealing at temperatures above 370°C. Two factors that may have contributed to this behaviour are discussed below by firstly considering the band structure and, secondly, the intermixing between the metal overlayers and the InP surface.

Digitised by the Department of Library Services in support of open access to information, University of Pretoria, 2021

It is a known fact that the classical approach of an ideal ohmic contact, as described in Chapter 3, is not observed in practice for InP and GaAs. Instead the barrier heights for metals to these two semiconductors are found to be largely independent of the respective metal work functions. For both InP and GaAs this is due to "Fermi level pinning" at the semiconductors surface, which occurs as a result of surface states. For n-GaAs the barrier height is roughly 0,8 eV for most metals, while for n-InP it is ~0,5 eV [Rh 88 and section 3.3]. However, contradicting this discussion are the observations of Chen [Ch 90] that the barrier height of metals deposited on an oxide layer grown prior to metal deposition on InP, is indeed dependent on the metal work function. However, from published results as well as experiments conducted in our laboratory, it may be observed that the barrier heights of metals deposited onto chemically cleaned InP do not follow the classical ohmic contact model [Rh 88, My 91 and section 3.3].

A further dissimilarity between these two semiconductors is the difference in depletion widths of the barriers under the same experimental conditions and carrier concentration. By using eq. 3.2, the calculated depletion width of InP is about 25% less than that for GaAs at zero bias. Hence, except for the fact that the barrier height for contacts to n-InP is roughly half that of GaAs, the depletion layer is also about 25% narrower. (This is schematically illustrated in Fig. 5.23.) Thus, the electrons have a much lower barrier to overcome and/or a narrower barrier to tunnel through, depending on the type of current transport mechanism. It is therefore not surprising that the measured specific contact resistance for Au-Ge/Ni contacts to InP is about a factor 5 lower than that of as-deposited contacts to GaAs [Ro 80 and this study]. This is also in qualitative agreement, (although not so drastically) with recent results published by Goldberg et al. [Go 88] for annealed In contacts to various n-type semiconductors. Their results emphasize the dependence of the specific contact resistance on the bandgap of the semiconductor (compare the bandgap of 1,35 eV for InP to that of 1,43 eV for GaAs) which can also indirectly be related to the barrier height of the semiconductor.

Digitised by the Department of Library Services in support of open access to information, University of Pretoria, 2021

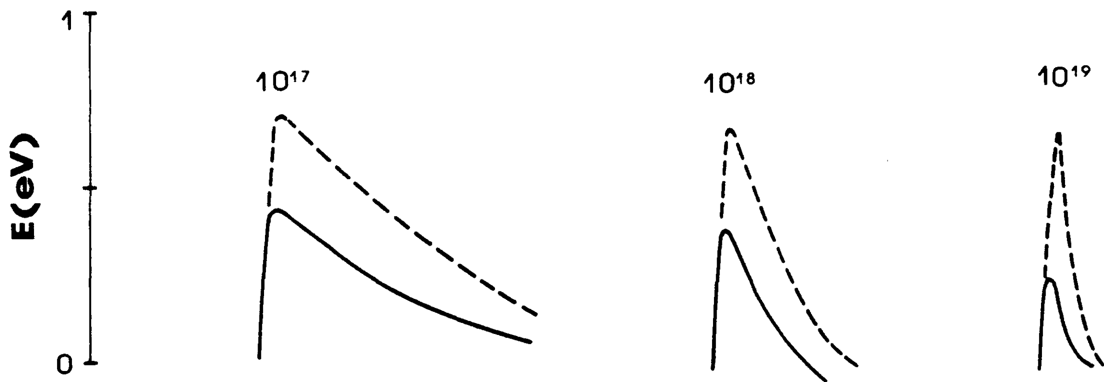

Figure 5.23: Schematic illustration of the difference in depletion widths and barrier heights at different doping levels for GaAs (---) and (InP) (——) respectively.

A further possible explanation for the as-deposited ohmic behaviour of contacts to InP can be found in the fact that the InP surface is In-rich after chemical etching as well as Ar^+ sputtering. A contact fabricated on such an In-rich surface, which is a degenerate n-type semiconductor [Sk 80, Tu 82 and Da 84], results in a reduced contact barrier height and width relative to that of the initial n-InP surface. It has previously been reported that a Schottky diode could not be made on such a surface and that evaporated metals made ohmic contacts [Sk 80 and Du 90b], which is in agreement with low barrier height contacts.

In the above discussion the band structure was considered. However, a second possibility also exists, which take into account the intermixing of the metal(s) and the InP during the deposition process. Intermixing between the metal overlayer and GaAs for as-deposited contacts are not known, despite the numerous reports of compound formation between metal overlayers

Digitised by the Department of Library Services in support of open access to information, University of Pretoria, 2021

with the InP surface that are published regularly. The most common example is the intermixing of Au and InP during the deposition step [He 77, Ch 78 and Br 81b]. (Although the as-deposited contacts are not intentionally heated, the measured substrate temperature during the deposition process rose to about 75°C for the experiments carried out in this study). The reason for this intermixing is the fact that the Au/InP interface is thermodynamically unstable at and above room temperature [Ts 86 and Pu 86] and will be discussed in more detail in the next sub-section. Recently it was also reported that Ni reacts readily with InP during the deposition step [Iv 88].

In Chapter 3 it was shown that for contacts to obey the ohmic tunneling contact model, a low barrier height, Φ_b, and high donor concentration N_d, are needed. However, this model is troublesome to apply quantitatively to all contact systems. The difficulty arises from the lack of precise knowledge of Φ_b or the effect of the interaction between the metal overlayer and InP on N_b. Furthermore, these mixed regions can cause different Schottky barrier heights for the same contact due to changes in the effective work function of the mixed and non-mixed regions, analogous to the model proposed by Freeouf and Woodall [Fr 81] for Au Schottky barrier contacts on compound semiconductors.

Although no evidence for such intermixing was observed with AES, it is possible that intermixing with the InP surface occurred below the detection limit of the AES conditions used during this study. Intermixing would cause low barrier height areas and result in localized ohmic regions. It is therefore reasonable to argue that upon annealing, a more uniform intermixing occurs with more localized ohmic regions. This also explains the increase of the breakthrough current density by a factor two for the annealed contacts.

From the discussion above it seems that the ohmic behaviour of the as-deposited Au-Ge/Ni contacts can be related to one or a combination of (a) a reduced contact barrier due to the indium-rich substrate surface and/or (b) the intermixing of the metal overlayers with the InP during the deposition step. This is in

Digitised by the Department of Library Services in support of open access to information, University of Pretoria, 2021

line with a comprehensive study by Williams [Wi 82b] on Schottky barrier formation to UHV cleaved InP surfaces where it was shown that barrier heights of ~0,15 eV are typical of contacts in which the metal overlayer react with the InP substrate.

Contacts to InP differ from those to GaAs, structurally as well as electrically. This is evident in the observation that Ni/Au-Ge/InP contacts which had been annealed at 450°C for 5 minutes revealed an increase of the contact diameter, when compared to the as-deposited contacts. The effect of contact spreading upon annealing is clearly visible in Fig. 5.24(b), while the photograph in (a) was obtained after evaporation of the contact, prior to any alloying step. The same observation has been made for Au-based contacts to InP by Keramidas [Ke 81 and Ke 82], Camlibel et al. [Ca 82] and Elias et al. [El 87]. This observation will have considerable implications for the fabrication of devices on InP.

AES spot analysis revealed Au on the edges of the annealed contacts. As a result, the spreading of the annealed contacts was related to the diffusion of Au on the substrate surface during the annealing step. In the following sub-section some of these and other aspects of the Au-InP interaction will be discussed.

5.3.3 Structural investigation of Au contacts to InP

Gold and gold-based alloys are extensively used as both ohmic and Schottky barrier contact material to InP, InGaAs, InGaAsP, etc. The stability of such contacts during device processing and their long-term reliability at moderate temperatures are of primary importance, as was observed in the above sub-section.

Before discussing the results, a brief summary of the most relevant observations reported in literature will be given. During recent years various techniques have been used to study reactions at the Au-InP interface, which ranged from optical microscopy [Ke 81, Ca 82 and El 87], Rutherford backscattering spectroscopy (RBS), transmission electron microscopy (TEM) [Pi

Digitised by the Department of Library Services in support of open access to information, University of Pretoria, 2021

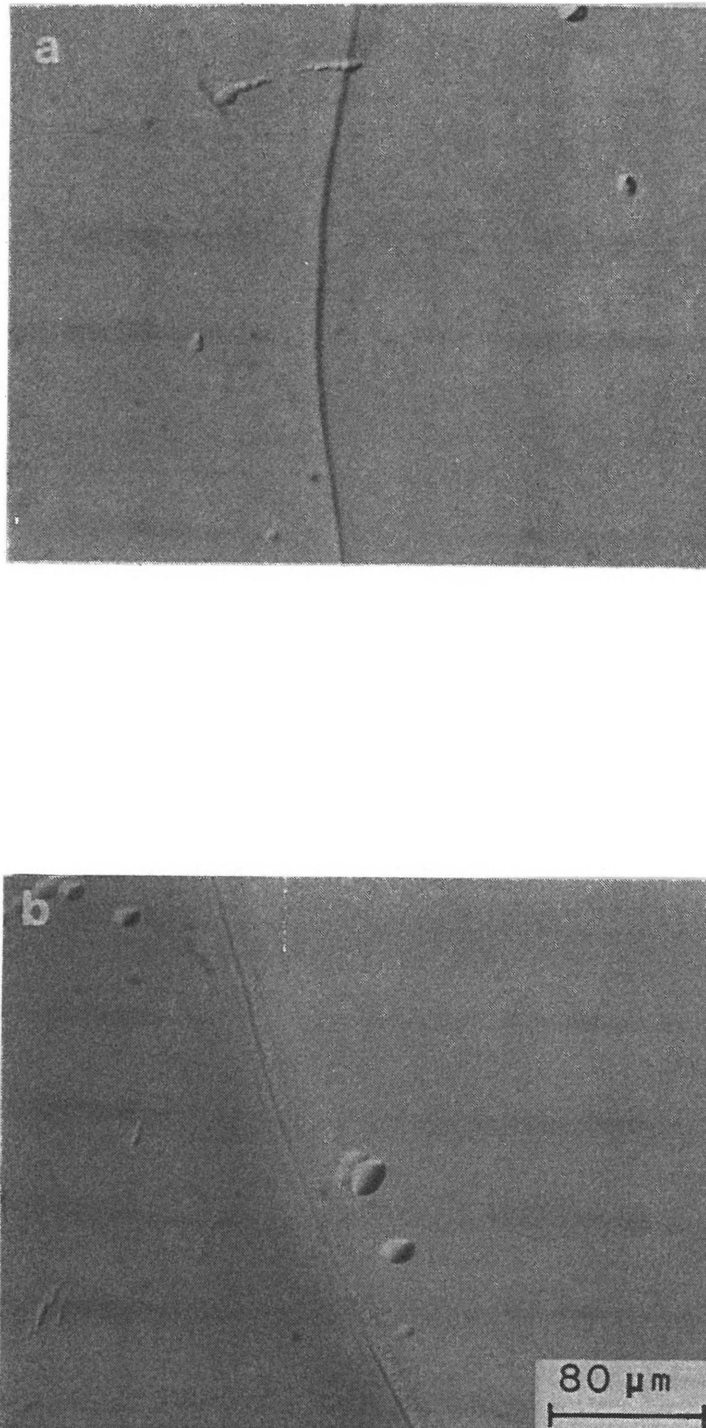

Figure 5.24: Optical photos of (a) as-deposited Au-Ge/Ni (150 nm/30 nm) contacts to InP and (b) after annealing at 450 °C for 5 minutes.

Digitised by the Department of Library Services in support of open access to information, University of Pretoria, 2021

81b and Ts 86], X-ray diffraction (XRD), energy dispersive X-ray analysis (EDX) [Pi 81b and Ts 86], Auger electron spectroscopy (AES) [Ba 81 and Wa 85], X-ray photoelectron spectroscopy (XPS) [Br 81b and Fa 89], secondary ion mass spectrometry (SIMS) [Wa 85 and Pa 87b], to the evolved gas analysis (EGA) technique [Mo 83 and Mo 86].

Some of the interesting observations published which relate the reactions of Au with InP upon annealing, are (i) colour change of the film [Pi 81b and Mo 86], (ii) diffusion of In into Au and Au into InP [Pi 81b, Wa 85 and Pa 87b], (iii) diffusion of P into Au [Br 81b, Ca 81 and Mo 86], (iv) formation of the Au_2P_3 compound [Pi 81b, Ca 82 and Fa 89], (v) formation of various Au-In intermetallic compounds [Ba 81, Wa 85 and Ts 86], (vi) lateral diffusion of Au on the InP surface [Ke 81, Wa 85 and El 87] and (vii) the evolution of gas-phase phosphorus species [Mo 83 and Mo 86]. Table 5.3 contains a summary of the various compounds that can be expected for Au contacts on InP at different temperatures, as determined by Hiscocks et al. [Hi 64] and Tsai et al. [Ts 86].

Table 5.3: Results of Au films on InP [Hi 64, Pi 81b and Ts 86].

Temp (°C)	Colour	Compounds[a]
as-deposited	yellow	α^b
295	yellow	α^b
330	yellow	α^b; Au_7In_2(ξ) Au_2P_3
365	pink	α^b; Au_7In_2 (ξ); Au_2P_3
395	pink	α^b; Au_7In_2 (ξ); Au_2P_3
410	pink	α^b; Au_7In_2 (ξ); Au_2P_3
450	silvery	Au_7In_3 or Au_9In_4 or Au_2In (γ); Au_2P_3; Au_3In_2 (ψ)
500	silvery	Au_7In_3 or Au_9In_4 or Au_2In (γ); Au_2P_3; Au_3In_2 (ψ)

a: Compounds identified from powder diffraction patterns of the films by XRD
b: Solid solution of In in Au.

In this sub-section AES and SEM were used to obtain information on the thermal reaction of Au-InP at elevated temperatures, but

Digitised by the Department of Library Services in support of open access to information, University of Pretoria, 2021

with special reference to the lateral or edge effects of this metal-semiconductor system.

Figure 5.25 shows SEM micrographs of an (a) as-deposited 1000Å Au contact and (b) the same contact after annealing at 450 °C for 10 minutes. The photograph in (c) is of the same sample as (b), but at a higher magnification (The uneven edge on the right-hand side of the as-deposited contact in (a) is due to the fact that a mechanical mask was used). From Fig. 5.25 it is clear that the contact diameter increases upon alloying, while a very uneven surface morphology appears. The darker areas in Fig. 5.25(c) appear as pink-coloured islands, surrounded by uneven silvery regions. The change in colour is probably due to different phases that exist between Au and InP, as is evident from Table 5.3.

The relative spreading rate of the contacts annealed at 450 °C was about 4 μm/min. However, noticeable lateral spreading was only observed for contacts annealed above 400 °C, while the most dramatic edge effects were visible between 430-500 °C annealing. At 500 °C and above the contact "disappears". This effect will be discussed in more details in a later paragraph.

AES spot analyses, depth profiles and line scans were used to obtain information of the Au/InP system after annealing at 450 °C for 10 minutes. According to AES spot analyses the pink coloured regions indicated an approximately 10% higher P concentration together with a lower In concentration than the surrounding silvery areas. The difference in the two coloured regions are clearly illustrated by the relevant depth profiles in Fig. 5.26. In Fig. 5.26(a) the depth profile of a silver coloured region is shown, while the depth profile of a pink area is illustrated in Fig. 5.26(b). The difference in the relative elemental distributions is clearly visible. These profiles can be related to a predominantly Au-In rich area (Fig. 5.26(a)) or a predominantly Au-P rich area (Fig. 5.26(b)), as detailed in Table 5.3. In both depth profiles a higher P than In concentration is observed at the interface region.

Digitised by the Department of Library Services in support of open access to information, University of Pretoria, 2021

(a)

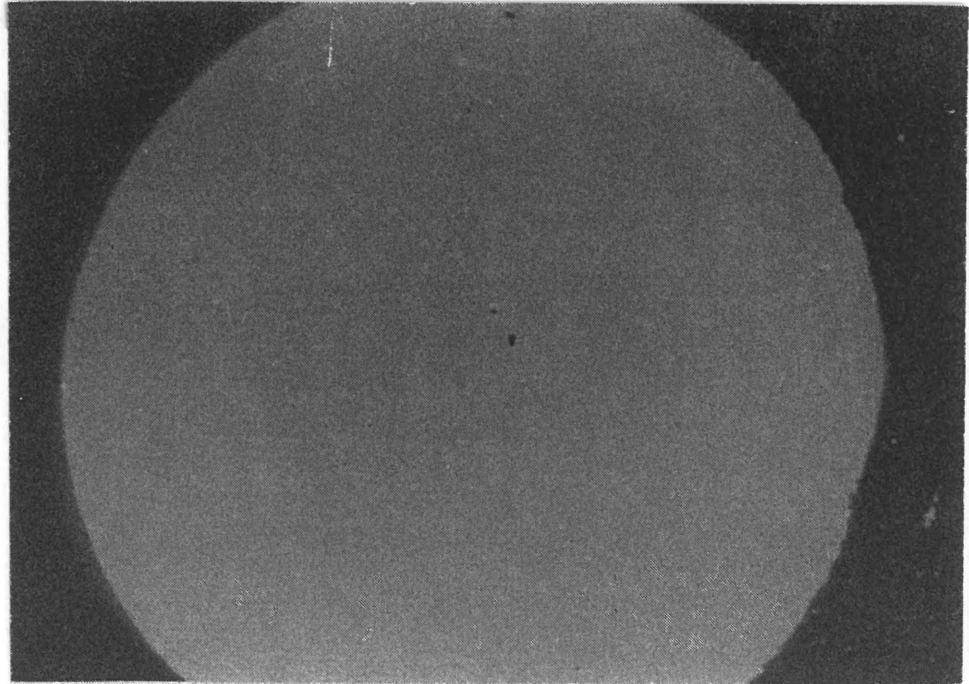

(b)

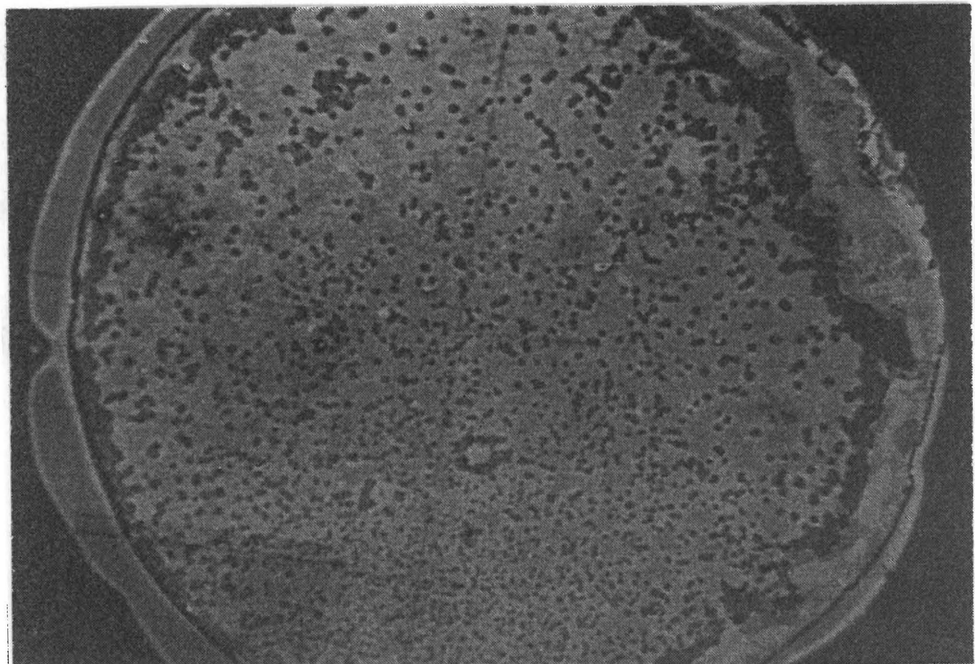

120 µm

Digitised by the Department of Library Services in support of open access to information, University of Pretoria, 2021

(c)

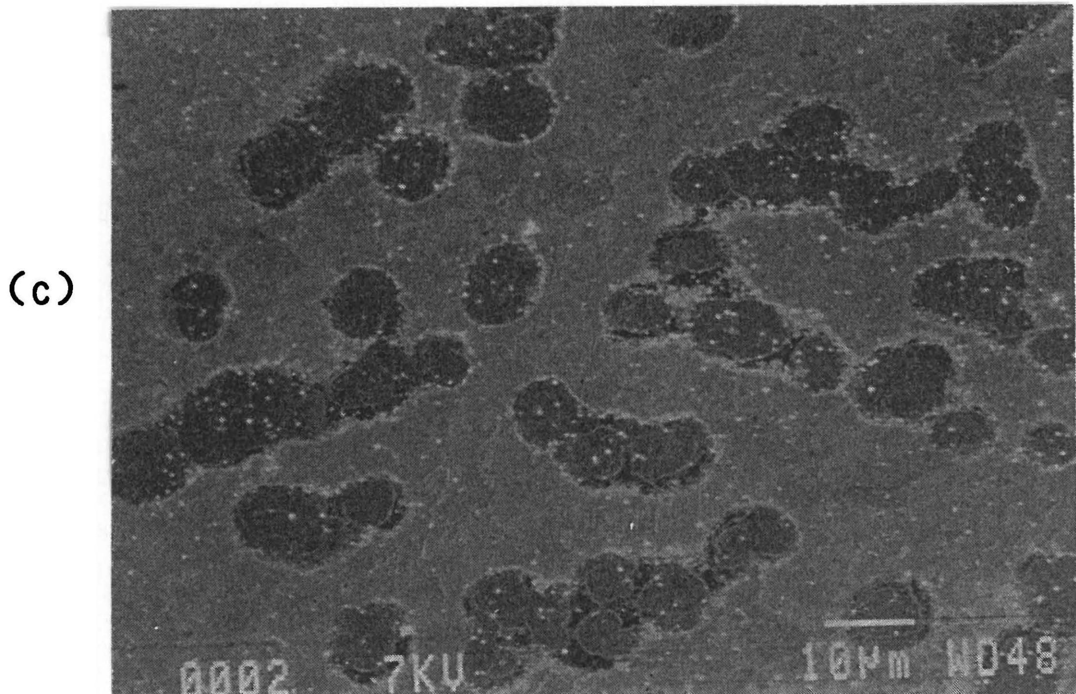

Figure 5.25: SEM micrographs of a 1000Å thick (a) as-deposited Au contact, (b) the contact after annealing at 450 °C for 10 minutes and (c) same as (b), but at a higher magnification.

Figure 5.27 shows elemental linescans obtained from an Au/InP contact edge region (a) after ±2 minutes and (b) after ±15 minutes of sputtering with 1 keV Ar^+ ions. For the linescans an electron beam with diameter in the order of 0,5 μm is scanned in a straight line over a specific region, while the relevant Auger signals are detected.(Only the Au, In and P scans are shown in Fig. 5.27, because no contamination was observed after ±15 minutes of sputtering).

According to Fig. 5.27, it is interesting to note that at the outer surface of the contact, the In and Au linescans follow each other very closely, while the P shows only in some cases correlation with Au. The Au spreading at the edge of the contact is also observed in the Au line profile, if this scan is compared with an as-deposited Au contact on InP (see Fig. 5.28). It is therefore clear that if no spreading is experienced, a much sharper edge of the elemental linescans is observed.

Digitised by the Department of Library Services in support of open access to information, University of Pretoria, 2021

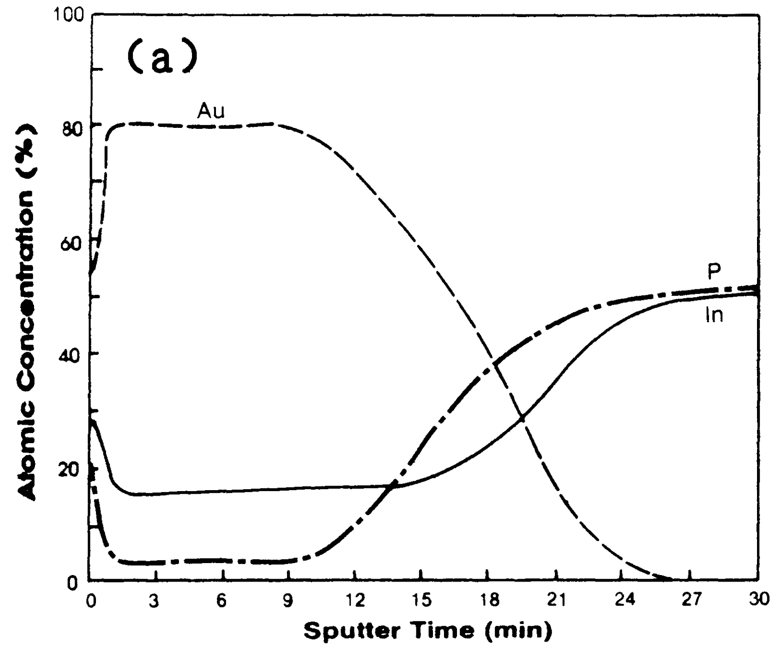

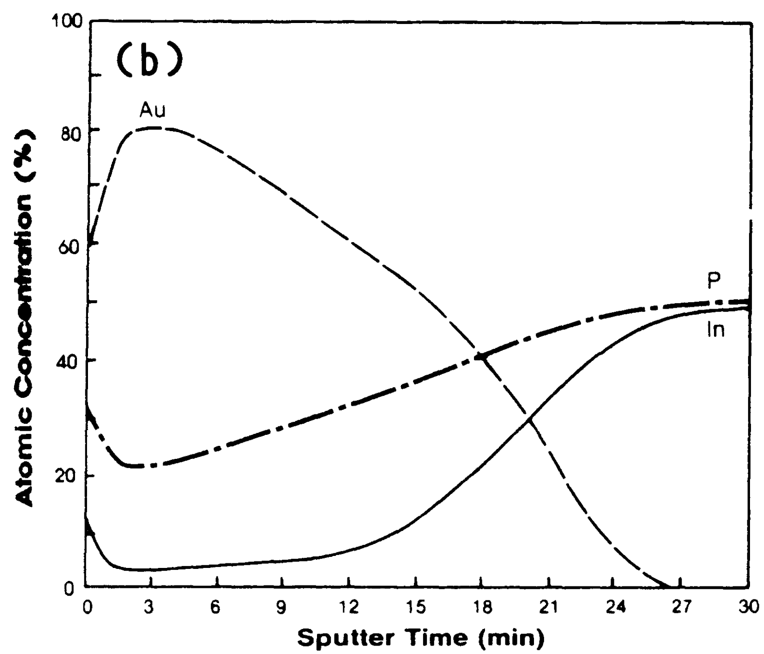

Figure 5.26: AES depth profiles of the (a) silver and (b) pink areas respectively.

Digitised by the Department of Library Services in support of open access to information, University of Pretoria, 2021

According to Fig. 5.27(b) a different pattern in the elemental profiles is observed after approximately 15 minutes of sputtering. From these results it is clear that the Au and P linescans coincide, while the In cannot be related to the other two elements.

It is believed that according to the results presented above for the Au contacts annealed at 450 °C, the following model can be proposed. The interface region between the InP and the Au consists mostly of Au-P phases, while the outer surface of the contact contains mostly Au-In rich phases (silver colour), together with Au-P phases (pink colour) which extend to the outer surface. It seems as if the P atoms initially stay at the interface, while the In atoms are distributed through the Au layer to the outersurface. This effect can be related to the fact that phosphorus is nearly insoluble in Au [El 65] and therefore will not diffuse through the Au, but rather form a compound at the interface. On the other hand, a solubility of 10 % has also been reported for phosphorus in gold [Ha 58 and El 65]. Further, this annealing temperature approximately coincides with the lowest eutectic melting point of the Au-In binary system at 451 °C [Ha 58]. The Au-In liquid phase therefore results in the degradation of the contact morphology upon cooling.

It is believed that the most frequently observed Au-P phase, viz. the Au_2P_3 compound, is formed here, while several Au-In compounds are also possible (see Table 5.3). Therefore, with the P accumulation and resultant Au_2P_3 phase that formed at the interface, it can be argued that the interdiffusion of the Au/InP system is controlled by this interfacial phase. From the observations reported above for contacts annealed at 450 °C a schematic illustration of the model is shown in Fig. 5.29.

Digitised by the Department of Library Services in support of open access to information, University of Pretoria, 2021

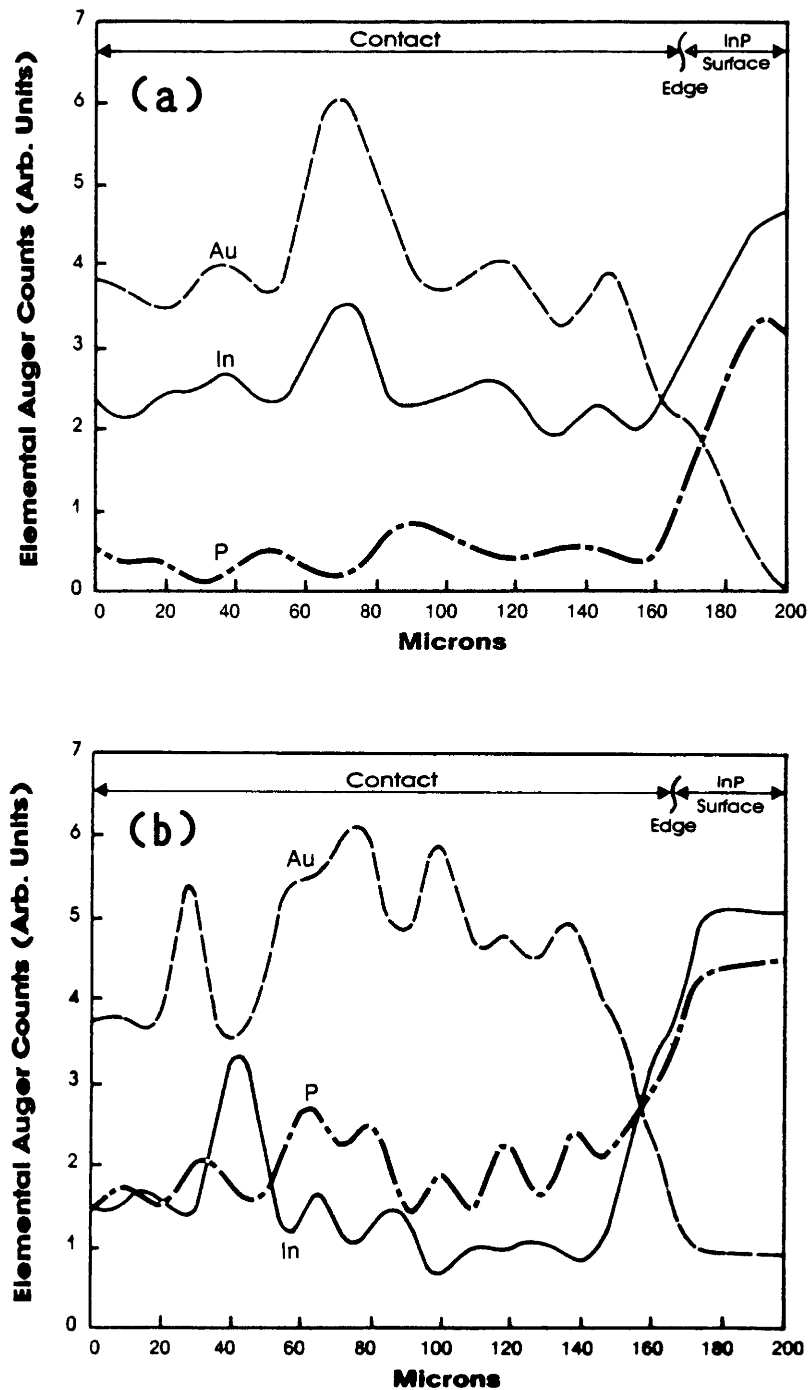

Figure 5.27: **Auger linescans of Au, In and P after (a) ±2 minutes and (b) ±15 minutes of Ar^+ sputtering.**

Digitised by the Department of Library Services in support of open access to information, University of Pretoria, 2021

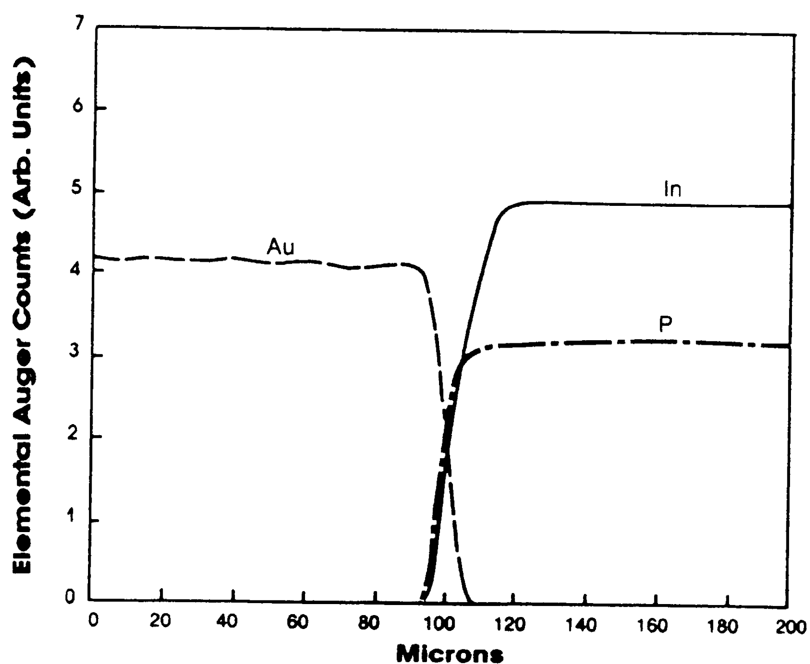

Figure 5.28: Auger linescans of an as-deposited Au contact on InP.

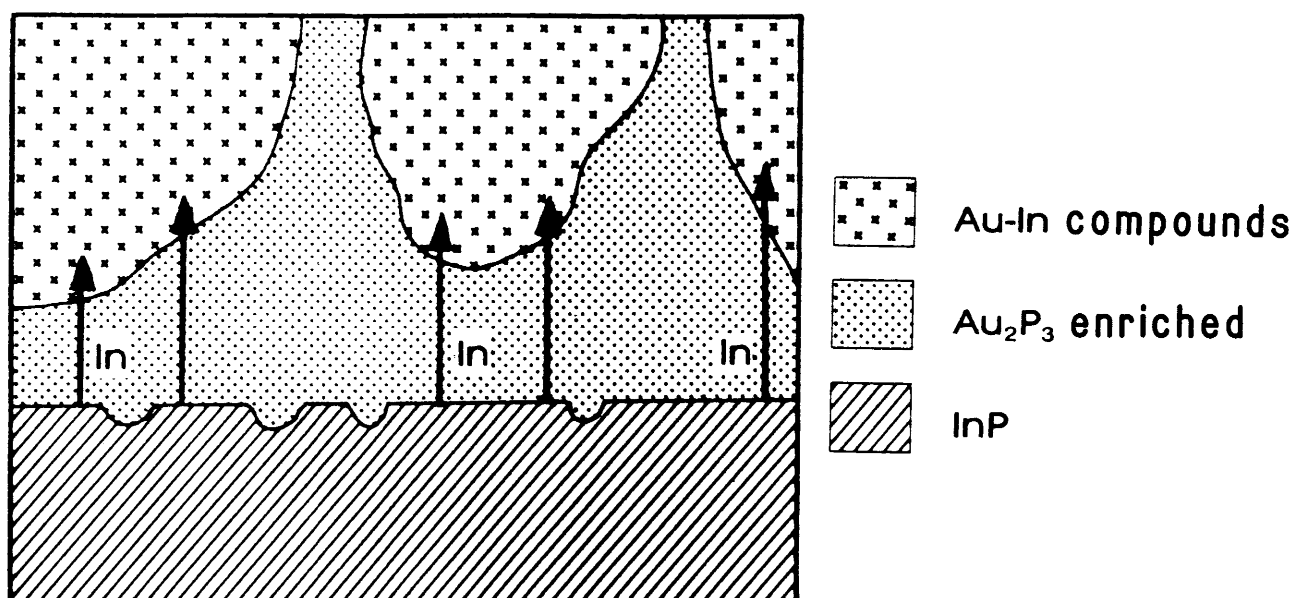

Figure 5.29: Schematic illustration of proposed structure for an Au contact to InP after annealing at 450 °C.

Digitised by the Department of Library Services in support of open access to information, University of Pretoria, 2021

The surface of Au contacts annealed at 500 °C for 10 minutes, had a silvery colour. The morphology was rougher compared to the contacts annealed at 450 °C, with square islands ("balling up" regions) as shown in Fig. 5.30. It is interesting to note that the squares are all orientated in the same direction with approximately 10 μm sidelengths. Figure 5.31 shows typical AES point analysis obtained on (a) the edge of a square island (on a "balling-up" region) and (b) on the surrounding areas.

From the AES spectrum in Fig. 5.31(a) it is evident that Au and P are the dominant elements present on the "balling-up" areas. The relative concentrations for these regions are ±50% Au, ±30% P and ±20% In, while the respective elemental concentrations for the surrounding areas are ±15%, ±15% and ±70% (see Fig. 5.31(b)).

AES sputter analyses revealed that the "balling-up" areas (light regions in Fig. 5.30(b)) predominantly consist of Au and P, with hardly any In, while the surrounding regions elemental distribution change with depth (see Fig. 5.32). It follows from this depth profile that large amounts of In diffused through the Au layer and formed various Au-In phases in an In matrix on the outer surface of the contact. However, the interface region consists of a combination of Au-P and Au-In phases, while Au diffusion into the InP is also evident. This depth profile will be referred to in the following paragraphs. The micrographs in Fig. 5.30 further show that the indium-rich areas (surrounding areas) make out a higher percentage coverage than the P-rich regions ("balling-up" areas). As with the 450 °C annealed contacts, it is also assumed that the Au-P phase consists of an Au_2P_3 compound, while a number of Au-In compounds may also occur (see Table 5.3).

Digitised by the Department of Library Services in support of open access to information, University of Pretoria, 2021

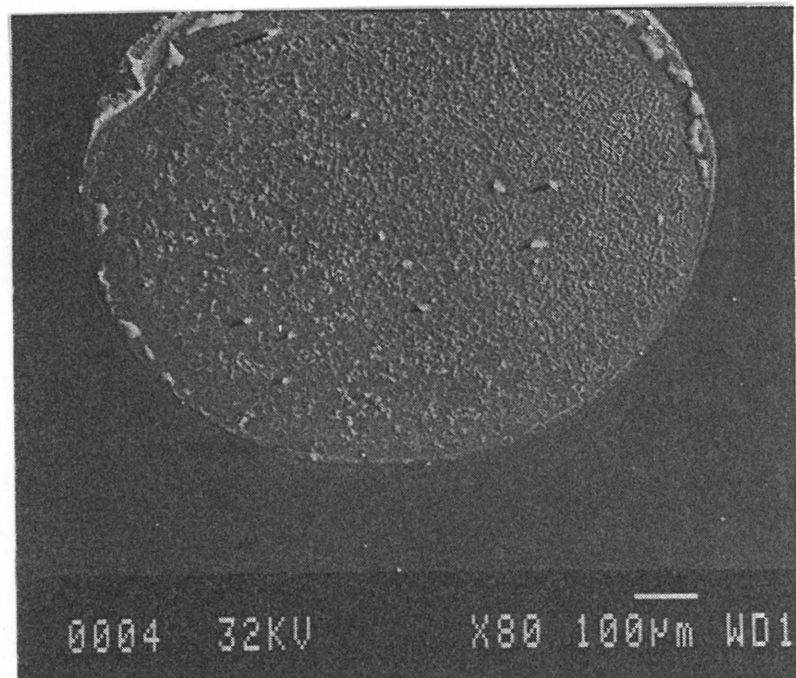

(a)

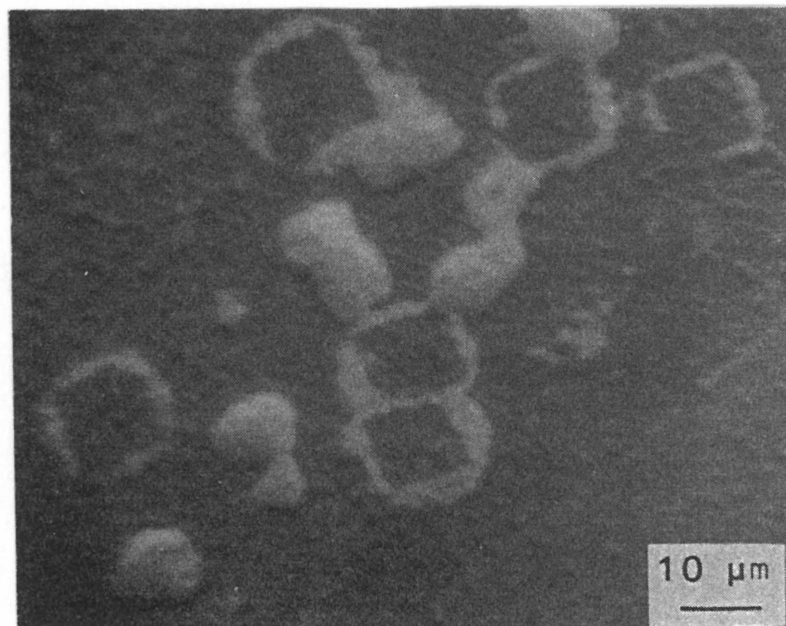

(b)

Figure 5.30: Photographs of an Au contact annealed at 500 °C for 10 minutes. The photo in (b) was obtained after ±4 minutes of sputtering.

Digitised by the Department of Library Services in support of open access to information, University of Pretoria, 2021

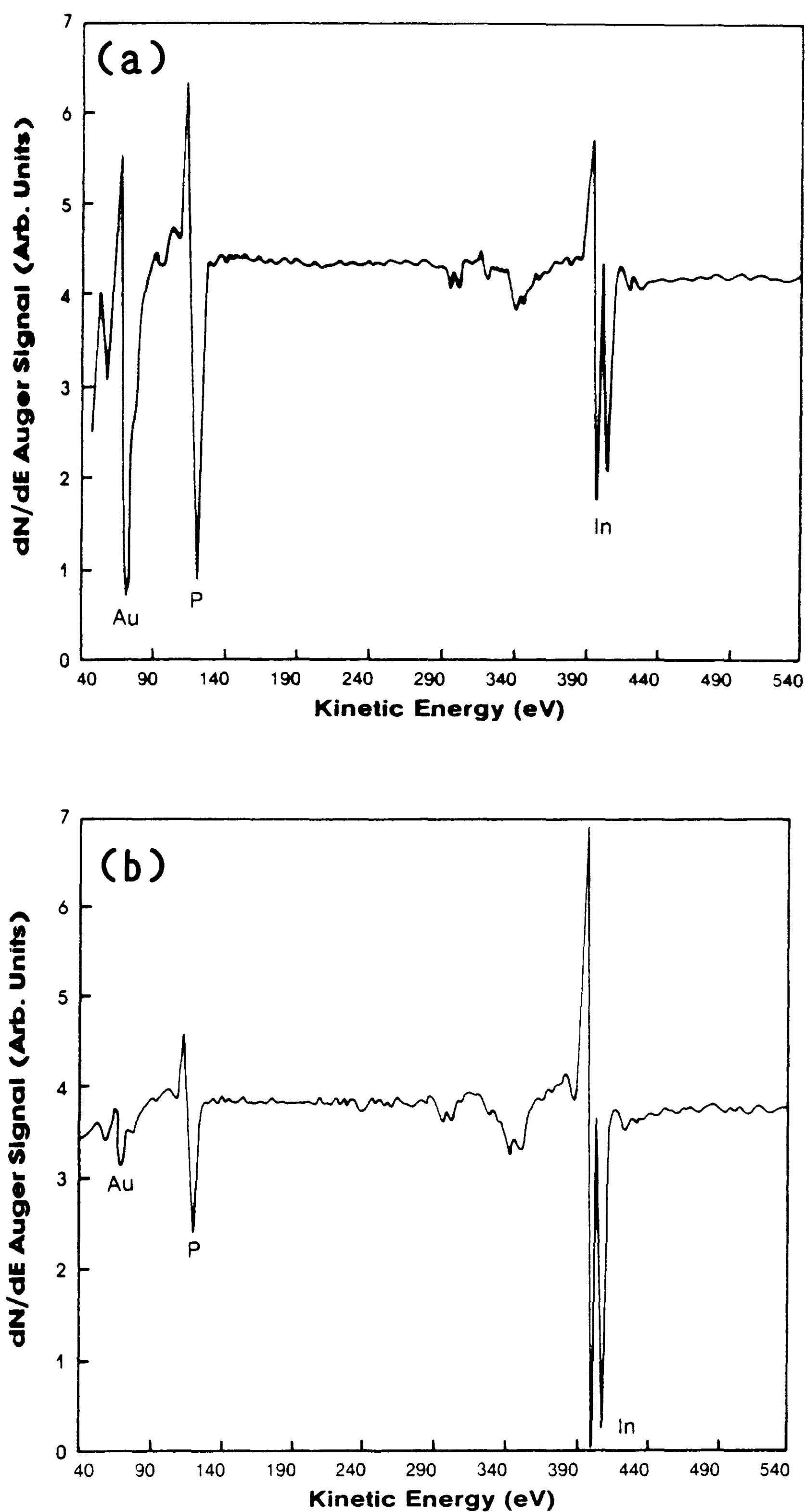

Figure 5.31: AES spectra from an Au contact annealed at 500 °C for 10 minutes. The spectrum in (a) was obtained from the edge of a square island and (b) from a spot on the surrounding area.

Digitised by the Department of Library Services in support of open access to information, University of Pretoria, 2021

Except for the morphological change observed between 450 °C and 500 °C annealing, a "swallow-hole" occurred on the whole area where the Au contact was originally evaporated, after annealing at 500 °C. The same effect was observed for the contacts annealed at 450 °C, but with a much shallower "swallow-hole". Figure 5.33(a) illustrates this effect very clearly for a 500 °C annealed Au contact. This micrograph was obtained with a very shallow angle between the secondary electron detector and the contact surface, in such a way that the shaded area is the bottom of the "swallow-hole". The step between the "swallow-hole" and the InP surface is clearly visible in the middle of the photograph. Figure 5.33(b) is a close-up view of this step, which is in the order of 10 μm. The latteral diffusion of the Au is also visible on the InP surface.

In order to explain this effect it is important to consider the thermodynamics of the reaction between Au and InP. According to Wada [Wa 85] and Williams et al. [Wi 78b] the reaction

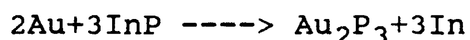

$$2Au+3InP \longrightarrow Au_2P_3+3In$$

has a positive heat of formation of +1,73 eV/mole. Thus, the Au_2P_3 compound is significantly less stable than InP. As a result, when annealed at 500 °C, the Au_2P_3 will start to sublimate, with the resultant diffusion of P to the surface. The surface P can interact with oxygen to produce P oxides, which are volatile. The same Au is again available to react with the InP and the process is repeated. Thus the P is actually eroded away from the InP, as is clearly observed in the depth profile in Fig. 5.32. (Compare the depth profile in Fig. 5.32 with the profiles in Fig. 5.26(a) and (b).) This eroding process also caused some free In and as a result the "swallow-hole" occurred. It must also be noted that a lower decomposition rate of InP at 450 °C

Digitised by the Department of Library Services in support of open access to information, University of Pretoria, 2021

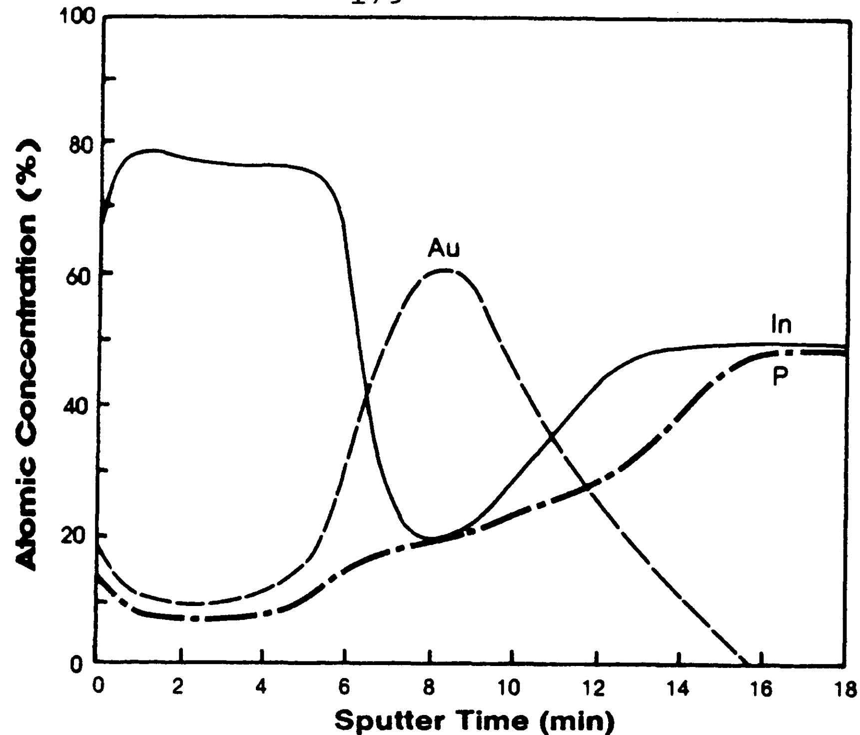

Figure 5.32: AES depth profile from a spot on the surrounding areas.

annealing is obtained when compared to that at 500 °C annealing. Therefore, the probability of the substrate to interact with Au also increases.

The exact origin of the squares observed in Fig. 5.30 is not known. However, it is to be noted that the squares which originally consisted of predominantly circular Au-P phases (at 450 °C), developed into these perfect squares. It seems therefore that the sublimation starts from the middle of the circular areas and develops gradually away in the form of a square in certain areas. This is in line with the observations of Sartorius et al. [Sa 88b] that the degration of InP is related to the volatilization of phosphorus upon heating. Further, this thermal degration of InP occurs inhomogeneously [Sa 88b]. The squares indicate a congruent evaporation at 500 °C. However, this is in contrast with the results of Mojzes et al. [Mo 86] and

Digitised by the Department of Library Services in support of open access to information, University of Pretoria, 2021

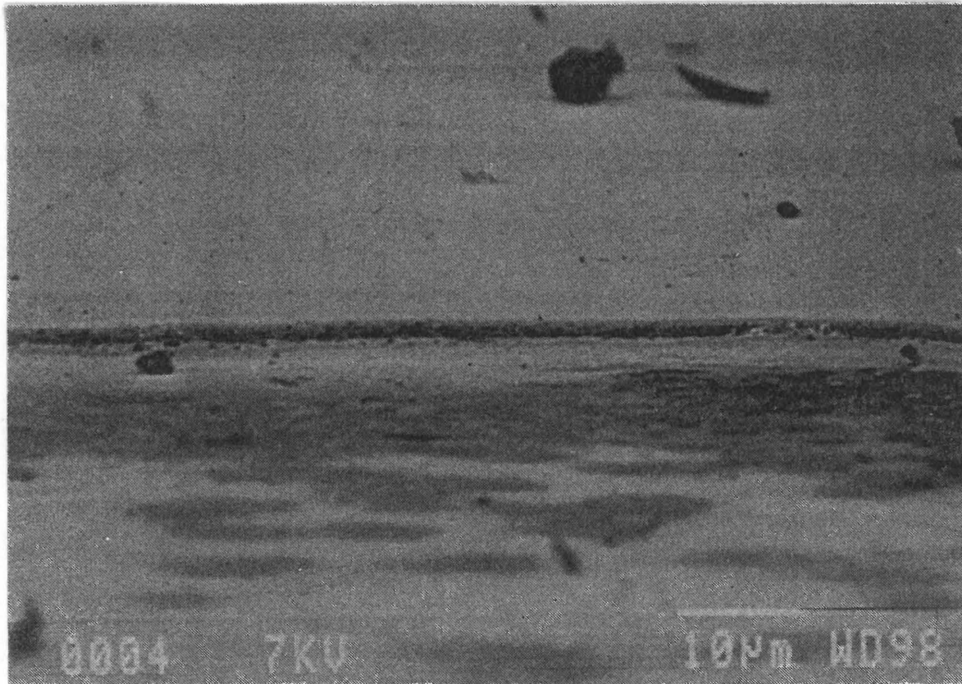

(a)

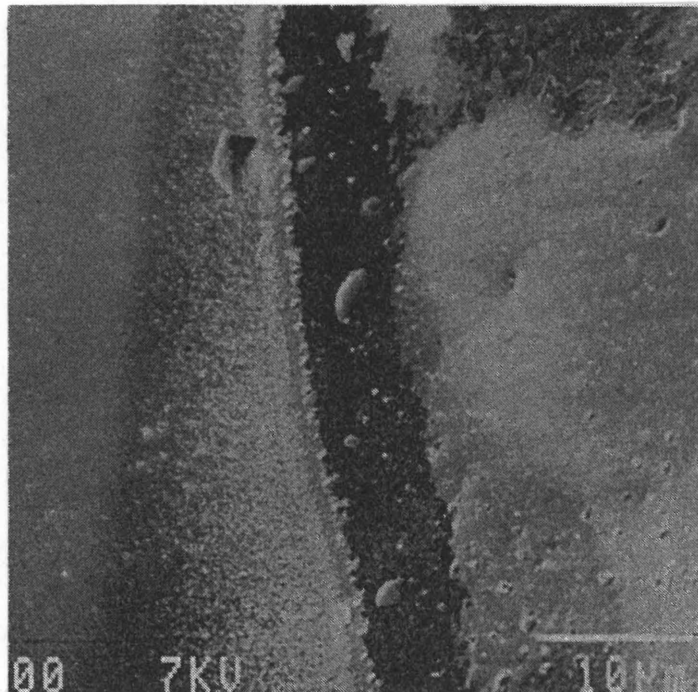

(b)

Figure 5.33: SEM micrographs of a "swallow-hole" which formed on the same area where the Au contact was originally evaporated, after annealing at 500 °C for 10 minutes. The micrograph in (a) was obtained in such a way that the shaded area is the bottom of the "swallow-hole". A close-up view of the step between the "shallow-hole" and the InP surface is shown in (b).

Digitised by the Department of Library Services in support of open access to information, University of Pretoria, 2021

Fatemi et al. [Fa 89], in which they reported non-congruent evaporation of In and P. This contradictive observation cannot be explained, but serve to illustrate that this topic is indeed a very complex one.

Based on the results presented above, it is important to keep in mind that these effects can also influence the stability of Au-based contacts to InP. However, it was reported that these problems can be reduced by utilizing very thin Au layers [Wa 85 and Mo 86]. In this way the decomposition of the semiconductor is decreased due to the fact that less Au is available to interact with the P at the substrate surface. Ideally it should be advantageous for device purposes to move away from Au-based metallization systems, or to prevent Au to react with the InP substrate by means of an effective diffusion barrier. The following sub-sections dealt with such metallization systems.

5.3.4 Ag based contacts to n-InP

From the above results of Au and Au-Ge contacts to InP it is clear that these contacts will present serious problems in device fabrication. It was therefore decided to investigate a non-Au based metallization system such as In/Sn/Ag. This system was first used by Mills and Hartnagel [Mi 75 and Mi 79]. However, no structural investigations have been reported in literature on this system. In this sub-section the structural and electrical behaviour of this metallization system, when annealed at different temperatures, will be discussed. These investigations were performed by AES, SIMS, optical microscopy and I-V measurements.

A large amount of data was collected, but only the results for the as-deposited contacts, contacts annealed at 300 °C, 350 °C and 400 °C for 2 minutes will be presented.

Figure 5.34 shows the optical micrographs of these contacts. It is clear that the surface morphology changes dramatically with increasing temperature. At 300 °C (see Fig. 5.34(b)) the surface

Digitised by the Department of Library Services in support of open access to information, University of Pretoria, 2021

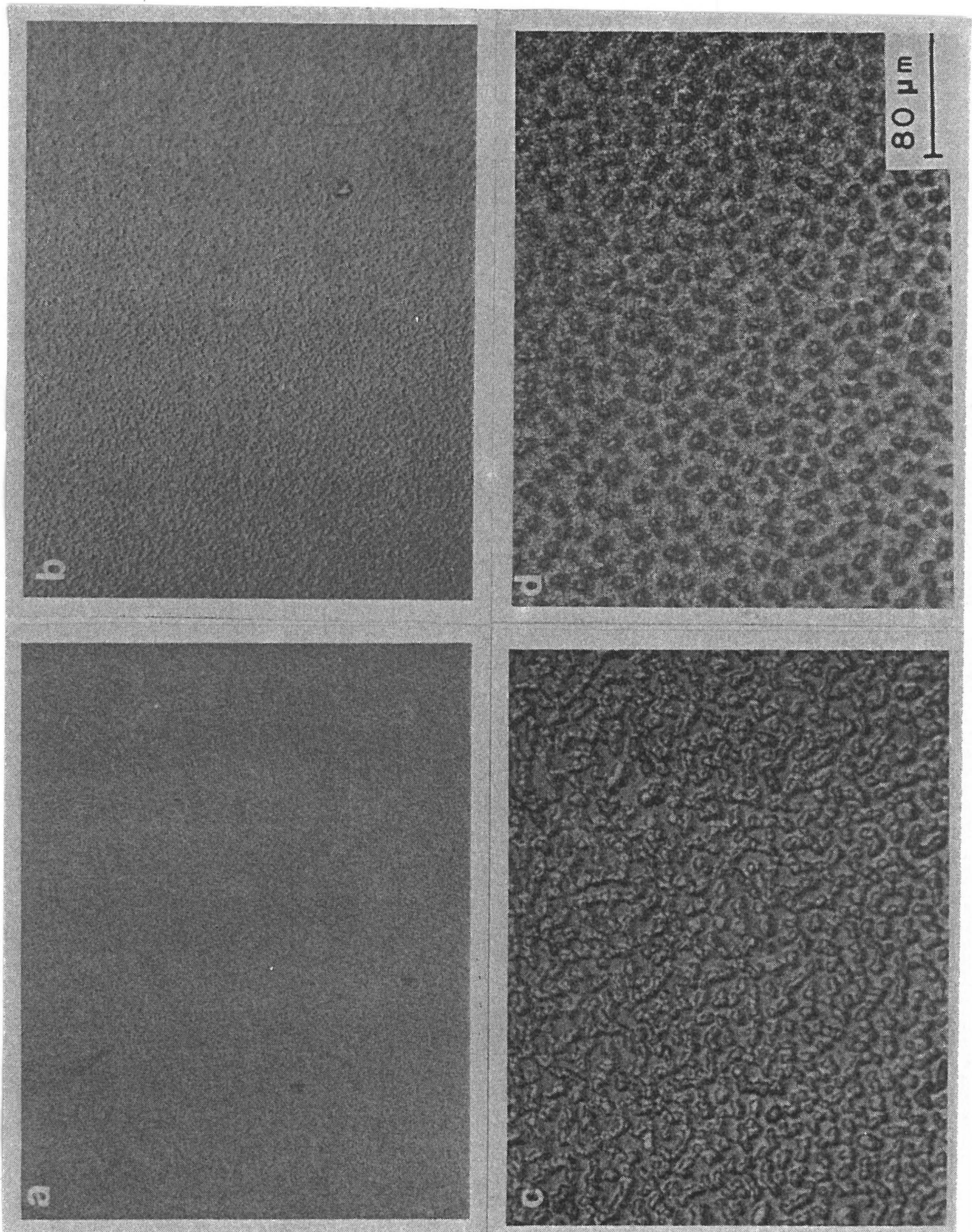

Figure 5.34: Optical micrographs of the Ag/Sn/In/InP metallization system (250 nm/75 nm/20 nm) for (a) an as-deposited contact, (b) contacts annealed at 300 °C, (c) 350 °C and (d) 400 °C for 2 minutes respectively.

Digitised by the Department of Library Services in support of open access to information, University of Pretoria, 2021

became very grainy. The morphology became worse at 350 °C (see Fig. 5.34(c)). The continuous grainy film observed at 350 °C disappears at 400 °C annealing (see Fig. 5.34(d)) and a highly irregular surface is formed with large inhomogeneous islands.

Figure 5.35(a) presents the Auger depth profile for an as-deposited contact. There are no sharp interfaces between the different metal layers and the substrate, which is an indication that diffusion has taken place, even without any deliberate heating. (As mentioned previously, the substrate temperature can increase to approximately 75 °C, during the evaporation process.) It is clear that the Ag has diffused through the Sn, as well as through the thin In layer to the substrate surface. Some Sn is also present on the InP surface. The movement of Ag and Sn is also evident in the SIMS depth profile shown in Fig. 5.36(a). Some of the In and Sn also moved out to the outer surface (see Figs 5.35(a) and 5.36(a)).

For the contacts annealed at 300 °C, the Auger and SIMS depth profiles indicate that a significant amount of Sn and In diffused towards the contact outer surface (Figs 5.35(b) and 5.36(b)). Outdiffusion of P is also noticeable as compared to the as-deposited samples. The Ag is now spread out uniformly through the metallization layer.

More In and Sn have diffused out towards the contact surface for the contact annealed at 350 °C, according to the profiles in Fig. 5.35(c) and Fig. 5.36(c), respectively. Auger point analyses revealed ±15% P and ±30% Ag atomic concentrations on the "valleys", in comparison with ±5% P and ±40% Ag atomic concentrations on the "hills". However, no dramatic differences were observed between the AES depth profiles obtained from the "hills" and the "valleys", except for the initial changes in the P and Ag concentrations. It must be noted that the SIMS depth profiles reflect an average elemental depth distribution, in comparison with the much more localized depth information obtained with AES. As a result, the differences in the "valley" and "hill" concentrations are not observed so easily with SIMS.

Digitised by the Department of Library Services in support of open access to information, University of Pretoria, 2021

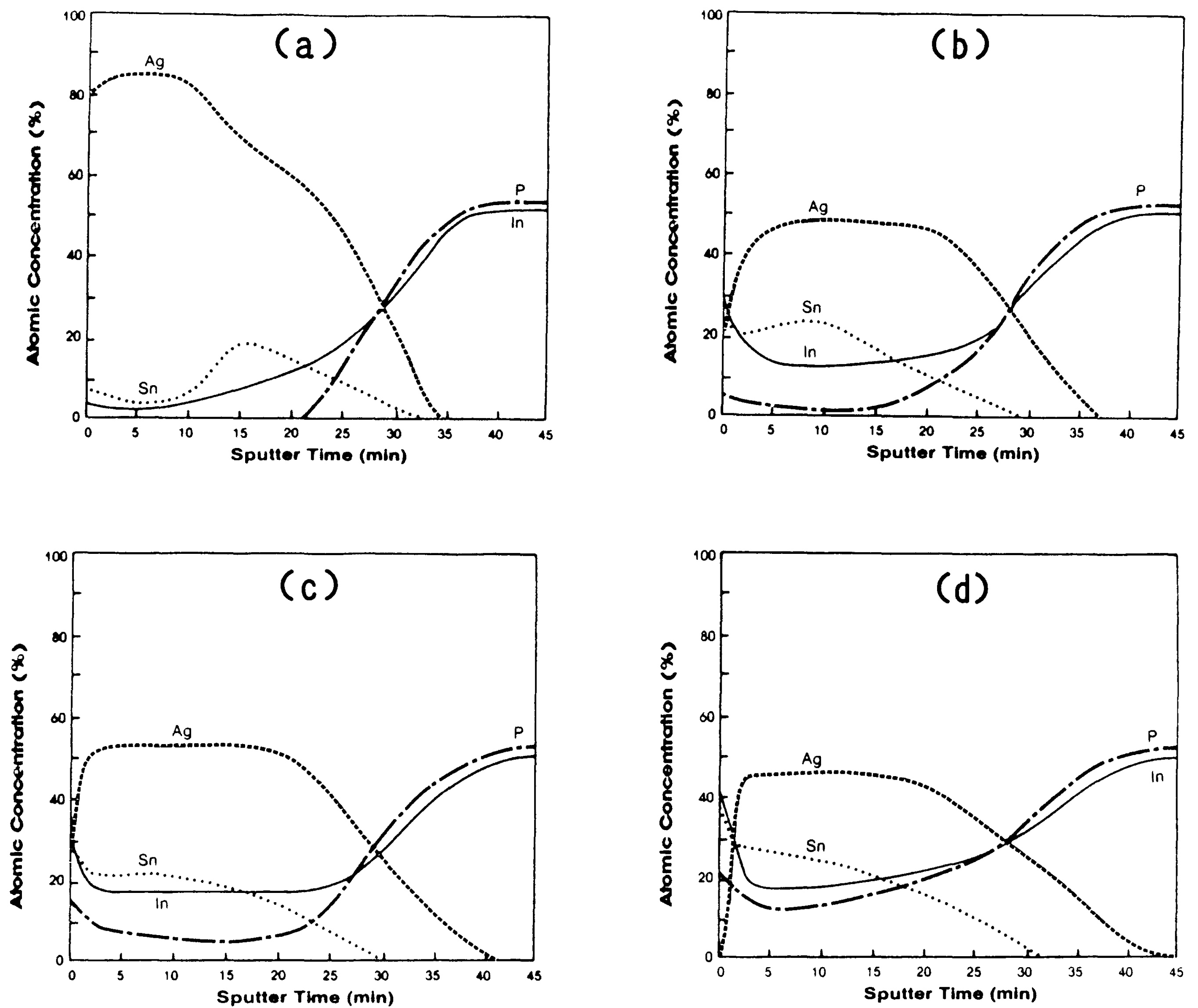

Figure 5.35: Auger depth profiles obtained for (a) as-deposited contacts, (b) contacts annealed at 300 °C, (c) 350 °C and (d) 400 °C for 2 minutes. The profiles in (c) and (d) were obtained from "valleys".

Digitised by the Department of Library Services in support of open access to information, University of Pretoria, 2021

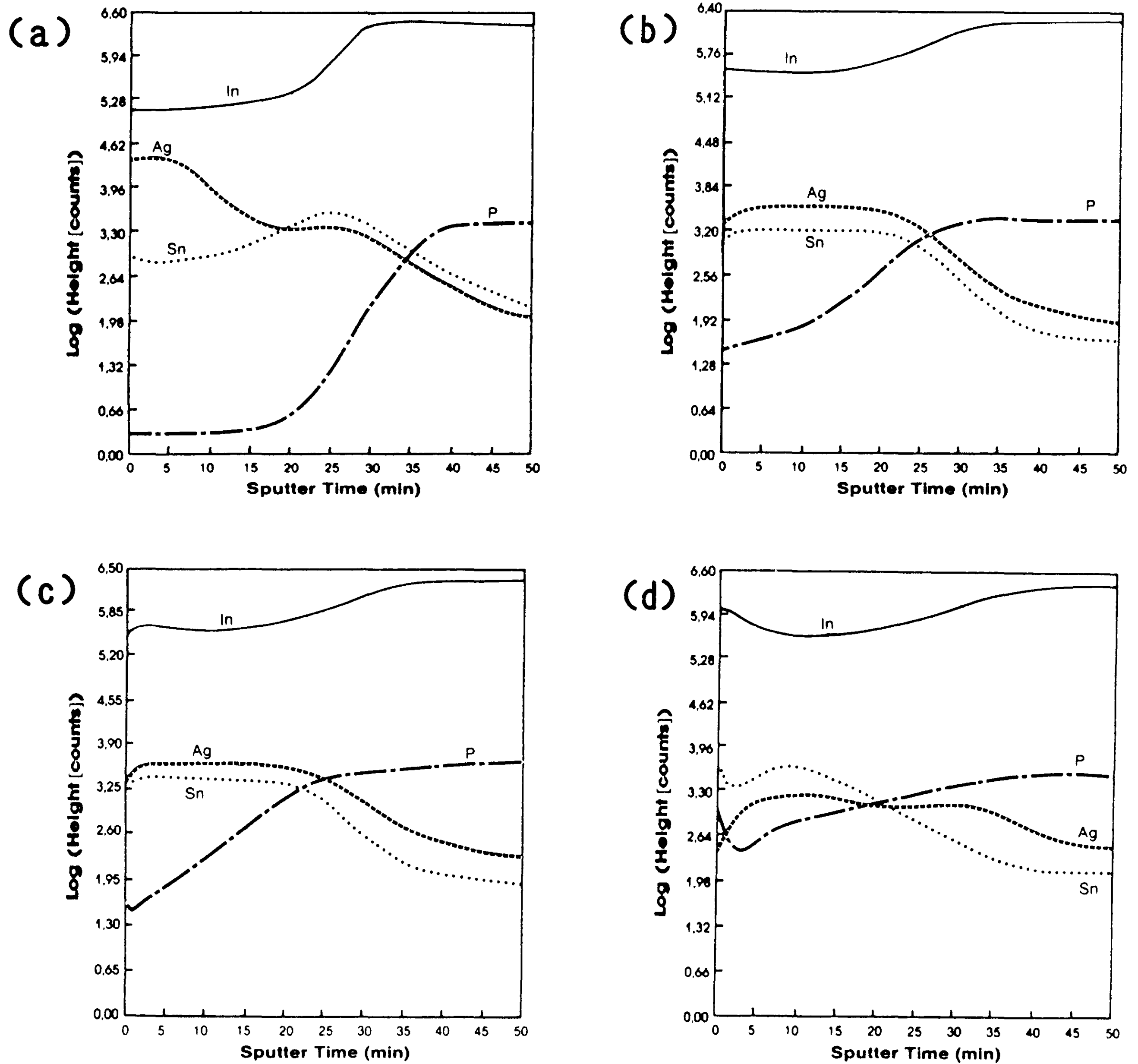

Figure 5.36: SIMS depth profiles show the elemental distribution for (a) as-deposited contacts, (b) contacts annealed at 300 °C, (c) 350 °C and (d) 400 °C for 2 minutes respectively.

Digitised by the Department of Library Services in support of open access to information, University of Pretoria, 2021

The elemental distribution for the contact annealed at 400 °C is shown in Fig. 5.35(d) and Fig. 5.36(d). According to the Auger results, more In and P have diffused out, while P and Sn also accumulate at the contact surface. However, more Ag has diffused into the InP substrate in comparison with the other annealing temperatures. This is also very clearly shown by the SIMS depth profile. Auger point analyses revealed ±20% P and ±3% Ag atomic concentrations on the "valleys" and ±5% P and ±15% Ag atomic concentrations on the "hills", while no dramatic changes were observed for the rest of the elements between the "hills" and the "valleys".

The I-V results for the as-deposited contacts, as well as for contacts annealed up to 450 °C are schematically shown in Fig. 5.37. As with the Ni/Au-Ge/InP contacts, these contacts are also ohmic, prior to any annealing step. It is also interesting to note that the total contact resistance (obtained from the slope of the I-V curves) increases again above 400 °C annealing. This is probably due to the fact that structural deterioration of the contact occurred after heating at and above 400 °C (for example see Fig. 5.34(d)) and hence also caused degradation of the electrical performance of the contacts.

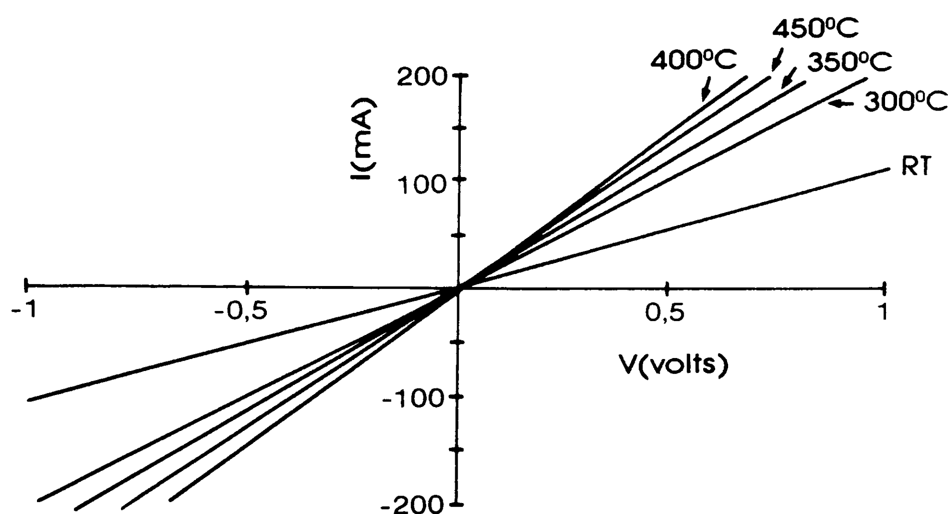

Figure 5.37: I-V measurements for the as-deposited contacts and contacts annealed for 2 minutes at different temperatures.

Digitised by the Department of Library Services in support of open access to information, University of Pretoria, 2021

From the AES results given above, it is clear that during the processing and annealing steps interdiffusion occurred between the deposited layers. The situation for the as-deposited case shown in Fig. 5.35(a) resembles that of the Au-In phase that formed for the as-deposited samples, discussed previously for the In/Au-Ge metallization system in section 5.2.2. According to the binary phase diagrams for Ag-Sn, Ag-In and In-Sn [Ma 87b], the only phase possible to form from about 70 °C up to 400 °C, is the $AgIn_2$ phase. It therefore appears that the evaporation temperature was high enough for solid-solid diffusion to occur between the metal layers at the various interface regions.

In contrast with the as-deposited case, P is detected throughout the whole contact layer up to the surface of the contact after annealing at 300 °C. Accordingly to the bulk binary phase diagrams (see Ma 87b) Ag and In will not react with P for the experimental conditions used here. However, Sn and P can form different phases at temperatures higher than 100 °C. Phases that can exist, depending on the different atomic percentages, are Sn_4P_3 and SnP_3, while a metastable Sn_3P_4 phase is also possible. With this in mind, together with the profiles shown in Figures 5.35(b) and 5.36(b), it is conceivable that one or other Sn-P compound formed at the interface between the thin film and the InP, which is responsible for the capturing of the outdiffused P. The intermixing which occurred in the as-deposited case between the Ag, Sn and In metal layers appears much more prominent at this annealing temperature. There exists a possibility that some ternary phase may also be present, but the presence of such a phase was not investigated.

Another interesting aspect is the movement of Ag into the InP for the 350 °C and 400 °C annealed contacts. This effect of Ag penetrating into the InP was also experienced with Au on InP (see previous sub-section). This might not be so surprising due to the fact that various similarities exist in the chemical properties of Ag and Au. Except for the fact that both are from the 1B sub-group in the periodic table, they also have the same crystal structure (face centred cubic), their melting points differ by only ~100 °C, they have basically the same atomic radius, atomic

Digitised by the Department of Library Services in support of open access to information, University of Pretoria, 2021

volume, resistivity and thermal conductivity. As a result, these similarities are reflected in the respective binary phases that they formed with In, according to the bulk phase diagrams given by Massalski [Ma 87b]. Thus, it seems that Ag, like Au, causes metallurgical problems when in contact with InP, but not to the same extent as Au.

From the abovementioned phase diagrams, it seems that even during the deposition process, a $AgIn_2$ phase could form as a result of the thin In deposited layer. At 300 °C annealing such a phase may be extended due to the increased availability of In from the substrate. As a result, more P is available to react with Sn, to form one or another Sn-P compound at the interface region. (It must be noted that the phase diagrams used to explain some of the phases that could form during the annealing process refer to bulk compositions.) The bad surface morphology observed in Fig. 5.34 can be related to the fact that the thermal degradation of the InP occurred inhomogeneously [Sa 88b]. Hence, the Ag and Sn also reacts non-uniformly with the free In and P at the interface region upon increasing the annealing temperature. (According to Sartorius et al. [Sa 88b] the degradation of InP is related to the volatilization of phosphorus.) Due to these non-uniform reactions, "valleys" and "hills" formed with different P and Ag concentrations.

The poor surface morphology experienced with this metallization system makes it unsuitable for device applications. However, it was reported by Weimann and Schlapp [We 78] that the surface can be improved by adding a Ag layer several microns in thickness. Further, Mills and Hartnagel [Mi 79] obtained very smooth surfaces with an In/Sn/Ag contact system (same thickness used as with this experiment), which were heat treated in a closed ampoule under a phosphorus overpressure. However, such an annealing technique is very time consuming and complicated.

It is the aim of the rest of this study to fabricate mechanically reliable ohmic contacts which show low specific contact resistance, smooth surface and good lift-off behaviour during the photolithography process.

Digitised by the Department of Library Services in support of open access to information, University of Pretoria, 2021

5.3.5 Alternative ohmic contact systems to n-InP

From the sub-sections above, it is clear that the metal/InP characteristics differ dramatically from those of GaAs due to (a) lower thermal stability of the InP surface, (b) the important role played by the InP surface chemistry and (c) the relatively low barrier heights obtained for most metals to n-type InP. The latter characteristic implies (also see sections 5.3.2 and 5.3.4) that the formation of ohmic contacts to n-InP is a less serious problem than with n-GaAs. As a result it is generally assumed that the commonly used ohmic contact systems to n-GaAs are also suitable for InP. Thus, the standard n-type contacts presently used for n-InP based devices are the alloyed Au/Sn or Au-Ge metallization schemes (see Chapter 2). However, these contacts are characterized by poor surface morphologies, poor edge definition and uneven penetration depths [Ba 87 and section 5.3.2]. In contrast, ohmic contacts with thermally stable microstructures and electrical properties are required. These characteristics are essential for high-speed devices, such as optoelectronic devices, which operate under high current densities, severe temperature conditions and with long term reliability constraints.

It is therefore no surprise that experiments with alternative metallization and fabrication methods have been performed. Dautremont-Smit et al. [Da 84] formed non-annealed ohmic contacts on Ar^+ etched n-InP surfaces. Contacts fabricated on such In-rich surfaces form ohmic contacts, independent of the particular contacting metal. Such surfaces permit the use of a barrier metal/noble metal combination, which can also act as an efficient diffusion barrier between the top Au layer and the substrate.

The purpose of this sub-section is the study of the microstructure and electrical nature of alternative systems such as Au/Pt/Ti/InP and Ti/Ni/Au/InP. These results are then compared with the Au-Ge/Ni/Au contact scheme. The final Au layer is necessary for bonding and heat sinking when used in actual devices. All three these systems were investigated for Ar^+-sputtered as well as chemically etched InP surfaces, prior to the

Digitised by the Department of Library Services in support of open access to information, University of Pretoria, 2021

metallization step. The Ti layer on the InP surface serves a dual purpose, firstly, as a diffusion barrier and secondly, it is the metal which forms the lowest barrier height on InP [Br 82]. The replacement of Pt with Ni is based on the fact that the latter metal is much cheaper than Pt, while chemically the metals are similar, except that Ni oxidizes very easily. However, the Ni is capped with a Au layer, which prevents the Ni from oxidizing.

Although Dautremont-Smit et al. [Da 84] and Katz et al. [Ka 90] published results on the Au/Pt/Ti/InP system, no studies on the Ti/Ni/Au metallization scheme as an ohmic contact to InP were reported in literature to date. The results of the Au/Ni/Au-Ge/InP system are presented and discussed first, followed by the Au/Pt/Ti/InP and Au/Ni/Ti/InP metallization systems, respectively.

5.3.5.1 Au/Ni/Au-Ge/InP contact system

Figure 5.38 presents the specific contact resistances of the Au/Ni/Au-Ge/InP contact system for as-deposited and annealed contacts at different temperatures for 2 minutes. Note that the results for the contacts fabricated on Ar ion sputtered and chemically etched surfaces are indicated by (△)and (□) respectively. The plotted values at the specific annealling temperature are averaged over the different diameters of the contacts, as well as for different r_c measurements as explained in section 4.3.6. The as-deposited contacts were ohmic prior to any intentional heating, also observed and discussed in section 5.3.2. Both sets of samples yield the lowest r_c values between 300 °C and 350 °C annealing, whereafter r_c increases up to 400 °C annealing. At 450 °C annealing the r_c values decrease again, however annealing above 500 °C the specific contact resistance increases dramatically. It is interesting to note that although there is a difference between the as-deposited r_c values of the sputtered and non-sputtered contacts, both contacts reveal the lowest specific contact resistance of ~2×10^{-6} Ωcm^2 between 300 °C and 350 °C annealing.

Digitised by the Department of Library Services in support of open access to information, University of Pretoria, 2021

AES investigations were carried out on various annealed contacts. However, Fig. 5.39 only shows AES depth profiles for (a) as-deposited contacts as well as contacts annealed for 2 minutes at (b) 250 °C, (c) 350 °C and (d) 400 °C respectively. The as-deposited elemental distribution is as expected, with some evidence of Ge interdiffusion into the Ni layer (see Fig. 5.39(a)). Although a difference is observed between the r_c of

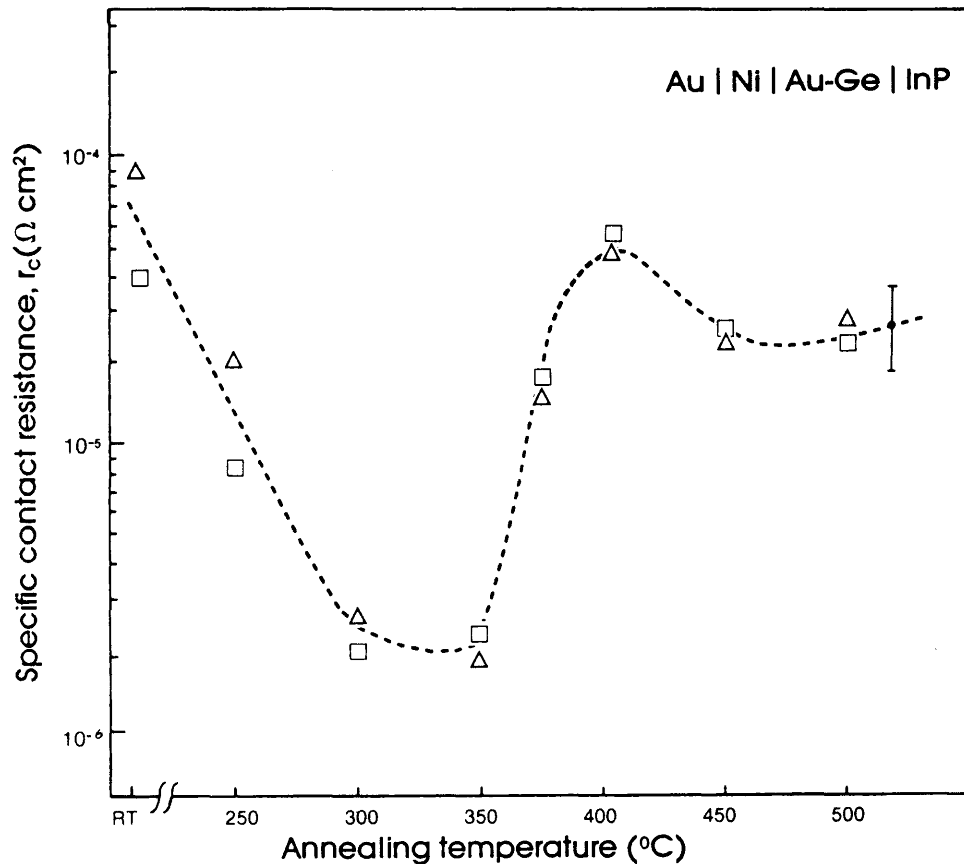

Figure 5.38: Specific contact resistance as a function of processing temperature (2 minutes) for Au/Ni/Au-Ge/InP contacts fabricated on Ar^+ sputtered (Δ) and only chemical etched surfaces (□). (The dotted line was hand drawn through the average points to indicate the general trend).

Digitised by the Department of Library Services in support of open access to information, University of Pretoria, 2021

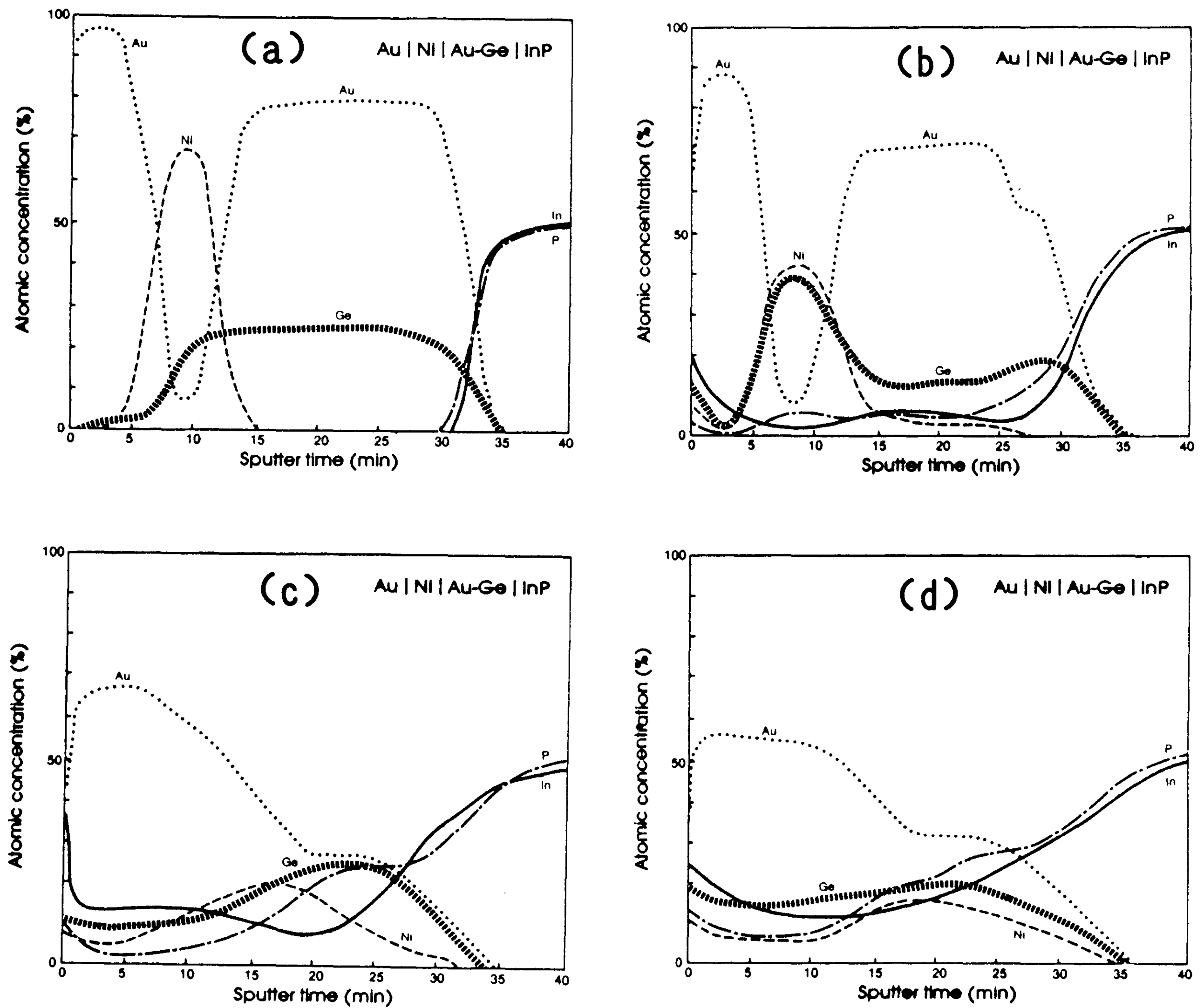

Figure 5.39: AES depth profiles of Au/Ni/Au-Ge/InP (50 nm/40 nm/100 nm) samples fabricated on chemical etched substrates and alloyed for 2 minutes at selected temperatures: (a) as-deposited, (b) 250 °C, (c) 350 °C and (d) 400 °C.

Digitised by the Department of Library Services in support of open access to information, University of Pretoria, 2021

as-deposited contacts fabricated on sputtered and on non-sputtered surfaces, no difference was observed in the AES depth profiles, between annealed Au-Ge/Ni/Au contacts to sputtered and non-sputtered InP substrates. Note that no O and C contamination is indicated in the AES profiles in Fig. 5.39, because the contamination distribution was as expected, with some contamination detected on the outer surface and at the interface between the substrate and the Au-Ge layer. Further no difference in the distribution and concentration of these contaminations was observed between contacts fabricated on sputtered and non-sputtered InP substrates. This is surprizing, because it is expected that the sputtered InP surface will reveal no or very low concentrations of C and O at the interface. The C and O detected are related to contamination originating from the photoresist during the sputtering process.

The Auger profile in Fig. 5.39(b) shows that upon annealing at 250 °C, Ge migrated out of the Au-Ge layer into the Ni layer. This appears to be independent of the substrate upon which the Ni/Au-Ge system is deposited or on the relative order of deposition of these elements, as was also observed in sections 5.2.2 and 5.2.3. Wittmer et al. [Wi 77b] also proved this statement by depositing the above metallization system on an inert SiO_2 substrate. Additionally, according to Fig. 5.39(b), some Ge also accumulated at the interface region, while some Ni is also present in the Au-Ge layer. The small Au shoulder at the interface region in comparison with the profile in (a) is also interesting. More In and P are observed in the metal overlayers, while In and P are also observed on the contact outer surface.

The elemental distributions for contacts annealed at 300 °C and 350 °C are essentially similar, except that for the 300 °C annealed contacts, more Au and less Ge are observed at the substrate interface region. However, there is a dramatic difference in the elemental distribution shown in (c), when compared to the Auger depth profile for contacts annealed at 250 °C in (b). The Ge and Ni are situated at the substrate interface area, while most of the Au is accumulated on the outer part of

Digitised by the Department of Library Services in support of open access to information, University of Pretoria, 2021

the contact system. A much broader P shoulder is also present at the interface region, with more In and P on the outer surface in comparison with the 250 °C annealed contacts.

The depth profiles for the contacts annealed respectively at 375 °C and 400 °C revealed essentially the same elemental distribution. The AES profile for a contact annealed at 400 °C is shown in Fig. 5.39(d). The elemental distribution at the substrate interface region is spread out more uniformly with no clear interface between the InP and the metallization layer or any significant elemental accumulation. Up to 350 °C annealing, more P than In is present at the substrate interface. However, at 400 °C annealing the same amount of In than P is observed at the interface area. (Note that the P profile at this interface does not change from profile (c) to (d), in contrast with the In profile which changed noticeably.)

The morphology of the contacts annealed at temperatures <375 °C was smooth and homogeneous. For higher temperatures the surface became rough and wrinkled and after annealing at 450 °C islands began to form, as can be seen in Fig. 5.40. The composition of the various areas were determined by AES depth profiling and is also shown in Fig. 5.40(a) and (b). The bright areas in the SEM micrographs can be correlated to a higher surface concentration of In, when compared with the homogeneous areas. In contrast to the contacts annealed at 375 °C and 400 °C, Au accumulated at the interface region in both cases. From both the profiles in Fig. 5.40 it is also clear that some of the elemental distributions concur, but with different relative concentrations.

The results presented above for the alloyed contacts are the result of a complex series of chemical reactions and inter-diffusion processes within the contact metallization layers and also between the metallization and the semiconductor interface. Much can be inferred from the data presented above and as a result meaningful conclusions can be drawn. Note that the specific contact resistances vs annealing temperature (see Fig. 5.38) for the contacts fabricated on sputtered and non-sputtered

Digitised by the Department of Library Services in support of open access to information, University of Pretoria, 2021

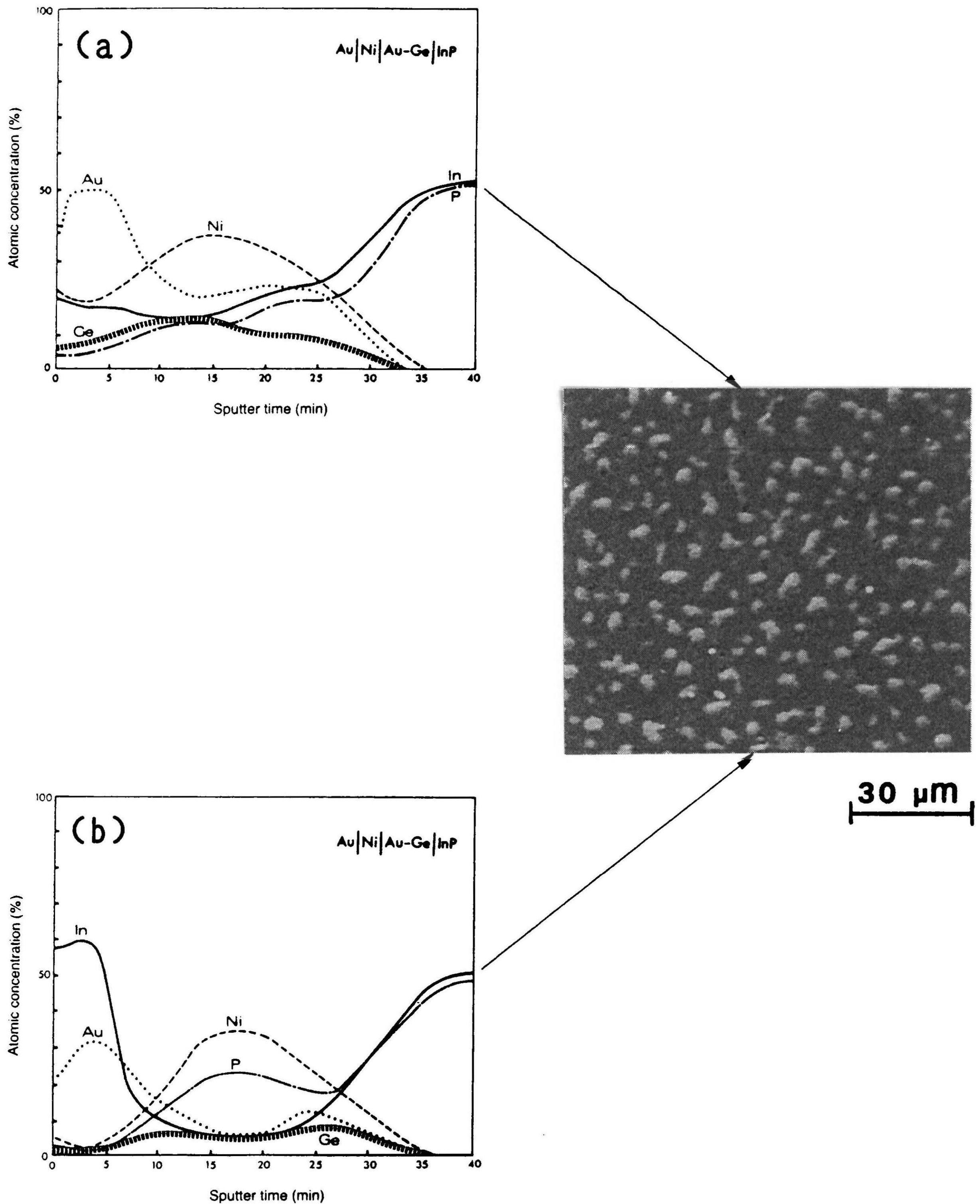

Figure 5.40: SEM photograph of the surface morphology of a contact annealed at 450 °C for 2 minutes. The AES profiles were obtained from (a) a homogeneous area and (b) an island respectively.

Digitised by the Department of Library Services in support of open access to information, University of Pretoria, 2021

surfaces reflect both the same tendencies. As a result, the rest of the discussion will focus only on the general trends in the specific contact resistances.

At low annealing temperatures, from ~120 °C to ~300 °C, Ge outdiffuse into the Ni layer, possibly forming Ni-Ge, as observed by Erickson et al. [Er 79] and Kuan et al. [Ku 83]. Further, in this annealing temperature range the presence of the Au leads to a P rich interface region, which is followed with a reaction between Au and In (also see section 5.3.3 and Table 5.3). Further the accumulation of Ge at the substrate interface region (see Fig. 5.39(b)) gives rise to the possibility of the existence of an AuGeP phase. This is in agreement with the interface model of Anderson et al. [An 88]. It is also claimed by them that this phase is mainly responsible for the current transport across the metal-semiconductor interface. This might explain the decrease in the r_c values after annealing at 250 °C.

At 350 °C annealing the contact elemental distribution changes dramatically (compare Fig. 5.39(b) with Fig. 5.39(c)). These changes are expected due to the fact that the Au-Ge eutectic temperature is ~360 °C [Ch 79] and the non-congruent evaporation temperature for InP is about 370 °C [Fa 74, Mo 83 and Mo 86]. Further, the role of Ni in this process is quite complicated. It was originally thought that the presence of Ni would serve to hold down the eutectic film during the melting and prevent the "balling" observed on these alloyed contacts. From the results of Erickson et al. [Er 79] and the results of this work, it is clear that Ni is a fast diffuser in the AuGe layer, diffusing toward the substrate interface, even at temperatures below 360 °C, to react with the InP. Graham et al. [Gr 83] and Del Alamo et al. [De 88] observed NiP_2 and Ni_2P in a Au-Ge/Ni/InP metallization system alloyed at the same temperature as above.

It is interesting to compare the electrical behaviour of this metallization scheme on n-InP with that of the same scheme on n-GaAs. For the InP system, the lowest r_c values were obtained for annealing temperatures between 300-350 °C, while for the GaAs the corresponding annealing temperatures were between 420-450 °C [Kr

Digitised by the Department of Library Services in support of open access to information, University of Pretoria, 2021

85, Gu 86 and section 5.2.3]. This difference can be related to the lower decomposition temperature of InP (~370 °C) [Fa 74 and Mo 86] in comparison with that of GaAs (~630 °C) [Ue 70]. Thus, intermixing between the metal overlayer and the substrate occurred at a much lower temperature in the case of InP. In the process, a dopant element such as Ge, can be captured on the surface of the InP at a lower annealing temperature.

According to the elemental distribution shown in Fig. 5.39(c), it is possible that the interface may contain a Au-Ge-P compound. However, the existence of a Ni-P compound is also possible, due to the increased Ni concentration at the interface region. Further, Au in its reaction with the InP at this annealing temperature is expected to form various Au-In alloys, as discussed in section 5.3.3. At this annealing temperature the interface is therefore dominated by the postulated Au-Ge-P compound, if compared with the 250 °C alloyed contacts. If it is assumed that this phase is mainly responsible for the current conduction between the metal overlayer and the InP semiconductor as claimed by Anderson et al. [An 88], the specific contact resistance of the ohmic contacts is expected to decrease. This was indeed observed from the r_c vs temperature curve shown in Fig. 5.38.

For the temperature regime 375 °C - 400 °C, the interface region consists of a nearly uniform elemental distribution (Fig. 5.39(d)) in comparison with contacts annealed at lower temperatures. The respective inwards and outwards movement of Ni and Ge in comparison with Fig. 5.39(c) is also evident. According to the interface model of Anderson et al. [An 88] for Au-Ge/Ni alloyed contacts to InP, the interfacial material consists mostly of an Au-Ge-P phase for low temperature annealed contacts. They also observed that upon increasing the alloying temperature from 350 °C, the thickness of this layer decreased due to a competing process which produced Au_2P_3. It is believed that the model of Anderson et al. [An 88a] is partly applicable to this annealed contact system. However, in addition, it is believed that a Ni-P compound also formed at the interface region. In agreement with previous observations of Erickson et

Digitised by the Department of Library Services in support of open access to information, University of Pretoria, 2021

al. [Er 79], the Auger profiles in Fig. 5.39(b) and (c) showed migration of Ni to the InP interface. Graham et al. [Gr 83], in fact, observed Ni_2P and NiP_2 in a AuGeNi/InP metallization system annealed at temperatures between 300 and 400 °C. Further, the possibility of various Au-In alloys cannot be ruled out for alloying temperatures in this region (see Table 5.3). The decreasing Au-Ge-P phase also explains the increased r_c values obtained for these alloyed contacts.

In the temperature region up to ~350 °C, the smooth surface morphology of the contacts were preserved. For contacts annealed at higher temperatures, temperatures are reached which are above or approximately coincident with the lowest eutectic melting points of some of the systems which formed in the contact overlayer. As a result the contacts are accompanied by the onset of roughness of the contact outer surface. This is evident from the SEM micrograph shown in Fig. 5.40 for a contact annealed at 450 °C for 2 minutes. According to the AES results in Fig. 5.40(a) and (b) respectively, the outer surface of the homogeneous areas consists predominantly of Au and the islands of In. This is the result of different reactions which occurred at the substrate interface. Decomposition of the InP substrate is also observed in the Auger depth profiles, which resulted in a considerable spreading of the various elements.

It seems from the above depth profiles (Fig. 5.40(a) and (b)) that beneath the respective areas, P reacts, among others, with either Au or Ni. According to the AES profile obtained from a homogeneous area, the interface area at the substrate surface consists of a Au-P and a different Au-In region with the possibility of low concentrations of Ni-P and Au-Ge-P. The Au-In region extends through to the contact outer surface. In contrast with the substrate underneath the island, Au-P, Au-Ge-P and Au-In regions occurred in much lower concentration, due to the low concentration of Au at the substrate. Instead, the whole substrate interface region is dominated by the presence of a Ni-P region, while the contact outer surface consists predominantly of an Au-In mixture. From these results the following simple model is proposed. It seems that a very stable Ni-P compound is

Digitised by the Department of Library Services in support of open access to information, University of Pretoria, 2021

initially formed underneath the island which prevents the Au from reacting with the substrate. The difference in the reaction between the metal overlayer and the InP substrate from one area to another might be related to the inhomogeneous thermal degradation of InP as reported by Sartorius et al. [Sa 88b]. The remaining reactions underneath the two respective areas are as discussed above. Further, the slight decrease in the specific contact resistance at this annealing temperature is probably the result of the increased Ni-P compound as suggested by Graham et al. [Gr 83].

Above 500 °C annealing the contact surface starts to degrade due to extensive decomposition of the InP. Free In becomes available in even larger quantities, with no difference in the r_c values if compared to the 450 °C annealed contacts. AES results reveal total intermixing of the metal and substrate. It also appears that the InP substrate has melted in some areas which has produced a very rough contact surface.

5.3.5.2 Au/Pt/Ti/InP contact system

Au-based alloys such as Au-Ge create contacts that are thermally stable only at relatively low temperatures, as a result of different interactions between Au and the InP. (This was shown in sections 5.3.2, 5.3.3 and 5.3.5.1.) As a result, specific attention has to be paid to the reliability and performance of ohmic contacts such as those used on optoelectronic devices, which operate under high current densities and severe temperature conditions. The most appropriate metals which meet these requirements are the refractory metals. As an example the Pt/Ti metallization scheme onto InP yielded good contacts which were thermally stable up to temperatures of 450 °C and exhibited extremely low specific contact resistance of $\sim 8 \times 10^{-7}$ Ωcm^2 [Da 84 and Ka 90]. In this sub-section the Ti/Pt/Au metallization system is characterized for contacts fabricated on Ar^+ sputtered and non-sputtered InP surfaces. The electrical properties of the contacts at different temperatures were correlated with the interface structure and morphology.

Digitised by the Department of Library Services in support of open access to information, University of Pretoria, 2021

Figure 5.41 summarizes the resistance measurements of the contacts to both sputtered (Δ) and non-sputtered (□) InP surfaces. In the as-deposited form, the evaporated contacts yielded r_c values of ~$3x10^{-4}$ Ωcm^2, whereas for the contacts to sputtered surfaces, r_c values of ~$1x10^{-3}$ Ωcm^2 were obtained. The contacts to sputtered surfaces exhibited a stepwise r_c decrease with increasing annealing temperature. In contrast, the r_c values of contacts fabricated on non-sputtered surfaces, show a slow decreasing from 250 °C to 450 °C. Both contacts reach a minimum specific contact resistance value of ~$2x10^{-5}$ Ωcm^2 at 450 °C annealing. Annealing at higher temperatures resulted in a moderate increase of the r_c values for both systems.

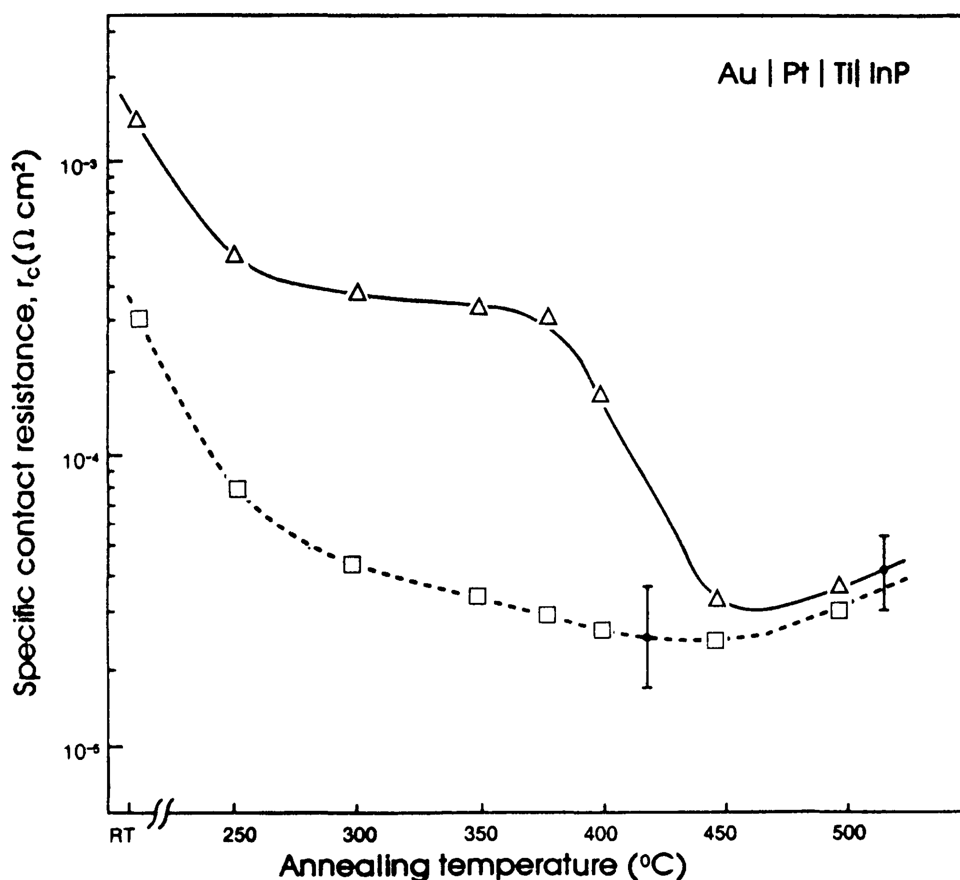

Figure 5.41: Specific contact resistance as a function of annealing temperature for 2 minutes of the Ti/Pt/Au contact system fabricated on sputtered (Δ) and non-sputtered (□) InP surfaces. (The lines were drawn through the average points to indicate the general trends.)

Digitised by the Department of Library Services in support of open access to information, University of Pretoria, 2021

Figure 5.42 shows AES depth profiles of as-deposited Ti/Pt/Au contacts to (a) sputtered and (b) non-sputtered InP surfaces. Both spectra show the same relative elemental distribution as expected. However, the profile obtained from the sputtered surface (Fig. 5.42(a)) shows contamination of oxygen and carbon at the upper region of the Ti layer in comparison with very low concentrations for contacts fabricated on non-sputtered InP surfaces. It may be concluded that the increase of the C- and O-concentrations in (a), are introduced into the sample during the sputtering process, due to decomposition of the photoresist. The carbon and oxygen react with the hot Ti during deposition and form an oxidized and carbonized layer. This layer can be related to the higher r_c values measured in general for the contacts on sputtered surfaces.

The initial decrease in r_c values for both type of contacts up to ~250 °C annealing can possibly be explained by the moderate reaction at the Ti/InP interface. This is shown in Fig. 5.43(a) for a contact deposited on a sputtered InP substrate. It is believed that an intermetallic compound Ti-P formed at this interface at 250 °C annealing. Except for the O- and C-concentrations in the Ti layer, hardly any additional changes were noticeable from the AES depth profiles obtained from as-deposited and annealed contacts to sputtered and non-sputtered substrates.

Figure 5.43(b) shows a typical depth profile of a contact to a sputtered InP surface after annealing at 400 °C. Only moderate interdiffusion of the metal overlayers at the different interfaces are evident in this depth profile. Different reactions are possible between the Pt and Ti at the Ti/Pt interface, between the Ti and the P that outdiffuse from the substrate and

Digitised by the Department of Library Services in support of open access to information, University of Pretoria, 2021

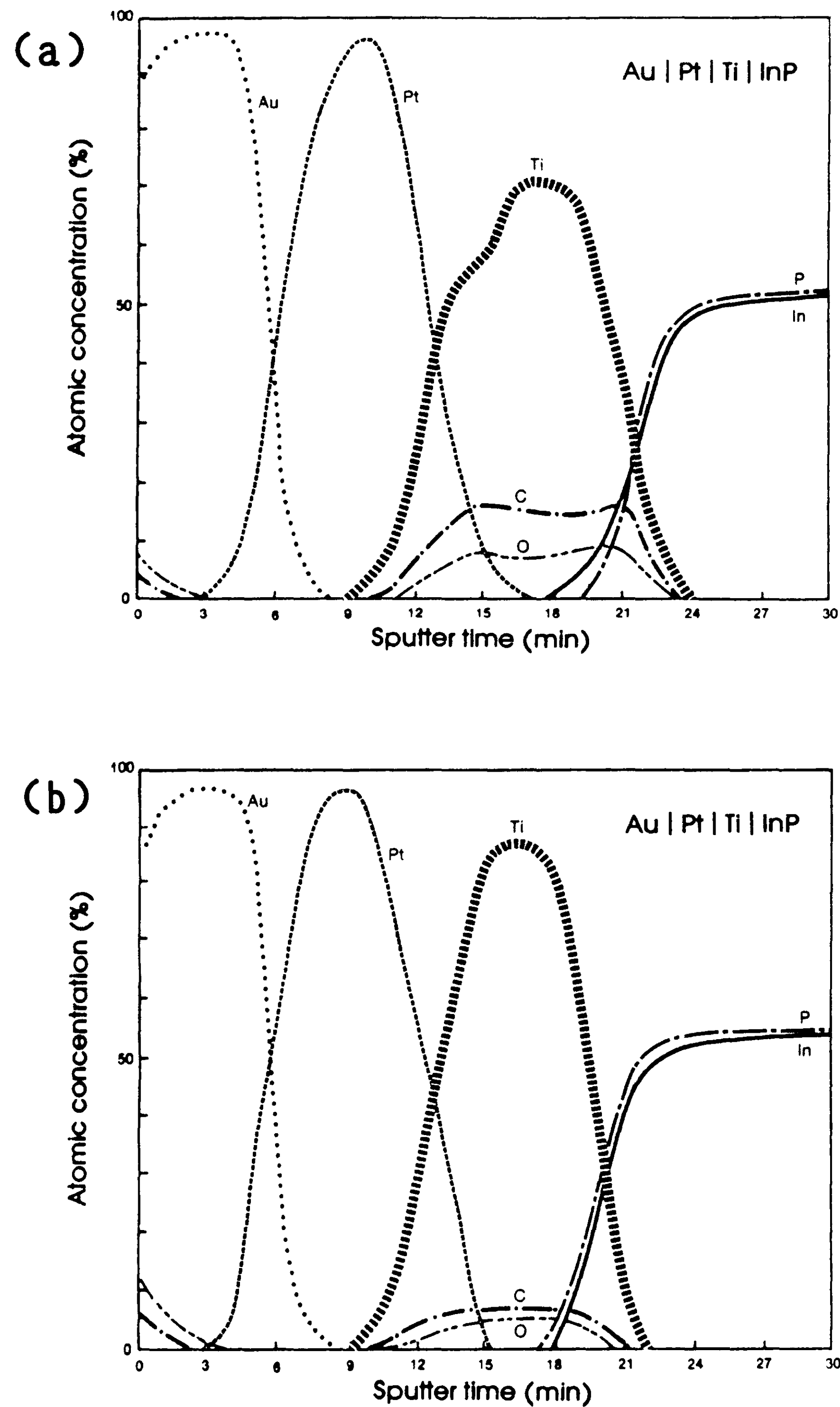

Figure 5.42: AES depth profiles of as-deposited Ti/Pt/Au (40 nm/40 nm/50 nm) contacts to (a) sputtered and (b) non-sputtered InP surfaces.

Digitised by the Department of Library Services in support of open access to information, University of Pretoria, 2021

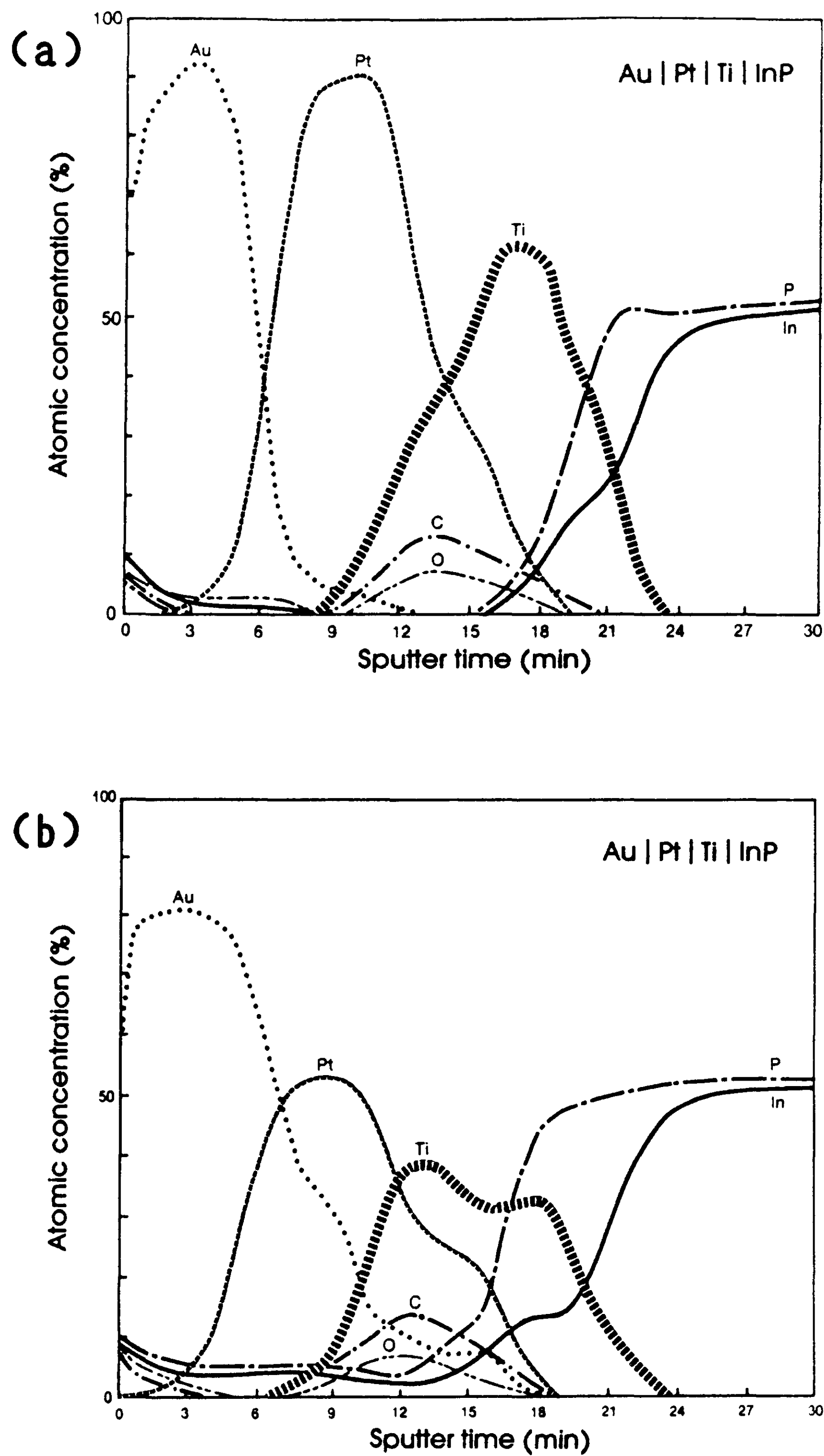

Figure 5.43: Elemental depth profiles obtained of Ti/Pt/Au contacts to sputtered InP surfaces after annealing for 2 minutes at (a) 250 °C and (b) 400 °C respectively.

Digitised by the Department of Library Services in support of open access to information, University of Pretoria, 2021

between the Ti and the In adjacent to the substrate. Some of the Au also diffuses through the Pt layer to react with some of the outdiffused P and In and probably form Au-P and Au-In compounds. The C- and O-contamination is also spread out towards the outer surface. The reaction at the Ti/InP interface is believed to result in a Ti-P intermetallic compound, as well as a Ti-In compound. These results are in good agreement with recent published results of Ti/Pt contacts to InP [Ka 90].

The sharp decrease of the r_c values obtained from contacts to Ar^+ sputtered surfaces after annealing at 350 °C can only be related to the movement of C and O towards the contact outer surface (see Fig. 5.43(b)), due to the destruction of the carbonized and oxidized layers. This statement is supported by the fact that only a marginal decrease is experienced in the r_c values of contacts to non-sputtered surfaces in the 350 °C - 400 °C temperature annealing range.

The metallization layers revealed smooth surfaces up to ~400 °C annealing. However, island formations appeared on the contact surface when annealed at higher temperatures, as is clearly visible in Fig. 5.44. (Contact annealed at 450 °C for 2 minutes.) From the AES depth profile in Fig. 5.44(b), the failure of the Ti as an effective diffusion layer is evident. As a result a reaction occurred in these areas and is responsible for the formation of islands on these contacts. The depth profile obtained from a homogeneous area shows Ti, P, In, O and C which diffuse out to the contact outer surface. However, the Au and Pt distributions are basically the same as that observed at 400 °C annealing, while the P shows a dramatic diffusion into the Ti layer. It therefore seems that the situation at the substrate interface region is the same as for the 400 °C annealed contacts. The O and C are now situated on the outer part of the contact, probably as a result of the outdiffused Ti.

Digitised by the Department of Library Services in support of open access to information, University of Pretoria, 2021

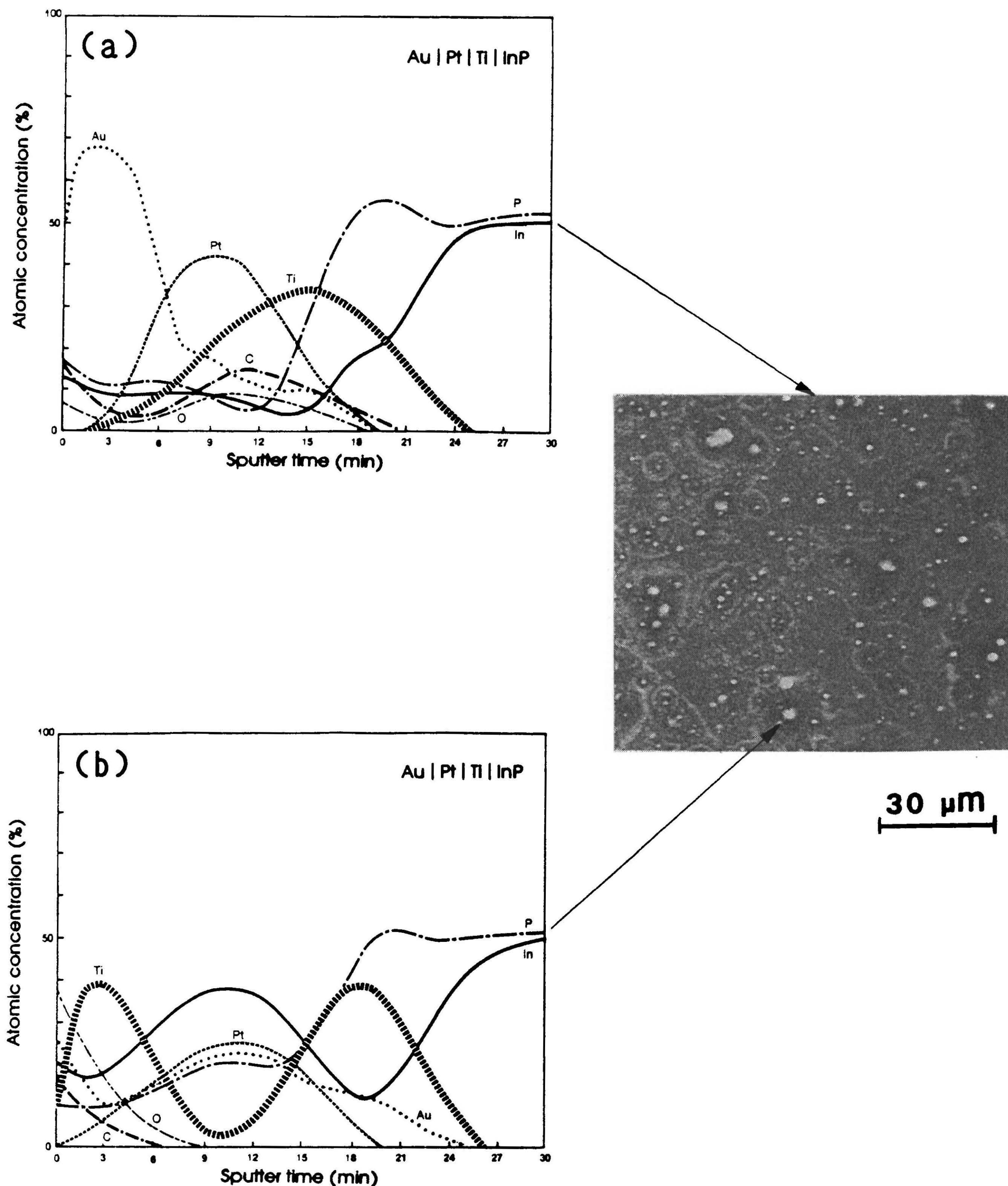

Figure 5.44: SEM and AES results from an Au/Pt/Ti/InP contact system after annealing at 450 °C. The depth profile in (a) was obtained from a homogeneous area and in (b) from an island.

Digitised by the Department of Library Services in support of open access to information, University of Pretoria, 2021

From the AES depth profile obtained from an island, (see Fig. 5.44(b)), it is clear that all elements, except Pt, diffuse out to the outer surface of the contact. Underneath these islands an enhanced reaction might have occured between Ti and P in comparison with the homogeneous areas, and resulted in a significant outdiffusion of In. Interesting is the accumulation of Ti on the outer surface of the island. The failure of the Ti layer as a diffusion barrier underneath the islands can be related to the excess In present in these areas. The outdiffused In is followed by some Ti through to the outer surface where it becomes oxidized.

Both types of contacts show essentially the same increase and values for r_c, when annealed at temperatures above 450 °C. The AES depth profiles obtained from both types of contacts annealed at 550 °C indicate similar elemental distribution to that of Fig. 5.44 (b). However, the relatively smooth surface of the contacts after 450 °C annealing is disturbed at this higher annealing temperature.

From the above results it is clear that in spite of these major differences in the metallurgical behaviour of this metallization system in the annealing region 250 °C - 450 °C, only a moderate decrease in the contact resistance values was detected for the contacts fabricated on non-sputtered surfaces. In contrast, the contacts to sputtered surfaces show the same r_c values as those obtained from non-sputtered surfaces, when annealed above 400 °C. These initial differences in the r_c values are related to the existence of C and O on the sputtered surfaces, which contaminated the Ti layer.

5.3.5.3 Au/Ni/Ti/InP contact system

The potential of using the Ti/Pt contact system for InP devices is evident from the above results. Since Pt is such an expensive material, it was decided to replace Pt with Ni. Both these elements are in the same group of the periodic table and as a result possess, in some cases, the same chemical characteristics. Although Ni oxidizes easily, gold is normally deposited as the

Digitised by the Department of Library Services in support of open access to information, University of Pretoria, 2021

final layer to provide contact to the external circuit, and also acts as a protective layer to prevent Ni from oxidizing. Furthermore, Ni contacts have been found to exhibit low r_c values on n-InP [Ap 86 and La 86c].

Recently, metallurgical studies of Ni and InP at elevated temperatures revealed extensive interreaction between the two constituents at 250 °C [Ap 86 and Ap 86b]. Obviously, for long term reliability it would be favourable to use a thermodynamically stable compound as metallization layer. It was therefore decided to investigate the electrical and structural characteristics of the Au/Ni/Ti/InP contact scheme at different annealing temperatures.

Figure 5.45 shows the specific contact resistance values vs different annealing temperatures at 2 minutes for contacts fabricated on sputtered (Δ) **and non-sputtered** (□) InP surfaces. It is interesting to note that the characteristics of the r_c values are basically the same as those obtained from the Ti/Pt contact system. The only difference is the fact that this system yielded a slightly better specific contact resistance value of $\sim 1 \times 10^{-5}$ Ωcm^2 in comparison with the $\sim 2 \times 10^{-5}$ Ωcm^2 obtained for the Ti/Pt metallization scheme. This lower r_c is probably the result of different compound formations which form between the Ni and InP, when compared to those between Pt and InP. It is also possible that the difference in r_c can be related to the slightly superior current conductivity of Ni. (Compare the electrical conductivity of $1,4 \times 10^5$ $\Omega^{-1}cm^{-1}$ for Ni to that of $9,6 \times 10^4$ $\Omega^{-1}cm^{-1}$ for Pt.) Structural investigations were therefore carried out in order to obtain an answer for these differences in the r_c values.

The resemblance of the r_c measurements of the two metallization systems is also reflected in the AES depth profiles in Fig. 5.46. These profiles were obtained from the Au/Ni/Ti/InP system for (a) as-deposited contacts to non-sputtered substrates, as well as for substrates annealed at (b) 375 °C and (c) 400 °C respectively. The same differences that were experienced for the C and O

Digitised by the Department of Library Services in support of open access to information, University of Pretoria, 2021

contamination between the contacts to sputtered and non-sputtered surfaces for the Ti/Pt/Au system were also observed here. This was also the case for the annealed contacts. As a result, the profiles in Fig. 5.46 and 5.47 were drawn without the C and O concentration distributions. Further, it also helps with the interpretation of the depth profiles, due to the fact that less elemental distributions are interlaced. Although slightly less interdiffusion occurred at the substrate interface area for the Au/Ni/Ti/InP system, the discussion on the specific contact resistances up to ~375 °C for the Au/Pt/Ti/InP system in the previous sub-section is also valid for the Ti/Ni/Au metallization scheme.

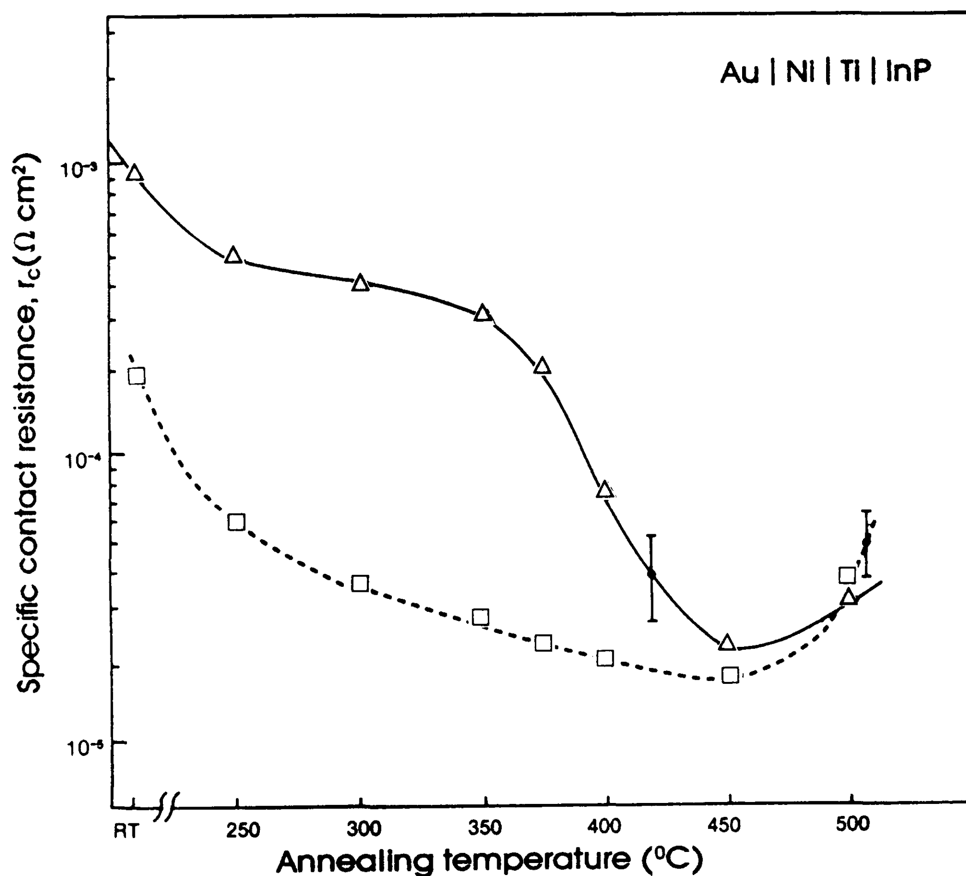

Figure 5.45: Specific contact resistance values vs different annealing temperatures (2 minutes) for Ti/Ni/Au contacts processed on sputtered (Δ) and non-sputtered (□) InP surfaces. (The lines were drawn through the average points to indicate the general trends.)

Digitised by the Department of Library Services in support of open access to information, University of Pretoria, 2021

However, at, and above, 375 °C annealing (see Fig. 5.46(b)) more reactions occurred at the different interfaces, in addition to those reported between Ti and InP in the previous sub-section. These effects are even more pronounced after annealing at 400 °C (see Fig. 5.46(c)). Ni diffused through both the Au and Ti layers to the substrate and outer contact surface respectively. This effect increased with increased annealing temperature from 375 °C - 400 °C. The Ti also started to diffuse towards the outer surface. It is interesting to note that no Au was detected at the substrate surface after 400 °C annealing, which is in contrast with the Au/Pt/Ti/InP contact system annealed at the same temperature.

As in the previous sub-section it is believed that up to ~375 °C annealing the reaction at the Ti/InP interface leads to the possible formation of a Ti-P and a Ti-In intermetallic compound. However, annealing at higher temperatures results in more In at the substrate interface allowing the possibility of the reaction $xNi+InP \rightarrow Ni_xP + In$, that was recently observed to occur between Ni and InP [Ap 87]. Some of this In reacts with the Ti, while the excess In diffuses through the Ti layer towards the Au. At this annealing temperature the surface region still consists of Au and Ni. However, under these experimental conditions and composition ratios of Au and Ni, no Au-Ni compound is possible according to the Au-Ni bulk phase diagram [Ma 87b]. Hence, it is believed that the Au and Ni diffuse through each other along grain boundaries.

It seems that the Ni together with the possible formation of a Ni-P compound prevents the Au from interacting with the InP, since the presence of Ni and/or the Ni-P compound are the only differences between the two metallization systems. This is in line with work by Appelbaum et al. [Ap 87], who concluded that a Ni_2P layer is an excellent diffusion barrier between a Au layer and InP. This also explains the better surface morphology obtained for the Ti/Ni/Au system in comparison with that of the Ti/Pt/Au metallization scheme after annealing at 400 °C. Again, as with the previous metallization system, the outward movement

Digitised by the Department of Library Services in support of open access to information, University of Pretoria, 2021

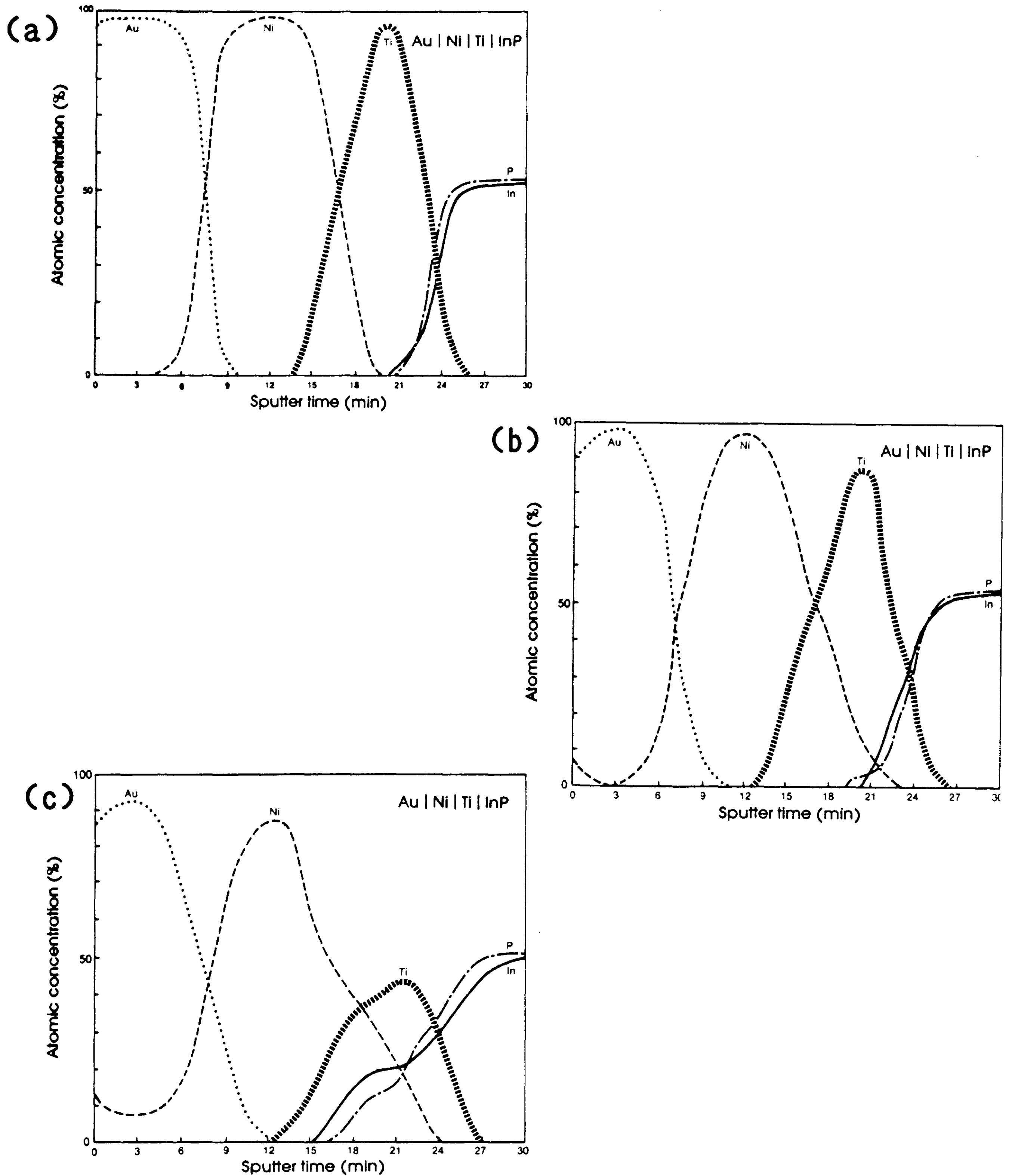

Figure 5.46: AES elemental depth profiles of the Au/Ni/Ti/InP (50 nm/40 nm/40 nm) contact system for (a) as-deposited contacts, (b) contacts annealed at 375 °C and (c) 400 °C respectively. These profiles were obtained from contacts to non-sputtered substrates.

Digitised by the Department of Library Services in support of open access to information, University of Pretoria, 2021

of the oxidized and carbonized layers is believed to be responsible for the dramatic decrease in the r_C values of the contacts fabricated on sputtered InP substrats after annealing at 400°C.

Small islands were visible on the contact surface after annealing at 450 °C, as indicated in Fig. 5.47. AES depth profiles revealed dramatic differences between the homogeneous areas (a) and the islands (b). However, very few changes are evident between the depth distributions in Fig. 5.47(a) and Fig. 5.46(c). It is interesting that even after 450 °C annealing no interaction between the Au and the InP is detected underneath the homogeneous area, when compared with Fig. 5.44(a). This stems from the fact that the Ni and/or the Ni-P compound layers act as diffusion barriers for Au. As a result, the Ti layer is not the only diffusion barrier between Au and InP.

The failure of the Ti and Ni layers and/or the Ni-P compound as effective diffusion barriers in some areas, can be related to the island formations (see Fig. 5.47(b). The reason for this failure is believed to originate from areas where localized decomposition of the InP surface occur [Sa 88b]. In these areas the Ti moves to the contact outer surface, where it is oxidized. Excess amounts of the volatile P are released. Both the decomposed P and In may form compounds with Ti. It appears that the Ni and/or the Ni-P compound which also prevent Au from reacting with the InP in some areas of the contacts, caused a better surface morphology. This is clearly evident from the SEM micrographs shown in Fig. 5.44 and Fig. 5.47 respectively.

Contacts annealed at 500 °C indicate an increase in the specific contact resistance (see Fig. 5.45) as well as a dramatic degrading of the contact surface morphology due to the increased decomposition of the InP. AES depth profiles revealed basically the same elemental distribution as that obtained from islands, as discussed in the previous paragraphs (also see Fig. 5.47(b)). This result supports a previous statement that decomposition of

Digitised by the Department of Library Services in support of open access to information, University of Pretoria, 2021

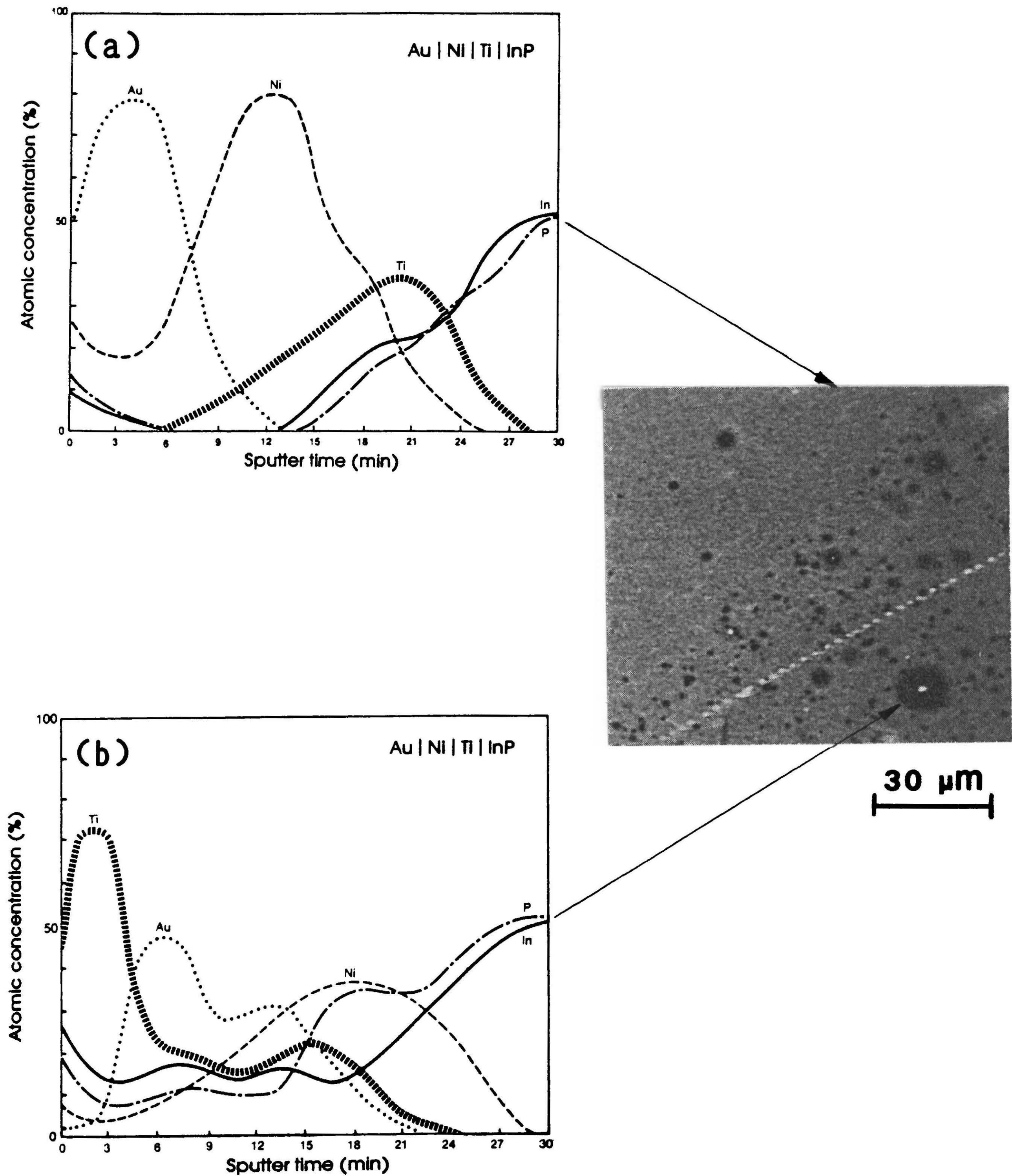

Figure 5.47: SEM and AES results from a Au/Ni/Ti/InP contact system after annealing at 450 °C (2 minutes.) The AES depth profiles in (a) were obtained from a homogeneous area and in (b) from an island.

Digitised by the Department of Library Services in support of open access to information, University of Pretoria, 2021

the InP substrate caused the formation of islands. This argument is strengthened by the observation that after 500 °C annealing the decomposition occurred extensively over a much larger area of the InP surface.

A comparison of the r_c values of the different metallization schemes on InP suggests that the interfacial reactions that take place in the Ti based systems without the presence of a doping element, cannot significantly improve the contact resistance when there is a relatively moderate background doping level of 1-$3x10^{18}$ cm^{-3}. This is clearly evident from the Au-Ge contacts where the lowest r_c value of $\sim 2x10^{-6}$ Ωcm^2 was obtained after annealing between 300-350 °C. In contrast, the Ti/Pt and Ti/Ni metallization schemes had at best r_c values of $\sim 1x10^{-5}$ Ωcm^2 after annealing between 400 °C - 450 °C. The introduction of a doping element such as Ge into the substrate during the annealing step resulted in a lower r_c ohmic contact, due to the influence of the doping levels on the dominant carrier transport mechanism (see section 3.4). According to Kuphal [Ku 81], the specific contact resistance can be related to a specific transport mechanism for contacts to InP. From his results it is suggested that the primary current conduction mechanism for the Au-Ge contacts is tunneling field emission, while for the Ti/Pt and Ti/Ni contacts it is restricted to thermionic field emission of the carriers through the top of the narrowed barrier between the metal and the semiconductor.

In conclusion, the lowest specific contact resistance for the three ohmic metallization systems to InP were obtained from the Au-Ge/Ni contact system, but the Ti/Ni/Au gave the best surface morphology. Furthermore, the Ti/Pt and Ti/Ni contacts revealed excellent adhesion in comparison with the Au-Ge metallization scheme in the so-called "Scotch-tape test". This test consists of a sticky tape experiment that is used to compare the adhesion ability of one metallization layer to a specific substrate to that of other metallization layers. In the Au-Ge metallization system case, the metallization layer can be peeled of with ease, in contrast with almost no layer removal from the former contacts, for contacts annealed at 400 °C.

Digitised by the Department of Library Services in support of open access to information, University of Pretoria, 2021

CHAPTER 6

CONCLUSIONS

6.1 INTRODUCTION

In this study n-type GaAs and InP were investigated with special reference to (a) surface studies on different chemically cleaned and etched samples, (b) structural investigations of various annealed metallization systems and (c) the electrical characterization of these annealed metallization schemes. The purpose of this chapter is to summarize the main conclusions which can be drawn from the experimental results and interpretations presented in Chapter 5. The conclusions are presented in the same sequence as the results in Chapter 5.

6.2 GaAs SURFACE AND OHMIC CONTACT CHARACTERIZATION

6.2.1 GaAs surface studies

i) The sensitivity factors for the LMM Ga and As Auger transition were calculated to be 0,13±0,01 and 0,11±0,02 respectively. (These factors apply to spectra obtained at 30° incidence in a PHI 595 system by using a primary electron beam of 3 keV.)

ii) For the Ar^+ sputtered GaAs surfaces, preferential sputtering of As is obtained.

iii) It seems as if the preferential sputtering of As is weakly dependent on the sputtered energy, but independent of the sputtered surface orientation.

iv) No striking differences are observed between the AES spectra obtained from the GaAs surfaces etched respectively in (a) $NH_3:H_2O_2:H_2O$, (b) $H_2SO_4:H_2O_2$ and (c) $H_3PO_4:H_2O_2:H_2O$.

Digitised by the Department of Library Services in support of open access to information, University of Pretoria, 2021

v) AES results indicate that a $NH_3:H_2O$ (1:15) dip left the uncovered substrate area after patterning with the same amount of contamination than before the lithographic process.

6.2.2 Comparison between Ni and In as wetting agents

(i) Indium as a wetting agent produced a very poor contact surface morphology, when compared to the Ni contacts.

ii) The "S" shape of the log I vs V characteristics for the In/Au-Ge system up to 350°C annealing, correlates well with both a theoretically predicted model for a dual phase system and the AES results.

iii) It is not possible to determine whether the NiAs(Ge) or Ni_2GeAs compound is responsible for the trapping of the Ge at the substrate interface region.

iv) The non-uniformity of the In contact system is related to an Au-Ge-As phase that formed at the substrate interface region.

6.2.3 Effect of ion implantation on ohmic contacts

i) The surface morphology of the Ar^+ implanted contacts is superior to that of the unimplanted contacts.

ii) The unimplanted and implanted contacts exhibited specific contact resistance values of 5×10^{-6} Ω cm^2 and 1×10^{-5} Ω cm^2 respectively.

iii) The higher contact resistance obtained for the implanted samples is related to the possible damage caused to the GaAs surface crystal structure during implantation.

Digitised by the Department of Library Services in support of open access to information, University of Pretoria, 2021

iv) The improved surface morphology for the ion-implanted contacts is related to:

(a) the absence of the Au-Ge-As compound;
(b) the uniform mixed metallization layer, and
(c) also the mixing of the interfacial layer.

6.3 INP SURFACE AND CONTACT CHARACTERIZATION

6.3.1 AES investigation of InP surfaces

i) The differentiated 120 eV P peak and its associated peaks are very sensitive to the chemistry of the InP surface and may, in some cases, act as a fingerprint of the treatment of a surface.

ii) The Ar^+ bombarded surface yielded an In enriched surface when compared to the vacuum cleaved surface.

iii) No differences were observed for the Ar^+ bombarded (100), (110) and vicinal surfaces.

iv) The same In/P peak ratio was obtained for the sputtered surface, independent of the ion energies used.

v) The HF treated surfaces provide lower oxide concentrations than the H_2SO_4:H_2O_2:H_2O and Br/methanol etched surfaces.

vi) The etched InP surfaces were depleted of phosphorus, in a similar way to that of the sputtered surfaces.

6.3.2 Au-Ge/Ni ohmic contacts to n-InP

i) These contacts revealed linear I-V characteristics prior to any intentional annealing.

Digitised by the Department of Library Services in support of open access to information, University of Pretoria, 2021

ii) The factors that might contribute to the above behaviour are:

a) the low barrier height most metals form to n-InP;
b) the formation of an In-rich surface after chemical etching, and
c) the possibility of intermixing between the metal overlayer and the InP substrate during the deposition step.

iii) Contact spreading of this contact system after annealing at 450°C for 5 minutes was observed. From the results of AES spot analyses it may be concluded that the lateral diffusion of the Au-Ge/Ni contacts on the substrate surface can be related to Au.

6.3.3 Au Contacts to InP

i) AES operated in different modes was used to obtain information on the Au/InP system.

ii) Noticeable lateral spreading of Au contacts to InP is observed after 400 °C annealing, while the most dramatic edge effects are visible between 430-500 °C annealing. The relative spreading rate of the Au-contacts annealed at 450°C is about 4 μm/minute.

iii) The interface region between the InP and the Au contacts after annealing at 450 °C consists mostly of an Au-P compound. However, the outer surface of the contact contains mostly Au-In rich compounds, together with the Au-P compound which also extends to the top surface.

iv) A "swallow-hole" occur after annealing at 500 °C for 10 minutes on the area where the Au contact was originally evaporated. This effect is related to the sublimation of the Au_2P_3 phase, with the resultant out-diffusion of P. The free Au is then again available to react with the InP

Digitised by the Department of Library Services in support of open access to information, University of Pretoria, 2021

and in the process it erodes the substrate away underneath the contact.

6.3.4 Ag based contacts to InP

i) The surface morphology of the In/Sn/Ag contact system became highly irregular with large inhomogeneous metallic islands, when the annealing temperature is increased from room temperature to ~400 °C.

ii) According to the AES results, interdiffusion occurred between the deposited metallization layers during the processing and annealing steps.

iii) The lowest total contact resistance for this metallization system is obtained after annealing at 400 °C.

vi) Ag, like Au in contact with InP, causes metallurgical problems when annealed. However, the effect of the Ag-based contact is less dramatic in comparison with Au contacts.

6.3.5 Alternative ohmic contacts to InP

6.3.5.1 Au/Ni/Au-Ge/InP contact system

i) The contacts to sputtered and non-sputtered InP surfaces yielded basically the same r_c values and tendencies when annealed.

ii) Both sets of samples produced the lowest r_c value of $\sim 2 \times 10^{-6}\ \Omega\ cm^2$ after annealing between 300-350 °C for 2 minutes.

iii) The introduction of Ge as a doping element into the substrate during the annealing step, resulted in a highly doped n^+ InP surface. This has a decreasing effect on the height and width of the barrier between the metal and InP.

Digitised by the Department of Library Services in support of open access to information, University of Pretoria, 2021

iv) According to the r_c values of these annealed contacts, tunneling field emission is the primary current conduction mechanism.

v) Poor adhesion and surface morphology are experienced for these contacts when annealed above ~375 °C.

6.3.5.2 Au/Pt/Ti/InP contact system

i) Up to 400 °C annealing, this contact system to sputtered susbstrate surfaces yielded higher r_c values than the same contacts to ion-sputtered surfaces.

ii) This difference in the r_c values is related to an oxidized and carbonized layer that formed during the deposition of the hot Ti. These contaminants are introduced into the samples during the sputtering process due to decomposition of the photoresist.

iii) The sharp decrease of the r_c values obtained from contacts to Ar^+ sputtered surfaces after annealing above 350 °C is related to the movement of C and O towards the contact outer surface.

iv) These metallization layers revealed smooth surfaces up to ~400 °C annealing.

v) The failure of the Ti as an effective diffusion barrier and the resultant island formations are related to the inhomogeneous thermal degradation of InP when annealed at and above ~450 °C.

6.3.5.3 Au/Ni/Ti/InP contact system

i) The conclusions i)-iv) drawn in 6.3.5.2 above, are also valid for this contact system.

Digitised by the Department of Library Services in support of open access to information, University of Pretoria, 2021

ii) A slightly better minimum r_c value of $\sim 1 \times 10^{-5}$ Ω cm^2 is obtained for this system, in comparison with $\sim 2 \times 10^{-5}$ Ω cm^2 for the Ti/Pt metallization scheme.

iii) In comparison with the other metallization combinations, this metallization system revealed the best surface morphology for contacts to InP, even when annealed at 450 °C.

iv) The possible existence of a Ni-P compound and/or the Ni in addition to Ti is believed to cause the improved surface morphology. This improved morphology has been related to a "double" diffusion layer.

v) The failure of this "double" diffusion layer and the formation of islands in certain areas are also related to the inhomogeneous thermal degradation of InP when annealed at and above ~450 °C.

vi) According to the minimum r_c values obtained for the Ti/Pt and Ti/Ni contacts, the current conduction mechanism is related to the thermionic field emission of the carriers through the top of the metal/semiconductor barrier.

Digitised by the Department of Library Services in support of open access to information, University of Pretoria, 2021

An 82b C.L. Anderson; Laser and electron-beam interactions with solids, eds. B.R. Appleton and G.K. Celler (Elsevier North- Holland, New York, USA, 1982) 653.

An 84 Y. Anand; Metal Semiconductor Schottky barrier junctions and their applications, ed. B.L. Sharma (Penum. Press, New York, USA, 1984) 35.

An 88 D.A. Anderson, R.J. Graham and J.W. Steeds; Semicond. Sci. Technol. 3 (1988) 63.

Ap 86 A. Appelbaum, P.M. Thomas and P.A. Barnes; Semiconductor-based heterostructors, Interfacial Structure and Stability, eds. M.L. Green, J.E.E.Baglin, G.Y. Chin, H.W. Deckman, W. Mayo and D. Narasinham; The Metallurgical Soc. Inc. (1986) 409.

Ap 86b A. Appelbaum, L.C. Feldman, L.A. Koszi, P.M. Thomas and P.A. Barnes; J. Electron. Mater. (1986).

Ap 87 A. Appelbaum, M. Robbins and F. Schrey; IEEE Trans. on Electron Devices **ED34** (1987) 1026.

Au 85 P. Auvray, A. Guivarc'h, H. L'Haridon, J.P. Mercier and P. Henoc; Thin Solid Films **127** (1985) 39.

Au 91 F.D. Auret, L.J. Bredell, G. Myburg and W.O. Barnard; To be published in Japn. J. Appl. Phys. **30** (1991).

Au 91b F.D. Auret, W.O. Barnard, G. Myburgh and L.J. Bredell; To be published in S.A. Journal of Sci. (1991).

Ay 81 A. Aydinli, and R.J. Mattauch; J. Electrochem. Soc. **128** (1981) 2635.

Ba 47 J. Bardeen; Phys. Rev. **71** (1947) 717.

Ba 75 J.S. Barrera and R.J. Archer; IEEE Trans. on Electron Devices. **ED22** (1975) 1023.

Ba 80 G. Badertscher, R.P.Salathe and W. Luthy; Electron. Lett. **16** (1980) 113.

Ba 80b J.E.E. Baglin, F.M. d'Heurle and C.S. Petersson; Appl. Phys. Lett. **36** (1980) 594.

Digitised by the Department of Library Services in support of open access to information, University of Pretoria, 2021

Ba 80c C.Barrett and T.B. Massalski; Structure of Metals. Crystallographic Methods, Principles and Data. International Series on Materialscience and Technology, ed. H.G. Hopkins, (Pergamon Press, UK, 1980) Vol. 35.

Ba 81 P.A. Barnes and R.S. Williams; Solid-St. Electron. **24** (1981) **907**.

Ba 84 J.E.E. Baglin, H.B. Harrison, J.L. Tandon and J.S. Williams; Conference on Ion implantation and beam processing. (Chapter 11), eds. J.S. Williams and J.M. Poate (Academic Press, Sydney, Australia, 1984) 387.

Ba 87 G. Bahir, L.J. Merz, J.R. Abelson and T.W. Sigmon; J. Electornic Materials **16** (1987) 257.

Ba 87b A.J. Barcy, M. Domanski, J. Jagielski and E. Kaminska; Nucl. Instrum. and Meth. Phys. Res. **B19/20** (1987) 773.

Ba 88 W.O. Barnard and A.J. Willis; Thin Solid Films **165** (1988) 77.

Ba 88b W.O. Barnard, J.B. Malherbe and B.M. Lacquet; Appl. Surf. Sci. **31** (1988) 437.

Ba 88c W.O. Barnard, H.J. Strydom, M.M. Kruger, C. Schildhauer and B.M. Lacquet; Nucl. Instr. Meth. Phys. Res. B. **35** (1988) 238.

Ba 89 R.K. Ball; Thin Solid Films **176** (1989) 55.

Ba 90 W.O. Barnard and G. Myburg: To be published in S. Afr. J. Science (1990).

Ba 91 W.O. Barnard, J.B. Malherbe and G. Myburg; To be published in S. Afr. J. Phys. (1991).

Be 42 H.A. Bethe; MIT Radiation Laboratory Report 43-12 (1942).

Be 72 H.H. Berger; Solid-St. Electron. **15** (1972) 145.

Be 72a H.H. Berger; J. Electrochem. Soc. **119** (1972) 507.

Be 81 P.A. Bertrand; J. Vac. Sci. Technol. **18** (1981) 28.

Digitised by the Department of Library Services in support of open access to information, University of Pretoria, 2021

Bh 85 R.S. Bhattacharya, A.K. Rai, A. Ezis, M.H. Rashid, P.P. Pronko; J. Vac.Sci. Technol. A. **3** (1985) 2316.

Bi 80 J.P. Biersack and L.G. Haggmark; Nucl. Inst. and Meth. **174** (1980) 257.

Bo 71 R.W. Bower; U.S. Patent, No. 3, 600 797 (August 1971).

Bo 86 A.P. Botha and E. Relling; Mat. Res. Soc. Symp. Proc. **54** (1986) 423.

Bo 87 Borland Software; Borland International, 4585 Scotts Valley Drive Scotts Valley, California, USA (1987).

Br 67 N. Braslau, J.B. Gunn and J.L. Staples; Solid-St. Electron. **10** (1967) 381.

Br 71 R.D. Brookes and H.G. Mathes; Bell Syst. Tech. Journal **50** (1971) 775.

Br 74 F. Brawn; Poggendorff's Annalen **153** (1974) 556.

Br 78 L.J. Brillson; Phys. Rev. Lett. **40** (1978) 260.

Br 81 N. Braslau; J. Vac. Sci. Technol. **19** (1981) 803.

Br 81b L.J. Brillson, C.F. Brucker, A.D. Katnani, N.G. Stoffel and G. Margaritondo; J. Vac. Sci. Technol. **19** (1981) 661.

Br 81c L.J. Brillson, C.F. Brucken, A.D. Katnani, N.G. Stoffel and G. Margaritondo; Appl. Phys. Lett. **38** (1981) 784.

Br 82 L.J. Brillson, C.F. Brucker, A.D. Katnani, N.G. Stoffel, R. Daniels and G. Margaritondo; J. Vac. Sci. Technol. **21** (1982) 564.

Br 83 D. Briggs and M.P. Seah; Practical Surface Analysis by Auger and X-Ray Photoelectron Spectroscopy (Wiley, Chichester, UK, 1983).

Br 86 N. Braslau; J. Vac. Sci. Technol. **A6** (1986) 3085.

Br 86b A. Brown, N.D. Gerrand, P. Humphrey, A.M. Patterson, J.C. Vickerman and J.O. Williams; Chemtronics **1** (1986) 64.

Digitised by the Department of Library Services in support of open access to information, University of Pretoria, 2021

Ch 90 M.-C. Chen; Binational Symposium on Electronic Materials and Devices, Univ. of Port Elizabeth, South Africa, July (1990).

Cl 80 D.T. Clark, T. Kok, G.G. Roberts and R.W. Sykes; Thin Solid Films **70** (1980) 261.

Co 65 A.M. Cowley and S.M. Sze; J. Appl. Phys. **36** (1965) 3212.4

Co 66 C.J. Cooke and W. Hume-Rothery; J. Less Common Met. **10** (1966) 42.

Co 67 R.H. Cox and H. Strack; Solid-St. Electron. **10** (1967) 1213.

Co 83 S.C. Cohen; Symp. Proc. Mat. Res. Soc. **18** (1983) 361.

Co 89 E.D. Cole, S. Sen and L.C. Burton; J. Electronic Mater. **18** (1989) 527.

Cr 66 C.R. Crowell and S.M. Sze; Solid-St. Electron. **9** (1966) 1035.

Cr 69 C.R. Crowell and V.L. Rideout; Solid-St. Electron. **12** (1969) 89.

Cz 75 A.W. Czanderna; Methods of Surface Analysis; (Elsevier Scientific Publishing Company, The Netherlands, 1975).

Da 78 L.E. Davis, N.C. MacDonald, P.W. Palmberg, G.E. Riach and R.E. Weber; Handbook of Auger Electron Spectroscopy (Physical Electronics Division, Perkin-Elmer Corp., USA, 1978).

Da 81 R. D'Angelo and P.A. Verlangieri; Electron. Lett. **17** (1981) 290.

Da 84 W.C. Dautremont-Smith, P.A. Barnes and J.W. Stayt; J. Vac. Sci. Technol. B. **2** (1984) 620.

Da 87 K. Daoud-Ketata, C. Dubon-Chevallier, C. Besombes, J.F. Bresse and P. Henoc; Electron. Lett. **23** (1987) 17.

De 80 W.J. Devlin, C.E.C. Wood, R. Stall and L.F. Eastman; Solid-St. Electron. **23** (1980) 823.

Digitised by the Department of Library Services in support of open access to information, University of Pretoria, 2021

De 88 J.A. Del Alamo and T. Mizutani; Solid-St. Electron. **31** (1988) 1635.

Di 86 W. Dingfen, D. Wang and K. Heime; Solid-St. Electron. **29** (1986) 489.

Di 87 J. Ding, J. Washburn, T. Sands and V.G. Keramidas; Proc. Int. Symp. on GaAs and Related Compounds (Inst. of Physics, Bristol, UK, 1987) 313.

Du 90 R. Dutta, A. Lahav, M. Robbins and V.G. Lambrecht; J. Appl. Phys. **67** (1990) 3136.

Du 90b J. Durr and G.B. Stringfellow; J. Electronic Materials. **19** (1990) L1.

Ec 80 G. Echardt; Laser and Electron Beam Processing of Materials, eds. C.W. White and P.S. Peercy (Academic Press, New York, USA, 1980) 467.

Ec 80b G. Eckhardt, C.L. Anderson, M.N.Coborn, L.D. Hess and R.A. Jullens; Laser and Electron beam Processing of Electronic Materials, eds. C.L. Anderson, C.K. Celler and G.A. Rozgonyi (Electrochem. Soc. Princeton, NJ, USA, 1980) 445.

El 65 R.P. Elliott; Constitution of Binary Alloys; First Supplement (MacGraw-Hill, New York, USA, 1965).

El 85 B. Elfsten and P.A. Tove; Solid-St.Electron. **28** (1985) 721.

El 87 R. Elias, S. Mahajan, C.L. Bauer, A.G. Milnes and W.A. Borner; J. Appl. Phys. **62** (1987) 1245.

Er 79 L.P. Erickson, A. Waseem and G.Y. Robinson; Thin Solid Films **64** (1979) 421.

Es 89 T.S. Eschrich, R.D. Carroll, R.N. Sacks and W.J. Tanski; IEEE Trans. on Electron Devices **36** (1989) 1213.

Fa 74 R.F.C. Farrow; J. Phys. D. **7** (1974) 2436.

Fa 78 R.F.C. Farrow, A.G. Cullis, A.J. Grant, J.E. Pattison; J. Cryst. Growth **45** (1978) 292.

Digitised by the Department of Library Services in support of open access to information, University of Pretoria, 2021

Fa 79 J.C.C. Fan, J.P. Donnely, C.O. Bozler and R.L. Chapman; Inst. Phys. Conf. Ser. **45** (1979) 472.

Fa 79a Y.K. Fang, C.Y. Chang and Y.K. Su; Solid-St. Electron. **22** (1979) 933.

Fa 84 D. Fathy, O.L. Krivanek, J.C.H. Spence and W.M. Paulson; Mat. Res. Soc. Symp. Proc. **25** (1984) 557.

Fa 89 N.S. Fatemi and V.G. Weizer; J. Appl. Phys. **65** (1989) 2111.

Fi 75 T.G. Finstad, T. Andreassen and T. Olsen; Thin Solid Films **29** (1975) 145.

Fl 87 F. Flores and C. Tejedor; J. Phys. C: Solid-St. Phys. **20** (1987) 145.

Fr 80 D. Fritzsche; Inst. Phys. Conf. Ser. No. **50** (1980) 258.

Fr 81 J.L. Freeouf and J.M. Woodall; Appl. Phys. Lett. **39** (1981) 727.

Fu 86 S. Furukawa, T. Asano, T. Fukada, H. Ishiwara and K. Tsutsui; Mat. Res. Soc. Symp. Proc. **54** (1986) 207.

Fu 87 T. Fukada, T. Asano, S. Frufawa and H. Ishiwara; Japn. J. Appl. Phys. **26** (1987) 117.

Ge 88 M. Genut and M. Eizenberg; Appl. Phys. Lett. **53** (1988) 672.

Gh 83 C. Ghosh, P. Yenigalla and K. Atkins; IEEE Electron Devices Lett. **EDL4** (1983) 301.

Gi 88 S.S. Gill and J.R. Dawsey; Thin Solid Films **167** (1988) 161.

Gl 78 K.R. Gleason, H.B. Dietrich, R.L. Henry, E.D. Cohen and M.L. Bark; Appl. Phys. Lett. **32** (1978) 578.

Go 70 Y. Goldberg and B.V. Isarenkov; Sov. Phys. Semicond. **3** (1970) 1497.

Go 88 Y.A. Gol'dberg, T.V. L'vova, R.V. Khasieva, B.V. Tsarenkov; Sov. Phys. Semicond. **22** (1988) 1081.

Digitised by the Department of Library Services in support of open access to information, University of Pretoria, 2021

Go 89 H. Goronkin, S. Tehrani, T. Remmel, P.L. Fejes and K.J. Johnson; IEEE Trans. on Electron Devices **36** (1989) 281.

Gr 79 A.C. Greenwald, A.R. Kirkpatrick, R.G. Little, J.A. Mannuci; J. Vac. Sci. Technol. **16** (1979) 1838.

Gr 80 H.R. Grinolds and G.Y. Robinson; Solid-St. Electron. **23** (1980) 973.

Gr 83 R.J Graham and J.W. Steeds; Inst. Phys. Conf. Ser., Section 10, **67** (1983) 507.

Gr 83b C.R.M. Grovenor; Thin Solid Films **104** (1983) 409.

Gr 87 W.H. Gries and K. Miethe; Microchim. Acta **1** (1987) 169.

Gr 88 R.J. Graham, H.H. Erkaya and R.J. Roedel; J. Electrochem. Soc. **135** (1988) 266.

Gu 76 W. Gudat and D.E. Eastman; J. Vac. Sci. Technol. **42** (1976) 831.

Gu 84 A. Guivarc'h, H. L'Haridon,G. Pelous, G. Hollinger and P. Pertosa; J. Appl. Phys. **55** (1984) 1139.

Gu 86 M. Gurvitch, A. Kastalsky, S. Schwarz, D.M. Hwang, D. Butherus, S. Pearton and C.R. Gardner; J. Appl. Phys. **60** (1986) 3204.

Gu 90 R.P. Gupta, W.S. Khokle, J. Wuerfl and H.L. Hartnagel; J.Electrochem. Soc. **137** (1990) 631.

Ha 58 M. Hansen; Constitution of Binary Alloys (McGraw-Hill, New York, USA, 1958).

He 48 D.F. Hewitt; Econ. Geol. **43** (1948) 408.

He 77 A. Heraki, K. Shuto, S. Kim, W. Kammura and M. Iwami; Appl. Phys. Lett. **31** (1977) 611.

He 82 M. Heiblum, M.I. Nathan and C.A. Chang; Solid-St. Electron. **25** (1982) 185.

He 84 H.G. Henry, D.E. Dawson, Z.J. Lemnios and H. Kim; IEEE Trans. on Electron Devices **ED31** (1984) 1100.

Digitised by the Department of Library Services in support of open access to information, University of Pretoria, 2021

He 84a H.K. Henisch; Semiconductor contacts: An approach to ideas and models; Intern. series of monograph's on Phys. No 70, eds. P.J. Elliott, J.A. Krumhansl and D.K. Wilkinson (Clarendon Press, Oxford, UK, 1984).

He 88 J. Herniman, D.A. Alan and P.J. O'Sullivan; IEE Proc. in Solid-St. Electronic Devices **135** (1988) 67.

He 89 H.G. Henry; IEEE Trans. on Electron Devices **36** (1989) 1390.

Hi 63 S.E.R. Hiscocks and W. Hume-Rothery; Proc. R. Soc. London Ser. **A282** (1963) 318.

Hi 88 I.R. Hill, W.M. Lau, G.R. Yang and R.A. North; Surf. and Inter. Anal. **11** (1988) 596.

Ho 71 P.L. Hower, W. Hooper, R. Cairns, R. Fairman and D. Tremere; Semicondocturs and Semimetals No. **7**, eds. R.K.Willardson and A.C. Beer (Academic Press, New York, USA, 1971) 147.

Hu 78 C.E. Hurwitz and J.J. Hsieh; Appl. Phys. Lett. **32** (1978) 487.

Il 83 A. Iliadis and K.E. Singer; Solid-St. Electron. **26** (1983) 7.

Im 87 S. Imanaga, H. Kawai, K. Kajiwara, K. Kaneko and N. Watanabe; J. Appl. Phys. **62** (1987) 2381.

In 85 T. Inada, H. Kakinuma, A. Shirota, J. Matsomoto, M. Ishikiriyama and Y. Funaki; Nucl. Instrum. and Meth. Phys. Res. B. **7/8** (1985) 576.

Ir 78 L.D. Irving, J.E. Pattison, P.W. Braddock and K.W. Gray; Elecron. Lett. **14** (1978) 116.

Is 84 A. Ismail, J.M. Palau and L. Lassabatere; Phys. Appl. **19** (1984) 205.

Is 86 K. Ishii, T. Ohshima, T. Futatsugi, T. Fujii, N. Yokoyama and A. Shibatomi; Int. Elec. Dev. Mtg., Technical Digest (1986) 274.

Is 87 A. Ismail, A.B. Brahim, M. Dumas and L. Lassabatere; J. Vac. Sci. Technol. B. **5** (1987) 621.

Digitised by the Department of Library Services in support of open access to information, University of Pretoria, 2021

It 84 H. Ito, T. Ishibashi and T. Sugeta; Japn. J. Appl. Phys. **23** (1984) L635.

Iv 88 D.G. Ivey, R. Bruce and G.R. Piercy; J. Electron. Mater. **17** (1988) 373.

Iv 89 Z.G. Ivanov; Phys. Stat. Sol. (a) **113** (1989) 439.

Ja 87 E. Jaroli, B. Pecz, J. Gyulai, M. Fried, L. Petras, E. Zsoldos, T. Lohner and I. Mojzes; Nucl. Instrum. and Meth. Phys. Res. B. **19/20** (1987) 767.

JCPDS Diffraction File. Distributed by the International Center for Diffraction Data, 1601 Park Lane Swarthmore, PA, USA.

Ji 88 Z. Jie and D.A. Thompson; J. Electronic Materials **17** (1988) 249.

Ka 80 T. Kawakami and M. Okamura; IEDM (1980) 445.

Ka 81 W. Katz, G. Smith, O. Aina and B.J. Baliga; Appl. Surf. Sci. **9** (1981) 122.

Ka 84 T.S. Kalkur, J.Dell and A.G. Nassibian; Int. J. Electron. **57** (1984) 729.

Ka 85 T.S. Kalkur, A.G. Nassibian and A. Rose; IEEE Electronic Device Lett. **EDL6** (1985) 489.

Ka 85b A.N. Kabanov, A.B. Kamnev and B.A. Lapshinov; Poverkhn. Fiz. Khim. Mekh. **2** (1985) 2.

Ka 86 Y.V. Kameneckas, V.S. Kulikauskas, G.B. Skorobogates and D.Y. Eidukas; Phys. Chem. Meth. Suf. **4** (1986) 616.

Ka 87 T.S. Kalkur and A.G. Nassibian; Solid-St. Electron. **30** (1987) 619.

Ka 87b T.S. Kalkur and A.G. Nassibian; Semicond. Sci. Technol. **2** (1987) 615.

Ka 88 R. Kaumanns, N.Grote, H.G. Bach and F. Fidorra; Gallium Arsenide and Related Compounds 1987, Proc. the 14th Internat. Symp., eds. A. Christou and H.S.Rupprecht (IOP, Bristol, UK, 1988) 501.

Digitised by the Department of Library Services in support of open access to information, University of Pretoria, 2021

Ka 89 H.J. Kang, Y.M. Moon, T.W. Kang, J.Y. Leem, J.J. Lee and D.S. Ma; J. Vac. Sci. Technol. A.**7** (1989) 3251.

Ka 89b A. Katz, W.C. Dautremont-Smith, P.M. Thomas, L.A. Koszi, J.W. Lee, V.G. Riggs, R.L. Brown, J.L. Zilko and A. Lahav, J. Appl. Phys. **65** (1989) 4319.

Ka 90 A. Katz, B.E. Weir, S.N.G. Chu, P.M. Thomas, M. Soler, T. Boone and W.C. Deutremont-Smith; J. Appl. Phys. **67** (1990) 3872.

Ke 81 V.G. Keramidas, H. Temkin and S. Mahajan; Inst. Phys. Conf. Ser. **56** (1981) Ch. 5.

Ke 82 V.G. Keramidas; Thin Solid Films **96** (1982) 347.

Ke 85 A.A. Ketterson, F. Ponse, T. Henderson, J. Klem, C.-K. Peng and H. Morkoc; IEEE Trans. on Electron Devices **ED32** (1985) 2257.

Ke 85a T. Kendelewicz, N.Newman, R.S. List, I. Lindau and W.E. Spicer; J. Vac. Sci. Technol. B.**3** (1985) 1206.

Ki 85 P.D. Kirchner, T.N. Jackson, G.D. Pettit and J.M. Woodall; Appl. Phys. Lett. **47** (1985) 26.

Ki 87 T. Kim, D.D.L. Chung and S. Mahajan; Mat. Res. Soc. Symp. Proc. **77** (1987) 749.

Kl 74 H.P. Klug and L.E. Alexander; X-ray Diffraction Procedures for Polycrystalline and Amorphous Materials; (John Wiley & Sons, New York, USA, 1974.

Ko 89 E. Kolawa, W. Flick, C.W. Nieh, J.M. Molarius, M.-A. Nicolet, J.L. Tandon, J.H. Madok and F.C.T. So; IEEE Trans. on Electron Devices **36** (1989) 1223.

Kr 85 H. Krautle and D. Wachenschwanz; Solid-St. Electron. **28** (1985) 601.

Ku 79 S.S. Kular, B.J. Sealy, M.H. Badawi, K.G. Stephens, D.Sadana and G.R. Booker; Electron. Lett. **15** (1979) 413.

Ku 81 E. Kuphal; Solid-St. Electron **24** (1981) 69.

Ku 82 A.K. Kulkarni and T.J. Blankinskip; Thin Solid Films **96** (1982) 285.

Digitised by the Department of Library Services in support of open access to information, University of Pretoria, 2021

Ku 83 T.S. Kuan, P.E. Batson, T.N. Jackson, H. Rupprecht and E.L. Wilkie; J. Appl. Phys. **54** (1983) 6952.

Ku 86 A.K. Kulkarni and J.T. Lukowski; J. Appl. Phys. **59** (1986) 2901.

Kw 79 H.L. Kwok and W.C. Siu; Thin Solid Film **61** (1979) 249.

Kw 86 J.H. Kwiatkowski; Mat. Res. Soc. Symp. Proc. **54** (1986) 427.

Kw 87 C.S. Kwon, I.H. Choi, M.S. Kim, K.N. Kang and J.C. Jeong; New Phys. **27** (1987) 66.

La 81 D.H. Laughlin and C.W. Wilmsen; Appl. Phys. Lett. **37** (1981) 915.

La 84 A.A. Lakhani; J. Appl. Phys. **56** (1984) 1888.

La 84b A.A. Lakhani and D.R. Urech; Mater. Res. Soc. Symp. Proc. **25** (1984) 551.

La 85 D. Lamouche, P. Clechet, J.R. Martin, G. Haroutiounian and J.P. Sandino; Surf. Sci. **161** (1985) L554.

La 85b T. Lalinsky, P. Kordos, B. Kovacs, I. Mojzes, B. Szentpali and A. Tichy-Racz; Phys. Stat. Sol.(a) **88** (1985) K87.

La 86 D. Lamouche, J.R. Martin, P. Clechet, G. Haroutiounian and J.P. Sandino; Solid-St. Electron. **29** (1986) 625.

La 86b A.A. Lakhani; J. Appl. Phys. **59** (1986) 2082.

La 86c A. Lahav, M. Eizenberg and A. Komen; J. Appl. Phys. **60** (1986) 991.

Le 80 C.P. Lee, J.L. Tandon and P.J. Stocker; Electron. Lett. **16** (1980) 849.

Le 81 C.P. Lee, B.M. Welch and W.P. Fleming; Japn J. Appl. Phys. **17** (1981) 407.

Le 81b C.P. Lee, B.M. Welch and T.L. Tandon; Appl. Phys. Lett. **39** (1981) 556.

Digitised by the Department of Library Services in support of open access to information, University of Pretoria, 2021

Li 79 R.G. Little and A.C. Greenwald; Semicond. Int. **2** (1979) 81.

Li 80 S.G. Liu, C.P. Wu and C.W. Magee; Laser and Electron Beam Processing of Materials, eds. C.W. White and P.S. Peercy (Academic Press, New York, USA, 1980) 341.

Li 86 Z. Liliental-Weber, R. Gronsky, J. Washburn, N. Newman, W.E. Spicer and E.R. Weber; J. Vac. Sci. Technol. B. **4** (1986) 912.

Lo 77 J.E. Loveluck, G.M. Rackham and J.W. Steeds; Inst. Phys. Conf. Ser. **36** (1977) 297.

Lo 86 F. Lonnum and J.S. Johannessen; Electron. Lett. **22** (1986) 632.

Lu 89 Z.H. Lu, C. Lagarde, E. Sacher, J.F. Currie and A. Yelon; J. Vac. Sci. Technol. A **7** (1989) 646.

Ma 80 J. Massies, F. Dezaly and N.T. Linh; J. Vac. Sci. Technol. **17** (1980) 1134.

Ma 81 G.M. Martin, A. Mitonneau, M. Cathelin, S. Makram-Ebeid, C. Venger, D. Barbier and A. Laugier; Laser and Electron-Beam Solid Interactions and Materials Processing, eds. J.F. Gibbons, L.D. Hess and T.W. Sigmon (North-Holland, New York, USA, 1981) 299.

Ma 81b J. Massies, J. Chaplart, M. Laviron and N.T. Linh; Appl. Phys. Lett. **38** (1981) 693.

Ma 81c F. Masszi, L. Stolt, P.A. Tove and K. Tarnay; Phys. Scripta **24** (1981) 456.

Ma 82 G.S. Marlow and M.B. Das; Solid-St. Electron **25** (1982) 91.

Ma 83 G.S. Marlow, M.B. Das and L. Tongson; Solid-St. Electron. **26** (1983) 259.

Ma 84 E.D. Marshall, C.S. Wu, D.M. Scott, S.S. Lau and T.F. Kuech; Proc. of Thin Films and Interfaces, eds. J.E.E. Baglin, D.R. Campbell and W.K. Chu (North-Holland, New York, USA, 1984) 63.

Digitised by the Department of Library Services in support of open access to information, University of Pretoria, 2021

Ma 85 D.C. Marvin, N.A. Ives and M.S. Leung; J. Appl. Phys. **58** (1985) 2659.

Ma 85b E.D. Marshall, W.X. Chen, C.S. Wu, S.S. Lau and T.F. Kuech; Appl. Phys. Lett. **47** (1985) 298.

Ma 86 D.C. Marvin, N.A. Ives and M.S. Leung; Mat. Res. Soc. Symp. Proc. **54** (1986) 443.

Ma 87 E.D. Marshall, B. Zhang, L.C. Wang, P.F. Jiao, W.X. Chen, T. Sawada, K.L. Kavanagh and T.F. Kuech; J. Appl. Phys. **62** (1987) 942.

Ma 87b T.B. Massalski (Editor-in-Chief), Eds. T.L. Murray, L.H. Bennett, H. Baker, L. Kacprzak; Binary Alloy Phase Diagrams (American Society of Metals, Metal Park, Ohio, USA, 1987) Volume 1 and 2.

Ma 89 J.B. Malherbe, W.O. Barnard, G. Myburg and L.J. Bredell; S. Afr. J. Phys. **12** (1989) 13c.

Ma 91 J.B. Malherbe and W.O. Barnard; To be published in Surf. Sci. (1991).

Mc 78 G.E. Mcguire; Surf. Sci. **76** (1978) 130.

Mc 79 G.E. McGuire; Auger Electron Spectroscopy Reference Manual (Plenum Press, New York, USA, 1979).

Mc 80 A. McKinley, A.W. Parke and R.H. Williams; J. Phys. C: Solid-St. Phys. **13** (1980) 6723.

Me 63 C.A. Mead and W.G. Spitzer; Phys. Rev. Lett. **10** (1963) 471.

Me 64 C.A. Mead and W.G. Spitzer; Phys. Res. **34** (1964) A713.

Me 69 C.A. Mead; Ohmic contacts to Semiconductors; ed. B.Schwartz (Electronical Soc., New York, USA, 1969).

Me 89 I. Mehdi, U.K. Reddy, J. Oh, J.R. East and G.I. Haddad; J. Appl. Phys. **65** (1989) 867.

Me 89a E. Meyer and G. Heymann; J. Vac. Sci. Technol. B. **7** (1989) 491.

Digitised by the Department of Library Services in support of open access to information, University of Pretoria, 2021

Mi 75 H.T. Mills and H.L. Hartnagel; Electronics Lett. 11 (1975) 621.

Mi 79 H.T. Mills and H.L. Hartnagel; Int. J. Electronics 46 (1979) 65.

Mi 80 D.C. Miller; J. Electrochem. Soc. **127** (1980) 476.

Mo 38 N.F. Mott; Proc. Camb. Phil. Soc. **34** (1938) 568.

Mo 76 N.M. Morris; Semiconductor Devices (The Macmillian Press Ltd., London, UK, 1976).

Mo 81 H. Morkoe, T.J. Drummond and C.M. Stanchak; IEEE Trans. on Electron Devices **ED28** (1981) 1.

Mo 81b D.V. Morgan; Reliability and Degradation, eds. M.J. Howes and D.V. Morgan (Wiley, Chichester, UK, 1981) 151.

Mo 81c D.V. Morgan, F.H. Eisen and A. Ezis; IEEE Proc. Pt 1 128 (1981) 109.

Mo 83 I. Mojzes, D. Szigethy and R. Veresegyhazy; Electron Lett. **19** (1983) 117.

Mo 84 I. Mojzes; Solid-St. Electron. **27** (1984) 925.

Mo 86 I. Mojzes, R. Veresegyhazy and V. Malina; Thin Solid Films **144** (1986) 29.

Mu 69 H. Murrmann and D. Widmann; IEEE Trans. Electron Devices **ED16** (1969) 1022.

Mu 69a H. Murrmann and D. Widmann; Solid-St. Electron. 12 (1969) 879.

Mu 85 S.D. Mukherjee and D.W. Woodard; Galluim Arsenide Materials, Devices and Circuits, eds. M.J. Howes and D.V. Morgan (John Wiley & Sons, Chichester, UK, 1985) Ch 4.

Mu 86 M. Murakami, K.D. Childs, J.M. Baker and A. Callegari; J. Vac. Sci. Technol. B. **4** (1986) 903.

Mu 87 M. Murakami, W.H. Price, Y. Shih, K.D. Childs, B.K. Furman and S. Tiwari; J. Appl. Phys. **62** (1987) 3288.

Digitised by the Department of Library Services in support of open access to information, University of Pretoria, 2021

Mu 87b M. Murakami, W.H. Price, Y.C. Shih, N. Braslau, K.D. Childs and C.C. Parks; J. Appl. Phys. **62** (1987) 3295.

Mu 87c M. Murakami and W.H. Price; Appl. Phys. Lett. **51** (1987) 664.

Mu 88 M. Murakami, Y. Shih, W.H. Price and E.L. Wilkie; J. Appl. Phys. **64** (1988) 1974.

Mu 88b M. Murakami, Y.C. Shih, H.J. Kim, W.H. Price; 20th Conference on Solid State Devices and Materials, (Bus. Center for Acad. Soc., Tokyo, Japan, 1988) 283.

Mu 89 M. Murakami, W.H. Price, J.H. Greiner and J.D. Feder; J. Appl. Phys. **65** (1989) 3546.

Mu 89b M. Murakami, H.J. Kim, Y.-C. Shih, W.H. Price and C.C. Parks; Appl. Surf. Sci. **41/42** (1989) 195.

My 91 G. Myburg; Ph.D. Thesis, Univ. of Pretoria, South Africa (1991).

Na 82 M.I. Nathan and M. Heiblum; Solid-St. Electron. 25 (1982) 1063.

Na 85 A.G. Nassibian and T.S. Kalkur; Appl. Surf. Sci. 22/23 (1985) 1019.

Ne 88 S.A. Neustroev, V.A. Bespalov, D.A. Nazarov and M.M. Artamonov; Mikroelektronika (USSR) **17** (1988) 8.

Ne 89 E. Nebauer and U. Lohse; Phys. Stat. Sol. (a) **115** (1989) K171.

Ni 71 V. Y. Niskov and G.A. Kubetskii; Sov. Phys. Semicond. 4 (1971) 1553.

Ni 81 Y.I. Nissim, J.F. Gibbons and R.B. Gold; IEEE Trans. on Electron Devices **ED28** (1981) 607.

Ni 82 Y.I. Nissim, M. Greiner, R.J. Falster, J.F. Gibbons, P. Chye and C. Huang; Laser and Electron Beam Interactions with Solids, eds. B.R. Appleton and G.K.Celler (North-Holland, Amsterdam, Netherlands, 1982) 677.

Digitised by the Department of Library Services in support of open access to information, University of Pretoria, 2021

Ni 86 T. Nittono, H. Ito, O. Nakajima and T. Ishibashi; Japn. J. Appl. Phys. **25** (1986) L865.

Ni 88 T. Nittono, H. Ito, O. Nakajima and T. Ishibashi; Jpn. J. Appl. Phys. **27** (1988) 1718.

Og 80 M. Ogawa; J. Appl. Phys. **51** (1980) 406.

Oo 76 A. Oostrom; J. Vac. Sci. Technol. **13** (1976) 224.

Or 81 A.H. Oraby, K. Murakami, Y. Yuba, K. Gamo, S. Namba and Y. Musuda; Appl. Phys. Lett. **38** (1981) 562.

Ot 88 T. Otsuki, H. Aoki, H. Takagi and G. Kano; J. Appl. Phys. **63** (1988) 2011.

Pa 66 F.A. Padovani and R. Stratton; Solid-St. Electron. 9 (1966) 695.

Pa 71 F.A. Padovani; Semiconductor and Semimetals; 6A, eds. R.K. Willardson and A.C. Beer (Academic Press, New York, USA, 1971) Ch. 2.

Pa 72 P.W. Palmberg; Auger Electron Spectroscopy (Balzers High Vacuum Report, 1972).

Pa 73 P.M. Palmberg; Anal. Chem. **45** (1973) 549a.

Pa 82 J.M. Palau, E.Testermale, A. Ismail and L. Lassabatere; Solid-St. Electron. **25** (1982) 285.

Pa 85 C.J. Palmstrom, K.L. Kavanagh, M.J. Hollis, S.D. Mukherjee and J.W. Mayer; Mat. Res. Soc. Symp. Proc. 37 (1985) 473.

Pa 85a C.J. Palmstrom and G.J. Galvin; Appl. Phys. Lett. 47 (1985) 815.

Pa 85b C.J. Palmstrom and D.V. Morgan; Gallium Arsenide Materials, Devices and Circuits, eds. M.J. Howes and D.V. Morgan (John Wiley & Sons, Chichester, UK, 1985) Ch. 6.

Pa 86 W. Patrick, W.S. Mackie, S.P. Beaumont, C.D.W. Wilkinson; Appl. Phys. Lett. **48** (1986) 986.

Digitised by the Department of Library Services in support of open access to information, University of Pretoria, 2021

Pa 87 K.P. Pande, E. Martin, D. Gutierrez and O. Aina; Solid-St. Electron. **30** (1987) 253.

Pa 87a D.G. Parker; GEC Journal of Research **5** (1987) 116.

Pa 87b V. Pargual, P.N. Favennec, M. Gauneau, Y. Rihet, R. Chaplain, H. L'Haridon and C. Vaudry; J. Appl. Phys. 62 (1987) 824.

Pa 88 A. Paccagnella, A. Migliori, M. Vanzi, B. Zhang and S.S. Lau; Proc. of the 17th European Solid-St. Devices Res. Conf., eds. G. Soncini and P.U. Calzolari (Elsevier North-Holland, Amsterdam, Netherlands, 1988) 839.

Pa 90 A. Paccagnella, L.C. Wang, C. Canali, G. Castellaneta, M. Dapor, G. Donzelli, E. Zanoni and S.S. Lau; Thin Solid Films **187** (1990) 9.

Pe 83 D.C. Peacock; Vacuum **33** (1983) 601.

Pe 88 C.K. Peng, G. Ji, N.S. Kumar and Morkoc; Appl. Phys. Lett. **53** (1988) 900.

Pf 50 H. Pfisterer and K. Schubert; Z. Metallkd. **41** (1950) 358.

Pi 80 P.A. Pianetta, C.A. Stolte and J.L. Hansen; Laser and Electron Beam Processing of Materials, eds. C.W. White and P.S. Peercy (Academic Press, New York, USA, 1980) 328.

Pi 80b P.A. Pianetta, C.A. Stolte and J.L. Hansen; Appl. Phys. Lett. **36** (1980) 597.

Pi 81 P.A. Pianetta, J. Amano, G. Wolhouse and C.A. Stole; Laser and electron beam processing of materials,eds. J.F. Gibbons, T. Sigman and L. Hess (Elsevier, North-Holland, New York, USA, 1981).

Pi 81b A. Piotrowska, A. Guivarc'h and G. Pelous; J. Appl. Phys. **52** (1981) 5112.

Pi 83 A. Piotrowska, A. Guivarc'h and G. Pelous; Solid-St. Electron. **26** (1983) 179.

Pr 83 S.J. Proctor, L.W. Linholm and J.A. Mazer; IEEE Trans. on Electron Devices **ED-30** (1983) 1535.

Digitised by the Department of Library Services in support of open access to information, University of Pretoria, 2021

Pr 86 M. Procop and B. Sandow; Phys. Stat. Sol. (a) **95** (1986) K211.

Pr 87 M. Procop, B. Sandow, H. Raidt and L.I. Do Son; Phys. Stat. Sol. (a) **104** (1987) 903.

Pr 88 K. Prasad, Z. Meglicki, L.Faraone and A.G. Nassibian; 7th Australian Microelectronic Conference Proceedings (IREE, Edgecliff, NSW, Australia, 1988) 61.

Pr 89 K. Prasad, L. Faraone and A.G. Nassibian; Semicond. Sci. Technol. **4** (1989) 657.

Pr 89b K. Prasad, L. Faraone and A.G. Nassibian; Semicond. Sci. Technol. **4** (1989) 458.

Pu 86 J.H. Pugh and R.S. Williams; J. Mater. Res. **1** (1986) 343.

Ra 73 P. Rai-Choudhury and P.L. Hower; J. Electrochem. Soc. **120** (1973) 1761.

Ra 77 G.M. Rackham and J.W. Steeds; Report on CVD, (Project RU41-4), Univ. of Bristol, UK, 1977.

Ra 81 G.M. Rackham and J.M. Steeds; Inst. Phys. Conf. Ser. 60 (1981) 397.

Ra 87 A.K. Rai, A. Ezis, A.W. McCormick, A.K. Petford-Long and D.W. Langer; J. Appl. Phys. **61** (1987) 4682.

Ra 89 J.N. Randall, C.H. Yang, Y.C. Kao and T.M. Moore; J. Vac. Sci. Technol. A. **7** (1989) 2007.

Re 88 E. Relling and A.P. Botha; Appl. Surf. Sci. **35** (1988) 380.

Rh 78 E.H. Rhoderick; Metala-Semiconductor contacts (Oxford University Press, Oxford, UK, 1978).

Rh 82 E.H. Rhoderick; IEEE Proc. **129** (1982) 1.

Rh 88 E.H. Rhoderick and R.H. Williams; Metal-Semiconductor Contacts; Monographs in electrical and electronic engineering, eds. P. Hammond and R.L. Grimsdale (Clarendon Press, Oxford, UK, 1988) No. 19.

Digitised by the Department of Library Services in support of open access to information, University of Pretoria, 2021

Ri 70 V.L. Rideout and C.R. Crowell; Solid-St. Electron. 13 (1970) 993.

Ri 75 V.L. Rideout; Solid-St. Electron. **18** (1975) 541.

Ro 80 G.Y. Robinson; Thin Solid Films **72** (1980) 129.

Ro 81 M.T. Robinson; Sputter by Partical Bombardment, ed. R. Behrisch (Springer, Berlin, FRG, 1981), Vol. 1.

Ro 85 G.Y. Robinson; Physics and Chemistry of III - V compound semiconductor interfaces, ed. C.W. Wilmsen (Plenum, New York, USA, 1985).

Sa 84 E. Sandow, W. Wesch and E. Nebauer; Phys. Stat.Sol. (a). **85** (1984) K169.

Sa 85 A. Saidane and D.L. Kirk; J. Phys. D: Appl. Phys. 18 (1985) 1609.

Sa 85b T. Savada, W.X. Chen, E.D. Marshall, K.L. Kavanagh, T.F. Kuech, C.S. Pai and S.S. Lau; Mat. Res. Soc. Symp. Proc. **54** (1985) 409.

Sa 88 B. Sandow, E. Nebauer and H. Strusny; Phys. Stat. Sol. (a) **109** (1988) K35.

Sa 88b B. Sartorius, M. Schlah, M. Rosenzweig and K. Parschke; J. Appl. Phys. **63** (1988) 4677.

Sa 89 T. Sands; Materials Science and Engineering **B1** (1989) 289.

Sc 38 W. Schottky; Naturwissenshaften **26** (1938) 843.

Sc 39 W. Schottky and E. Spenke; Wiss. Veroff. Siemens-Werken **18** (1939) 225.

Sc 65 D.L. Scharfetter; IEEE Proc. **8** (1965) 299.

Sc 88 A. Scorzoni and M. Finetti; Materials Science reports 3 (1988) 79.

Se 80 T. Sebestyen, I. Mojzes and D. Szigethy; Electron. Lett. **16** (1980) 504.

Digitised by the Department of Library Services in support of open access to information, University of Pretoria, 2021

Sh 64 W. Shockley; Report A1-TOR-64-207 (Air Force Atomic Laboratory, Wright Patterson Air Force Base, OH, USA, 1964).

Sh 72 K.K. Shih and J.M. Blum; Solid-St. Electron. **15** (1972) 1177.

Sh 81 B.L. Sharma; Semiconductors and Semimetals, No. 15, eds. R.K. Willardson and A.C. Beer (Academic Press, New York, USA, 1981) 1.

Sh 84 B.L. Sharma; Metal-Semicondoctur Schottky barrier junctions and their applications, ed. B.L. Sharma (Plenum Press, New York, USA, 1984).

Sh 85 J. Shappirio, J. Finnegan, R. Lux, D. Fox, J. Kwiatkowski, H. Kattelus and M. Nicolet; J. Vac. Sci. Technol. A. **3** (1985) 2255.

Sh 86 J.R. Shappirio, R.A. Lux, K.J. Finnegan, D.C. Fox and J.H. Kwiatkowski; Mat. Res. Soc. Symp. Proc. **54** (1986) 427.

Sh 87 K. Shenai; IEEE Trans. on Electron Devices **ED34** (1987) 1642.

Sh 87b Y.-C. Shih, M. Murakami, E.L. Wilkie and A.C. Callegari; J. Appl. Phys. **62** (1987) 582.

Sh 89 Y. Shih, M. Murakami and W.H. Price; J. Appl. Phys. 65 (1989) 3539.

Si 77 V. Simic and Z. Marinkovic; Thin Solid Films, **41** (1977) 57.

Si 81 I.L. Singer, J.S. Murday and L.R. Cooper; Surf. Sci. 108 (1981) 7.

Si 84 P. Sircar and M. Aubin; Phys. Stat. Sol. (a). **85** (1984) 649.

Si 86 P. Sircar; Phys. Stat. Sol. (a) **97** (1986) K69.

Si 87 P. Sircar; Revue. Phys. Appl. **22** (1987) 967.

Sk 80 D.K. Skinner; J. of Electron Mater. **9** (1980) 67.

Digitised by the Department of Library Services in support of open access to information, University of Pretoria, 2021

Sk 89 T. Skrabka, M.J. Slaby and B. Mizera; Phys. Stat. Sol. (a). **112** (1989) K105.

Sm 69 B.L. Smith; Ph.D. Thesis, Manchester University (1969).

Sm 85 S.M. Smith and J.S. Solomon; Materials Lett. **3** (1985) 294.

Sm 86 S.R. Smith and J.S. Solomon; Stable Ohmic Contacts for Gallium Arsenide Semiconductors (US Patent 4, 570, 324, 1986).

So 63 A.L. Southern, W.R. Willis and M.T. Robinson; J. Appl. Phys. **34** (1963) 153.

So 88 R.N.S. Sodhi, W.M. Lau and S.I.L. Ingrey; Surf. Interface Anal. **12** (1988) 321.

Sp 79 W.E. Spicer, P.W. Chye, P.R. Skeath, C.Y. Su and I. Lindau; J. Vac. Sci. Technol. **16** (1979) 1422.

Sp 80 W.E. Spicer, I. Lindau, P. Skeath and C.Y. Su; J. Vac. Sci. Technol. **17** (1980) 1019.

Sp 80b W.E. Spicer, I. Lindau, P. Skeath, C.Y. Su and P.W. Chye; Phys. Rev. Lett. **44** (1980) 420.

Sp 82 W.E. Spicer, S. Eglash, I. Lindau, C.Y. Su and P. Skeath; Thin Solid Films **89** (1982) 447

Sp 86 W.E. Spicer, T.J. Kendelewicz, N. Newman, K.K. Chin and I. Lindau; Surf. Sci. **168** (1986) 240.

St 71 Y.E. Strausser and J.J. Uebbing; Varian Chart of Auger electron Energies (Varian Ass., Palo Alto, USA, 1971).

St 81 R.A. Stall, C.E.C. Wood, K. Broad, N. Dandekar, L.F. Eastman and J. Devlin; J. Appl. Phys. **52** (1981) 4062.

St 81b J.W. Steeds, G.M. Rackham and D. Mertonlyn; Inst. Phys. Conf. Ser., No. **60** (1981) 387.

St 90 G. Stremsdoerfer, C. Calais, J.R. Martin, P. Clechet and D. Nguyen; J.Electrochem. Soc. **137** (1990) 835.

St 90b G. Stemsdoerfer, J.R. Martin, P. Clechet and D. Nguyen; J. Electrochem. Soc. **137** (1990) 256.

Digitised by the Department of Library Services in support of open access to information, University of Pretoria, 2021

Sz 81 S.M. Sze; Physics of Semiconductor Devices (Second edition) (John Wiley & Sons, New York, USA, 1981).

Sz 82 M. Szymonski; Nuclear Instruments and Methods, 194 (1982) 523.

Ta 80 J.L. Tandon, C.G. Kirkpatrick, B.M. Welch and P.Fleming; Laser and Electron beam Processing of Materials, eds. C.W. White and P.S. Peercy (Academic Press, New York, USA, 1980) 487.

Ta 82 E. Taglauer; Appl. Sur. Sci. **13** (1982) 803.

Te 69 L.E. Terry and R.W. Wilson; Proc. IEEE **57** (1969) 1580.

Te 77 C. Tejedor, F. Flores and E. Louis; J. Phys. C: Solid-State Phys. **10** (1977) 2163.

Ti 83 S. Tiwari, T.-S. Kuan and E. Tierney; Int. Elec. Dev. Mtg., Technical Digest. (1983) 115.

To 83 P.J. Topham, D.K. Skinner and B.J. Sealy; Inst. Phys. Conf. Ser. Section 3, **67** (1983) 183.

Tr 86 P. Trung-Dung and M. Laznicka; Electrotech. Cos. 37 (1986) 345.

Ts 80 B.Y. Tsaur; Proc. Symp. on Thin Film Interface and Interactions, eds. J.E.E. Baglin and J.M. Poate (The Electrochemical Society, Princeton, NJ, USA, 1980) Vol. 2, 205.

Ts 80b J.C. Tsang, A. Kahn and P. Mark; Surf. Sci. **97** (1980) 119.

Ts 81 W. Tseng, A. Christou, H. Day, J. Davey and B. Wilkins; J. Vac. Sci. Technol. **19** (1981) 623.

Ts 83 S. Tsou, W. Wang, C. Lin and G. Xia; Ion implantation: Equipment and Techniques; Proc. of 4th Internat. Conf., eds. H. Ryssel and H. Glawisching (Springer-Verlag, Berlin, Germany, 1983) 538.

Ts 84 K. Tsutsui and S. Furukawa; J.Appl. Phys. **56** (1984) 560.

Ts 86 C.T. Tsai and R.S. Williams; J. Mater. Res. **1** (1986) 820.

Digitised by the Department of Library Services in support of open access to information, University of Pretoria, 2021

Tu 80 T.W. Turner, J.C.C. Fan and J.J. Hsieh; Appl. Phys. Lett. **37** (1980) 400.

Tu 82 C.W. Tu and A.R. Schlier; Appl. Surf. Sci. **11/12** (1982) 355.

Ty 84 M.S. Tyagi; Metal-semiconductor Schottky barrier juntions and their applications, ed. B.L. Sharma (Plenum Press, New York, USA, 1984) 1.

Ue 70 J.J. Uebbing; J. Appl. Phys. **11** (1970) 802.

Wa 31 C. Wagner; Phys. Z. **32** (1931) 641.

Wa 71 J.N. Walpole and K.W. Nill; J. Appl. Phys. **42** (1971) 5609.

Wa 81 J.F. Wager, D.L. Ellsworth, S.M. Goodnick and C.W.J. Wilmsen; J. Vac. Sci. Technol. **19** (1981) 513.

Wa 83 J.F. Wager, K.M. Geib, C.W. Wilmsen and L.L. Kazmerski; J. Vac. Sci. Technol. B.**1** (1983) 778.

Wa 84 J.R. Waldrop; J. Vac. Sci. Technol. B. **2** (1984) 445.

Wa 84b Y-X. Wang and P.H. Hollway; J. Vac. Sci. Technol. B. 2 (1984) 613.

Wa 85 O. Wada; J. Appl. Phys. **57** (1985) 1901.

Wa 88 L.C. Wang, F. Fang, E.D. Marshall and S.S. Lau; Defect and Diffusion Forum **59** (1988) 111.

We 78 G. Weimann and W. Schlapp; Phys. Stat. Sol. (a). 50 (1978) K219.

We 79 G. Weimann; Thin Solid Films **56** (1979) 173.

We 81 J.G. Werthen and D.R. Schifres; J. Appl. Phys. **52** (1981) 1127.

Wh 78 A.M. White, A.J. Grant and B. Day; Electron. Lett. 14 (1978) 409.

Wi 75 R.H. Williams and I.T. McGovern; Surf. Sci. **51** (1975) 14.

Digitised by the Department of Library Services in support of open access to information, University of Pretoria, 2021

Wi 77 R.H. Williams, R.R. Varma and A. McKinley; J. Phys. C: Solid-St. Phys. **10** (1977) 4545.

Wi 77b M. Wittmer, R. Pretorius, J.W. Mayer and M.-A. Nicolet; Solid- St. Electron. **20** (1977) 433.

Wi 78 C.W. Wilmsen and R.W. Kee; J. Vac. Sci. Technol. **15** (1978) 1513.

Wi 78b R.H. Williams, V. Montgomery and R.R. Varma; J. Phys. C. **11** (1978) L735.

Wi 82 R.S. Williams, Solid-St. Commum. **41** (1982) 153.

Wi 82b R.H. Williams; Contemp. Phys. **23** (1982) 329.

Wi 84 R.E. Williams; Gallium Arsenide processing techniques (Altech House, Dedham, MA, USA, 1984).

Wi 85 R.H. Williams; Physics and Chemistry of III-V Compound semiconductor interfaces, ed. C.W. Wilmsen (Plenum Press, New York, USA, 1985).

Wi 86 R.H. Williams, A.B. McLean, D.A. Evans and W.G. Herrenden-Harker; J. Vac. Sci. Technol. B. **4** (1986) 966.

Wi 87 J. Willer and H. Oppolzer; Thin Solid Films **147** (1987) 117.

Wi 87a A.J. Willis; Ph.D. Thesis; Ohmic and Schottky Contacts to GaAs for device applications (UPE, 1987).

Wi 88 J. Willer, D. Ristow, W. Kellner and H. Oppolzer; J. Electrochem. Soc. **135** (1988) 179.

Wo 81 J.M. Woodall, J.L.Freeouf, G.D. Pettit, T. Jackson and P. Kirchner; J. Vac. Sci. Technol. **19** (1981) 626.

Wo 81a J.M.Woodall and J.L. Freeouf; J. Vac. Sci. Technol. 19 (1981) 794.

Wo 82 J.M. Woodcock; Laser and Electron-Beam Interactions with Solids, eds. B.R. Appleton and G.K. Celler (North-Holland, New York, USA, 1982) 665.

Wo 82a J.M. Woodall and J.L. Freeouf; J. Vac. Sci. Technol. 21 (1982) 574.

Digitised by the Department of Library Services in support of open access to information, University of Pretoria, 2021

Wo 87 J.M. Woodall, N. Braslau and J.L. Freeouf; Phys. of Thin Films **13** (1987) 199.

Wr 86 S.L. Wright, R.F. Marks, S. Tiwari, T.N. Jackson and H. Baratte; Appl. Phys. lett. **49** (1986) 1545.

Wu 84 D. Wu, H. Daembkes and K. Heime; Chin J. Semicond. 5 (1984) 99.

Wu 87 J. Wurfl, R.P. Gupta and H.L. Hartnagel; Advanced Processing of Semiconductor Devices **79** (1987) 218.

Wu 89 J. Wurfl, A.G. Nassibian, H.L. Hartnagel, R. Langfeld and C. Maurer; Int. J. Electronics **66** (1989) 213.

Wu 89b K. Wuyts, J. van Grunderbeek, R.E. Silverans, M. Van Hove and M. van Rossum; Appl. Sur. Sci. **36** (1989) 511.

Xi 87 H. Xiaoyuan, Y. Mingren and W. Xun; Chin. Phys. **7** (1987) 854.

Ya 81 E. Yamaguchi, T. Nishioka and Y. Ohmachi; Solid-St. Electron. **24** (1981) 263.

Ya 84 S. Yasuami, Y. Saito and A. Hojo; Japn. J. Appl. Phys 23 (1984) 379.

Yo 80 M.N. Yoder; Solid-St. Electron **23** (1980) 117.

Yo 84 T. Yoshiie, C.L. Bauer and A.G. Milnes; Thin Solid Films **111** (1984) 149.

Yu 68 A.Y.C. Yu and E.H. Snow; J. Appl. Phys. **39** (1968) 3008.

Yu 70 A.Y.C. Yu; Solid-St. Electron. **13** (1970) 239.

Yu 89 L.S. Yu, L.C. Wang, E.D. Marshall, S.S. Lau and T.F. Kuech; J. Appl. Phys. **65** (1989) 1621.

Za 88 D.R.T. Zahn, A.B. McLean, R.H. Williams, N. Esser and W. Richter; Appl. Phys. Lett. **52** (1988) 739.

Zu 86 R. Zuleeg, P.E. Friebertshauser, J.M. Stephens and S.H. Watnabe; IEEE Electron. Dev. Lett. **11** (1986) 603.

Digitised by the Department of Library Services in support of open access to information, University of Pretoria, 2021

LIST OF WORK PUBLISHED DURING THIS STUDY

1. W.O. Barnard and A.J. Willis; Au-Ge/In ohmic contacts to n-type GaAs; Thin Solid Films **165**(1988) 77.

2. W.O. Barnard, J.B. Malherbe and B.M. Lacquet; Formation of ohmic contacts to n-GaAs by ion beam mixing and annealing; Appl. Surf. Sci. **31** (1988) 437.

3. W.O. Barnard, H.J. Strydom, M.M. Kruger, C.Schildhauer and B.M. Lacquet; Characteristics of ion beam mixed and alloyed Au-Ge/Ni ohmic contacts to n-GaAs; Nucl. Instr. and Meth. in Phys. Res. **B35** (1988) 238.

4. H.J.Strydom, W.O. Barnard and A.P. Botha; Angle-dependent X-ray photoelectron spectroscopy studies of epitaxial layers on single-crystal substrates; S. Afr. J. Sci. **84** (1988) 685.

5. J.B. Malherbe, W.O. Barnard, G. Myburg and L.J. Bredell; Auger electron spectroscopy: a review of selected topics; S. Afr. J. Phys. **12** (1989) 13c.

6. H.J. Strydom, A.P. Botha and W.O.Barnard; Dynamic SIMS: applications to semiconductor technology; S. Afr. J. Phys. **12** (1989) 7c.

7. F.D. Auret, W.O. Barnard, G. Myburg and L.J. Bredell; Electrical characterization of Argon ion sputter induced defects in GaAs; To be published in S. Afr. J. Sci. 87 (1991).

8. W.O. Barnard and G. Myburg; Ohmic contacts for GaAs devices; To be published in S. Afr. J. Sci. **87** (1991).

9. W.O. Barnard, J.B. Malherbe and G. Myburg; AES study of InP surfaces subjected to chemical cleaning and Ar^+ sputtering; To be published in S. Afr. J. Phys. (1991).

Digitised by the Department of Library Services in support of open access to information, University of Pretoria, 2021

10. F.D. Auret, L.J. Bredell, G. Myburg and W.O. Barnard; Simultaneous observation of sub- and above threshold electron irradiation induced defects in GaAs; To be published in Japn. J. of Appl. Phys. **30** (1991).

Digitised by the Department of Library Services in support of open access to information, University of Pretoria, 2021